Theoretical and numerical study of microstructure formation in multi-component alloys

A Thesis

Submitted for the Degree of

Doctor of philosophy

in the **Faculty of Engineering**

by

Arka Lahiri

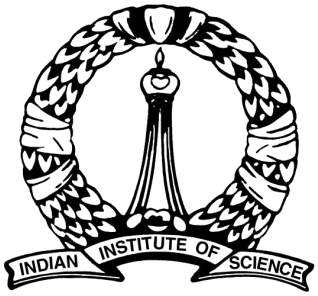

Department of Materials Engineering
Indian Institute of Science
Bangalore – 560 012 (INDIA)

JANUARY 2018

DEDICATED TO

My Parents

Acknowledgements

I begin by thanking my thesis advisors Prof. T. A. Abinandanan and Prof. Abhik Choudhury from whom I learnt almost everything required for the creation of this thesis. Their knowledge, understanding and intuition of the subject is something that I would like to work towards inculcating in the coming years.

With all the academic needs of a student taken care of at IISc, one still yearns for a social life, even more so while pursuing a PhD, given its extremely arduous nature. In this regard I would like to thank a few of my friends and colleagues, without whom life would have been very monotonous. It was a pleasure working with my lab-mates: Rajdip, Naveen, Chaitanya (Chintu), Bhalchandra (Bunty), Arnab, Sukriti, Supriyo, Pramod, Akash, Apaar, Ajay, Abhijeet, Sumeet, Fiyanshu, Pradeep and Kiran. We had great camaraderie and it was always fun to hang out with them. I also had long associations with Sambit and Manu. Including Chaitanya, the four of us were together since our M.E. days. Amongst the numerous friends I had from other departments, Arup from Mechanical Engineering and Santanu from Nano-sciences, deserve special mention. My other friends with whom I had food in the mess were a joyful bunch. It was because of them that I always looked forward to the prospect of eating in mess, despite the usual unpalatable stuff that was served. A big thanks to all of you.

Synopsis

The properties and performance of engineering alloys are a direct consequence of their microstructures. In general, the term microstructure can be treated as a function describing the state of the material system, in terms of the several variables that one can characterize, such as the length scales, composition, size distribution, volume fractions, spatial distribution etc. Amongst the microstructural characteristics of significance is its length scale, which is a parameter characterizing the size of the principal heterogeneity in the microstructure, e.g., the dendrite arm spacings in single phase alloys, and the lamellar widths in multi-phase eutectics. The other crucial parameters are the phase concentrations which are known to have a distinct bearing on the performance of the material. There are also a host of other microstructural factors like the volume fractions and distributions of the phases, which have a profound effect on the eventual structure→property correlations.

In this thesis, our discussion will be related to the formation of microstructures and our principal concern will be related to the length scales that arise in material systems as a result of the processing conditions. In this regard, one can categorize the mechanisms of microstructure formation into two broad categories. The first of these deals with structural formation resulting out of "diffusive instabilities" which lead to the formation of dendrites in single-phase growth and colonies in multi-phase growth like that found in eutectic solidification, discontinuous precipitation etc. The second mechanism results in the formation of composite microstructures formed again during multi-phase growth, but here the microstructural formation occurs as a result of the self-organization of the phases which is mediated by the interaction of the long-range diffusion fields either in the liquid during solidification or in the matrix during reactions like the eutectoid growth. Our work in this thesis will be dealing with the first of these mechanisms and particularly concentrating on the influence of multiple components and contrasting the results against those in binary alloys. Additionally, we will restrict ourselves to pure diffusion controlled growth regimes without incorporating strain-fields originating either from coherency effects at the interface or volumetric expansions during phase transformation. Further, since most of our discussion in the thesis will be utilizing solidification as an exemplary

phase transformation reaction, the preceding assumptions are reasonable because the relevant microstructural scales are much larger than those where the strain-effects due to coherency as well as volumetric expansions are applicable.

Diffusive instabilities originate in Stefan-like problems which one usually encounters in transport phenomena, where typically the velocity of the interface is related to the gradients of the respective state variables like "temperature" for heat transport, "chemical/diffusion potential" for mass transport. This condition is commonly referred to as the "Stefan-condition", which for the case of mass transport in a binary alloy where diffusion is restricted to the liquid writes as,

$$V\left(c^l - c^s\right) = -D^l \frac{\partial c^l}{\partial n}\bigg|_{interface}, \tag{1}$$

where c^s and c^l are the equilibrium phase concentrations of the precipitate and the matrix. V is the velocity of the interface, D^l the solute diffusivity in the liquid and n denotes the unit normal at the interface pointed outwards into the parent phase. As a result of this condition, re-distribution of material from the solid to the liquid which is proportional to the velocity V, leads to the generation of a solutal boundary layer ahead of this interface, leading to a "steady-state" condition where the interfacial compositions do not change with time. In other words in a diffusion controlled regime, the velocity of the interface is directly proportional to the strength of the solutal gradients that are developed in the liquid. A perturbation of this "steady-state" interface, leads to the the modification of the chemical potential gradients ahead of the interface, which makes the gradients ahead of the protrusions in the solid more favorable for growth than regions in the trenches leading to a positive feedback to the growth of such instabilities. Therefore, an understanding of the nature of solutal boundary layers is critical to the investigation of the propagation of these instabilities. This problem has been studied by Mullins-Sekerka [1] in binary alloys and we will refer to this as the MS theory hereafter in the thesis. This problem has also been studied through simulations using boundary integral methods and phase-field models. Our emphasis in this thesis is going to be extension of these theories and numerical modeling approaches based on phase-field methods, generically to multi-component alloys.

A principal difference between binary and multi-component alloys can be appreciated by noting the governing equations and the Stefan-boundary condition. In a binary alloy, fixing the far-field composition and the temperature, the velocity V of the interface is the only unknown in the problem, which is determined by solving the diffusion equation in conjunction with the

Stefan condition and the far-field boundary condition. This solution is the classical Zener solution [2]. In contrast to Eq. 1, the Stefan condition at the interface for a multi-component system writes as,

$$V\left(c_i^l - c_i^s\right) = -D_{ij}\frac{\partial c_j^l}{\partial n}\bigg|_{interface}, \tag{2}$$

where, the subscript i denotes the i-th component, and the solute diffusivity is now a matrix whose (i,j)-th component is given by D_{ij}. So, for example in a ternary system, there are two independent Stefan-conditions at the interface for each of the components, which must be satisfied together. In general, there will be $K-1$, independent Stefan conditions, K being the number of components in the system. This implies that, once the far-field compositions and the temperature is fixed, the velocity V must be consistent together with all of the respective Stefan conditions for each of the components. This is possible only by allowing the selected interfacial phase-equilibria to be a function of the growth conditions, which then allows a self-consistent determination of the both the interfacial compositions as well as the velocities which satisfies all of the Stefan- conditions. This is also thermodynamically consistent, because in any system higher than a binary, two-phase equilibria is multi-valued, and thereby there are multiple possibilities of the interfacial compositions for the same temperature, in contrast to binary alloys. A natural consequence of this is that the boundary layers in a multi-component alloy are a much stronger function of solute diffusivities in contrast to binary alloys where equilibrium phase concentrations are known *a-priori* from the phase diagram. Therefore, the development of diffusive instabilities which arise as a result of the perturbation of these solute boundary layers and thereby the length-scales that arise are more strongly related to not only the processing conditions but also the kinetic parameters such as the diffusivity of the elements.

In this thesis, we firstly investigate steady-state growth process followed by the study of unstable microstructure formation. We repeat such a procedure for both single-phase and multi-phase, lamellar growth. In single phase growth, we firstly extend the Zener solutions of steady-state growth for any generic multi-component alloy. Thereafter, we perform the linear stability analysis of the steady-state growth problem, by extending the Mullins-Sekerka problem for the any generic multi-component alloy, for both isothermal and directional solidification conditions. Subsequently, we study the growth of well-developed dendritic structures, far into the non-linear regime, where we also extend, classical LGK [3, 4] theories of dendritic growth for application to multi-component alloys.

For two-phase and in general multi-phase eutectic growth, the corresponding steady-state

solution for directional solidification is provided analytically by performing the Jackson-Hunt analysis for multi-component alloys. Here again, we have investigated the influence of solute diffusivities not only in determining the undercooling at the interface, but also the volume fractions during growth. Subsequently, we have performed a phase-field simulation study of the growth features during the development of diffusive instabilities in multi-phase growth situations which typically arise in multi-variant eutectics, where usually a solutal boundary layer of one or more elements develops over time. The perturbation of the two/multi-phase front then behaves in a manner similar to that discussed during single phase growth.

In the following, we describe briefly the particular details in each of the above studies and the novel results obtained in each of them.

Single phase growth in multi-component alloys in the scaling regime

In multi-component systems, during diffusion controlled growth of a precipitate from a supersaturated matrix, differential diffusivities will lead to selection of tie-line compositions different from the thermodynamic tie-line containing the alloy composition. In this study [5], we address the multi-component version of the growth problem by extending Zener's [2] theory, and derive analytical expressions for predicting tie-lines and composition profiles in the matrix during growth of planar, cylindrical and spherical precipitates for independent as well as coupled diffusion of solutes in the scaling regime. Our analytical derivations do not assume an *a-priori* knowledge of all the possible equilibrium tie-lines in the system, as we directly invoke the information about the variation of the free energy as a function of phase compositions in our calculations. This renders our analytical method to be easily extensible to alloy systems with any number of components with an arbitrary diffusivity matrix. We confirm our calculations by sharp interface and phase field simulations in a ternary setting, in which we also extend the tie-line and growth constant predictions for two well-known limiting cases, namely partition and negligible partition under local equilibrium (PLE and NPLE). In the following figure (Fig. 1), we present the predictions of tie-lines selected in a ternary alloy (A is the solvent; B and C are the solutes) as a function of alloy supersaturation (ν).

In a nutshell, the analytical technique developed here not only predicts the velocity of the interface separating the parent and the product phases, but also completely describes the solute boundary layer ahead of the interface, in the parent phase. This description of the solute boundary layer is utilized in our following study of diffusive instabilities in multi-component

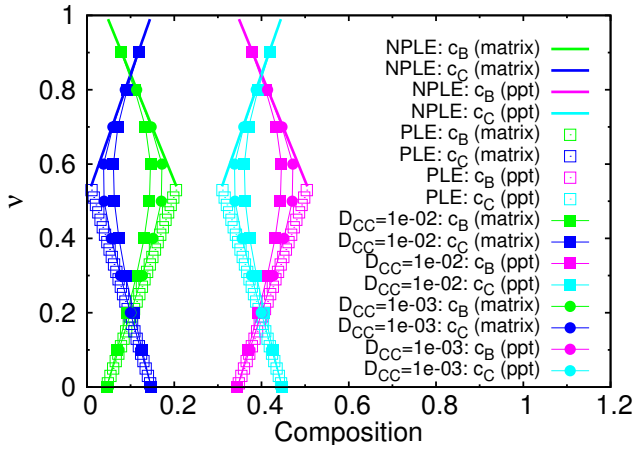

Figure 1: Tie-lines as a function of ν which depicts that the predictions from local equilibrium approaches the NPLE and PLE predictions as the diffusivity ratios (D_{CC}/D_{BB}) become smaller and smaller ($D_{BB} = 1$). The bulk compositions lie on the tie-line $c_B^\alpha = 0.044935$, $c_C^\alpha = 0.147450$, $c_B^\beta = 0.344935$, $c_C^\beta = 0.447450$.

alloys.

Diffusive instabilities during single solid phase alloy solidification

Random perturbations of the interface during solidification of a single solid phase by a planar interface leads to the perturbation of the solutal boundary layers too, in turn setting up diffusion feedback loops which promote amplification of these perturbations. The effect of the interfacial energy is to hinder the growth of these perturbations, which in combination with the accentuating effect of diffusion, constitutes the classic Mullins-Sekerka instability of solidification. Diffusive instabilities of the Mullins-Sekerka type are one of the principal mechanisms through which microstructures form during solidification. In this study [6], we perform a linear stability analysis of a perturbed planar interface, where we derive analytical expressions to calculate the amplification rate of each wavelength constituting the perturbation in multi-component alloys under directional and isothermal solidification conditions. This allows the determination of the "dispersion curve" characterizing the behavior of the instabilities in the linear regime. Subsequently, we confirm our calculations using phase-field simulations for different choices of the inter-diffusivity matrices. An example of such a calculation performed for a quaternary alloy (A,B and C are the solutes; D is the solvent) is presented in Fig. 2. The quantity $\dot{\delta}/(\delta V \omega_{max})$ denotes the normalized rate of amplification of a wave with wavenumber $\omega(= 2\pi/\lambda$; λ is the

corresponding wavelength), and amplitude δ, whose time derivative is denoted by $\dot{\delta}$. V denotes the velocity of the steady-state planar front. ω_{max} is the wavenumber corresponding to the highest normalized growth rate $\dot{\delta}/(\delta V \omega_{max})$. Thereafter, we highlight the characteristics of

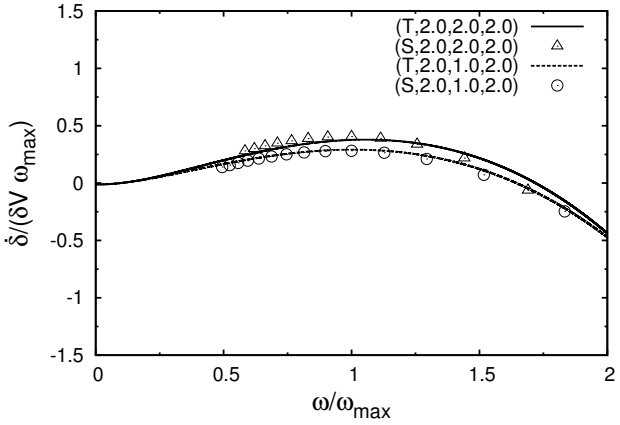

Figure 2: $\dot{\delta}/\delta$ versus ω from phase-field and theoretical calculations. The growth rates of the perturbation are scaled with $V\omega_{max}$, while the ω is scaled with ω_{max}, where $\omega_{max} = \dfrac{2\pi}{\lambda_{max}}$, λ_{max} being the maximally growing wavelength (in the phase-field simulation). In the legends the titles T : stands for 'Theoretical', while S : stands for 'Simulation'. The three numbers following T and S in the legends represent the values of D_{AA}, D_{BB} and D_{CC}, respectively.

the instability upon change of the diffusivity matrix and the velocity. Finally, we also depict conditions for absolute stability of a planar interface under directional solidification conditions.

Our study of the Mullins-Sekerka instability in multi-component alloys is a linear stability analysis and hence its predictions are only restricted to the very early stages. The growth of these interfacial perturbations eventually lead to the formation of cells and dendrites, which are the most commonly observed solidification microstructures. In our next study, we take up the problem of isothermal dendrite growth in multi-component alloys.

Isothermal dendrites in multi-component alloys

In this study, we develop a theory for determining the dendrite tip growth velocity, the dendrite tip radius and the phase concentrations during free dendrite growth in an uniformly undercooled melt. In this regard, our work is an extension of the classic Ivantsov theory for dendrite growth to multi-component alloys. Continuing with the previous cases requiring the solution to the diffusion problem ahead of a planar interface, here, we solve the diffusion problem ahead of a parabolic interface. Also, we generalize the well known estimates for the dendrite tip-radius, like

"Marginal Stability", and "Microsolvability" to multi-component alloys. Phase-field simulations are performed not only to provide an estimate for the tip-radius to be used in our analytical calculations, but also to provide an independent assessment of the accuracy of our theoretical predictions. Fig. 3 shows a comparative study of the variations of the dendrite tip velocity (V), and dendrite tip-radius (R_{tip}) with the undercooling (ΔT). The figure legends indicate the different sources of estimates of R_{tip}.

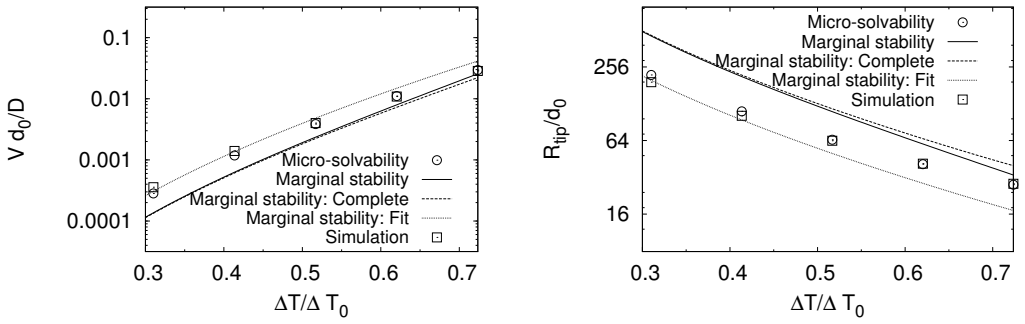

(a) (b)

Figure 3: Plots showing the variation of, (a)tip velocity (V), (b) tip radius (R_{tip}) with undercooling (ΔT). The diffusivity matrix is diagonal with $D_{AA} = 2.0, D_{BB} = 1.0$, and the anisotropy strength is $\zeta = 0.01$. The quantities ΔT_0 (the freezing range), d_0 (the capillary length), and d_0^2/D (D denotes diffusivity) are chosen to scale temperature, length, and time respectively.

This concludes the topics we have considered involving the formation of a single product phase from a parent phase. The next couple of studies concern the eutectic transformation leading to the formation of multiple solid phases from the liquid phase.

Theoretical and numerical investigation of multi-phase growth in a multi-component system

A steady-state eutectic transformation involves the growth of several solid phases in a coupled manner from the liquid. For a lamellar morphology of the solidifying phases, the determination of the lamellar width which is selected by the system is important as it sets the length scale of the resultant microstructure.

For directional solidification conditions, a straight-forward extension of the Jackson-Hunt theory for multi-phase growth where the number of components exceeds the number of solid

phases becomes difficult on account of the absence of the required number of equations to determine the boundary layer compositions ahead of the interface.

In this work [7], we therefore revisit the Jackson-Hunt(JH) [8] type calculations for any given situation of multi-phase growth in a multi-component system and self-consistently derive the variations of the compositions of the solid phases as well as their volume fractions, which grow such that the composite solid-liquid interface is isothermal. In this regard, we have relaxed two of the assumptions of the classical Jackson-Hunt solution. In their calculations, Jackson and Hunt derive closed form solutions for the undercooling at the solid-liquid interface using the assumption that the volume fractions of the solid-phases are still given by the lever rule pertaining to the alloy composition at the eutectic temperature, additionally assuming that the compositions of the solid and the liquid phases are the same as the ones predicted by the phase diagram at the eutectic temperature. These assumptions are reasonably valid for low-Peclet number growth, but results show deviation in binary alloys both under conditions of higher growth velocities as well as situations where the densities of the phases are markedly different. In our work we relax both of these assumptions relating to the constancy of the volume fractions and the phase compositions, while still retaining two of the other assumptions, the first which assumes the solid-liquid interface to be planar for the solution to the diffusion-field and second the condition of isothermal solid-liquid interface for the closure of the equations. This allows us to unify the JH calculation schemes for both in-variant as well as multi-variant eutectic reactions. The derived analytical expressions are then utilized to study the effect of dissimilar solute diffusivities and interfacial energies on the undercoolings and the solidified fractions. We also perform phase field simulations to confirm our theoretical predictions and find a good agreement between our analytical calculations and model predictions for model symmetric alloys as well as for a particular Ni-Al-Zr alloy. In Fig. 4, we present the variations of undercoolings (ΔT) at the eutectic growth front and the phase fractions (η_α), with the lamellar width (λ) in a ternary alloy for different choices of the solute diffusivities.

Having studied the steady-state growth behavior of eutectics in multi-component alloys, we move on to the study of an unstable pattern formation phenomenon in similar systems, as described below.

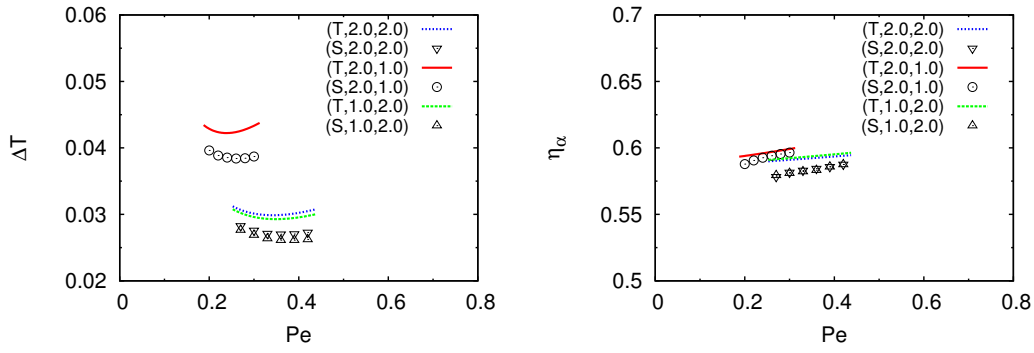

(a) (b)

Figure 4: Plots showing variations of (a)ΔT, and, (b) η_α, with Peclet number ($Pe = \lambda V/2D$), during two-phase growth in a ternary alloy. D represents the diffusivity of the fastest moving solute, and V the sample pulling velocity during directional solidification. The first element from the figure legends denotes whether the data comes from theory (T) or simulations(S), with the following two numbers denoting the solute diffusivities in this ternary alloy.

Eutectic colony formation in systems with interfacial energy anisotropy

Instability of a binary eutectic solidification front to morphological perturbations due to rejection of a ternary impurity leads to the formation of eutectic colonies [9, 10]. Whereas, the instability dynamics and the resultant microstructural features are reasonably well understood for isotropic systems, several experimental observations point to the existence of colonies in systems with anisotropic interfaces. In this study [11], we extend the understanding of eutectic colonies to anisotropic systems, where certain orientations of the solid-liquid or solid-solid interfaces are associated with a lower free energy than the others. Through phase field simulations in 2D and 3D, we have systematically probed the colony formation dynamics and the resulting microstructures, as functions of the pulling velocity and the relative orientation of the equilibrium interfaces with that of the imposed temperature gradient. We find that in 2D, stabler finger spacings are selected with an increase in the magnitude of anisotropy introduced, either in the solid-liquid or in the solid-solid interface. The fingers have a well-defined orientation for the case of anisotropy in the solid-liquid interface, with no fixed orientations for the lamellae constituting the colony. For the case where anisotropy exists in the solid-solid interface, the lamellae tend to orient themselves along the direction of the imposed temperature gradient, with tilted solid-liquid interfaces from the horizontal. The 3D simulations reveal existence of eutectic spirals which might become tilted under certain orientations of the equilibrium inter-

faces. Our simulations are able to explain several key features observed in our experimental studies of solidification in Ni-Al-Zr alloy. In Fig. 5, we present eutectic colony morphologies observed in systems with anisotropic solid-solid as well as solid-liquid interfaces.

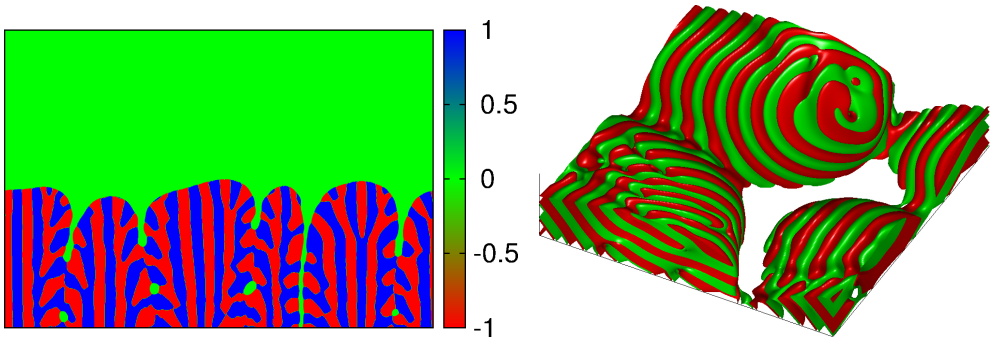

(a) (b)

Figure 5: Plots showing, (a) 2D simulation with anisotropic interfaces between the two eutectic solids, resulting in vertically oriented lamellae, (b) 3D simulation with anisotropic solid-liquid interfaces leading to tilted spirals.

Contents

List of Figures

List of Tables

Chapter 1

Introduction

The process of microstructure formation involves transformation of phases, mediated by the motion of the interface separating the parent from the product phases. Phase transformations can be "diffusional" or "diffusionless". By "diffusional", we imply that the transformation requires diffusion of solute atoms over distances which are several order of magnitudes larger than interatomic distances. In diffusional phase transformations the motion of the interfaces(or the rate of transformation) is controlled by elemental re-distribution ahead of the growing front because the transformation is usually characterized by parent and product phases differing significantly in phase concentrations, e.g., the austenite-ferrite transformation in steels. On the other hand, in "diffusionless" transformations, atoms move in a well-coordinated fashion at the interface, in response to driving forces, to affect the change of structure required to create the product phase from the parent phase. A classic example would be the martensitic transformation observed in steels.

Considering "diffusional" transformations, the process of microstructure formation during growth of a single phase from a supersaturated (or undercooled) parent phase is usually through an instability of the interface separating the parent and the product phases. In order to understand the onset of an instability, we consider the process of diffusion controlled growth from the very early stages. As a supercritical nuclei of the product phase begins to grow, it either rejects or consumes solute from the parent phase resulting in the creation of a solute boundary layer ahead of the interface in the matrix. The process of creation of the solute boundary layer is identified as the "initial transient" phase of growth, which terminates when the maximum in the boundary layer composition is invariant. At this point, local equilibrium has been established at the interface, with both the parent and the product phases assuming concentrations at the interface which are in equilibrium with each other. This marks the onset of the "quasi-steady-state" phase of growth where the interfaces separating the two phases propagate self-similarly

with a solute boundary layer ahead of the interface proportional to the solute diffusivities and inversely proportional to the velocity of the interface.

Due to the disturbances in the surrounding thermal and solute fields, an interface separating the parent and the product phases develops random infinitesimal perturbations. In such a perturbed state, the solute boundary layers are no longer uniform across the interface, and the crests of the perturbations experience sharper concentration gradients ahead, than the troughs. This sets up a diffusion feedback loop which causes the crests to grow much faster, resulting in an amplification of the perturbation with time leading to some of the most commonly observed features in microstructures, e.g., cells and dendrites seen during solidification. The dissimilar diffusion rates at different points on the interface amplifying the instability does not operate unhindered. A perturbed interface is also associated with dissimilar interfacial curvatures at different locations. As a result of the Gibbs-Thomson effect, the interfacial compositions are so modified that softens the sharper concentration gradients at the crests and steepens the softer concentration gradients at the troughs. Thus, capillarity acts as a force restraining the growth of the perturbations. This is the classic Mullins-Sekerka type of instability [1] where the solute diffusion works to accentuate the perturbations while the interfacial energy tries to attenuate them.

A second way by which microstructures form is by the coupled growth of the multiple product phases from a single parent phase. Here, the diffusion also happens laterally, just ahead of the growing interface. The solutes rejected by one of the product phases is consumed by another phase just adjacent to it. This re-distribution of solute leads to steady-state boundary layers ahead of each of the individual phases which in binary alloys are typically balanced such that the volume fraction-weighted sum of the solid-phase compositions equates to the far-field composition. Thus, the cumulative boundary layer ahead of the composite front is usually much smaller than that occurring in single phase growth, unless in asymmetric situations such as growth in off-eutectic/eutectoid compositions or asymmetric interfacial or kinetic properties. This situation is modified however, when a ternary impurity is added which partitions into the liquid during growth of both the solid-phases. This re-distribution then leads to a solutal boundary layer, which behaves in a manner similar to single-phase growth, where perturbations at the interface may get magnified under suitable conditions. Examples of such a transformation would be the formation of multi-phase cells and dendrites during solidification.

The microstructures obtained by the transformations described above have been widely seen experimentally, in both binary as well as in multi-component alloys. Exemplary studies of dendrite growth during single phase solidification would include the one by Huang and Glicksman [12] in binary systems and the study by Galenko et al., [13] in a ternary Ni-Al-Zr

alloy. Experimental observations of binary eutectics include those by Ginibre et al. [14] in CBr_4-C_2Cl_6, and in ternary systems by Contieri et al., [15] in an Nb-Ni-Al system. Colonies in eutectic system have been experimentally observed by Akamatsu et al., [10].

These phenomena of microstructure formation are also theoretically well understood for single component and binary alloy systems. Seminal studies would include the works by Zener [2] on steady-state single phase growth, Mullins and Sekerka [1] on diffusive instabilities of the solidification front in a binary alloy, Langer and Müller-Krumbhaar on dendritic solidification, Jackson and Hunt [8] on the undercooling of a growing eutectic front for a given lamellar spacing. Eutectic colonies are only seen during non-invariant reactions in multi-component alloys. Plapp and Karma [16] performed phase-field simulations to investigate the simplest scenario of colony formation in a ternary alloy.

Despite the existing theoretical understanding of microstructure formation in binary alloys, multi-component alloys present a higher level of complexity which merits a thorough study. In order to understand the source of this complexity, we consider the growth of a single solid phase from a parent phase in a binary alloy. It is a two-phase equilibrium in a binary alloy and hence has only a single degree of freedom. Thus, the temperature at a growing interface, completely determines the phase concentrations that are in local equilibrium at the interface. But a similar transformation in a multi-component alloy with K components ($K-1$ of them being independent) is associated with $K-1$ degrees of freedom. Hence, the phase concentrations are no longer determined by equilibrium thermodynamics alone, but in combination with the kinetic parameters of solute diffusivities as well. As the selection of the velocity of the interface and the choice of the equilibrium compositions happens concurrently, they are highly interdependent. Thus, the selection of equilibrium compositions is another mode by which the solute diffusivities exert its influence on the velocity of the interface in a multi-component alloy. This leads to formation of solutal boundary layers at the interface in multi-component alloys which are much stronger functions of solute diffusivities, compared to the same in binary alloys. The fact that the relative fluxes of the solutes at the growing interface determines the equilibrium compositions of the phases is a phenomenon which is not observed in binary alloys and only seen in multi-component systems will assume significance in all our ensuing discussions.

Similar observations also hold true for multi-phase growth in multi-component alloys, where solute diffusivities can play a dominant role in deciding the dynamics. This is clearly evident for multi-phase growths which are multi-variant (associated with a degree of freedom greater than or equal to 1) as the arguments enunciated in the previous paragraphs can be directly applied.

Multi-component alloys are different from binary alloys as the solute diffusivities play a

much stronger role in microstructure formation in the former than in the latter. Furthermore, multi-phase systems in such alloys display a much richer variety in the microstructures that are observed compared to a binary system. Despite several interesting studies on understanding microstructure formation in such alloys, the intricacies of the processes have not yet been completely understood. In this thesis, we explore the above described mechanisms of microstructure formation in such alloys. We derive analytical theories and perform numerical simulations to understand the effect of solute diffusivities in determining the various characteristics of these transformations. As we have discussed earlier, in order to gain an understanding of the diffusive instabilities during growth of a single phase or multiple phases, it is essential to study the properties of the solute boundary layers whose perturbation triggers the onset of the instability. Thus, in this thesis, we present detailed studies of the steady-state growth phenomenon first, followed by a study on the instabilities in such systems and follow the same pattern for both single-phase and multi-phase growth. Due to the rich variety of transformations observed in multi-component systems undergoing solidification, most of our analytical and numerical studies are carried out in that context.

Our thesis begins with a study of steady-state single phase growth in multi-component alloys. This is followed by a study on diffusive instabilities in solidifying multi-component systems. Our consideration of single phase growth in multi-component alloys concludes with the problem of free dendritic growth in uniformly undercooled alloys. We also consider the problem of multi-phase growth by first studying the steady-state dynamics, following it up with a study on unstable pattern formation in such systems. In each of the following paragraphs, we introduce each of these problems and present a brief outline of the studies we have conducted to advance the understanding of each of these phenomena. As our techniques of choice are theoretical in nature, i.e., analytical and numerical, we present a motivation for our work from a similar perspective. We present a detailed review of all the experimental, analytical and numerical studies relevant to our work in the succeeding Chapter of "Literature Review". We begin with the problem of steady-state single phase growth in multi-component alloys.

1.1 Single phase growth in multi-component alloys in the scaling regime

The problem of isothermal steady-state single phase growth of a product phase from supersaturated/undercooled parent phase is a problem that is of relevance to both solid-state transformations and solidification. Quenching a high temperature phase to a lower temperature where

a two-phase mixture is stable, makes the original alloy supersaturated with respect to one or more solutes. During an isothermal anneal at that temperature, second phase nuclei forms, grows and coarsens. The same life-cycle can be observed during solidification in an uniformly undercooled melt too. In this chapter, we will present a theory of diffusion controlled growth of the second phase nuclei under isothermal conditions. Though, our discussion will be presented in the parlance of precipitate growth from a supersaturated matrix in solid-state transformation, it is equally applicable to solidification in an uniformly undercooled melt. We begin our introduction to this problem with the problem of precipitation in binary alloys.

Zener [2] showed that in a binary alloy, during steady-state growth, a unique scaling constant can be identified depending on the matrix supersaturation and the solute diffusivity, which multiplies the elapsed time to give the square of the displacement of the interface. The composition of the phases at the interface which are in local equilibrium with each other are determined completely by the temperature at the interface. Thus, the problem of single phase growth in a binary couple involves the determination of a single quantity which is the scaling constant, which once determined can be used to describe all the other characteristics of single phase growth in such alloys, e.g., the composition fields ahead of the growing interface.

On the other hand, such a two-phase equilibrium in a multi-component alloy is multi-valued and the choice of the equilibrium phase concentrations are determined by a combined effect of solute diffusivities and the supersaturations in the matrix in each of the components. Thus, during single phase growth in multi-component alloys, the phase concentrations are also unknowns in addition to the scaling constant. Seminal theoretical studies to solve this problem include the ones by Coates [17, 18, 19], where the inverse problem of determining bulk alloy compositions which equilibrate to pre-determined phase concentrations, for a given diffusivity matrix, in a ternary alloy is addressed. Bourne et al., [20] employed a parameterized knowledge of the tie-lines in a two phase region in a ternary phase diagram to solve for the diffusivity ratios in such an alloy, which equilibrates to a particular tie-line, for a given supersaturation of the matrix. While all of these approaches do address the problem of considering the extra degree of freedom with respect to the choice of equilibria, their approaches require parameterization of the two-phase regions of the phase diagrams, whereby the variation in the equilibrium compositions of the product phase can be coupled to those of the parent phase using the geometric properties of the tie-lines as well the co-existence lines. This makes it complicated however, to extend the solution to any generic multi-component systems.

Thus, this brings us to the motivation of this chapter where we extend the Zener solution of precipitate growth in a binary alloy to a generic multi-component alloy. Our contribution in this chapter is described as follows:

Firstly, we derive an analytical theory for diagonal as well as for diffusivity matrices containing off-diagonal terms (for both planar and curved geometries), following previous work of Coates [17, 18] and Bourne et al., [20], that allows a direct calculation of the quantities of interest (tie-lines and composition fields in the matrix) for a given bulk alloy composition and diffusivity matrix. To this end, we have employed nothing more than the basic thermodynamic information associated with the variation of the free-energies of the phases with compositions, which differentiates it from the previous approaches [20]. Additionally, it presents a more elegant way of prediction of tie-lines given the bulk alloy composition and a diffusivity matrix. Furthermore, it allows for an easy extension to any given multi-component alloy. Our theory of precipitate growth can therefore be seen as a generalization of the earlier studies [17, 18, 20] where it is specific to ternary systems.

Secondly, we formulate a multi-component phase field model based on a grand-potential formalism [21, 22] to study precipitate growth which is described in Chapter 3. The model itself has the possibility to incorporate information from thermodynamic databases in an effective manner [23], which will allow its subsequent utilization for study of precipitation process in real systems. The phase field results are then compared with both the analytical theory and an independent sharp interface (front tracking) numerical model.

A note about the role of critical comparison between sharp interface and phase field results is in order. Experimental validation of growth theory is difficult even in binary alloys due to overlap of the solute diffusion fields from neighboring precipitates. In multi-component alloys, however, this problem is made much worse by the overlap in the diffusion field of the fastest diffusing species well before that of the slower species enters the scaling regime. Thus, the only viable test of the theory is by comparison between its results with those from numerical simulations from a model.

The converse also holds: the phase field model needs to be validated before it can be applied to more realistic systems (e.g., by incorporating thermodynamic information from databases) and / or more complicated systems (e.g., simultaneous precipitation of multiple phases). A critical comparison of its results against those from sharp interface results serves this purpose.

The natural consequence of the discussion beforehand about the selection of the local interfacial compositions being a function of the diffusivity matrices, are two limiting cases which arise when the diffusivity of one of the elements is very different from the others. For example let us consider a ternary setting where one of the elements is much faster than the other. Given the two Stefan conditions that need to be satisfied at the growing interface, in the slow growth regime which is achieved in the limit of vanishing super-saturations, the diffusion potential gradients of the faster moving species would need to be insignificantly small(given the higher

diffusivity) such that the two Stefan-conditions are satisfied. Conversely, under fast growth conditions achieved at higher super-saturations, the growth conditions are controlled by the gradients of the faster moving species while the slower moving species is assumed to have the largest possible solutal gradients which occur for the conditions of negligible partitioning of the slow-moving species. Coates [19] formalizes these limits of local equilibrium. The two limiting cases called "partition under local equilibrium" (henceforth referred to as "PLE") and "negligible partition under local equilibrium " (henceforth referred to as "NPLE") are the relevant limits approached as the diffusivity differences become larger for low and high supersaturations in the matrix, respectively. As the final aspect of our study, we incorporate the constraints characterizing PLE and NPLE in our analytical calculations and calculate the tie-lines and growth constants corresponding to these approximations for a given bulk alloy. Coupled with our calculations performed for local equilibrium, this allows us an understanding of the regimes over which the PLE and NPLE limits are valid and the kind of differences in the solute diffusivities at which these limits are appropriate. We additionally restrict our discussion to conditions of local equilibrium, whereby other corresponding limits such as "paraequilibrium" [24, 25, 26] will be reserved for future work. This is primarily because the construct of paraequilibrium theory ideally is relevant where one or more of the constituents diffuse through an interstitial mechanism. This requires a corresponding reformulation of our analytical theory and numerical simulation methods.

Our analytical theory and its predictions alongside those obtained from Phase-field modeling are presented in Chapter 4. This chapter develops a theoretical understanding of the solutal boundary layers observed in steady-state growth in multi-component alloys, which provides the natural premise for understanding diffusive instabilities during single phase growth in multi-component alloys, discussed in the following section.

1.2 Diffusive instabilities during single solid phase alloy solidification

Morphological instability of a solid-liquid interface to small perturbations is the basis for the most commonly observed solidification microstructure of dendrites. Experimentally, a planar solidification front during solidification is usually perturbed, either by random thermal fluctuations or due to interactions with insoluble impurities [27]. An unstable solidification front is characterized by amplification of such interfacial perturbations which ultimately develop into cellular or dendritic structures. Any random infinitesimal perturbation can be thought of as

a linear combination of a multitude of wavelengths of different amplitudes (which are small during early stages). Thus, the stability of a solid-liquid interface to the amplification of these perturbations can be understood by investigating the growth behavior of the individual modes. Mullins and Sekerka in their classical work [1] present a linear stability analysis of an interface perturbed by any generic wavelength and provide expressions for their growth rates for a binary alloy. This allows the determination of the maximally (fastest) growing wavelength that can be approximately related to the length scales in the cellular or dendritic microstructures.

For multicomponent systems, a linear stability analysis assuming no diffusional interaction between solutes of a directionally solidifying ternary alloy is first reported by Coates et al. [28]. The effect of coupled solute diffusivities on the stability of the system to infinitesimal perturbations in directionally solidifying systems is studied by Hunziker [29].

In this chapter, we have three principal aims. Firstly, we derive analytical expressions for the growth rates of the perturbations as a function of imposed wavelengths by performing a linear stability analysis for directional as well as isothermal solidification conditions, in a generic multi-component alloy. Here, while the problem of directional solidification is well posed in that there exists a steady-state condition (constant velocity) for the planar interface which is to be perturbed, the problem of isothermal solidification has a planar growth solution which only admits a relation where the displacement of the interface scales with the square root of time. We show that an equivalent perturbation analysis can be performed for both conditions, notwithstanding this difference in the initial states which are being perturbed. Secondly, we utilize a phase-field model based on a grand-canonical density formulation [21, 22] and validate our analytical calculations for both sets of solidification conditions by performing simulations for a varied set of diffusivity matrices. Thirdly, we comment on the nature of the dispersion curves in terms of the maximal growth rates and maximally growing wavelengths and their variation with the change in the diffusion length scales. Here, we also highlight the conditions for absolute stability which is applicable for directional solidification conditions. This study constitutes Chapter 5 in our thesis.

The amplification of perturbations at the solid-liquid interface under conditions of anisotropic interfacial energy lead to the formation of dendrites, which are the next topic of study in our thesis, and described in the next paragraph.

1.3 Isothermal dendrites in multi-component alloys

As discussed in the previous section, random perturbations of the solidification front in a uniformly undercooled melt gets amplified with time and leads to the formation of dendritic

arms along well-defined crystallographic directions minimizing the extent of the interfacial orientations with higher energy. The dendrite tip-radius (R_{tip}) can be related to the dendrite primary arm spacing, which sets the principal length scale in the microstructure. Thus, an analytical prediction of such a quantity as a function of growth conditions is extremely valuable. This in conjunction with the problem of predicting the dendrite growth velocity (V), and the phase concentrations at the growing interface in a generic multi-component system, constitute an important problem, the one which we take up in Chapter 6.

The theoretical understanding behind the phenomenon of dendrite growth in pure materials begins with the determination of the diffusion fields in the liquid ahead of a single growing dendrite arm (known as "free growth"), which is first presented by Ivantsov [30] (hence forth referred to as "IS" for Ivantsov's solution). Horvay and Cahn [31] also solve the same problem but with a drastically different approach. The solution proposed by Ivantsov [30] fails to predict the dendrite tip velocity V, and the tip-radius R_{tip} uniquely. This is attributed to the lack of consideration of the capillarity in these theories. Langer and Müller-Krumbhaar [32, 33, 34] extend these calculations to binary alloys and also consider the effects of surface tension in proposing an estimate for R_{tip} determined by a balance between the diffusion and capillarity length scales, known as the "Marginal Stability" criterion. Though, the theory by Langer and Müller-Krumbhaar [32, 33, 34], could predict a unique V and tip-radius R_{tip}, they found the parabolic (paraboloid) dendritic interface in 2D (3D) to be unstable to perturbations. Hunziker [29] presented a theory of dendrite growth in directionally solidifying multi-component alloys where they extended the "Marginal Stability" criterion by Langer and Müller-Krumbhaar to a multi-component setting.

The growth of the dendrites along specific crystallographic directions, along with the theoretical instability of the dendritic envelope in an isotropic system, necessitated a consideration of anisotropic interfacial energies in the mathematical description of this problem. As the introduction of anisotropy in interfacial energy renders an analytical solution extremely difficult, it is solved numerically by Kessler and Levine [35]. Their sharp interface calculations confirmed the parabolic shape of the dendrite to be stable with a unique selection of V and R_{tip}. The R_{tip} obtained from their numerical calculation is a function of anisotropy, and this estimate constitutes the "Microscopic solvability" (or the "Microsolvability") criterion.

In this chapter, we present a theory of free dendrite growth during isothermal solidification for any generic multi-component alloy, for any diffusivity matrix. Our work can be seen as a parallel theoretical development for isothermal solidification, to that presented by Hunziker [29] for directional solidification, except for two important differences. By employing thermodynamic relationships to express phase concentrations c_i, as functions of the diffusion potentials μ_i (and

undercooling ΔT), our system of equations is expressed in terms of the unknown diffusion potentials, μ_i, which are conjugate intensive variables to the unknown phase concentrations c_i in [29]. This eliminates the need to invoke the equilibrium tie-line relationships during the solution process, which is always an approximation when considering growth by curved interfaces. Thus, our methodology provides an easy and elegant way to consider any number of components, once the thermodynamic behavior of the phases are available. The second salient feature of our work is the benchmarking of our analytical predictions against those obtained from phase-field simulations. To our knowledge, this has not been undertaken before, and it is through this exercise that we determine the relative accuracies of the various estimates of R_{tip}, e.g., "Marginal Stability" and "Microsolvability". As 3D simulations are computationally expensive especially in multi-component systems, we restrict our analytical derivations and phase-field simulations to 2D only.

This concludes our consideration of microstructure formation by growth of a single phase in a multi-component alloy which is presented in detail in Chapters 4, 5 and 6, and we move on to microstructure formation due to steady-state and unstable growth in multi-phase, multi-component systems in the following paragraphs.

1.4 Theoretical and numerical investigation of multi-phase growth in a multi-component system

Eutectic solidification offers interesting examples of multi-phase microstructural formation wherein two or more phases typically self-organize while growing from the liquid giving rise to a wide array of microstructures with varied morphologies. Theoretically, one of the interesting questions is the investigation of steady-state eutectic growth and establishing the relationship between the undercooling, the spacings and the velocities, which is essentially a relationship between the microscopic length scale that is described by the spacing λ, and the macroscopic diffusion length scale ($2D/V$, D is the diffusivity in liquid, V is the velocity). A very nice review on the developments in the theoretical models for describing eutectic growth as well as its close counterpart in eutectoid growth can be found in [36]. In this regard, one of the most applied theories for directional solidification conditions is the Jackson and Hunt theory (JH) [8], where expressions for the undercooling (ΔT) versus spacing (λ) are derived for given velocities, for both lamellar and rod configurations of growth. The operating scale of the eutectics that may arise in experiments is discussed based on the the minimum undercooling spacing as a marginal stability point. Conditions for transition between rod and lamellae

morphologies is also discussed. Extension of the (JH) formalism for two-phase lamellar growth in ternary alloys, has been attempted by McCartney [37] and Plapp et al. [16], while similar extensions for investigation of invariant growth in three-phase eutectics has been performed by Himemiya and Umeda [38] and Choudhury et al. [39].

The theoretical development as per (JH) firstly provides for a solution to the Stefan problem at the multi-phase solidification front with the assumption of a planar interface. Capillary effects are introduced using the average curvature of each of the solid-liquid interfaces that are calculated with the equilibrium slopes of the solid-liquid interface at the tri-junction point. From this, the average curvature undercooling is computed using the interfacial properties and superposed upon the constitutional undercooling in order to derive the total undercooling at the solid-liquid interface. While the system of equations as posed by Jackson and Hunt are quite generic, the authors impose certain assumptions, in order to simplify the equations and derive closed-form solutions analytically. Two of these assumptions are respectively the constancy of phase compositions as well as volume fractions with undercooling, i.e the values are approximated from the phase diagram at the eutectic temperature.

In general however, these assumptions in the JH theory are valid for low Peclet number ($\lambda V/2D$) growth which is achieved at lower solidification velocities. For higher Peclet numbers, the phase fractions as well as the compositions of the phases change considerably from the values at the eutectic temperature, and thereby need to be accounted for. Trivedi et al., [40] (also referred to as the TMK model) provide solutions in the high Peclet number regime for specific phase diagrams using the more generic analysis of the solute diffusion problem as discussed by Donaghey and Tiller [41].

In multi-component alloys, one of the additional reasons due to which the phase compositions may change from their equilibrium values at the eutectic temperature is due to the difference of solute diffusivities. This can result in modified phase fractions even at the same undercooling, which is in contrast to binary alloys, where the composition of the phases necessarily change only due to a increase in the undercooling. Furthermore, in multi-variant eutectic reactions, where the number of components exceed the number of solid-phases, just the equality of undercoolings at the interface does not present a closure of the systems of equations as in the classical invariant eutectic growth problem, unless certain phase diagram related assumptions are implied as in [37, 16]. This is because the number of boundary layer compositions exceed the number of available equations (equality of phase undercoolings), and requires the solution to the complete solute diffusion problem, without the assumption of the constancy of the phase compositions and phase fractions with undercooling.

A couple of recent theoretical studies in this regard have been presented for two-phase

mono-variant growth. The study by Catalina et al. [42] presents a linearized theory without allowing for the changes in composition in one of the solidifying phases. A more rigorous extension again for multi-component two-phase growth is provided recently by Senninger and Voorhees [43], where they take into account the composition variations of both the solid phases.

In this chapter, we extend the works by Catalina et al. [42] and Senninger and Voorhees [43] and in general the classical JH theory for any given multi-phase configuration in a generic multi-component alloy. While we relax two of the assumptions in the classical (JH) theory relating to the constancy of phase compositions as well as the phase fractions, two other assumptions of planarity of the interfaces to determine the diffusion field as well as the assumption of equal undercooling of the solid-liquid interfaces to effect closure of the equations, is retained. Further, the equality of molar volumes for the components is assumed in both the analytical calculations as well as phase-field simulations that are performed later. An influence of these assumptions are discussed at the end of this chapter. Our work shares the same spirit as [42] and [43], however, one of the major differences is that we relate the deviations of the phase compositions to the departures of the diffusion potentials and temperature and thereby the functional dependence between the variations of the solid and liquid compositions is more elegantly retrieved. In addition, we verify our analytical calculations with phase-field simulations considering model symmetric alloys as well as a monovariant eutectic reaction in the Ni-Al-Zr alloy. In all the studies mentioned above, the effect of solute diffusivities in modifying the selection of solid phase fractions have not been explored. We investigate this aspect using our phase-field simulations as well as analytical calculations.

After addressing the problem of steady-state multi-phase growth in a multi-component alloy, which is presented in detail in Chapter 7, we move on to a study of an unstable growth in such systems, described in the next paragraph.

1.5 Eutectic colony formation in systems with interfacial energy anisotropy

Two-phase growth in a ternary alloy where the two phases exchange two components and reject an impurity into the liquid, results in the formation of a boundary layer of this component ahead of the solidification front. This interface is then unstable to morphological perturbations much in the same manner as in a Mullins-Sekerka instability [1] (henceforth will be referred to as MS instability) of the solidification front during single phase growth. The amplification of these instabilities leads to the formation of eutectic colonies (also called two-phase fingers) which are

cells made up of two-phase lamellae.

Theoretical understanding of this problem begin with the study by Plapp and Karma [44], where they perform linear stability analysis to establish that the instability leading to colony formation is oscillatory compared to the one operating on a single phase binary solid-liquid interface.

Numerical computations performed to study eutectic colony formation dynamics augment theoretical understanding in regimes outside the purview of linear analysis. In this regard, phase field simulations of eutectic colonies by Plapp and Karma [16] not only validate their theory in [44], but also highlight the lack of a stable cellular morphology under isotropic conditions.

While the studies in the previous cases concentrate on isotropic eutectics, alloys systems in general contain phases which either have anisotropic solid-liquid interfaces or where the interfacial boundaries between the solid phases have a preferred alignment of crystallographic planes giving rise to defined orientation relationships for these interfaces. Experimentally, anisotropic interfacial energies of the solid-solid interfaces have been found to result in spirals in binary eutectic alloys [45, 46].

Ni-Al-Zr is another exemplary system consisting of two solid intermetallic phases (Ni_3Al and Ni_7Zr_2) whose crystallographic planes share a well defined orientation relationship as revealed by the TEM diffraction patterns in Fig. 1.1(a) and 1.1(b). The two-phase eutectic in this alloy is also a monovariant reaction and is therefore unstable to morphological perturbations. Detailed characterization of the colonies shows that the central stem of the colonies have well aligned lamellar feature as seen in Fig. 1.1(c). Further resolution of the colony microstructures at the interface between two colonies reveals features resembling spiraling of two solid phases.

The influence of a well defined orientation relationship between the eutectic solids in a binary system on its steady-state growth morphologies has been studied theoretically, numerically and experimentally in [47, 48, 49]. Pusztai et al. [50] and Ratkai et al. [51], investigate the influence of kinetic anisotropy in stabilizing the spiral microstructures during two-phase eutectic colony formation in a ternary alloy by conducting phase field simulations. However, no studies exist which systematically investigate the influence of anisotropy in the interfacial energies on the colony morphology arising out of the destabilization of steady-state two-phase growth interface, in either thin-film geometry or during bulk solidification.

This motivates the two principal aims in this chapter. Firstly, we perform phase field simulations to investigate the influence of the anisotropy of the different interfaces on eutectic colony morphologies in thin-film geometry. Secondly, through phase-field simulations in three-dimensions we characterize the influence of anisotropy both in the solid-solid and solid-liquid interfaces on the morphologies of the spirals and the colony structures.

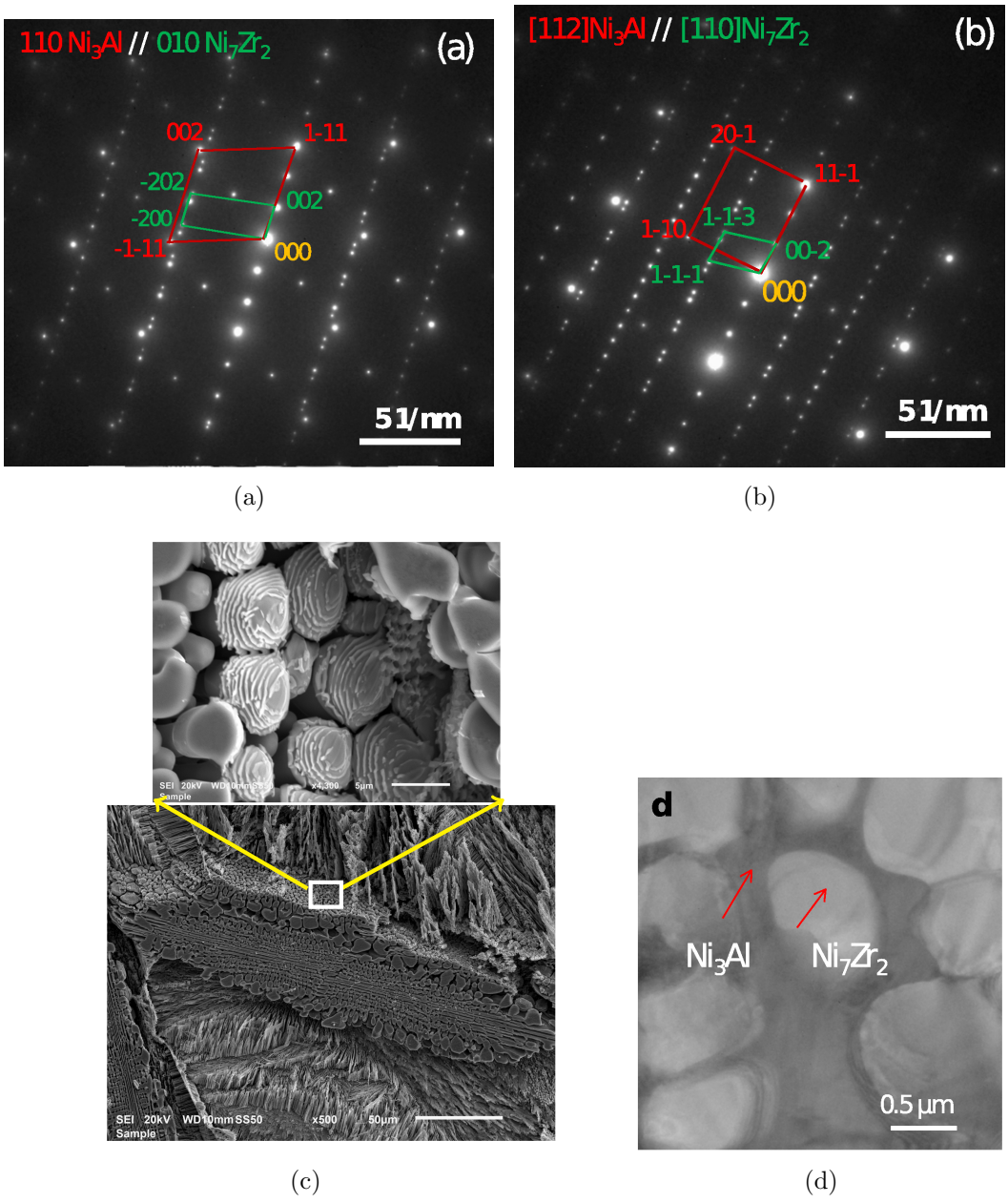

(a) (b)

(c) (d)

Figure 1.1: The anisotropy in solid–solid interfacial energy is indicated by the existence of a well defined orientation relationship between the two phases in (a) and (b). The orientation of the lamellae along the axis of the colony finger along with some spiral like features is displayed in (c). The two eutectic phases are identified from their contrast in (d).

In what follows, we perform phase-field simulations of the following directionally solidifying systems: one where the interfacial energy is isotropic, followed by systems with anisotropic solid-liquid and solid-solid interfacial energies in 2D. Our simulations in this regard can be thought to be representative of the solidification experiments carried out for thin samples [9]. The colony formation dynamics and the resultant lamellar morphologies for each of these situations are studied as functions of the anisotropy strength and the sample pulling velocity.

We also perform 3D simulations in order to understand the effect of an introduction of a third dimension on the lamellar structures in directionally solidified systems with anisotropic solid-liquid and solid-solid interfacial energies. Our simulations are numerical studies of the eutectic spiraling observed experimentally in [10]. The computational cost involved in these simulations restricts us to a single choice in both the pulling velocity and the strength of anisotropy. Chapter 8 in our thesis presents this phenomena in detail.

Chapter 2

Literature review

This chapter contains a comprehensive review of the existing literature, on each of the phenomena we consider in this thesis. We also present a short review of the phase-field models employed to study the various phenomena presented in this thesis. We begin by reviewing the steady-state single phase growth phenomena in multicomponent alloys. The instability of a planar front to random perturbations is taken up next followed by the problem of radius and velocity selection at the dendrite tip. After this, we move on to reviewing studies involving growth of multiple phases in multi-component alloys.

2.1 Single phase growth in multi-component alloys in the scaling regime

Diffusion driven growth of precipitates in an infinite medium is a classical problem in phase transformations in materials. In binary alloys, it has been studied by Zener [2], Frank [52] and Ham [53]. The classical result from Zener [2] and Frank [52] is that the growth of a precipitate of any dimensionality (planar, cylindrical and spherical) into a super-saturated matrix in the diffusion-controlled regime can be described through a scaling law, where the square of the displacement of the interface is directly proportional to the time, and the proportionality constant is characteristic of the chosen super-saturation as well as of the diffusivity. Ham [53] extends the work by Zener [2] and Frank [52] to growth of spheroids to confirm the presence of a scaling regime where the particle grows with a constant eccentricity.

Theoretical developments of single phase growth in multi-component alloys have mainly been limited to ternary systems. As a two-phase equilibrium in such alloys are is associated with as many degrees of freedom as there are independent components, the phase concentrations

that are selected at the interface under conditions of local equilibrium are unknowns to be determined in addition to the scaling constant characterizing the growth phenomena. The phase concentrations are now functions of both the matrix supersaturations and solute diffusivities. The earliest study in this regard is due to Coates [17, 18], who solved the inverse problem of determining the supersaturated matrix compositions which equilibrate to a given tie-line for a given diffusivity matrix. A solution assuming diagonal diffusivity matrix is presented in [17], while it is generalized to include off-diagonal entities in [18]. The problem of equilibrium tie-line selection and the composition profiles in the supersaturated parent phase ahead in the matrix in a ternary alloy is addressed by Bourne et al., [20]. In this paper, they solve for the ratio of the diffusivity of the two solutes, which leads to the choice of a particular tie-line equilibrium for a given supersaturation in the matrix. Furthermore, the composition profiles ahead of the matrix are also calculated once the equilibrium concentrations at the interface are determined. The studies by Coates [17, 18] and Bourne et al., [20] utilize a parameterized knowledge of the two-phase equilibria in the phase diagram, in order to solve for the compositions of the bulk alloy and the equilibrium phase concentrations, respectively. This requirement of a prior knowledge of the tie-lines in the system prevents the easy extension of these theories to any generic multi-component alloy. This requirement of a prior knowledge of the tie-lines in the system makes the extension of these theories to any generic multi-component alloy very complicated.

The fact that solute interdiffusivities play an important role in the selection of phase compositions at the interface has been observed in diffusion couple experiments which explore the different regions of phase stability in isothermal sections of ternary phase diagrams; see for example the studies by Van Beek et al. in Ag-Fe-Ti [54] and Cu-Fe-Ti [55] systems. Detailed reviews of such ternary diffusion couple studies can be found in Kodentsov et al. [56], the textbook on diffusion by Paul et al. [57] (see also Chapter 6 in the Handbook of Solid State Diffusion: Volume 2, by Kodentsov and Paul [58]). Theoretical studies on diffusion paths in ternary diffusion couples presented by Maugis et al. [59, 60], and earlier by Coates and Kirkaldy [61] solve for the two sided diffusional growth problem to determine the interfacial compositions and velocities. In parallel, theoretical studies of melting and solidification in binary alloys by Coriell et al. [62, 63] where the solid and the liquid phases have different temperature and compositions, consider temperature as a second independent variable in addition to the phase compositions and hence is a study which is fundamentally similar to the studies on solid-state diffusion couples.

As the analytical theories described till now involve an *a-priori* knowledge of the possible thermodynamic equilibria in the system, their usefulness is restricted to the availability of such data. Numerical sharp interface techniques address this issue in a practical fashion where

there is direct coupling of the growth problem to the thermodynamic databases. The most prominent amongst them constitutes the present day software DICTRA [64, 65]. It solves the diffusion equation under local equilibrium at the interface separating parent and product phases in conjunction with thermodynamic databases through softwares like Thermo-Calc [66] and PANDAT [67, 68]. There are several interesting studies [69, 70, 71, 72] of growth in multi-component systems using DICTRA. While these procedures are certainly efficient and reasonably generic to be applied to any multi-component alloy for which a thermodynamic database is available, closed form solutions in corollary to those written down for the case of binary precipitate growth in the scaling regime cannot be derived through this approach.

In another important work by Coates [19], two limiting cases to the problem of local equilibrium at the interface is discussed. The case of "Partition under conditions of local equilibrium" (PLE) is applicable under situations of extremely low supersaturations in the matrix, where the kinetics is largely controlled by the diffusion of the slower moving component needed for achieving equilibrium concentrations in the precipitate and the matrix. The other situation corresponding to a highly supersaturated bulk alloy leads to no partitioning of the slower moving species and it retains the same concentrations in the precipitate and the matrix. The rate of transformation in such a case is controlled by the diffusion of the faster moving species and it is known as the case of "Negligible partition under conditions of local equilibrium" (NPLE). The limiting cases of PLE and NPLE being applicable for substituitional alloys only, a well known analog of NPLE for interstitial solutes is the case of "paraequilibrium" [73, 19, 24, 25, 26]. It is commonly observed in steels with composition Fe-C-X, where X is the substitutional solute, and is characterized by complete partitioning of the interstitial (C) which diffuse much faster than the substituitional solute (X) remaining unpartitioned.

Steady-state growth in a single phase alloy has also been studied through simulations. Phase-field simulations by Mukherjee et al., [74, 75] deal with steady-state growth of cylindrical precipitates in binary alloys. To our knowledge, although phase field models have been used for multi-component studies (Ti-Al-V [76], Al-Si-Cu-Fe [77], Al–Si–Cu–Mg–Ni [78], Mg-Al-Mn [79], Ni-Al-Cr-Ta-W [80], Al-Si-Cu-Fe-Mg-Mn-Ni-Zn [81], Fe-C-B [82], and in ternary two phase diffusion couples [83]), the influence of diffusivity matrices on the choice of equilibria has not been dealt in detail. For example in [84], while the authors do investigate the particular case of 'paraequilibrium' in the case of an Fe-C-Mn alloy, the simulations are not directed towards deriving the phase compositions in the relevant scaling regime during growth.

The lack of a theory predicting tie-line selections in a generic multi-component alloy for any generic diffusivity matrix motivates us to take up this problem in Chapter 4. Our analytical predictions of tie-line selection and composition profiles in the matrix are confirmed against the

same from phase-field simulations and sharp interface calculations.

In the next section, we review the literature concerning the instability of the steady-state solid-liquid interface in a multi-component alloy.

2.2 Diffusive instabilities during single solid phase alloy solidification

Random perturbations to the steady-state planar interface during solidification, gets amplified with time leading to their breakdown. Rutters and Chalmers [85] and Tiller et al., [86], developed the criterion of constitutional supercooling for binary alloys which predicted growth of protuberances at the planar interface whenever there is a zone of supercooled liquid ahead of the interface. This constitutional supercooling criterion didn't consider the stabilizing effect of capillarity on the perturbations and the first theoretical attempt to include the effect of interfacial energy is due to Temkin [87]. In this paper, the behavior of the interface in the presence of perturbations is studied by comparing the growth velocities of a hemispherical protuberance on a planar interface to that of the planar interface itself. The diffusion fields ahead of the hemisphere are not calculated exactly and the solutions conjectured show inconsistencies with the boundary conditions to be satisfied. Furthermore, the interfacial perturbations are generally of complex shapes and an accurate prediction of their growth behavior may not be obtained by a consideration of a hemispherical protuberance alone.

An analysis which predicts the behavior of the perturbed interface by rigorously solving for the diffusion fields is presented by Mullins and Sekerka [1]. They considered that at very early stages, random interfacial perturbation can be described by a linear superposition of Fourier modes. An understanding of the growth behavior of each of those modes tantamounts to an understanding of the behavior of the interfacial perturbation itself. Mullins and Sekerka [1] performed a linear stability analysis of a perturbed planar interface in directionally solidifying binary alloys to derive analytical expressions for the amplification rates of each mode. They showed that a constitutionally undercooled interface is stable for very large wavelengths due to the large diffusion distances of the solute and for very small wavelengths due to capillarity, and unstable for all the wavelengths of perturbations in between. Also, the growth rates reach a maximum for a wavelength in between the two stable regimes observed for the two extremes of very large and very small wavelengths. The analytical predictions in [1] have also been confirmed by phase-field simulations reported by Echebarria et al., [88].

The linear stability analysis of Mullins and Sekerka [1] assumed the wavelength of pertur-

bations to be much smaller than the thermal diffusion lengths. This approximation restricts the analysis to the consideration of very small wavelengths when the growth velocity is higher. Thus, such an approximation is applicable to conditions of slow growth only and is revoked by Trivedi and Kurz [89] when developing a theory for rapid solidification in binary alloys. A consideration of perturbation wavelengths comparable to the thermal diffusion lengths allow them to show the existence of a condition of absolute stability during solidification of a pure material from an undercooled melt. The condition of absolute stability, where for sufficiently high velocities of growth, the diffusion lengths are smaller than the capillary lengths for all possible wavelengths of perturbation, is a criterion which is predicted to be unattainable during growth of pure materials from undercooled melts by the analysis of Mullins and Sekerka [1], but a more complete analysis by Trivedi and Kurz [89] provides a proof to the contrary. Non-equilibrium effects including a velocity dependent partitioning of the solute between the solid and the liquid as well as a temperature of the interface which is determined by the velocity are introduced into the linear stability analysis for rapid solidification conditions by Merchant and Davis [90], and Huntley and Davis [91].

A similar linear stability analysis along the lines of Mullins and Sekerka [1] for multi-component alloys is first performed by Coates et al., [28] in the setting of a directionally solidifying ternary alloy. Here, Coates et al., [28] assumed an existence of a steady-state growth behavior in the perturbed state as well, while performing the linear stability analysis. The appropriateness of this assumption is verified by Coriell et al. [92] who solved the complete time-dependent problem to conclude that an assumption of a steady-state in the perturbed state is quite reasonable. Hunziker [29] generalized the linear stability analysis to directionally solidifying multi-component alloys with arbitrary diffusivity matrices.

In Chapter 5, we perform a linear stability analysis of a steady-state growth interface in a multi-component alloy, for situations of isothermal as well as directional solidification. Here, we build upon the concepts of concurrent tie-line and growth velocity selection during steady-state growth in multi-component alloys presented in Chapter 4 and extend these concepts to the case of unstable growth.

2.3 Isothermal dendrites in multi-component alloys

There are several experimental evidences of dendritic growth in materials. In pure materials, it is observed in Pb [93], Zn [94], and succinonitrile [95, 12, 96]. It is also reported in aqueous solutions [97]. In binary systems, dendritic solidification has been studied by Glicksman et al. [98] in a succinonitrile(SCN)-argon system. There has been a couple of studies [99, 100]

reporting dendrites in a succinonitrile(SCN)-acetone system, as well. Another observation of dendrites is reported by Liu and Kirkaldy [101] during directional solidification studies in a SCN-0.66 wt% Salol alloy. Experiments have also been performed in Al-Zn systems to study the orientation selection process in dendrites [102]. In multi-component alloys, dendrites have been observed in a spot-weld in a Ni-based superalloy [103], and in a Ni-Al-Zr alloy [13]. A study in Al-Mn-Pd system by Schroers et al. [104] presents the variation of dendrite tip growth velocity as a function of undercoolings.

Dendrite growth has also been studied through phase-field simulations. Phase-field studies of dendrite growth have been reported in pure materials [105, 106], in binary alloys [107, 108, 109, 110, 111, 102] and in multi-component alloys [78, 112, 113].

The theoretical understanding of dendrites begin with the solution of thermal diffusion field ahead of a growing dendrite in an undercooled pure melt by Ivantsov [30]. The problem considered the steady-state growth of a free dendrite, whose thermal diffusion field ahead in the melt is not influenced by the growth of similar structures. Horvay and Cahn [31] solved the same problem, but with a completely different approach. In both these studies by Ivantsov [30] (referred to as "IS") and Horvay and Cahn [31], the shape of the dendrite is assumed to be a parabola in 2D and a paraboloid of revolution in 3D. The solution to the diffusion fields ahead of a dendrite growing self-similarly (i.e., in steady-state) is obtained in terms of the thermal Peclet number ($Pe_{th} = VR_{tip}/2\alpha$), where V is the tip-velocity, R_{tip} is the tip-radius and α is the thermal diffusivity. As there are multiple combinations of V and R_{tip} which can lead to the same Pe_{th}, the theories in [30, 31] are unable to predict a unique selection of V and R_{tip} seen in the experiments by Huang and Glicksman [12] and Glicksman [96]. The inability to predict V and R_{tip} uniquely is attributed to the lack of consideration of interfacial energy in the theories presented in [30, 31].

The introduction of capillarity at the solid-liquid interface results in an equilibrium shape of the dendrite which is no longer given by the parabola (in 2D) or the paraboloid (in 3D) as shown by Ben-Jacob et al., [114], which complicates the consideration of the Stefan boundary condition at the interface. Thus, there has been several studies which continued to approximate the shape of the dendrite by a parabola/paraboloid, while integrating the effects of capillarity into the mathematical solution of the problem. The foremost study in this regard is the one by Temkin [87], which introduced an additional undercooling at the interface due to curvature, when re-considering the IS. This lead to an identification of the smallest radius of curvature of the dendrite tip, corresponding to which the velocity of dendrite growth vanishes. Furthermore, the theory also predicts a maximum in the growth velocity (V), for a certain tip-radius (R_{tip}), which was believed to be the condition selected in experiments until proved otherwise by the

experiments in [12, 96]. The theory by Temkin [87] is extended to situations with large Peclet number by Trivedi [115]. Another theoretical study of dendrite growth considering interfacial energy is presented by Nash and Glicksman [116], which involve a Green's function solution to the diffusion problem. Their predictions are similar to those of Temkin [87].

The first attempt at a numerical solution to the Ivantsov problem in a pure material is presented by Oldfield [117]. where he finds that the IS, even after including capillarity, predicts a dendrite shape which is unstable. This observation is generalized and confirmed by Langer and Müller-Krumbhaar [32, 33, 34] where they find the solutions to be unstable for all values of interfacial energy. Also, they suggest an estimate for R_{tip}, considering an interaction between the capillarity and the diffusion length scales in the problem, which might be selected during growth. This estimate is the classic "Marginal Stability" criterion and predicts V and R_{tip} found to be in good agreement with experiments. The inability of the "Marginal Stability" criterion in predicting the stable growth of dendritic arms along well-defined crystallographic directions, prompted investigations of the effects of anisotropic interfacial energy on the stability of the solution. An analytical solution to the problem in the presence of anisotropy being extremely difficult, Kessler and Levine [35] solved the problem numerically. They confirm the selection of a unique V and R_{tip}, for a given growth condition, and suggest that an estimate for R_{tip}, must be a function of the magnitude of the anisotropy in the system. This estimate is known as the "Microscopic solvability" (or the "Microsolvability") criterion. The accuracy and correctness of "Microsolvability" criterion has been confirmed through phase-field simulations as well. The predictions from "Microsolvability" are found to be in great agreement with those obtained from simulations, in 2D [118]. In 3D, the discrepancies between the two is attributed to the assumption of axisymmetric dendritic shapes in the "Microsolvability" criterion [119, 120, 121]. The phenomenon of dendrite growth in pure materials is reviewed in detail in [12].

The first analysis of dendrite growth in alloys is presented by Langer and Müller-Krumbhaar [32, 33, 34], which considers the solute diffusion fields in binary alloys. This is extended to include a velocity dependent partition coefficient and a temperature dependent diffusivity for rapid directional solidification of binary alloy dendrites, by Kurz et al. [122]. The extension of this theory to directionally solidified dendrites in ternary alloys has been presented by Bobadilla et al. [123], and the corresponding modification to describe rapid solidification is presented by Rappaz et al. [124]. The theories in [123, 124] are limited to independent solute diffusion in ternary alloys. An extension of this theory for any generic multi-component alloy, for any generic diffusivity matrix, is presented by Hunziker [29].

A corresponding theoretical development describing isothermal free dendrites in alloys begins with the study of Langer [125] in binary alloys, which is continued and elaborated by

Karma and Langer in [126], where the effects of the second component are restricted to dilute concentrations only. A parallel theoretical development by Lipton et al. [3, 4] is found to be in excellent agreement with the experiments in [12, 96] and the theory in [126].

In Chapter 6, we present a theory for describing the growth of free dendrites from a uniformly undercooled multi-component alloy melt. Our derivations are applicable to any generic multi-component alloy with an arbitrary diffusivity matrix. Also, we compare the analytical predictions of the various parameters like tip-velocity V and tip-radius R_{tip} during the solidification of thin samples with the ones obtained from phase-field simulations in this chapter.

2.4 Theoretical and numerical investigation of multi-phase growth in a multi-component system

Eutectic solidification leads to a wide variety of microstructures which are characterized by the arrangement of the solid phases relative to each other. In binary eutectics, these microstructures range from lamella [127, 128, 129, 130, 131, 14, 132] to rods [133, 134, 135] and mixture of morphologies, depending on the volume fractions of the phases and the interfacial energies. For more than two solid phases, the number of possibilities is still larger and some of the experimental evidences of three phase growth are obtained during directional solidification of metallic alloy systems, such as, Pb-Sn-Cd [136, 137, 138], Al-Cu-Mg and Zn-Sn-Pb [139],Al-Cu-Ni [140], Bi-In-Sn [141, 142], Nb-Ni-Al [15], Al-Ag-Cu [143, 144, 145]. Experimental evidence of eutectic solidification in quaternary organic alloys is reported in [146, 147]. Phase-field simulations of bulk-two phase growth have also been performed in [148, 149, 150] and corresponding examples of simulations of three-phase growth can be found in [151, 152, 153, 154, 155, 156]. A review of studies of multiphase solidification in multi-component alloys is presented in [157].

The length scales of such steady-state eutectic microstructures are defined by the unit structure whose periodic repetition constitutes the entire microstructure. For lamellar structures, this is described by a single wavelength of the eutectic solid lamellae, while for the case of a two-phase microstructure where one of the solid phases is dispersed as rods in the matrix of the solid phase constituting the larger volume fraction, the length scale is given by half the average distance between any two second phase rods. A theoretical understanding of the factors determining the length scales in such microstructures has been of significant interest. The first study in this regard is due to Zener [158] who carried out the study in the context of a eutectoid transformation in steels (Fe-C alloys). The growth of pearlite is a coupled growth of ferrite and cementite phases in a lamellar form from the parent austenite and hence is con-

ceptually similar to a concurrent eutectic transformation of a liquid phase into two solids in a binary alloy. Zener [158] found that at any particular undercooling, pearlite could grow from the austenite with a variety of interlamellar spacings, with the growth velocity being different for each of the spacings. In order to explain the observation of a dominant length scale of the pearlitic microstructure in experiments, Zener [158] conjectured that the length scale (interlamellar spacings) which corresponds to the highest growth rate is the one that is seen experimentally. This sets the operating state for the eutectoid transformation where at a given undercooling of the system the observed length scales are unique. He also predicted the classic scaling relationship of coupled lamellar growth, between the lamellar width (λ) and the growth velocity (V) at the operating point, given by the constancy of $\lambda^2 V$. A study by Brandt [159] on pearlite growth predicted solutions to the problem of solute diffusion in the parent austenite in the form of a Fourier series with the unknown Fourier coefficients determined by considering the the coupled growth of the eutectoid phases as a result of the diffusion of the solute (carbon) from the ferrite to the cementite. The first theoretical consideration of eutectic solidification is presented by Tiller [160] where he reconsiders the ideas presented by Zener [158] to render them suitable for eutectic solidification. He re-frames the criterion of the dominant length scale selection from a maximization of the growth velocity at a particular undercooling to one where the system selected length scale corresponds to a minimum undercooling of the solidification front under conditions of directional solidification. Hillert [161] utilized Zener's [2] maximum growth rate criterion in conjunction with a solution of the diffusion problem assuming a planar interface to predict the shape of the solidification interface. Jackson et al., [162] solved for the interface shapes by considering an electric analog to the diffusion problem. Their derivation of the diffusion fields assuming planar interfaces lead to interface shapes which are close to the ones seen experimentally.

Jackson and Hunt [8] present a theory of two phase eutectic growth in a binary alloy where they derive expressions of the undercooling of the solidification front as a function of the length scales during lamellar or rod type growth. The solute diffusion fields are computed by assuming a planar solid-liquid interface and the composition variation in the liquid at the solid-liquid interface is expressed as a Fourier series assuming the solid phase fractions and their respective compositions to be given by the equilibrium phase diagram. All the Fourier coefficients except for the zeroth order term are determined by invoking the mass balance condition (Stefan condition) at the interface in conjunction with the mutual orthogonality of the Fourier basis functions. An application of the Stefan condition to determine the zeroth order term leads to its value being computed as zero, which is just a reflection of the underlying assumptions of the solid phase fractions and their compositions being determined by the phase diagram. Thus,

Jackson and Hunt [8] leave the zeroth order terms as unknowns to be determined from the equations obtained by assuming equality of undercoolings, averaged over the individual lamellar widths for all the different solid-liquid interfaces constituting a basic unit of the eutectic structure. A force balance at a triple junction formed by the intersection of the two solid-liquid interfaces and a solid-solid interface determines the contact angles of the solid-liquid interfaces with the horizontal. Thus, the solidification front is not planar and assuming so while determining the diffusion fields is only done to keep the mathematics tractable. The liquid compositions at the solid-liquid interface are used to compute the constitutional undercooling while the curvature undercooling is determined by a knowledge of the Gibbs-Thomson coefficients, contact angles and the solid phase fractions assuming the shapes of the solid-liquid interfaces to be given by circular arcs. The total undercooling at the interface is given by a sum of the constitutional and curvature undercoolings. The condition of equal average undercoolings at the different solid-liquid interfaces is an approximation which is reasonable when the volume fraction of the two eutectic solids are similar along with similar properties of the two solid-liquid interfaces. An asymmetric phase diagram and dissimilar solid-liquid interfacial properties lead to different solid-liquid interfaces selecting different average undercoolings as seen from their different relative positions in the imposed thermal gradients in experiments, and in such cases the equal undercooling criterion proposed by Jackson and Hunt [8] is associated with larger errors. The other assumptions of solid phase fractions and their compositions being given by the equilibrium phase diagram are also limited to situations of slow growth characterized by small Peclet numbers as they change with undercooling at the interface which is higher for faster solidification.

All the theoretical developments discussed till now assume the solid phase fractions and compositions to be given by the phase diagram where in reality the solidification front is always undercooled which introduces deviations. Though the deviations are small for growth characterized by low Peclet number a concomitant theoretical modification is necessary for faster solidification conditions. One of the first attempts in this regard has been from Series et al. [163] which provides error-estimates w.r.t the classical Jackson-Hunt calculations using an electrical analogue to solve the solute-diffusion problem. Donaghey and Tiller [41] presented a solution to the solute diffusion problem for a binary alloy as a Taylor series expansion about the Peclet number. Though, they restricted themselves to the solution of the diffusion problem only and did not include their solutions in the expressions for undercoolings at the growth fronts, two succeeding studies by Trivedi et al., [40] and Ludwig and Leibbrandt [164] build upon the ideas put forth by them to perform a JH type calculation. Trivedi et al., [40] (also known as the TMK model) extend the Jackson-Hunt (henceforth referred to as JH) type calculations to

high Peclet number growth for some special phase diagrams. Their analysis still invokes the equilibrium solid phase fractions and compositions but considers the Peclet numbers appearing in the higher order terms in the expressions of average liquid compositions as functions of the lamellar width λ, and predicts a different operating point of the eutectic from that obtained predicted by the JH theory. Ludwig and Leibbrandt [164] generalized the ideas proposed by Trivedi et al. [40] to arbitrary phase diagrams. In addition to higher velocities, one of the other reasons due to which phase fractions could change, are due to the different densities of the phases. This has been addressed in the work by Magnin and Trivedi [165, 166], wherein one of the additional assumptions in the original JH calculations [8] that is the equality of phase undercoolings which is imposed in order to close the system of equations for determining the composition field in liquid, is relaxed.

The theory by Jackson and Hunt [8] forms the premise of several important theoretical studies of coupled growth in multi-component systems as well. Unlike binary alloys, multi-component systems have the possibility of multi-variant coupled growth of solid phases, i.e., a situation where the number of components are greater than the number of phases solidifying and hence associated with degrees of freedom greater than or equal to one. Following the classical JH-route here becomes a problem as the condition of equal interfacial undercooling presents an under-determined system of equations for the solution to boundary layer compositions, which as we recall from the previous discussion is a term that is left as an unknown in the JH formulation of two-phase growth in binary alloys. The major challenge here is the under-determined nature of the problem where the number of components and hence the unknown zeroth order terms in the Fourier expansion of each of the components exceed the number of equations which are given by the number of solid phases in the system. For a ternary monovariant system where two solid phases form out of a single liquid phase, McCartney et al., [37] are the first to circumvent this difficulty by introducing an additional constraint relating the magnitude of the composition boundary layers of the two independent components assuming the solid phase fractions to be given by the equilibrium phase diagram. Plapp and Karma [16] present a particularized estimate of the undercoolings at the interface for a ternary monovariant eutectic where the two growing solid phases reject a common component. For invariant reactions in multi-component systems, however, the system of equations derived from the conditions of equal interfacial undercooling are always enough to determine the unknowns. Exemplary studies in this regard are reported by the studies by Himemiya and Umeda [38] and Choudhury et al., [39] provide expressions for computing the undercoolings at the solidification front for different arrangements of the solid phases.

The other difficulty with approximating solid phase fractions and compositions from the

phase diagram is compounded in a multi-component setting where the diffusivity matrix introduces additional departures from phase diagram predictions. These observations necessitate a theoretical development where the compositions and volume fractions of the solid phases are unknowns which have to be determined as part of the solution. Catalina et al., [42] presented a theory for two phase growth in multi-component alloys where the unknowns are expressed as functions of the volume fractions and compositions of the solidifying phases. They obtain a solution to this problem by assuming a constancy of the compositions of the one of the solidifying phases. This constraint is relaxed by Senninger and Voorhees [43] to obtain a theory which predicts the compositions as well as the phase fractions during two phase solidification in a multi-component alloy.

In Chapter 7 we present a theory extending the JH calculations to describe a coupled growth of multiple solid phases from a multi-component alloy melt. Our theory treats invariant as well as multi-variant growth in multi-component alloys in a unified manner to predict the solid phase fractions and compositions as functions of the solute diffusivities and coupled growth conditions.

2.5 Eutectic colony formation in systems with interfacial energy anisotropy

Eutectic solidification in multi-component systems can be multi-variant, i.e. the number of degrees of freedom can be equal to or greater than one. In such systems, it might so happen that all the eutectic solids reject (consume) one of the components into (from) the liquid. This leads to the formation of a solutal boundary layer ahead of the moving interface akin to the one observed in single phase solidification. The presence of such a boundary layer ahead makes the interface susceptible to the growth of interfacial perturbations. This is essentially a Mullins-Sekerka (MS) type instability of the eutectic growth front leading to the formation of eutectic cells (or colonies) whose counterpart in the case of single phase solidification leads to the formation of single phase dendrites.

Experimentally, eutectic colonies have been extensively studied, as in [127, 167, 168, 169, 170, 171, 140]. including a study on their dynamics during directional solidification of thin samples [9]. Furthermore, Akamatsu et al. [10] are the first to observe and characterize the helical arrangement of two eutectic solids about a finger axis, which they anoint as “eutectic spirals”. They also point out the presence of such structures in studies that predate their observation, like the one in Al-Cr-Nb systems carried out by Souza et al. [172].

Plapp and Karma [44] showed that though the instability of a eutectic growth front leading to the formation of the cells or colonies is conceptually similar to the one observed during single phase solidification, the nature of the instability in the former is oscillatory compared to the MS instability operative during single phase solidification. In this study, they performed a linear stability analysis of the eutectic growth front with a solutal boundary layer ahead to arrive at such conclusions. Another important theoretical work in this regard is presented by Akamatsu et al., [173] where the establish the scaling of the eutectic spiral tip-radius (ρ) with $V^{-0.5}$, where V is the spiraling dendrite tip growth velocity.

A theoretical understanding of the entire process of formation of multi-phase cells or colonies could only be derived from simulations as a linear stability analysis is only applicable to the very early stages of growth. Phase-field simulations of colony formation in a ternary monovariant system with isotropic interfacial energies is first reported by Plapp and Karma [16] where they study not only the early stages of eutectic colony formation but also the late stage dynamics. Their simulations confirm and validate their theory in [44] and highlight several interesting features of the colonies in isotropic systems. Plapp and Karma [16] show that the two-phase cells (or colonies) in an isotropic system are unstable. They do not have well defined orientations and are not associated with a particular length scale. Once formed, they broaden and split continuously, a behavior which is similar to the cells in single phase materials. The lamellae pairs constituting the fingers are found to be roughly orthogonal to the solidification front. Stable colonies and spirals are observed in the phase-field studies conducted by Pusztai et al., [50] and Ratkai et al., [51] in the presence of kinetic anisotropy. As we will see later in Chapter 8, two-phase spirals are a result of co-ordinated growth of the two solid phases about a common axis. A recent phase-field study by Hötzer et al. [155] explores the microstructures associated with the coupled rotation of the rods belonging to one of the eutectic solids about a common axis aligned with the temperature gradient during directional solidification of an Ag-Al-Cu alloy, under conditions when the soldification front is planar.

Experimental observations of eutectic solidification are replete with instances where at least one of the solid-liquid or the solid-solid interfaces are anisotropic in character. Spiraling structures observed during steady-state of binary eutectic alloys are reported by Fullman and Wood [45] and by Liu and Jones [46] in Zn-Mg alloys and by Fullman and Wood in Al-Th alloys [45], which are attributed to the anisotropic nature of the interface between the two eutectic solids. A recent experimental study of the steady-state lamellar eutectic growth modes with anisotropic solid-solid interfaces is reported by Akamatsu et al., [49]. Theoretical studies which explore the implications of anisotropic interfaces between the two eutectic solids during steady state binary eutectic growth are presented by Akamatsu et al., [48] and Ghosh et al., [47].

These studies provide analytical predictions of the orientations of the solid-solid interface in a directional solidification setting.

Our motivation for the study presented in Chapter 8 is to explore the eutectic colony formation dynamics and their features in a system with anisotropic solid-liquid or solid-solid interfacial energies. We conduct phase-field simulations in 2D and 3D to explore the behavior in such systems.

2.6 Phase-field modeling

In our thesis, phase-field modeling serves two important purposes. The first is to benchmark the predictions from our analytical theories and the second is to understand the non-linear regimes of transformations which are analytically inaccessible. In the following paragraphs we present a survey of the key developments in this discipline culminating in the models we have employed in this thesis.

The inception of phase-field modeling as a scientific discipline to study transformation in materials started with the descriptions by Cahn, Hilliard [174] and Allen, Cahn [175]. In any microstructure, the coexisting phases can be identified one the basis of several parameters like phase compositions, degree of ordering, etc.,. Cahn, Hilliard [174] and Allen, Cahn [175] described the interface separating any two phases as a region where the characteristic parameter differentiating the two phases varies continuously between the values assumed for either phases. Temporal evolution of such a microstructure thus parameterized can be studied by solving for the appropriate evolution equations for the phase-fields as described by Cahn [176] for conserved variables, and by Allen and Cahn [175] for non-conserved variables. A crucial feature of their descriptions is that the width of the diffuse interface in their models is determined by different physical properties of the system and hence is a quantity which is a property of the chosen system. The Cahn-Hilliard model assumes a position of central importance in the modeling of solid-state phase transformations. It allows for an easy integration of the changes in elastic energy, which is extremely common in transformations involving solid phases and hence has been extensively employed to study such transformations, e.g., the studies by Hu and Chen [177], Gururajan and Abinandanan [178] and Lahiri et al., [179].

Langer [180] introduced diffuse interface models with a different philosophy to the Cahn-Hilliard [174, 176] and Allen-Cahn models [175]. In Langer's [180] model, the phase-fields are mathematical field variables describing the spatial distribution of the different phases constituting a microstructure. In contrast to the earlier models in [174, 176, 175], the phase-fields no longer represent physical quantities with the width of the diffuse interface separating any

two phases being a parameter which can be chosen to model the relevant length scales in the problem. This model, based on the Model C of Halperin and Hohenberg [181], marks the beginning of a long chain of developments which brings us to the phase-field models employed for studying solidification today.

Collins and Levine [182] also proposed a model of solidification in pure materials where a non-conserved order parameter is employed to differentiate between the two phases. In all these models, the evolution of the phase-field is driven by the temperature field, which itself is governed by the heat diffusion equation. Large scale computer simulations of dendritic growth in pure materials is first reported by Kobayashi [105] based on a model along the lines of that proposed by Collins and Levine [182]. The models presented in [180, 182, 105] incorporate the effects of the interface migration on the evolution equations for the temperature field by introducing an additional source term which represents the evolution of latent heat with the migration of the solidification front. Penrose and Fife [183] presented an alternate formulation based on the maximization of a single entropy functional which is equivalent to the models in [180, 182, 105]. The idea of Penrose and Fife [183] is extended by Wang et al., [184] to describe the models by Langer [180], Collins and Levine [182] and Kobayashi [105] as special cases obtainable from a generalized framework of models derivable from entropy maximization. A phase-field model for the solidification of binary alloys is presented by Warren and Boettinger [107] based on the entropy maximization principles presented by Penrose and Fife in [183]. Phase-field models which take into account the simultaneous existence of multiple phases when each of them can be described by a different order parameter is presented by Steinbach et al. [185] and Garcke et al., [186]. Nestler et al. [187] present a model to simulate the evolution of multiple phases in a multi-component alloy governed by a maximization of entropy functional.

Despite the enormous computational benefits offered by phase-field models, it is important to confirm their quantitative accuracy by comparing their predictions in the sharp-interface limit to those obtained from sharp-interface models themselves. Studies by Caginalp et al., [188], Wang and Sekerka [189] and Wheeler et al., [106] show that for predictions from phase-field models to be quantitatively similar to those obtained from sharp interface moving boundary problem, the interface width in phase-field models needs to be small. As discussed earlier, using a smaller interface width is associated with higher computational costs and this revelation from [188, 106, 189] pits the accuracy of phase-field models versus their computational efficiency. Analyzing the phase-field models in the limit of vanishing interface thickness also shows that a finite kinetic undercooling of the interface is always present in a diffuse interface model. This is a numerical artifact of the diffuse interface model and is not representative of solidification

at low undercoolings where the interface attachment kinetics is negligible. Smaller interface widths are chosen to limit the interface effects which severely increases the computational load to simulate solidification at low undercoolings where larger interface widths should be chosen in accordance with the diffusion length scales which are large. Instead of performing sharp-interface asymptotics on phase-field models, Karma and Rappel [118, 121] explore the behavior of diffuse interface models at a small (w.r.t the diffusion lengths) but finite interface thicknesses and derive expressions for values of certain parameters which would lead to a disappearance of the spurious interface kinetic effects. Thus, the study by Karma and Rappel [118, 121] propose the idea that instead of insisting for an equivalence between sharp and diffuse interface models at vanishing interface thicknesses of the latter, both models can be found to be in much closer quantitative agreement at a small but finite width of the interface in phase-field models. These ideas are extended to solidification in binary alloys by Losert et al., [190].

Quantitative accuracy of a phase-field models involving solute diffusion has also been keenly scrutinized. A popular model for isothermal solidification in binary alloys proposed by Wheeler et al., [191] shows an existence of a excess in grand potentials arising due to the diffuseness of the solid-liquid interface. Kim et al., [192] showed that this grand potential excess restricted the width of the interface that can be used for a given interfacial energy. In a succeeding paper Kim et al. [193] relaxed this limitation by expressing the solute concentration at a given point in the simulation domain by a weighted average of the solid and the liquid phase compositions, which are themselves determined by a common tangent construction. Folche and Plapp [194, 148] extended these concepts of quantitative phase-field models to models describing two phase growth.

Ahmad et al., [195] discuss another artifact associated with phase-field modeling of alloy solidification which is the phenomenon of solute trapping. In phase-field models the diffusivities in the solid are usually neglected in comparison to the diffusivities in the liquid. This is a realistic approximation given the several orders of magnitude of differences in the solid and the liquid diffusivities observed experimentally. The change in diffusivity across a diffuse interface results in differences in chemical potentials on either side of the interface which represents incomplete distribution of the solute during the motion of the interface. Solute trapping is an experimentally observed phenomenon during rapid solidification and should be reflected in phase-field models as well. The fact that solute trapping is observed in phase-field models even during slow growth is an anomaly which has been attributed to the diffuseness of the interface. As the interface width in phase-field models is often chosen such that realistic domain sizes are computationally accessible, it leads to the observation of solute trapping even at slow growth rates. Karma [196, 88] suggested introduction of an artificial solute current from the solid to

liquid to neutralize the anomalous solute trapping. Though the introduction of this term has no thermodynamic justification, it is widely accepted as the way to tackle this problem. An excellent review of phase-field modeling techniques in solidification is presented by Choudhury and Nestler [197].

The latest in the long series of development of quantitative phase-field models for solidification is one where the free energy functional is replaced by an equivalent grand-potential functional. This model is independently proposed by Plapp [198] and Choudhury, Nestler [199] and provides the most computationally efficient alternative for tackling the excess grand potential associated with the diffuseness of the interface. This model allows a complete decoupling of the bulk and the interfacial contributions to the grand potentials and facilitates a choice of the interfacial width which is appropriate for the domain sizes to be studied. In this thesis, we employ both two-phase and multi-phase versions of this model to simulate various phenomena related to single phase and multi-phase growth in multi-component alloys. We describe the grand-potential formulation of phase-field models in detail in Chapter 3.

In this thesis, we have performed phase-field simulations employing the Grand potential model [199, 198] for benchmarking all of our analytical calculations. Some late stage microstructures of dendritic growth in multi-component alloys have also been obtained using this model. We employ a combined Cahn-Hilliard [174, 176] and Allen-Cahn [175] model to simulate the eutectic colonies. This model has been explained in Chapter 8 alongside the simulations of eutectic colonies with anisotropic interfaces.

Chapter 3

Phase-field model: The grand-potential formulation

In our thesis, we employ two different kinds of phase-field models to study the problems of interest. One of them is the latest variant in the long line of diffuse interface models employed to model solidification. This is the Grand-Potential model, independently proposed by Plapp [198] and Choudhury, Nestler [199] and incorporates all the features of a phase-field model designed to be equivalent to sharp interface models in the limit of thin interfaces. This model is employed to quantitatively validate all our analytical predictions corresponding to the linear regime and also to provide important information regarding the process of microstructure formation during the analytically inaccessible non-linear regime. In the following four chapters, we employ this model for performing phase-field simulations, while a different phase-field model is invoked and described in Chapter 8 to simulate the unsteady growth of eutectic colonies.

The Grand-Potential model derives its name by considering the driving forces for phase transformation as a difference between grand-potentials of the two phases. In the next section, we present a short review of the thermodynamic relationships which establishes the grand-potential as the appropriate function for treating phase transformation in multi-component alloys.

3.1 Motivation from sharp interface

The salient feature of the model we are about to discuss is that it takes cue from the conditions determining equilibrium between two phases, in a sharp-interface context, to formulate a description of the energy of the system containing diffuse interfaces. Thus, a short review of

the criteria of equilibrium and the description of driving forces in a sharp interface model is of value. In a sharp interface description, the equilibrium between two phases is obtained under an equality of all the intensive quantities at the interface, i.e., temperature (T), pressure (P) and the chemical potentials ($\tilde{\mu_i}$). A dis-equilibrium is identified by a pressure difference between the two phases which provides the necessary driving force for the motion of the interface leading to growth of one of the phases at the expense of the other. Considering a K component alloy, with one mole of the parent phase (α) and the product phase (β), the pressure acting on a phase is then given by the expression obtained by a re-arrangement of the integral form of the Helmholtz free energy $F = -PV_m + \sum_{i=1}^{K} \tilde{\mu_i} N_i$, for one mole of material, and is stated as,

$$P^{\alpha,\beta} = -(f^{\alpha,\beta} - \sum_{i=1}^{K} \tilde{\mu_i} \rho_i^{\alpha,\beta}). \tag{3.1}$$

We have invoked local equilibrium by equating the chemical potentials of the components in both the phases: $\tilde{\mu_i^{\alpha}} = \tilde{\mu_i^{\beta}} = \tilde{\mu_i}$. $f^{\alpha,\beta}$ denotes the Helmholtz free-energy density of the phases. $\rho_i^{\alpha,\beta} = N_i^{\alpha,\beta}/V_m$ is the number density of any particular component in a phase, under the assumption that the molar volumes (V_m) of the phases are the same. $N_i^{\alpha,\beta}$ denotes the number of particles of the component i per mole of a phase. The chemical potentials are computed according to their classical definition,

$$\tilde{\mu_i}^{\alpha,\beta} = \left.\frac{\partial F^{\alpha,\beta}}{\partial N_i}\right|_{N_j, j \neq i}. \tag{3.2}$$

$F^{\alpha,\beta}$ denotes the total Helmholtz free energy of one mole of the corresponding phase. The constraint denoting the constancy of the number of particles in each phase is given by,

$$\sum_{i=1}^{K} N_i^{\alpha,\beta} = N_0 \tag{3.3}$$

where N_0 denotes the Avogadro's number. Dividing this expression throughout with the molar volume V_m leads to,

$$\sum_{i=1}^{K} \rho_i^{\alpha,\beta} = \tilde{\rho} = N_0/V_m. \tag{3.4}$$

Substituting for $\rho_k^{\alpha,\beta}$ from Eq. 3.4 in Eq. 3.1, we can obtain a condition of equilibrium given by $P^\alpha = P^\beta$, written as,

$$f^\alpha - \sum_{i=1}^{K-1}(\tilde{\mu_i} - \tilde{\mu_K})\rho_i^\alpha = f^\beta - \sum_{i=1}^{K-1}(\tilde{\mu_i} - \tilde{\mu_K})\rho_i^\beta, \tag{3.5}$$

where we have considered the K-th component as the solute. The difference in chemical potentials $(\tilde{\mu_i} - \tilde{\mu_K})$ can be related to diffusion potentials (μ_i) stated as,

$$(\tilde{\mu_i} - \tilde{\mu_K}) = \frac{\mu_i}{N_0}, \tag{3.6}$$

which follows from,

$$\begin{aligned}\mu_i = \frac{dF}{dc_i} = N_0\frac{dF}{dN_i} &= N_0\left(\frac{\partial F}{\partial N_i} + \frac{\partial F}{\partial N_K}\frac{dN_k}{dN_i}\right) \\ &= N_0(\tilde{\mu_i} - \tilde{\mu_K}).\end{aligned} \tag{3.7}$$

Employing Eqs. 3.6 into Eq. 3.5, we can express the criterion of equilibrium between two phases in a sharp interface description as,

$$f^\alpha - \frac{1}{V_m}\sum_{i=1}^{K-1}\mu_i c_i^\alpha = f^\beta - \frac{1}{V_m}\sum_{i=1}^{K-1}\mu_i c_i^\beta. \tag{3.8}$$

In Eq. 3.8 the phase compositions are denoted by $c_i^{\alpha,\beta}$ and they are related to the number densities $\rho_i^{\alpha,\beta}$ by,

$$c_i^{\alpha,\beta} = \frac{N_i^{\alpha,\beta}}{N_0} = \frac{\rho_i^{\alpha,\beta}}{\tilde{\rho}}. \tag{3.9}$$

A driving force for the transformation of α into β, is expressed by a difference in pressures in the two phases for the same chemical/diffusion potentials and temperature. For a growth of β phase at the expense of α phase, we can write,

$$\Delta P^{\alpha,\beta} = P^\beta - P^\alpha = \left(f^\alpha - \frac{1}{V_m}\sum_{i=1}^{K-1}\mu_i c_i^\alpha\right) - \left(f^\beta - \frac{1}{V_m}\sum_{i=1}^{K-1}\mu_i c_i^\beta\right). \tag{3.10}$$

From the definition of a grand-potential, $\Psi = F - \sum_i^K \tilde{\mu_i}N_i$, the pressures are equivalent to negative grand-potential densities of the phases, i.e., $P^{\alpha,\beta} = -\Psi^{\alpha,\beta}$, and thus an alternate

description of the driving force for transformation can be expressed as,

$$\begin{aligned}\Delta P^{\alpha,\beta} = P^{\beta} - P^{\alpha} &= \Psi^{\alpha} - \Psi^{\beta} \\ &= \Delta\Psi^{\alpha,\beta} = \left(f^{\alpha} - \frac{1}{V_m}\sum_{i=1}^{K-1}\mu_i c_i^{\alpha}\right) - \left(f^{\beta} - \frac{1}{V_m}\sum_{i=1}^{K-1}\mu_i c_i^{\beta}\right),\end{aligned} \tag{3.11}$$

where,

$$\Psi^{\alpha,\beta} = f^{\alpha,\beta} - \frac{1}{V_m}\sum_{i=1}^{K-1}\mu_i c_i^{\alpha,\beta}. \tag{3.12}$$

This concludes our discussion of the driving forces of phase transformation in a sharp interface setting where we have seen the differences in the grand-potentials of the phases acting as the driving force for transformation.

We begin with a description of the Grand-Potential model employed to simulate single phase solidification in a multi-component system. The model is general enough to tackle the simultaneous growth of several solid phases, as will be made clear during our description of the completely general multi-phase version of the model later on. The simpler setting of growth of a single product phase (which also forms the backdrop of the following three chapters) serves a context in which some of the details of the Grand Potential model can be easily introduced and hence we begin with a description of that scenario.

3.2 Grand-potential model: Two phases in equilibrium

Moving on to the description of a phase-field model, the fact that differences in grand-potential densities describe the driving forces during phase transformation, is utilized to construct the energetics of a system with diffuse interfaces. The grand-canonical density functional (Ω) of the system is given by,

$$\begin{aligned}\Omega\left(\boldsymbol{\mu}, T, \phi\right) = \int_V \Bigg[&\Psi\left(\boldsymbol{\mu}, T, \phi\right) + \\ &\left(\epsilon a\left(\nabla\phi\right) + \frac{1}{\epsilon} w\left(\phi\right)\right)\Bigg] dV,\end{aligned} \tag{3.13}$$

where $\boldsymbol{\mu}$ denotes the set of diffusion potentials corresponding to each independent component in the multi-component system, $\boldsymbol{\mu} = \{\mu_1, \mu_2, \cdots, \mu_{K-1}\}$ and T denotes temperature. The

values of the order parameter (ϕ, also known as the phase-field) demarcates regions of pure product phase β ($\phi = 1$), pure parent phase α ($\phi = 0$) and the interface between the two (where ϕ is a positive fraction), in the two phase microstructure. The double-welled polynomial $w(\phi) = 9\sigma\phi^2 (1-\phi)^2$, introduces a potential barrier between the parent and the product phases which are at equilibrium. The parameter ϵ controls the interface width. A penalty in grand potential associated with the gradients in ϕ is introduced into the model through the term $a(\nabla\phi)$ which for the case of the two phase equilibrium under consideration is just a function of the gradients in the phase-fields (ϕ), given by,

$$a(\nabla\phi) = \sigma a_c^2(\hat{n}) (\nabla\phi)^2 , \tag{3.14}$$

where σ denotes the interfacial energy and the anisotropy is introduced through the function $a_c(\hat{n})$, written as,

$$a_c(\hat{n}) = 1 \pm \zeta \left[3 - 4 \left(\sum_{i=d} n_i^4 \right) \right] , \tag{3.15}$$

where, d indicates the number of dimensions, $d = 2$ for 2D, $d = 3$ for 3D, and $\hat{n}$ denotes the unit normal vector pointing towards the liquid, defined as,

$$n_i = \frac{(\nabla\phi)_i}{|\nabla\phi|}. \tag{3.16}$$

The parameter ζ denotes the magnitude of the anisotropy ($\zeta = 0$ denoting isotropy) in the solid-liquid interfacial energy, while n being the number of folds of symmetry in the anisotropy function. The $\pm$ sign in Eqs. 3.15 represents the two possibilities in the orientation of the low energy directions in a laboratory frame which are conjugates of each other.

In the diffuse interface model, the grand potential density Ψ at any point in the system is obtained by an interpolation of the grand potentials of the α and the β phases as given by,

$$\Psi(\boldsymbol{\mu}, T, \phi) = \Psi^{\alpha}(\boldsymbol{\mu}, T) h(1-\phi) + \Psi^{\beta}(\boldsymbol{\mu}, T) h(\phi) , \tag{3.17}$$

where Ψ^{β} and Ψ^{α} are functions of the diffusion potential vector $\boldsymbol{\mu} = \{\mu_1, \ldots, \mu_{K-1}\}$ and the temperature (T) in the system. The exact forms of the functions $\Psi^{\alpha,\beta}(\mu_i, T)$ are discussed in a later section on the system thermodynamics. $h(\phi) = \phi^2 (3 - 2\phi)$ is an interpolation polynomial with the property $h(\phi) + h(1-\phi) = 1$.

The compositions in every phase can be derived as functions of the diffusion potential vector

$\boldsymbol{\mu}$ as given by (see Eqs. 3.12),

$$c_i^{\alpha,\beta}\left(\boldsymbol{\mu},T\right)=-V_m\frac{\partial\Psi^{\alpha,\beta}\left(\boldsymbol{\mu},T\right)}{\partial\mu_i}. \tag{3.18}$$

The molar V_m is taken to be a constant for both the phases.

The phase transformation manifesting by a motion of the diffuse interface is captured by the evolution of ϕ, which is obtained by solving,

$$\tau_{sl}\epsilon\frac{\partial\phi}{\partial t}=\epsilon\left(\nabla\cdot\frac{\partial a}{\partial\nabla\phi}-\frac{\partial a}{\partial\phi}\right)-\frac{1}{\epsilon}\frac{\partial w\left(\phi\right)}{\partial\phi}-\frac{\partial\Psi\left(\boldsymbol{\mu},T,\phi\right)}{\partial\phi}. \tag{3.19}$$

τ_{sl} is the relaxation constant with its value set to obtain a diffusion controlled interface motion [21].

For solidification in a multi-component system, the evolution of $\boldsymbol{\mu}$ can be expressed as,

$$\begin{aligned}&\left\{\frac{\partial\mu_i}{\partial t}\right\}=\\&\left[\sum^{p=\alpha,\beta}h_p\left(\phi\right)\frac{\partial c_i^p\left(\boldsymbol{\mu},T\right)}{\partial\mu_j}\right]^{-1}_{ij}\left\{\nabla\cdot\left(\sum_{j=1}^{K-1}M_{ij}\left(\phi\right)\nabla\mu_j-\mathbf{J}_{at,i}\right)\right.\\&\left.-\sum^{p=\alpha,\beta}c_i^p\left(\boldsymbol{\mu},T\right)\frac{\partial h_p\left(\phi\right)}{\partial t}-\frac{\partial T}{\partial t}\sum^{p=\alpha,\beta}\left(\frac{\partial c_i^p\left(\boldsymbol{\mu},T\right)}{\partial T}\right)_{\boldsymbol{\mu}}h_p\left(\boldsymbol{\phi}\right)\right\}.\end{aligned} \tag{3.20}$$

where $[\cdot]$ denotes a matrix of dimension $((K-1)\times(K-1))$ while $\{\cdot\}$ represents a vector of dimension $(K-1)$, and we have used $h_l\left(\phi\right)=h\left(1-\phi\right)$ and $h_s\left(\phi\right)=h\left(\phi\right)$. The atomic mobility $M_{ij}\left(\phi\right)$, is obtained by interpolating the individual phase mobilities,

$$M_{ij}\left(\phi\right)=M_{ij}^{\alpha}(1-\phi)+M_{ij}^{\beta}\phi, \tag{3.21}$$

where, the mobility matrices $M_{ij}^{\alpha,\beta}$ are defined by,

$$\left[M_{ij}^{\alpha,\beta}\right]=\left[D_{ik}^{\alpha,\beta}\right]\left[\frac{\partial c_k^{\alpha,\beta}\left(\boldsymbol{\mu},T\right)}{\partial\mu_j}\right], \tag{3.22}$$

where $D_{ij}^{\alpha,\beta}$ are the solute inter-diffusivities. In our calculations, the solute diffusivities are assumed to be negligibly small in the solid compared to that in the liquid. This assumption leads to an anomalous solute trapping that is corrected by using an anti-trapping current [21].

In order to perform simulations using a temperature gradient, a linear temperature gradient

in the growth direction with the following profile is initialized,

$$T(z) = T_b + G\left(z - Vt\right), \tag{3.23}$$

where T_b is a reference temperature, G is the thermal gradient, V is the pulling velocity, t is the time, while z is the co-ordinate in the growth direction.

In the preceding discussion of the phase-field model for a two phases, there are several thermodynamic relationships that are yet to be specified, e.g., $c_i(\boldsymbol{\mu}, T)$ etc. There are several possibilities of such dependencies which will be discussed in detail in the section titled "Thermodynamics" presented later.

3.3 Grand-potential model: Multiple phases in equilibrium

In this section we present a generalized version of the Grand-potential model which can consider the simultaneous evolution of a number of phases. The simplified model described above for studying the growth of a single product phase from a parent phase is a special case of the model we present below.

In the concurrent presence of N phases, the grand potential functional(Ω) can be expressed as,

$$\begin{aligned}\Omega\left(\boldsymbol{\mu}, T, \boldsymbol{\phi}\right) = \int_V \Bigg[& \Psi\left(\boldsymbol{\mu}, T, \boldsymbol{\phi}\right) \\ & + \left(\epsilon a(\boldsymbol{\phi}, \nabla\boldsymbol{\phi}) + \frac{1}{\epsilon} w\left(\boldsymbol{\phi}\right)\right)\Bigg] dV,\end{aligned} \tag{3.24}$$

where $\boldsymbol{\phi} = [\phi_1, \phi_2, \cdots, \phi_N]$ are the phase-fields representing the spatial arrangement of N phases and $\boldsymbol{\mu} = [\mu_1, \mu_2, \cdots, \mu_{K-1}]$ are the diffusion potentials associated with each one of the $K-1$ independent solutes. The functionals w and a represent the surface potential and the gradient energy density respectively. The minimization of Ω leads to the evolution of the spatial arrangement of the phases ($\boldsymbol{\phi}$) denoted by,

$$\begin{aligned}\tau\epsilon\frac{\partial\phi_p}{\partial t} = \epsilon\left(\nabla\cdot\frac{\partial a(\boldsymbol{\phi}, \nabla\boldsymbol{\phi})}{\partial\nabla\phi_p} - \frac{\partial a(\boldsymbol{\phi}, \nabla\boldsymbol{\phi})}{\partial\phi_p}\right) \\ -\frac{1}{\epsilon}\frac{\partial w\left(\boldsymbol{\phi}\right)}{\partial\phi_p} - \frac{\partial\Psi\left(\boldsymbol{\mu}, T, \boldsymbol{\phi}\right)}{\partial\phi_p} - \Lambda,\end{aligned} \tag{3.25}$$

where Λ is calculated to ensure $\sum_{m=1}^{N} \phi_m = 1$ at every mesh point in the simulation domain. τ is the relaxation constant with its value set based on the criterion stated in [200] and [21] to obtain a diffusion controlled interface motion.

The driving force for growth of any generic phase p from m in this model, is given by,

$$\Delta\Psi^{mp} = \Psi^m - \Psi^p. \tag{3.26}$$

All the grand-potentials of the participating phases (Ψ^p)'s at any particular point in the simulation domain are interpolated to obtain Ψ as,

$$\Psi\left(\boldsymbol{\mu}, T, \phi\right) = \sum^{p} \Psi^p(T, \boldsymbol{\mu}) h_p(\boldsymbol{\phi}), \tag{3.27}$$

where,

$$h_p(\boldsymbol{\phi}) = \phi_p^2\left(3 - 2\phi_p\right) + 2\phi_p \sum_{\substack{m=1,n=1,\\ m<n,m\neq p,n\neq p}}^{N,N} \phi_m\phi_n. \tag{3.28}$$

The gradient energy density ($a(\boldsymbol{\phi}, \nabla\boldsymbol{\phi})$) is written as,

$$a(\boldsymbol{\phi}, \nabla\boldsymbol{\phi}) = \sum_{p=1,m=1,p<m}^{N,N} \sigma_{pm} a_c^2(q_{pm}) |q_{pm}|^2, \tag{3.29}$$

where the indices p and m iterate over the phases in the system. σ_{mp} is the interfacial energy. The form of the anisotropy function is already mentioned in Eq. 3.15 where the vector q now plays the role of the outward normal $\hat{n}$. The vector q can be written as,

$$q_{pm} = \phi_p \nabla\phi_m - \phi_m \nabla\phi_p. \tag{3.30}$$

The surface potential $w(\phi)$ is given by,

$$w\left(\boldsymbol{\phi}\right) = \begin{cases} \dfrac{16}{\pi^2} \displaystyle\sum_{\substack{m,p=1 \\ (m<p)}}^{N,N} \gamma_{mp}\phi_m\phi_p + \\ \displaystyle\sum_{\substack{m,p,n=1 \\ (m<p<n)}}^{N,N,N} \gamma_{mpn}\phi_m\phi_p\phi_n, & \text{if } \boldsymbol{\phi} \in \sum \\ \infty, & \text{elsewhere} \end{cases}$$

where $\sum = \{\boldsymbol{\phi} \,|\, \sum_{m=1}^{N} \phi_m = 1 \text{ and } \phi_m \geq 0\}$, γ_{mp} is the surface entropy density and γ_{mpn} is a term added to maintain the solution at an mp interface strictly along the two phase interface.

The evolution of $\boldsymbol{\mu}$ is expressed as,

$$\begin{aligned} &\left\{\frac{\partial \mu_i}{\partial t}\right\} = \\ &\left[\sum_p h_p\left(\boldsymbol{\phi}\right) \frac{\partial c_i^p\left(\boldsymbol{\mu}, T\right)}{\partial \mu_j}\right]_{ij}^{-1} \\ &\left\{\nabla \cdot \left(\sum_{j=1}^{K-1} M_{ij}\left(\boldsymbol{\phi}\right) \nabla \mu_j - \mathbf{J}_{at,i}\right)\right. \\ &\left. - \sum_p c_i^p\left(\boldsymbol{\mu}, T\right) \frac{\partial h_p\left(\boldsymbol{\phi}\right)}{\partial t} - \frac{\partial T}{\partial t} \sum_p \left(\frac{\partial c_i^p\left(\boldsymbol{\mu}, T\right)}{\partial T}\right)_{\boldsymbol{\mu}} h_p\left(\boldsymbol{\phi}\right)\right\}_j, \end{aligned} \tag{3.31}$$

where i and j iterate over the $(K-1)$ independent components. $[\cdot]$ denotes a matrix of dimension $((K-1)\times(K-1))$ while $\{\cdot\}$ represents a vector of dimension $(K-1)$. The anti-trapping current $\mathbf{J_{at,i}}$ has a sense and magnitude which nullifies solute trapping at the solid-liquid interface and is determined by the expressions given in [21] and [200].

The atomic mobility, $M_{ij}\left(\boldsymbol{\phi}\right)$ is obtained by interpolating the individual phase mobilities as,

$$M_{ij}\left(\boldsymbol{\phi}\right) = \sum_p M_{ij}^p g_p(\boldsymbol{\phi}), \tag{3.32}$$

where the individual phase mobilities are given by,

$$\left[M_{ij}^p\right] = \left[D_{ik}^p\right] \left[\frac{\partial c_k^p\left(\boldsymbol{\mu}, T\right)}{\partial \mu_j}\right], \tag{3.33}$$

where D_{ij}^{p} are the solute inter-diffusivities in the p-th phase and $g_p(\boldsymbol{\phi})$ are interpolants given as,

$$g_p(\boldsymbol{\phi}) = \phi_p^2 \left(3 - 2\phi_p\right). \tag{3.34}$$

The composition fields are obtained as functions of $\boldsymbol{\mu}$ and $\boldsymbol{\phi}$ as,

$$\begin{aligned} c_i &= \sum_p c_i^p \left(\boldsymbol{\mu}, T\right) h_p(\boldsymbol{\phi}), \\ c_i^p \left(\boldsymbol{\mu}, T\right) &= -V_m \frac{\partial \Psi_p \left(\boldsymbol{\phi}, \boldsymbol{\mu}, T\right)}{\partial \mu_i}. \end{aligned} \tag{3.35}$$

with the molar V_m is taken to be a constant for all the phases.

We employ a finite difference explicit method to numerically time-integrate the Allen-Cahn equation 3.25 and the diffusion equation 3.31 as it lends itself naturally to parallelization over multiple CPU cores in a distributed memory system, accomplished by invoking the Message-Passing Interface (MPI).

The descriptions of the two-phase and the multi-phase being given, we now focus on the thermodynamic relationships that are invoked while solving for the phase-field equations.

3.4 Thermodynamics

In this section, we discuss the thermodynamic relationships which are part of the phase-field model. In this thesis, we invoke two different thermodynamic descriptions. They differ from each other in the order of terms in diffusion potentials appearing in the expressions for driving forces. We discuss each of them in the following subsections.

3.4.1 Parabolic driving forces

In this case, we approximate the variation of free energy densities of the phases as functions of compositions, by paraboloids. During multi-phase growth there are several two-phase equilibria, between each one of the product phases with the parent phase. We present the description of free energies and the resultant thermodynamic relationships for one such two phase equilibrium, which can be extended to others by an appropriate choice of the constant parameters. For any generic multicomponent alloy with K components, out of which $K-1$ are independent, the

expression of the molar free energy of one of the product phases (denoted by β) is given by,

$$F^{\beta} = \sum_{i=1,j=1,i<=j}^{K-1} A_{ij}^{\beta} c_i^{\beta} c_j^{\beta} + \sum_{j=1}^{K-1} B_j^{\beta}(T) c_j^{\beta} + D^{\beta}(T), \tag{3.36}$$

and the one corresponding to the parent phase (denoted by α) is given by,

$$F^{\alpha} = \sum_{i=1,j=1,i<=j}^{K-1} A_{ij}^{\alpha} c_i^{\alpha} c_j^{\alpha}, \tag{3.37}$$

where $A_{ij}^{\alpha,\beta}$, $B_{ij}^{\beta}(T)$ and $D^{\beta}(T)$ are constants to be determined out of whom $B_{ij}^{\beta}(T)$ and $D^{\beta}(T)$ are temperature dependent. The diffusion potentials of the components can be expressed as,

$$\mu_i^{\beta} = \frac{\partial F^{\beta}}{\partial c_i^{\beta}} = 2A_{ii}^{\beta} c_i^{\beta} + \sum_{j,j\neq i}^{K-1} A_{ij}^{\beta} c_j^{\beta} + B_i^{\beta}(T), \tag{3.38}$$

and,

$$\mu_i^{\alpha} = \frac{\partial F^{\alpha}}{\partial c_i^{\alpha}} = 2A_{ii}^{\alpha} c_i^{\alpha} + \sum_{j,j\neq i}^{K-1} A_{ij}^{\alpha} c_j^{\alpha}. \tag{3.39}$$

The relationships described in Eqs. 3.38 and 3.39 can be written in a vector-matrix form as,

$$\begin{Bmatrix} \mu_1^{\beta} \\ \mu_2^{\beta} \\ \vdots \\ \mu_{K-1}^{\beta} \end{Bmatrix} = \begin{bmatrix} 2A_{11}^{\beta} & A_{12}^{\beta} & \cdots & A_{1(K-1)}^{\beta} \\ A_{21}^{\beta} & 2A_{22}^{\beta} & \cdots & A_{2(K-1)}^{\beta} \\ \vdots & & \ddots & \\ A_{(K-1)1}^{\beta} & A_{(K-1)2}^{\beta} & \cdots & 2A_{(K-1)(K-1)}^{\beta} \end{bmatrix} \begin{Bmatrix} c_1^{\beta} \\ c_2^{\beta} \\ \vdots \\ c_{K-1}^{\beta} \end{Bmatrix} + \begin{Bmatrix} B_1^{\beta}(T) \\ B_2^{\beta}(T) \\ \vdots \\ B_{K-1}^{\beta}(T) \end{Bmatrix}, \tag{3.40}$$

and,

$$\begin{Bmatrix} \mu_1^{\alpha} \\ \mu_2^{\alpha} \\ \vdots \\ \mu_{K-1}^{\alpha} \end{Bmatrix} = \begin{bmatrix} 2A_{11}^{\alpha} & A_{12}^{\alpha} & \cdots & A_{1(K-1)}^{\alpha} \\ A_{21}^{\alpha} & 2A_{22}^{\alpha} & \cdots & A_{2(K-1)}^{\alpha} \\ \vdots & & \ddots & \\ A_{(K-1)1}^{\alpha} & A_{(K-1)2}^{\alpha} & \cdots & 2A_{(K-1)(K-1)}^{\alpha} \end{bmatrix} \begin{Bmatrix} c_1^{\alpha} \\ c_2^{\alpha} \\ \vdots \\ c_{K-1}^{\alpha} \end{Bmatrix}. \tag{3.41}$$

Computing the derivatives of the diffusion potentials ($\mu_i^{\alpha,\beta}$) given in Eqs. 3.38 and 3.39 w.r.t compositions ($c_i^{\alpha,\beta}$), we find,

$$\left[\frac{\partial \mu}{\partial c}\right]^{\alpha,\beta} = \begin{bmatrix} 2A_{11}^{\alpha,\beta} & A_{12}^{\alpha,\beta} & \cdots & A_{1(K-1)}^{\alpha,\beta} \\ A_{21}^{\alpha,\beta} & 2A_{22}^{\alpha,\beta} & \cdots & A_{2(K-1)}^{\alpha,\beta} \\ \vdots & & \ddots & \\ A_{(K-1)1}^{\alpha,\beta} & A_{(K-1)2}^{\alpha,\beta} & \cdots & 2A_{(K-1)(K-1)}^{\alpha,\beta} \end{bmatrix}. \tag{3.42}$$

Using Eq. 3.42 in Eqs. 3.39 and 3.38, we can write,

$$\left\{\mu_i^{\beta}\right\} = \left[\frac{\partial \mu_i}{\partial c_j}\right]^{\beta} \left\{c_i^{\beta}\right\} + \left\{B_i^{\beta}(T)\right\}, \tag{3.43}$$

and,

$$\left\{\mu_i^{\alpha}\right\} = \left[\frac{\partial \mu_i}{\partial c_j}\right]^{\alpha} \left\{c_i^{\alpha}\right\}. \tag{3.44}$$

These relationships of $\mu_i\left(c_j, T\right)$ expressed in Eqs. 3.43 and 3.44, can be inverted to express the phase compositions as functions of diffusion potentials and temperature, as given by,

$$\left\{c_i^{\beta}\right\} = \left[\frac{\partial c_i}{\partial \mu_j}\right]^{\beta} \left\{\mu_i^{\beta} - B_i^{\beta}(T)\right\}, \tag{3.45}$$

and,

$$\left\{c_i^{\alpha}\right\} = \left[\frac{\partial c_i}{\partial \mu_j}\right]^{\alpha} \left\{\mu_i^{\alpha}\right\}, \tag{3.46}$$

The matrices $[\partial c/\partial \mu]^{\alpha,\beta}$ in Eqs. 3.45 and 3.46 are obtained by inverting the matrices $[\partial \mu/\partial c]^{\alpha,\beta}$. The relationships $c_i\left(\mu_j, T\right)$ presented in Eqs. 3.45 and 3.46 are still expressed in the form of constants $A_{ij}^{\alpha,\beta}$ and $B_j^{\beta}(T)$ which have to be determined.

Another thermodynamic relationship of crucial importance in the phase-field model is an expression of the driving force for a transformation of α into β. As we have already demonstrated in the beginning of this chapter, a difference in grand-potential densities of the two phases constitutes the driving force written as,

$$\Delta\Psi = \Psi^{\alpha} - \Psi^{\beta} = \left(f^{\alpha} - \frac{1}{V_m}\sum_{i=1}^{K-1}\mu_i^{\alpha}c_i^{\alpha}\right) - \left(f^{\beta} - \frac{1}{V_m}\sum_{i=1}^{K-1}\mu_i^{\beta}c_i^{\beta}\right). \tag{3.47}$$

By employing Eqs. 3.36, 3.37, 3.45 and 3.46 into Eq. 3.47, it can be expressed as functions of the diffusion potentials $\mu_i^{\alpha,\beta}$ and the constants $A_{ij}^{\alpha,\beta}$, $B_j^{\beta}(T)$ and $D^{\beta}(T)$. It is evident from Eq. 3.47 and Eqs. 3.36 and 3.37 that this representation of driving force contains terms which are second order in diffusion potentials $\mu_i^{\alpha,\beta}$.

As the key thermodynamic relationships represented by Eqs. 3.46, 3.45 and 3.47 can be completely described a knowledge of the diffusion potentials ($\mu_i^{\alpha,\beta}$) and the parameters $A_{ij}^{\alpha,\beta}$, $B_i^{\beta}(T)$ and $D^{\beta}(T)$, we focus our attention on the procedure to determine these constants. The constants $A_{ij}^{\alpha,\beta}$ are determined by the curvatures of the free energy functions as obtained from thermodynamic databases (see Eq. 3.42) or from other solution models like the "Regular solution model". They are assumed to remain constant with temperature, as apparent from the form of the free energy function in Eqs. 3.36 and 3.37.

The constants B_i^{β} and D^{β} are functions of temperature and they are determined by the temperature dependence of the $\alpha - \beta$ equilibrium from the phase diagram. The values of these constants are determined by employing the different thermodynamic criteria of equilibrium between the two phases, at different temperatures. The first set of equilibrium criteria requires the equality of diffusion potentials in the two phases, given by,

$$\mu_i^{\alpha} = \mu_i^{\beta}. \tag{3.48}$$

This allows us to write,

$$B_i^{\beta} = 2\left(A_{ii}^{\alpha} c_i^{\alpha *} - A_{ii}^{\beta} c_i^{\beta *}\right) + \sum_{j,j\neq i}^{K-1}\left(A_{ij}^{\alpha} c_j^{\alpha *} - A_{ij}^{\beta} c_j^{\beta *}\right). \tag{3.49}$$

The other condition of equilibrium corresponds to an equality of grand-potential densities, stated as,

$$\begin{aligned} \Psi^{\beta} &= \Psi^{\alpha}, \\ f^{\beta} - \frac{1}{V_m}\sum_{i=1}^{K-1}\mu_i^{\beta} c_i^{\beta *} &= f^{\alpha} - \frac{1}{V_m}\sum_{i=1}^{K-1}\mu_i^{\alpha} c_i^{\alpha *}, \end{aligned} \tag{3.50}$$

which leads to an expression for calculating D^{β}, given by,

$$D^{\beta} = \sum_{i=1, j>=i}^{K-1}\left(A_{ij}^{\beta} c_i^{\beta *} c_j^{\beta *} - A_{ij}^{\alpha} c_i^{\alpha *} c_j^{\alpha *}\right). \tag{3.51}$$

The $*$ in the superscript to compositions in Eqs. 3.49 and 3.51 denote quantities which are predicted by the equilibrium phase diagram.

In order to compute $c_i^{\alpha*,\beta*}$ as a function of temperature (T), we invoke an approximation that with a change in temperature the projection of the tie-lines from an isothermal section for a higher temperature on to a section at a lower temperature are collinear with the thermodynamic tie-lines at the lower temperature. In other words, our assumption ensures that a vertical section, parallel to the temperature axis, when drawn through the multicomponent equilibrium parallelepiped (for ternary; it's a higher dimensional object for multi-component alloys) such that it contains a tie-line at any one temperature, such a vertical section will continue to contain the corresponding tie-lines at all the other temperatures over which the two phases coexist. This can be mathematically represented as,

$$\frac{c_i^{\alpha*,\beta*}(T) - c_i^{\alpha*,\beta*}(T^*)}{c_i^{\beta*}(T^*) - c_i^{\alpha*}(T^*)} = \frac{c_j^{\alpha*,\beta*}(T) - c_j^{\alpha*,\beta*}(T^*)}{c_j^{\beta*}(T^*) - c_j^{\alpha*}(T^*)}, \forall i,j \in K-1. \tag{3.52}$$

Eq. 3.52 works well for situations where the solidus and liquidus surfaces are reasonably flat and don't have a pronounced curvature. In the event it is not so, the intersection of the vertical plane containing the original tie-line with the solidus and the liquidus surfaces does not contain the equilibrium tie-lines at temperatures other than the one at which the original tie-line is considered. An alternate approach then would be to parameterize all the liquidus compositions lying on the intersection of the vertical plane with the liquidus surface and their corresponding solidus compositions (as obtained from the thermodynamic databases of Thermo-Calc and CALPHAD) as functions of temperature (T) and utilize them to compute the constants B_i^β and D^β from Eqs. 3.49 and 3.51.

There are only $(K-2)$ independent equations of the form Eq. 3.52 amongst the $\frac{1}{2}(K-1)(K-2)$ possible, for each of the phases α or β. An expression for the undercooling in the system can be obtained by considering either boundaries of the two-phase coexistence, written as,

$$\sum_i^{K-1} m_i^{\alpha,\beta} \left(c_i^{\alpha*,\beta*}(T) - c_i^{\alpha*,\beta*}(T^*) \right) = T - T^*. \tag{3.53}$$

Now, we substitute for any of the $(K-2)$, $\left(c_i^{\alpha*,\beta*}(T) - c_i^{\alpha*,\beta*}(T^*) \right)$'s in Eq. 3.53 in terms of the departure in concentration (due to temperature change) of the one remaining specie from Eq. 3.52. This process is repeated for all the components, resulting in an expression for a change

in their concentration as a function of temperature as,

$$c_i^{\alpha*,\beta*}(T) = c_i^{\alpha*,\beta*}(T^*) + \frac{c_i^{\alpha*}(T^*) - c_i^{\beta*}(T^*)}{\Delta T_f^{\alpha,\beta}} (T - T^*) , \tag{3.54}$$

where,

$$\Delta T_f^{\alpha} = \sum_{i=1}^{K-1} m_i^{\alpha} \left(c_i^{\alpha*}(T^*) - c_i^{\beta*}(T^*) \right) , \tag{3.55}$$

$$\Delta T_f^{\beta} = \sum_{i=1}^{K-1} m_i^{\beta} \left(c_i^{\alpha*}(T^*) - c_i^{\beta*}(T^*) \right) . \tag{3.56}$$

A knowledge of the constants $A_{ij}^{\alpha,\beta}$, $B_i^{\beta}(T)$ and $D^{\beta}(T)$ completely specifies the relationship $c_i^{\alpha,\beta}(\mu_j, T)$, where now, $\mu_i^{\alpha} = \mu_i^{\beta} = \mu_i$, due to imposition of equilibrium. Also, the driving forces for phase transformation $\Delta\Psi^{\alpha\beta}$ can now be completely specified in terms of the diffusion potentials μ_i and temperature T. It must added that in order to successfully employ the parabolic approximations to free energies and driving forces, we need to approximate the curvatures of the free energy functions obtained from thermodynamic databases by constants. In addition, the phase diagram information corresponding to each of the two-phase equilibrate is also required.

In this subsection, we have described the formalism where the driving forces for phase transformation contains terms which are second order in diffusion potentials μ_i. In the next subsection, we present an alternate formalism which expresses the driving forces as functions of diffusion potentials to the linear order only.

3.4.2 Linearized driving forces

An alternate description of the thermodynamic relationships can be obtained where $c_i^{\alpha,\beta}(\mu_j, T)$ and the driving force $\Delta\Psi^{\alpha\beta}(\mu_i, T)$ are presented as a Taylor series expansion to the linear order term in diffusion potentials. For phase compositions, this is expressed as,

$$\left\{ c_i^{\alpha,\beta} \right\} = \left\{ c_{i,eq}^{\alpha*,\beta,*}(T) \right\} + \left[\frac{\partial c_i^{\alpha,\beta}}{\partial \mu_j} \right]_{\mu_{j,eq}^*(T)} \left\{ \mu_j - \mu_{j,eq}^*(T) \right\} , \tag{3.57}$$

where, $c_{i,eq}^{\alpha*,\beta*}(T)$ represent the tie-line compositions about which the linearization is performed at a particular temperature, corresponding to the reference diffusion potentials denoted by $\mu_{i,eq}^*(T)$. It must be noted that we no longer distinguish between μ_i^{α} and μ_i^{β} as they must

be equal under conditions of local equilibrium at the interface separating the parent and the product phases. This relationship is similar to the corresponding expression given by Eqs. 3.45 and 3.46 obtained from a parabolic approximation of driving forces in that only the first order terms in departures in diffusion potentials μ_i appear in the expression.

The difference from a parabolic approximation to driving forces is apparent when we consider the expression of the grand-potential densities. In a linearized description, they are also expressed by a Taylor series expansion about the equilibrium diffusion potentials given by,

$$\Psi^{\alpha,\beta} = \Psi^{\alpha*,\beta*}(\boldsymbol{\mu}^*_{eq}, T) + \sum_{i=1}^{K-1} \left\{ \frac{\partial \Psi^{\alpha,\beta}}{\partial \mu_i} \right\}_{\mu^*_{j,eq}(T)} \left\{ \mu_i - \mu^*_{i,eq}(T) \right\}. \tag{3.58}$$

This leads to an expression of the driving force,

$$\begin{aligned} \Delta\Psi^{\alpha\beta} = \Psi^{\alpha} - \Psi^{\beta} &= \sum_{i=1}^{K-1} \left\{ \left. \frac{\partial \Psi^{\alpha}}{\partial \mu_i} \right|_{\mu^*_{i,eq}(T)} - \left. \frac{\partial \Psi^{\beta}}{\partial \mu_i} \right|_{\mu^*_{i,eq}(T)} \right\} \left(\mu_i - \mu^*_{i,eq}(T) \right) \\ &= \frac{1}{V_m} \sum_{i=1}^{K-1} \left\{ c_i^{\beta*}(T) - c_i^{\alpha*}(T) \right\} \left\{ \mu_i - \mu^*_{i,eq}(T) \right\}, \end{aligned} \tag{3.59}$$

where, we have employed the relation,

$$c_i^{\alpha*,\beta*}(T) = -V_m \left. \frac{\partial \Psi^{\alpha,\beta}}{\partial \mu_i} \right|_{\mu^*_{i,eq}(T)}, \tag{3.60}$$

obtained by differentiating the expression $\Psi^{\alpha,\beta} = f^{\alpha,\beta} - \frac{1}{V_m} \sum_{i=1}^{k-1} \mu_i c_i^{\alpha,\beta}$, to derive the second equality in Eq. 3.59. The grand-potentials densities $\Psi^{\alpha*}(\boldsymbol{\mu}^*_{eq}, T)$ and $\Psi^{\beta*}(\boldsymbol{\mu}^*_{eq}, T)$ are equal to each other due to the existence of an equilibrium corresponding to $\mu^*_{i,eq}(T)$ and hence drop off from Eq. 3.59. Isothermal sections of the equilibrium phase diagram at any temperature (T) are obtained by setting,

$$\Delta\Psi^{\alpha\beta} = 0. \tag{3.61}$$

This provides a relation between the $K-1$ diffusion potentials, and for monotonic variations of any $K-2$ of them, the equilibrium compositions comprising the coexistence curves/planes can be calculated.

The relationships given by Eqs. 3.57 and 3.59 are complete, except for the dependence of

$\mu_{i,eq}$ on temperature (T) which needs to be specified. For the simulations in this thesis, we will assume that the second derivatives of the free-energy w.r.t composition (i.e., the $[\partial\mu/\partial c]$ matrix) to be invariant of temperature. This renders the matrices $\left[\partial c^{\alpha,\beta}/\partial\mu\right]$ in Eq. 3.57 to be constant. A point to note here is that a constancy of the $[\partial\mu/\partial c]$ matrices precludes the possibility of simulating spinodal decomposition. But as the presented model has been mainly developed for studying solidification, the concurrent modeling of spinodal decomposition in the solid which is far from the solidification front by employing temperature dependent curvatures of free energies, poses a couple of other challenges too. The first difficulty arises from the fact that diffusivity in the solid is assumed to be negligibly small compared to that in the liquid while modeling solidification. The introduction of finite solute diffusivities in the solid to allow spinodal decomposition invalidates some of the mathematical constructs of the phase-field model like the anti-trapping current, which are specifically derived to accurately model the vanishing solute diffusivities in the solid compared to that in the liquid. A second source of difficulty arises due to the diffusion potentials (μ) being the independent variables in this particular formulation, where the phase compositions are determined as functions of them. The presence of a negative curvature in the variation of free-eenrgy as a function of composition introduces non-uniqueness in the mapping from diffusion potentials to compositions.

In order to determine the change in $\mu^*_{i,eq}$ with a change in temperature, we consider a vertical section drawn parallel to the temperature axis which passes through the tie-line given by $c_i^{\alpha*,\beta*}$ at temperature T^*. We compute the behavior of $\mu^*_{i,eq}$ as a function of temperature in this section, and restrict the influence to first order terms only, which is expressed as,

$$\left.\frac{d\mu^*_{i,eq}}{dT}\right|_{T^*} = \sum_j \left.\frac{\partial\mu_i^\alpha}{\partial c_j}\frac{dc^{\alpha*}_{j,eq}}{dT}\right|_{T^*}, \tag{3.62}$$

where the terms $\dfrac{dc^{\alpha*}_{j,eq}}{dT}$ determine the variation of the compositions $c^{\alpha*}_{j,eq}$ with T in the section parallel to the temperature axis discussed above. The new equilibrium diffusion potentials at temperature T, are now given by,

$$\mu^*_{i,eq}(T) = \mu^*_{i,eq}(T^*) + \left.\frac{d\mu^*_{i,eq}}{dT}\right|_{T^*}(T - T^*). \tag{3.63}$$

The quantity $[d\mu_{i,eq}/dT]$ is calculated by considering only one of the two phases in equilibrium. This is due to the same assumption regarding the collinearity of tie-line compositions at different isothermal sections, as mentioned in the subsection on parabolic driving forces. By invoking

this approximation, we can associate $\mu^*_{i,eq}(T)$ computed by considering the properties of one of the coexistence surfaces to the other one as well. The variation of $\dfrac{dc^{\alpha*,\beta*}_{j,eq}}{dT}$ can be computed from the variation of the equilibrium compositions $c^{\alpha*,\beta*}_{i,eq}$ with temperature, as derived in the previous section, given by,

$$c^{\alpha*,\beta*}_{i,eq}\left(T\right) = c^{\alpha*,\beta*}_{i,eq}\left(T^*\right) + \frac{\left(T-T^*\right)\left(c^{\beta*}_{i,eq}\left(T^*\right) - c^{\alpha*}_{i,eq}\left(T^*\right)\right)}{\Delta T^{\alpha,\beta}_f}, \tag{3.64}$$

which leads to,

$$\frac{dc^{\alpha,\beta}_{i,eq}}{dT} = \frac{\left(c^{\beta*}_{i,eq}\left(T^*\right) - c^{\alpha*}_{i,eq}\left(T^*\right)\right)}{\Delta T^{\alpha,\beta}_f}, \tag{3.65}$$

where T^* is the temperature about which the linearization is performed. The quantities $\Delta T^{\alpha,\beta}_f$ are given by,

$$\Delta T^{\alpha,\beta}_f = \sum_i m^{\alpha,\beta}_i \left(c^{\beta,*}_{i,eq}\left(T^*\right) - c^{\alpha,*}_{i,eq}\left(T^*\right)\right), \tag{3.66}$$

with $m^{\alpha,\beta}_i$ as the slopes of the coexistence surfaces. For the simulations under non-isothermal conditions, we make an additional approximation, that $m^{\alpha}_i = m^{\beta}_i$, thereby, the properties of the original tie-line about which the system is linearized is maintained, i.e., $\left(c^{\beta,*}_{i,eq}(T) - c^{\alpha,*}_{i,eq}(T)\right)$ remains constant. With this, the driving force in Eq. 3.59 writes as,

$$\Delta\Psi^{\alpha\beta} = \frac{1}{V_m}\left\{c^{\beta,*}_{i,eq}(T^*) - c^{\alpha,*}_{i,eq}(T^*)\right\}\left\{\mu_i - \mu^*_{i,eq}\left(T\right)\right\}. \tag{3.67}$$

Thus, the phase compositions described by Eqs. 3.57, will be modified by including the dependence of the $c^{\alpha*}_{i,eq}$, $c^{\beta*}_{i,eq}$ on temperature as described by Eqs. 3.64 and due to $\mu^*_{i,eq}\left(T\right)$ by following Eq. 3.63. For isothermal simulations, the set of all equilibrium diffusion potentials $\mu_{i,eq}$ are independent of temperature. Additionally, the last term in the brackets of Eq. 3.20 is set to zero. For non-isothermal description, such as the simulations in a temperature gradient G, which is driven with a velocity V, the last term in this equation requires the terms $\dfrac{\partial T}{\partial t}$ which can be worked out as $-GV$.

Since the departure of the diffusion potentials from their equilibrium values at the interface are at leading order, functions of the interfacial curvature (through the Gibbs-Thomson relationship), for most experimental situations where the microstructural length scales are in

the order of microns, this deviation is small, and thereby the leading order term in the driving force suffices. This is true even for the linearization of the compositions as functions of the diffusion potentials, where again the linearization constant matrices $\left[\frac{\partial c_i}{\partial \mu_j}\right]$ are assumed to be independent of temperature. In summary, all of the approximations are going to be reasonably valid for small departures from equilibrium, for slow solidification conditions.

For faster solidification conditions involving smaller microstructural features, additional higher order terms in $(\mu_i - \mu_{i,eq})$ need to be added to the driving force to model the real behavior appropriately. The contributions of the higher order terms can be ascertained through the magnitude of $\left[\frac{\partial c_i}{\partial \mu_j}\right]$, as well as from the length scales.

A point to note about the determination of $[\partial c/\partial \mu]$ matrices in a thermodynamic description involving linearized driving forces. The matrices $[\partial \mu/\partial c]^{\alpha,\beta}$ are obtained by computing the double derivatives of the free-energy w.r.t composition, by considering the free energies of the phases to be given by an ideal solution model. The typical expression for the free energies of the phases in such a model are given by,

$$f^{\alpha,\beta} = \frac{RT}{V_m} \sum_{i=1}^{K} c_i^{\alpha,\beta} \log c_i^{\alpha,\beta}. \tag{3.68}$$

whose double-derivative w.r.t. the composition leads to,

$$\left[\frac{\partial \mu}{\partial c}\right]^{\alpha,\beta} = \frac{RT}{V_m} \begin{bmatrix} \frac{1}{c_1^{\alpha,\beta}} + \frac{1}{c_K^{\alpha,\beta}} & \frac{1}{c_K^{\alpha,\beta}} & \cdots & \frac{1}{c_K^{\alpha,\beta}} \\ \frac{1}{c_K^{\alpha,\beta}} & \frac{1}{c_2^{\alpha,\beta}} + \frac{1}{c_K^{\alpha,\beta}} & \cdots & \frac{1}{c_K^{\alpha,\beta}} \\ \vdots & & \ddots & \\ \frac{1}{c_K^{\alpha,\beta}} & \frac{1}{c_K^{\alpha,\beta}} & \cdots & \frac{1}{c_{K-1}^{\alpha,\beta}} + \frac{1}{c_K^{\alpha,\beta}} \end{bmatrix}, \tag{3.69}$$

which is a $(K-1) \times (K-1)$ matrix corresponding to the $(K-1)$ independent components; the K-th component is considered to be the solute. The $[\partial \mu/\partial c]$ matrix is evaluated at the tie-line compositions $c_i^{\alpha*,\beta*}$ at temperature T^* about which the thermodynamic functions are linearized.

This concludes our discussion of the Grand-potential model alongside all the necessary thermodynamic relationships which will be used in the following chapters.

Chapter 4

Single phase growth in multi-component alloys in the scaling regime

In this chapter, we consider the steady-state growth of a product phase from a parent phase in a multi-component alloy. The treatment is generically presented to be applicable to either precipitation or single phase solidification, during the scaling regime. Though, in the following discussion we refer to the second phase as precipitates, the discussion is equally applicable to the growth of a solid nucleus into the liquid. We begin this chapter with the theoretical extension of the Zener problem to multi-component alloys followed by validation with numerical simulation methods (phase-field and sharp-interface (front tracking)) and end with a discussion of the particular relevant limits operable at very low diffusivity ratios.

4.1 Theory: Local Equilibrium

In this section, we derive a unified theory of precipitate growth for all possible dimensions(i.e., planar, radial or spherical growth), where we solve the coupled problem of determining the kinetically determined tie-line compositions as well as the growth coefficient characterizing the parabolic growth regime for a generic multi-component alloy. In the following, we discuss two cases, firstly a particular situation where the diffusion of each of the solutes occurs independently or the diffusivity matrix is diagonal. Thereafter, we extend the derivation to the case of a generic diffusivity matrix by choosing an appropriate basis set in the composition space whose evolution can still be determined by a diagonal diffusivity matrix. Alongside all our following

discussions, we also additionally place the assumptions that the diffusivities are independent of the composition, and further that the diffusion is one-sided that is the growth of the interface is determined completely by the mass-diffusion in the matrix. In order to help the reader, we present a complete list of symbols used in the analytical derivation in Table. 4.1.

K	the no. of components
c_i^{α}	concentration of i-th component in α
c_i^{β}	concentration of i-th component in β
$c_{i,eq}^{\alpha,*}$	the linearization point of the concentration of i-th component in α
$c_{i,eq}^{\beta,*}$	the linearization point of the concentration of i-th component in β
$c_{i,eq}^{\alpha}$	concentration of i-th component in α at the interface in local equilibrium
$c_{i,eq}^{\beta}$	concentration of i-th component in β at the interface in local equilibrium
c_i^{∞}	concentration of i-th component in the far-field
x or r	location
x_f or r_f	location of the interface
t	time
η	$x/\sqrt{t}$ or $r/\sqrt{t}$
η_s	$x_f/\sqrt{t}$ or $r_f/\sqrt{t}$
σ	interfacial energy
κ	curvature of the interface
μ_i	diffusion potential of the i-th component
$\mu_{i,eq}^{*}$	the linearization point of diffusion potential of the i-th component
$\Psi^{\alpha,\beta}$	the Grand-potential density of the phases
D_{ij}	(i,j)-th component of the diffusivity matrix
d	the number of dimensions

Table 4.1: The symbols used in the analytical derivation.

4.1.1 Independent solute diffusion

We begin with the analysis of the diffusional growth of a precipitate in a system displaying independent diffusion of solutes, i.e., a diagonal diffusivity matrix.

The generic expression of the governing equation in the matrix as given by,

$$\left\{\frac{\partial c_i}{\partial t}\right\} = \frac{1}{r^{d-1}}\left[D_{ij}\right]\left\{\frac{\partial}{\partial r}\left(r^{d-1}\frac{\partial c_j}{\partial r}\right)\right\}, \tag{4.1}$$

which is expressed in the vector-matrix notation, where $\{\cdot\}$ represents a vector and $[\cdot]$ represents a matrix. The indices i and j iterate over all the $(K-1)$ solute components in a K component system. The symbol d assumes a value representing the dimensionality of the problem, i.e.,

$d = 1, 2, 3$, for planar, cylindrical and spherical growth, respectively. The space coordinate is represented by r; this appears to be an intuitive choice when we cast the diffusion equation in cylindrical or spherical coordinates and invoke azimuthal and poloidal symmetries leading to an expression involving only the radial axis given by r. The Stefan boundary condition at the interface writes as,

$$v\left\{c^{\alpha}_{i,eq} - c^{\beta}_{i,eq}\right\} = -\left[D_{ij}\right]\left\{\frac{\partial c_j}{\partial r}\right\}\Bigg|_{r_f}, \tag{4.2}$$

with $c^{\alpha,\beta}_{i,eq}$ as the equilibrium compositions at the interface for the matrix (α) and the precipitate (β) and v being the velocity of the interface with its position being denoted by r_f.

Under independent diffusion of solutes we can simplify Eq. 4.1,

$$\frac{\partial c_i}{\partial t} = \frac{1}{r^{d-1}} D_{ii} \frac{\partial}{\partial r}\left(r^{d-1}\frac{\partial c_i}{\partial r}\right). \tag{4.3}$$

We perform a co-ordinate transformation, writing $\eta = r/\sqrt{t}$. In these co-ordinates the governing equations transform to,

$$-\left(\frac{\eta}{2D_{ii}} + \frac{d-1}{\eta}\right)\frac{\partial c_i}{\partial \eta} = \frac{\partial^2 c_i}{\partial \eta^2} \tag{4.4}$$

while the Stefan-boundary condition at the interface reads,

$$\left\{\frac{\partial c_i}{\partial \eta}\right\}\Bigg|_{\eta_s} = \frac{-\eta_s}{2}\left\{\frac{\Delta c_i}{D_{ii}}\right\}, \tag{4.5}$$

where $\eta_s = r_f/\sqrt{t}$ is the corresponding value at the interface, which is at a position r_f at a given time t. We have used, $\Delta c_i = \left(c^{\alpha}_{i,eq} - c^{\beta}_{i,eq}\right)$.

Integrating Eq. 4.4 once, we derive,

$$\left\{\frac{\partial c_i}{\partial \eta}\right\} = \left\{\frac{\lambda_i}{\eta^{d-1}}\exp\left(\frac{-\eta^2}{4D_{ii}}\right)\right\}, \tag{4.6}$$

where λ_i's are integration constants. Using the Stefan's conditions in Eq. 4.5, the value of the

integration constants can be derived as,

$$\{\lambda_i\} = \frac{-\eta_s^d}{2} \left\{ \frac{\Delta c_i}{D_{ii} \exp\left(\frac{-\eta_s^2}{4D_{ii}}\right)} \right\}, \tag{4.7}$$

where, since λ_i's are independent of η, the value of η_s must be a constant for a given alloy composition and is known as the growth constant. It must be noted that Δc_i in Eq. 4.7 is not known at this point and must be determined as part of the solution.

For cylindrical and spherical precipitate growth, the difference in compositions of the matrix and the precipitate in local equilibrium at the interface (Δc_i) and the equilibrium matrix and precipitate compositions $c_{i,eq}^{\alpha,\beta}$ are functions of the particle radius (R) determined by the Gibbs-Thomson correction. As a particular radius R can correspond to non-unique combinations of η_s and time t, consideration of curvature effects would compel an introduction of the time t in our formulation which precludes a solution corresponding to the scaling regime. Avoiding the capillarity effects however admits a solution in the scaling regime. Thus, in our analysis, we additionally assume that when the growth conditions reach the scaling regime the precipitate sizes are large enough that the capillarity effects will be negligible and thus ignored in our calculations.

Integrating Eq. 4.6 once again and invoking the boundary condition that the far-field compositions corresponding to $\eta = \infty$ are known as $\{c_i^\infty\}$ and the compositions at the interface $\eta = \eta_s$ are the equilibrium compositions $\left\{c_{i,eq}^\alpha\right\}$, we derive,

$$\left\{ \frac{c_i^\infty - c_{i,eq}^\alpha}{\int_{\eta_s}^\infty \frac{1}{\eta^{(d-1)}} \exp\left(-\frac{\eta^2}{4D_{ii}}\right) d\eta} \right\} = \frac{-\eta_s^d}{2} \left\{ \frac{\Delta c_i}{D_{ii} \exp\left(\frac{-\eta_s^2}{4D_{ii}}\right)} \right\}, \tag{4.8}$$

The system of $K-1$ equations represented by Eq. 4.8 can now be solved for the growth constant η_s, and the equilibrium compositions in the matrix side $c_{i,eq}^\alpha$ with a prior knowledge of equilibrium tie-lines in the system that enables the precipitate compositions $c_{i,eq}^\beta$ to be expressed as functions of the matrix compositions $c_{i,eq}^\alpha$. The other technique, and the one which we are going to employ, involves expressing the equilibrium compositions $c_{i,eq}^{\alpha,\beta}$ as functions of the diffusion potentials μ_i. This approach requires a knowledge of the behavior of the free energy functions with change in compositions, which are readily available from various thermodynamic databases, in contrast to the complete knowledge of all the equilibrium tie-lines in the system,

for the former approach. The details of the solution procedure is presented through a discussion of the system thermodynamics in the following section.

The converse problem of determining the bulk compositions which would equilibrate at a given tie-line as functions of the growth constant η_s can be tackled directly by substituting for $c^{\alpha}_{i,eq}$ and η_s in Eq. 4.8, to determine c^{∞}_i. Furthermore, Eq. 4.8 can also allow the determination of the composition profiles in the matrix ($\eta > \eta_s$) during the scaling regime. This can be seen by integrating Eq. 4.6 between the limits η and ∞ to obtain,

$$\left\{c_i\left(\eta\right)\right\} = \left\{ c^{\infty}_i - \left(c^{\infty}_i - c^{\alpha}_{i,eq}\right) \frac{\int_{\eta}^{\infty} \frac{1}{\eta^{(d-1)}} \exp\left(-\frac{\eta^2}{4D_{ii}}\right) d\eta}{\int_{\eta_s}^{\infty} \frac{1}{\eta^{(d-1)}} \exp\left(-\frac{\eta^2}{4D_{ii}}\right) d\eta} \right\}. \tag{4.9}$$

4.1.2 Thermodynamics

For the solution to the complete problem of the equilibrium compositions of the precipitate and the matrix as well as the growth coefficient representing the parabolic growth regime, one needs to find additional (K-2) relations between the precipitate and matrix compositions.

In order to relate the equilibrium compositions in the precipitate and the matrix one of the possibilities is to parameterize the information from two-phase region of the phase diagram. The other possibility and the one which we adopt in this chapter is to encapsulate this information by capturing the variation of each of the equilibrium compositions as functions of the diffusion potentials, which being intensive variables are equal in the two phases at equilibrium. Thus, in the place of solving 2(K-1) equilibrium compositions in the precipitate and the matrix, we will now solve for just (K-1) diffusion potentials. The equilibrium and precipitate compositions can in turn be determined from the diffusion potentials by inverting the functions $\mu_i\left(c\right)$ which are known for each phase once the free-energy expressions are described.

Additionally, local thermodynamic equilibrium at the interface also requires that along with the equality of the diffusion potentials, the driving force at the interface also vanishes. One of the ways to describe the driving forces at the interface is the difference of the grand-potential densities at the interface which for a phase transformation from α to β writes as $\Delta\Psi^{\alpha\beta} = \Psi^{\alpha} - \Psi^{\beta}$, where Ψ^{α} and Ψ^{β} are the individual grand-potential densities of the phases. For our present studies, we utilize a linearized phase diagram around the compositions of interest, which also allows for a simple coupling to thermodynamic databases. The driving force, $\Delta\Psi$ is derived by linearly expanding the individual grand-potential densities in terms of the departure of the diffusion potential (state variable of the grand-potential density) from a

given equilibrium value $\boldsymbol{\mu}^*_{eq} = \left\{\mu^*_{i,eq}\right\}$ as,

$$\Psi^{\alpha,\beta}\left(\boldsymbol{\mu}, T\right) = \Psi^{\alpha,\beta}\left(\boldsymbol{\mu}^*_{eq}, T\right) + \left\{\frac{\partial \Psi^{\alpha,\beta}}{\partial \mu_i}\right\}_{\mu^*_{i,eq}} \left\{\mu_i - \mu^*_{i,eq}\right\}, \tag{4.10}$$

and therefore, the leading order term in the driving force for the phase transformation α to β writes as,

$$\Delta\Psi^{\alpha\beta} = \frac{1}{V_m}\left\{c^{\beta,*}_{i,eq} - c^{\alpha,*}_{i,eq}\right\}\left\{\mu_i - \mu^*_{i,eq}\right\}. \tag{4.11}$$

Thus, an equilibrium at a planar interface leads to,

$$\Delta\Psi^{\alpha\beta} = 0, \tag{4.12}$$

which modifies around curved interfaces to,

$$\Delta\Psi^{\alpha\beta} = \sigma\kappa. \tag{4.13}$$

The Eqs. 4.12 and 4.13 relate the departure of diffusion potentials, as given by,

$$\left(\mu_1 - \mu^*_{1,eq}\right) = \frac{-1}{\left(c^{\beta,*}_{1,eq} - c^{\alpha,*}_{1,eq}\right)} \sum_{j=2}^{K-1} \left(c^{\beta,*}_{j,eq} - c^{\alpha,*}_{j,eq}\right)\left(\mu_j - \mu^*_{j,eq}\right), \tag{4.14}$$

for growth by a planar interface, and

$$\left(\mu_1 - \mu^*_{1,eq}\right) = \frac{\sigma\kappa - \sum_{j=2}^{K-1}\left(c^{\beta,*}_{j,eq} - c^{\alpha,*}_{j,eq}\right)\left(\mu_j - \mu^*_{j,eq}\right)}{\left(c^{\beta,*}_{1,eq} - c^{\alpha,*}_{1,eq}\right)}, \tag{4.15}$$

for growth by the motion of a curved interface. The phase compositions as a function of the chemical potential being linearly extrapolated from the chosen equilibrium points $\left\{c^*_{i,eq}\right\}$ writes as,

$$\left\{c^{\alpha,\beta}_i\right\} = \left\{c^{\alpha,\beta}_{i,eq}\right\}^* + \left[\frac{\partial c^{\alpha,\beta}_i}{\partial \mu_j}\right]_{\mu^*_{i,eq}} \left\{\mu_j - \mu^*_{j,eq}\right\}, \tag{4.16}$$

where the susceptibility matrix $\left[\frac{\partial c^{\alpha,\beta}_i}{\partial \mu_j}\right]_{\mu^*_{i,eq}}$ is a term that can be also retrieved from the

thermodynamic databases. Invoking the conditions for local equilibrium from Eqs. 4.14 or 4.15 which relates one of the arbitrarily chosen diffusion potentials $(\mu_1 - \mu_{1,eq})$ to the rest of the diffusion potentials, into the preceding equation, gives us the loci of all possible phase compositions corresponding to local thermodynamic equilibrium either on a planar or curved interface respectively. Each of the possible equilibrium phase compositions will then correspond to a unique set of $\mu_i's$.

Ignoring capillarity this relation for the set of equilibrium phase compositions thus writes as,

$$\left\{c_{i,eq}^{\alpha,\beta}\right\} = \left\{c_{i,eq}^{\alpha,\beta}\right\}^{*} + \sum_{j=2}^{K-1}\left[\frac{\partial c_i^{\alpha,\beta}}{\partial \mu_j} - \frac{1}{\rho_j}\frac{\partial c_i^{\alpha,\beta}}{\partial \mu_1}\right]_{\mu_{i,eq}^{*}} \left\{\mu_j - \mu_{j,eq}^{*}\right\}, \tag{4.17}$$

where $\rho_j = \left(c_{1,eq}^{\beta,*} - c_{1,eq}^{\alpha,*}\right) / \left(c_{j,eq}^{\beta,*} - c_{j,eq}^{\alpha,*}\right)$. Substituting Eq. 4.17 into Eq. 4.8, we obtain a set of $K-1$ equations which can be solved to determine $(K-2)$ μ_j's and η_s. The knowledge of μ_j's allows the determination of compositions $c_{i,eq}^{\alpha,\beta}$ from Eq. 4.17. Thus, given a far-field alloy composition in the matrix and the solute inter-diffusivities, we can analytically determine the tie-line compositions $c_{i,eq}^{\alpha,\beta}$ and growth coefficient η_s during the growth of a precipitate phase having a planar as well as curved interface with the matrix, for any generic multi-component alloy.

4.1.3 Coupled diffusion of solutes

Generalizing, for the case of arbitrary diffusion matrices, we adopt the following transformation strategy. Consider the governing equation describing planar growth with the diffusivity matrix now containing off-diagonal components as well, as given by, Eq. 4.1. We assume the diffusivity matrix to be constant and diagonalizable, as given by,

$$\tilde{D} = P^{-1}DP, \tag{4.18}$$

where $\widetilde{D}$ is the diagonalized diffusivity matrix, and P being a matrix whose column vectors are the eigenvectors of D. Using Eq. 4.18 to substitute for D in Eq. 4.1 we obtain,

$$\left\{\frac{\partial c_i}{\partial t}\right\} = \left[P\tilde{D}P^{-1}\right]_{ij}\left\{\frac{\partial^2 c_j}{\partial x^2}\right\}. \tag{4.19}$$

Defining,

$$P_{ij}^{-1} c_j = \widetilde{c_i}, \tag{4.20}$$

and multiplying Eq. 4.19 on both sides by P^{-1}, we obtain by invoking the constancy of the matrix P^{-1} (due to the constancy of the D matrix),

$$\left\{ \frac{\partial \widetilde{c_i}}{\partial t} \right\} = \left[\tilde{D}_{ij} \right] \left\{ \frac{\partial^2 \widetilde{c_j}}{\partial x^2} \right\}. \tag{4.21}$$

The Stefan condition is also transformed accordingly, and by mapping the far-field compositions to the space defined by the eigenvectors of D as $P_{ij}^{-1} c_j^{\infty} = \widetilde{c_i^{\infty}}$, we can write an analog of Eq. 4.8 in the new coordinate system of the compositions as,

$$\left\{ \frac{\widetilde{c_i^{\infty}} - \widetilde{c_{i,eq}^{\alpha}}}{\int_{\eta_s}^{\infty} \frac{1}{\eta^{(d-1)}} \exp\left(-\frac{\eta^2}{4\widetilde{D_{ii}}} \right) d\eta} \right\} = \frac{-\eta_s^d}{2} \left\{ \frac{\widetilde{\Delta c_i}}{\widetilde{D_{ii}} \exp\left(\frac{-\eta_s^2}{4\widetilde{D_{ii}}} \right)} \right\}. \tag{4.22}$$

The closure conditions can also be derived accordingly where we substitute for $\widetilde{c_{i,eq}^{\alpha}}$ by multiplying both sides of Eq. 4.17 by P^{-1}. The resulting set of equations can then be solved for the unknown μ_j's and η_s like described in the case for independent diffusion of solutes.

In the next section we study the limiting cases to the full local equilibrium problem just described, which become relevant as the differences in diffusivities of solutes increases to several orders of magnitude. There are two such limiting conditions, corresponding to low and high supersaturations, respectively, which are described in the next section.

4.2 Theory: Limiting cases to local equilibrium

Under circumstances where one or more of the solutes have diffusivities lower by several orders of magnitude than the faster moving solute, we can invoke constraints described by Coates [19] which serve as limiting situations to the complete local equilibrium problem. These constraints usually concern the partitioning (attainment of different concentrations for different phases) of the slower moving species between the parent and the product phases and there are two different types which can be invoked depending upon whether the growth rate is slow or fast. We discuss the procedure for computing the phase concentrations and growth constants for each of the two limiting cases in the following subsections.

4.2.1 Partition under local equilibrium (PLE)

Under conditions of slow growth corresponding to low supersaturations, the kinetics is determined by the partitioning of the slower moving species between the matrix and the precipitate phases, as the faster moving species are partitioned almost instantly. Coates' [19] realized this situation as one where the faster moving species experience negligibly small driving forces for diffusion, resulting in the growth rate to be controlled by the slower moving species. Denoting the faster moving species by 'k', the absence of a driving force for its diffusion for the case of diagonal diffusivity matrix would be attained when the following condition is satisfied which reads,

$$c_k^{\alpha} = c_k^{\infty}. \tag{4.23}$$

Eq. 4.23 can be translated into an expression involving the diffusion potentials (μ_i) by employing Eq. 4.16 to express c_k^{α}. This allows us to express μ_k in terms of the other μ_i's as,

$$\mu_k = \mu_{k,eq}^{*} + \frac{(c_k^{\infty} - c_k^{\alpha,*}) - \sum_{j\neq k}^{K-1} \left[\frac{\partial c_k^{\alpha}}{\partial \mu_j}\right]_{\mu_{i,eq}^{*}} (\mu_j - \mu_{j,eq}^{*})}{\left[\frac{\partial c_k^{\alpha}}{\partial \mu_k}\right]_{\mu_{i,eq}^{*}}}. \tag{4.24}$$

Eq. 4.24 in conjunction with the existence of local equilibrium at the $\alpha - \beta$ interface given by Eq. 4.14 reduces the number of unknown diffusion potentials to $K-3$. The lack of a driving force for the diffusion of the faster moving species eliminates the corresponding diffusion equation. We are thus left with $K-2$ equations to determine exactly $K-2$ unknowns which are the $K-3$ diffusion potentials and the growth constant η_s. This concept can be extended to a situation where there are several species with diffusivities much lower than the rest. In that case, we can write versions of Eq. 4.24 for all of the faster moving species and eliminate their corresponding diffusion potentials. The resultant set of equations obtained by eliminating the diffusion equations of the faster species, are enough to consistently solve for the unknowns.

4.2.2 Negligible partition under local equilibrium (NPLE)

During fast growth in highly supersaturated alloys, the concentration of the slower moving species in the bulk is retained for the precipitate (negligible partitioning) while faster moving species assume different concentrations in the precipitate and the matrix. A physical understanding of this situation [19] is that the driving force for the diffusion of the slower moving

species is rendered infinite by the lack of partitioning, resulting in a thin spike in its concentration ahead of the interface in the α. The presence of such sharp gradients in composition at the interface precludes a solution of the concerned diffusion equation and the kinetics is given by the diffusion of the faster moving species. The relevant constraint in this case which indicates the lack of partitioning is given by,

$$c_l^{\beta} = c_l^{\infty}, \tag{4.25}$$

where l denotes the slow moving species. This condition coupled with Eq. 4.16 yields a similar relationship between the diffusion potentials as seen in the case of PLE, given by,

$$\mu_l = \mu_{l,eq}^{*} + \frac{(c_l^{\infty} - c_l^{\beta,*}) - \sum_{j\neq l}^{K-1} \left[\frac{\partial c_l^{\beta}}{\partial \mu_j}\right]_{\mu_{i,eq}^{*}} (\mu_j - \mu_{j,eq}^{*})}{\left[\frac{\partial c_l^{\beta}}{\partial \mu_l}\right]_{\mu_{i,eq}^{*}}}. \tag{4.26}$$

Eq. 4.26 when used in conjunction with the equation for local equilibrium in Eq. 4.14, leads to a situation similar to PLE where $K-2$ unknowns ($K-3$ diffusion potentials and η_s) have to be determined from $K-2$ diffusion equations, but with the diffusion equation for the slower moving species neglected instead of the faster moving ones for PLE. As described for the case of PLE, this can also be extended to capture the situation corresponding to the presence of several species whose diffusivities are orders of magnitude lower than the rest.

4.2.3 PLE and NPLE: Extension to coupled diffusion of solutes

We extend the limiting conditions to coupled solute diffusion [19],where for every slow moving species (l), we write,

$$\frac{\partial c_l}{\partial t} = D_{ll}\nabla^2 c_l, \tag{4.27}$$

as $D_{ll} >> D_{lk}$. But for the faster moving species (k) the diffusion equation reads,

$$\frac{\partial c_k}{\partial t} = D_{kk}\nabla^2 c_k + \sum_j D_{kj}\nabla^2 c_j, \tag{4.28}$$

where j iterates over all the slower moving species. The reason for the cross-terms appearing in Eq. 4.28 is that gradients in compositions of the slower moving species in the matrix are large

enough to offset the small values of the cross-diffusivities. So, in the PLE regime, the growth kinetics being determined by the diffusion of the slower moving species, solution to the set of equations in Eq. 4.27 which do not contain any coupled terms can be obtained in an identical manner to the situation for independent diffusion of solutes. But for NPLE, the diffusion of the faster species being the rate controlling step, the cross-diffusion terms are significant and need to be incorporated. This can be understood for a ternary system where the component 1 is much faster than component 2. Diagonalizing the system of equations given by Eqs. 4.27 and 4.28 we obtain the eigenvalues to be D_{11} and D_{22}. Thus, even in the diagonalized basis one of the equations continue to represent the diffusion of the sluggish species and hence can be neglected. The remaining equation represented by Eq. 4.22 is then solved for η_s by mapping the knowledge of the compositions at the interface in the matrix as determined by imposing the conditions represented by Eq. 4.25 and Eq. 4.14. The crucial aspect of the solution process just described is the emergence of D_{22} as one of the eigenvalues which allows us to disregard the corresponding diffusion equation in the eigen-space of the diffusivity matrix citing the smallness of D_{22}. This observation holds true for generalization to multi-component alloys as well, where in the eigen-space of the diffusivity matrix there should be as many equations representing diffusion of sluggish species (linear combinations of original compositions), as there are in the original representation for a solution to be obtained. This may not be possible always and we have to obtain predictions under assumptions of diffusion of the faster species being negligibly affected by the diffusion of the slower moving species.

This concludes our discussion of the analytical techniques for determining the tie-lines and the scaling constants during single phase growth in a scaling regime in a multi-component alloy. In the following section, we present a short description of the sharp-interface technique which we employ to benchmark our theory along with the predictions from phase-field simulations. The phase-field model employed for this purpose is the Grand-Potential model, with the driving forces approximated as functions of departures from equilibrium diffusion potentials till the first order term only. This choice of the thermodynamic relationships to be used in the phase-field model is completely consistent with the ones invoked in our analytical theory. The detailed description of the Grand-Potential model is presented in Chapter 3 alongside a discussion on the thermodynamic relationships under the heading of "Linearized driving forces". Before proceeding to a discussion of our results we tabulate the parameters (see table 4.2) used in phase-field simulations and the values of the different thermodynamic constants used in our calculations. The phase-field simulation parameters are:

The choice of ϵ and Δx is such that there are at least ten points describing the diffuse interface.

σ	1.0
ϵ	4.0
Δx	1.0
Δt	0.01

Table 4.2: The phase-field simulation parameters

The value of the relaxation constants $\tau_{\alpha\beta}$ are presented in the figure captions depending on the respective diffusivity ratios that are used for the phase-field computations.

The non-dimensional $\partial c/\partial \mu$ thermodynamic parameter that is common to all calculations is given by,

$$\frac{\partial c}{\partial \mu} = \begin{bmatrix} 1.1548 & 0.0535 \\ 0.0535 & 1.0025 \end{bmatrix}, \tag{4.29}$$

which is calculated by inverting the $\left[\frac{\partial \mu}{\partial c}\right]$ matrix. The $\left[\frac{\partial \mu}{\partial c}\right]$ matrix is determined by assuming the molar free energies of the matrix phase(α) to be given by,

$$F^{\alpha}(\mathbf{c}^{\alpha}) = \sum_{i=1,j=1,i<=j}^{K-1,K-1} A_{ij}^{\alpha} c_i^{\alpha} c_j^{\alpha} + \sum_{j=1}^{K-1} B_j^{\alpha} c_j^{\alpha} + E^{\alpha}, \tag{4.30}$$

while that of the β phase is given by,

$$F^{\beta}(\mathbf{c}^{\beta}) = \sum_{i=1,j=1,i<=j}^{K-1,K-1} A_{ij}^{\beta} c_i^{\beta} c_j^{\beta}. \tag{4.31}$$

For simplicity, we have taken the matrices A^{α} and A^{β} to be constant and equal to each other, which are given by,

$$A^{\alpha,\beta} = \begin{bmatrix} 0.434049 & -0.046327 \\ -0.046327 & 0.5 \end{bmatrix}. \tag{4.32}$$

The constants B_j^{α} and E^{α} are thereafter determined by enforcing the condition of equilibrium between the α and the β phases, at the desired equilibrium composition values. The constants B_j^{α} are calculated by equating the diffusion potentials ($\mu_i^{\alpha,\beta} = \partial F^{\alpha,\beta}/\partial c_i$) of the two phases, while E^{α} is computed by equating the grand-potentials ($\Psi^{\alpha,\beta} = f^{\alpha,\beta} - \frac{1}{V_m}\sum_{j=1}^{K-1} \mu_j c_j^{\alpha,\beta}$) of the two phases; $f^{\alpha,\beta} = F^{\alpha,\beta}/V_m$ being the molar free energy densities. The molar volumes (V_m) of the two phases are taken to be constants. For our choice of the thermodynamic tie-line given by $c_B^{\alpha} = c_C^{\alpha} = 0.1$ and $c_B^{\beta} = c_C^{\beta} = 0.4$, we compute, $B_1^{\alpha} = 0.24653$ and $B_2^{\alpha} = 0.28610$ and $E^{\alpha} = -0.13316$. It must be mentioned, that the thermodynamic calculation just described to

compute the $[\partial\mu/\partial c]$, is completely independent of the thermodynamic relationships invoked in our phase-field and analytical calculations. The matrix $\left[\frac{\partial\mu}{\partial c}\right]$ computed in this manner is inverted and introduced into the phase-field and analytical models as the only thermodynamic parameter which appears in these calculations and is treated as a constant determined *a-priori*. In the next section we review the Sharp-interface (front-tracking) technique which is employed in addition to phase-field models to validate our theory numerically.

4.3 Sharp-interface model

The governing Eq. 4.1 can be solved numerically along with the boundary condition at the interface given by Eq. 4.2 using an advective scheme where the motion of the interface is accounted for by an equal and opposite advective term which brings the interface back to its original place (this is a numerically effective way of treating the front tracking problem as the interface cell remains invariant). Thereby, the interface stays stationary in this frame of reference. The modified governing equations in the vector-matrix notation are written as,

$$\left\{\frac{\partial c_i}{\partial t} - v\frac{\partial c_i}{\partial r}\right\} = \frac{1}{r^{d-1}}\left[D_{ij}\right]\left\{\frac{\partial}{\partial r}\left(r^{d-1}\frac{\partial c_j}{\partial r}\right)\right\}, \tag{4.33}$$

where v is the instantaneous local velocity of the interface. The position of the interface is marked by the interface cell, where the equilibrium compositions of the precipitate and the matrix are specified. For a ternary system with B and C as solutes, the gradients $\partial c_{B,C}/\partial r$ are written in discrete form using these compositions at the interface cell and the bulk compositions on the matrix side, next to the interface. To compute the interfacial compositions, the pair of equations in Eq. 4.2 are self-consistently solved for both the velocity and the equilibrium chemical potentials $\mu_{B,eq}, \mu_{C,eq}$ at the interface. This requires that the composition functions $c_{B,C}^{\alpha,\beta}(\mu_B, \mu_C)$ as in Eq. 4.16 are known from thermodynamics along with the equilibrium relation between the two chemical potentials, $\mu_{B,eq}(\mu_{C,eq})$, including Gibbs-Thomson effect, for 2D as can be seen in Eqs. 4.14 and 4.15.

Using these, the pair of equations in Eq. 4.2, can be transformed such that the unknowns are the equilibrium chemical potential of a given component ($\mu_{C,eq}$) and the velocity (v). Once the chemical potential $\mu_{C,eq}$ is known, the other chemical potential $\mu_{B,eq}$ can also be fixed using the thermodynamic relation between them and thereby also the individual phase compositions at the interface, $c_{B,C}^{\alpha,\beta}(\mu_B, \mu_C)$. The compositions are then utilized to compute the gradients in the governing equations in Eq. 4.33 and thereby evolve the compositions $c_{B,C}$ in the matrix

phase through one time-step, using also the velocity that is derived from the Stefan condition. The scaling regime can be identified by the constancy of η_s along with the constancy of interfacial compositions during planar growth. The corresponding composition profiles can then be compared with the theoretical analysis described in the chapter. This method, gives a fast accurate benchmark in all three dimensions, in comparison to the more computationally intensive method of phase field models.

4.4 Comparison with simulations

In this section, we present analytical predictions of dynamically determined tie-lines for different diffusivity matrices for a ternary alloy. Though, our calculations are generic to any multi-component alloy we choose to present our calculations in the simplest setting of a multi-component alloy. An important point to note here is that our analytical expressions are derived for a system where the precipitate phase grows into a supersaturated matrix which is infinite in extent. To ensure that our numerical calculations, in spite of being performed on finite systems, are representative of infinite systems, necessitate a few modifications. Phase field calculations are performed in a simulation box attached to the diffuse interface during planar growth, which allows us to capture the scaling regime, otherwise impeded by the change in far-field compositions at the system boundaries due to growth, while sharp interface calculations are performed by expressing the governing equations in a reference frame attached to the interface. Thus, both our numerical techniques are attuned to capture growth in an infinite system.

We begin with a study of the tie-lines and the growth constants selected with a smooth variation in the far-field alloy composition along a thermodynamic tie-line with $c_B = c_C$, in a ternary alloy. The growth constants η_s varies smoothly as a function of the supersaturation $\nu = (c_B^{\infty} - c_B^{\alpha})/(c_B^{\beta} - c_B^{\alpha})$ as presented in the Fig. 4.1. The higher growth rates observed for higher dimensionalities of the precipitate at the same supersaturation in the matrix is a well-known fact and can be physically interpreted as the ability of the precipitate to absorb (or reject) solutes from a wider range of directions. Fig. 4.1 also highlights the lowering of the growth rates for smaller diffusivities of one of the species, i.e., $D_{CC} = 0.5$, which is another important difference to the situation for an identical diffusivity matrix aside from the change in tie-lines reported in Fig. 4.2. We compare our theoretical predictions with tie-line compositions obtained from sharp interface calculations for two different diffusivity matrices and they are in excellent agreement with each other.

In addition to the prediction of the tie-line compositions, we can also compute the composition profiles ahead of the interface in the supersaturated matrix as described in the theoretical

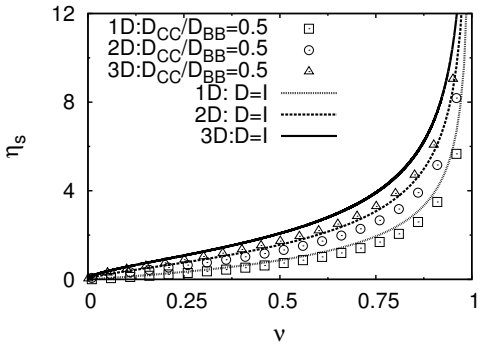

Figure 4.1: Variation in η_s with ν, for diagonal diffusivity matrices. The supersaturated matrix compositions lie on a thermodynamic tie-line given by $c_B^\alpha = c_C^\alpha = 0.1$ and $c_B^\beta = c_C^\beta = 0.4$.

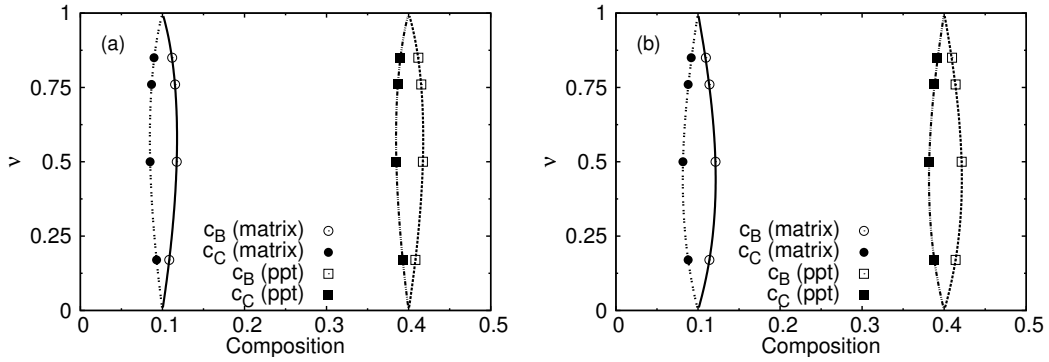

(a) (b)

Figure 4.2: The choice of tie-lines with change in supersaturation. Analytical predictions are plotted against sharp interface calculations for (a) a diagonal diffusivity matrix with $D_{BB} = 1.0$, $D_{CC} = 0.5$, and (b) $D_{BB} = 1.0$, $D_{CC} = D_{BC} = D_{CB} = 0.5$.

discussion. This is shown in Fig. 4.3 where we compare the composition profiles in the matrix from analytical, phase-field and sharp interface calculations find them to be in excellent agreement with each other. This also demonstrates that our analytical predictions are accurate even when the solute diffusivities differ by an order of magnitude. We have performed such comparisons of the composition profiles obtained from analytical calculations to that obtained from phase-field simulations for radial growth as well and present them in Fig. 4.4.

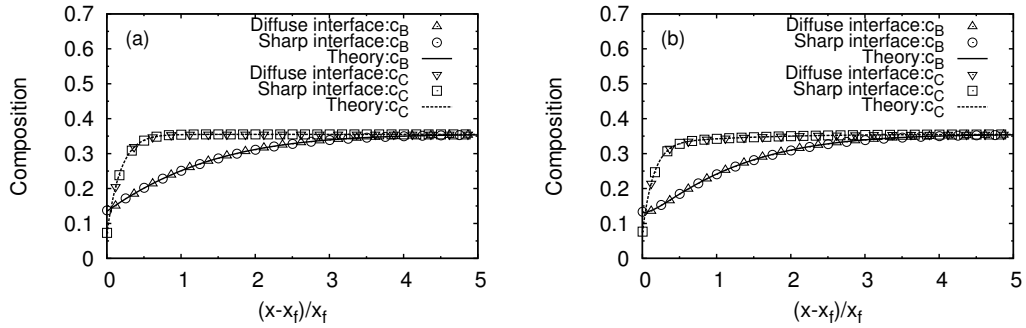

(a) (b)

Figure 4.3: Composition profiles in the matrix for $c_B^\infty = c_C^\infty = 0.355$, for (a) $D_{BB} = 1.0, D_{CC} = 0.1$, $D_{BC} = D_{CB} = 0.0$, (b)$D_{BB} = 1.0, D_{CC} = 0.1$, $D_{BC} = D_{CB} = 0.1$. The phase-field simulations employ the values of $\tau_{\alpha\beta}$ given by (a)0.618888, and (b)0.569789. The far field compositions are varied along the tie-line mentioned in the caption to Fig. 4.1.

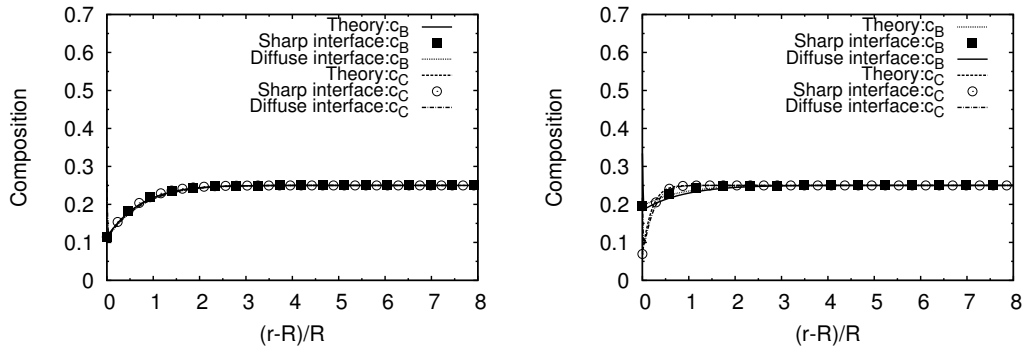

(a) (b)

Figure 4.4: Composition profiles at a $t = 10000$ with the far-field liquid compositions being $c_B = 0.25$ and $c_C = 0.25$. The diffusivity matrix is the same as an identity matrix in (a), while it is $D_{BB} = 1.0$ and $D_{CC} = 0.1$ with the off-diagonal entries zero for (b). The phase-field simulation is performed on an 800×800 box with $dx = dy = 1.0$, $dt = 0.01$, with the same maintained for sharp interface calculations as well.

The influence of capillarity

The discussion until now has been in the spirit of the Zener type calculations, which neglects the influence of capillarity in the calculations. It is true that incorporating capillarity would not lead to a solution that allows growth following a scaling law. However, in physical situations after a small transient growth regime, where the precipitates are small and the capillarity effects are large, the precipitates soon become large enough and the Gibbs-Thomson effects have little influence. The influence of capillarity can be understood by the following Figs. 4.5(a) and 4.5(b) where we compare the selection of the scaling constants (η_s) as a function of the supersaturation ν from analytical and sharp interface calculations. The analytical calculations are performed by neglecting the curvature effects while the sharp interface calculations include them. The close agreement between the values of η_s reflects that the effects of capillarity are limited to the initial transients when the particle is small and it quickly approaches the scaling regime with increase in size. The agreement between the two is better for smaller supersaturations while for larger supersaturations the differences can be attributed to the larger initial transients where the sharp interface solution deviates.

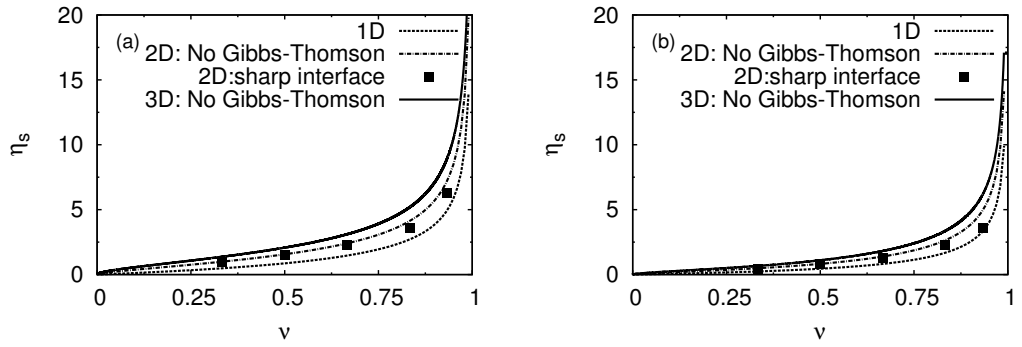

(a) (b)

Figure 4.5: Variation in η_s with ν, for a 2D system with Gibbs-Thomson correction from sharp interface calculations, for (a) $D_{BB} = 1.0$ and $D_{CC} = 1.0$, and (b) $D_{BB} = 1.0$ and $D_{CC} = 0.1$. The other terms in the diffusivity matrix are zero. The results are presented in the context of similar variations obtained for 1D as well as for 2D and 3D systems neglecting the influence of capillarity.

The variation of tie-line compositions with time during radial growth, as obtained from sharp interface calculations are compared against the corresponding from analytical predictions in Fig. 4.6. The tie-line compositions from sharp interface calculations are modified by curvature and hence deviate from the analytical predictions during initial stages of growth when the particle radius is small (curvature is large). In order to differentiate between the shifts in tie-

line compositions due to capillarity and solute diffusivity, we consider the case where the solute diffusivities are equal and the analytical prediction of tie-line compositions remain unchanged from the ones the far field composition belongs to. The tie-line predictions from sharp interface calculations for such a system are presented in Fig. 4.6(a) where the differences from analytical predictions can be solely attributed to capillarity. The deviations are along the same tie-line, i,e., the c_B/c_C ratio of the analytically predicted tie-line compositions are reproduced by the sharp interface predictions. Thus, for either the precipitate or the matrix, capillarity causes both the c_B and c_C to go up equally to maintain $c_B/c_C = 1$, which is the same as the analytically predicted tie-line. Also, an assumption of the equal $\partial c/\partial \mu$ matrices for the precipitate and the matrix phase lead to equal deviations from analytical predictions for both the matrix and the precipitate. Thus, the effect of capillarity is to push the phase coexistence lines parallel to themselves towards higher solute concentrations. However, for the case of unequal solutal diffusivities presented in Fig. 4.6(b), the analytically predicted tie-lines are no longer given by the tie-line the far field compositions belongs to. The effect of capillarity during the initial transients in such a system is complicated. At the very early stages, capillarity dominates and the tie-lines are pushed far towards the higher composition side as discussed in the case for equal solute diffusivities, while the shifts in tie-line compositions due to the effects of the diffusivity matrix are still small. With the growth of the particle, the curvature effects are attenuated and the tie-lines slowly move towards the original coexistence lines. Concurrently, the diffusion fluxes of the solutes exert an increasing influence on the tie-line selection causing it to move towards the ones predicted analytically neglecting capillarity.

Limiting conditions to local equilibrium

The limiting conditions to the local equilibrium described by PLE and NPLE can be understood by the bulk matrix compositions which would equilibrate to a given tie-line conditions for different growth constants. From Fig. 4.7 we can see that with lowering of the diffusivity ratios the series of bulk compositions corresponding to the same tie-line bows out farther from the tie-line in question and approach the straight line segments calculated from the PLE and NPLE approximations. The slope of the lines depicting the series of bulk alloy compositions corresponding to a given diffusivity ratio in Fig. 4.7 can be computed by taking the derivative

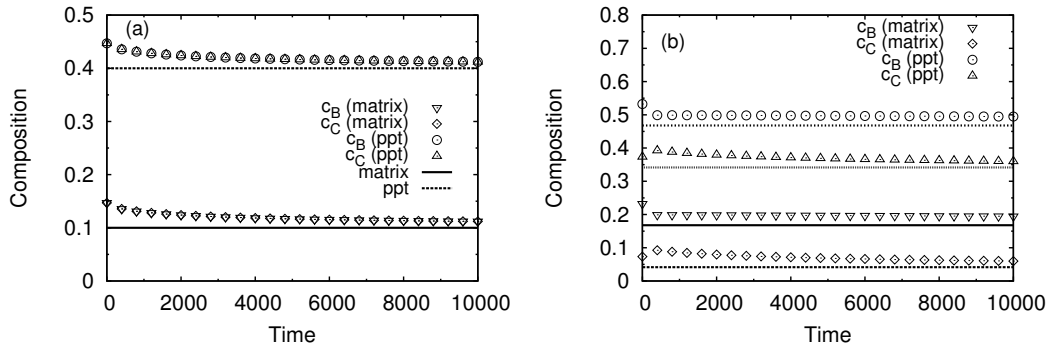

(a) (b)

Figure 4.6: Variation of tie-line compositions with time, with the non-zero diffusivity components being, (a)$D_{BB} = D_{CC} = 1$, and (b) $D_{BB} = 1$, $D_{CC} = 0.1$, during radial growth of a precipitate with the far field matrix composition given by $c_A = c_B = 0.25$. The far field compositions are varied along the tie-line mentioned in the caption to Fig. 4.1. The lines plotted along side the data-points refer to the analytical calculations without incorporation of capillarity (time is plotted in non-dimensional units).

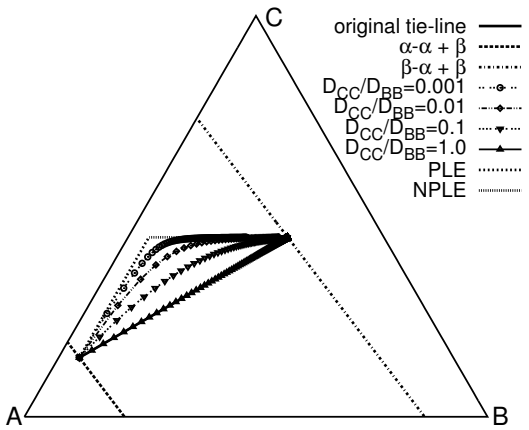

Figure 4.7: Bulk alloy compositions corresponding to different diffusivity ratios which equilibrate to a given thermodynamic tie-line under local equilibrium at the interface. The depicted bulk compositions equilibrate to a tie-line given by: $c_B^\alpha = 0.044935$, $c_C^\alpha = 0.147450$, $c_B^\beta = 0.344935$, $c_C^\beta = 0.447450$.

of Eq. 4.8 w.r.t the growth constant η_s for $d = 1$. This can be written as,

$$\frac{\partial c_i^\infty}{\partial \eta_s} = -\frac{\Delta c_i}{2}\sqrt{\frac{\pi}{D_{ii}}}\left[\frac{\operatorname{erfc}\left(\frac{\eta_s}{2\sqrt{D_{ii}}}\right)}{\exp\left(\frac{-\eta_s^2}{4D_{ii}}\right)} - \frac{\eta_s}{\sqrt{\pi D_{ii}}} + \frac{\eta_s^2}{2D_{ii}}\frac{\operatorname{erfc}\left(\frac{\eta_s}{2\sqrt{D_{ii}}}\right)}{\exp\left(\frac{-\eta_s^2}{4D_{ii}}\right)}\right] \tag{4.34}$$

For $\eta_s \to 0$, applying $\operatorname{erfc}(0) \to 1$ and $\exp(0) \to 1$, we obtain from Eq. 4.34,

$$\frac{\partial c_i^\infty}{\partial \eta_s} = -\frac{\Delta c_i}{2}\sqrt{\frac{\pi}{D_{ii}}}. \tag{4.35}$$

The above expression reveals that the rate of change in bulk composition in terms of any one of the species with the growth constant is inversely proportional to its solute interdiffusivity D_{ii} while being directly proportional to the degree of partitioning of that species between the matrix and the precipitate phases, Δc_i. From Eq. 4.35 we can compute the slope at $\eta_s = 0$, to be,

$$\frac{\partial c_B^\infty}{\partial c_C^\infty} = \frac{\partial c_B^\infty}{\partial \eta_s} \Big/ \frac{\partial c_C^\infty}{\partial \eta_s} = \sqrt{\frac{D_{CC}}{D_{BB}}}\frac{\Delta c_B}{\Delta c_C}. \tag{4.36}$$

Thus, the slope is finite at infinitesimal supersaturations ($\nu \to 0$, corresponding to which η_s's are infinitesimal) and is dependent on the ratio of the solute diffusivities and the ratio of the degree of partitioning of each of the solutes at the interface.

It can be seen from Fig. 4.7 that the NPLE line serves as a tangent to the lines representing the series of bulk alloy compositions corresponding to different diffusivity ratios at different η_s's; the η_s's being determined by the diffusion of the faster species B. Specifically, higher the diffusivity ratio, higher is the η_s, at which the NPLE line assumes tangency to it. In order to quantify this phenomenon, we solve for the diffusivity of the slower moving species (the faster moving species has a diffusivity $D_{BB} = 1$) which results in the bulk alloy composition of the element C to be the same as that in the precipitate. Thus, setting $c_C^\infty = c_C^\beta$, we solve for D_{CC}

from Eq. 4.8 in order to obtain,

$$\frac{\eta_s \operatorname{erfc}\left(\frac{\eta_s}{2\sqrt{D_{CC}}}\right)}{\exp\left(\frac{-\eta_s^2}{4D_{CC}}\right)} = 2\sqrt{\frac{D_{CC}}{\pi}}. \tag{4.37}$$

Eq. 4.37 is solved iteratively starting from large initial guesses of D_{CC} of the order of magnitude of 1 and the solution is terminated when the required tolerance levels are reached. This is done to ensure that the largest value of D_{CC} which leads to tangency with the NPLE line is identified for a particular η_s. Another interesting feature of Eq. 4.37 is that it is independent of of Δc_C, which ascribes a generality to the predictions of Eq. 4.37 by being valid across phase diagrams. In Fig. 4.8 we present a variation of the diffusivity ratio against a normalized supersaturation in B given by $\nu_B = (c_B^{\infty} - c_{B,eq}^{\alpha})/(c_{B,eq}^{\beta} - c_{B,eq}^{\alpha}) = 0.5\sqrt{\pi}\eta_s \operatorname{erfc}(\eta_s/2\sqrt{D_{BB}})/(\sqrt{D_{BB}}\exp(-\eta_s^2/4D_{BB}))$ (from Eq. 4.8 employing $d = 1$), as a change in this parameter is what determines the change in growth constant η_s in the NPLE regime. In order to understand the selection of tie-lines

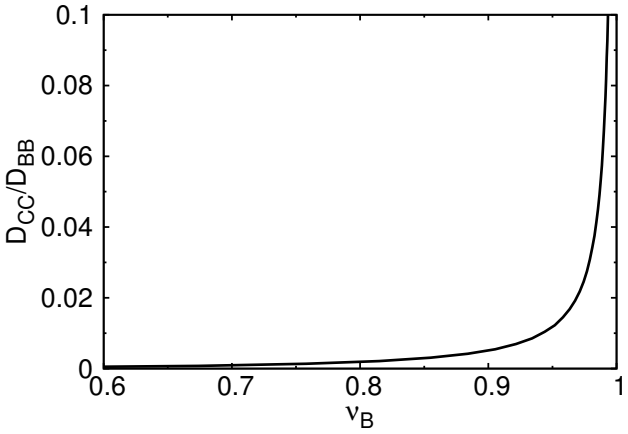

Figure 4.8: The diffusivity ratio D_{CC}/D_{BB} (with $D_{BB} = 1$) corresponding to which the line containing the series of bulk alloy compositions intersect the NPLE line at a given ν_B. The thermodynamic tie-line is chosen to be the same as mentioned in the caption to Fig. 4.7.

under PLE and NPLE at the interface, we refer to Fig. 4.9, where it is evident that the variation of different tie-line compositions with the supersaturation in the matrix (lying on the tie-line mentioned in the caption to Fig. 4.7) follows linear relationship. Furthermore, Fig. 4.9 also reveals that the limiting conditions of PLE and NPLE are limited to well-defined supersaturation regimes. This can be understood by referring to Fig. 4.10 where the PLE curve diverges away from the one obtained for local equilibrium at higher matrix supersaturations,

while the NPLE curve predicts growth only at higher supersaturations where it is also in agreement with the predictions of growth constants from local equilibrium.

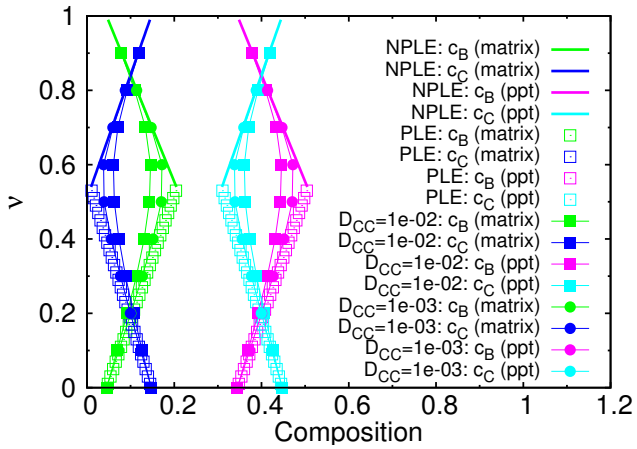

Figure 4.9: Tie-lines as a function of ν which depicts that the predictions from local equilibrium approaches the NPLE and PLE predictions as the diffusivity ratios become smaller and smaller. The bulk compositions lie on the tie-line mentioned in the caption to Fig. 4.7.

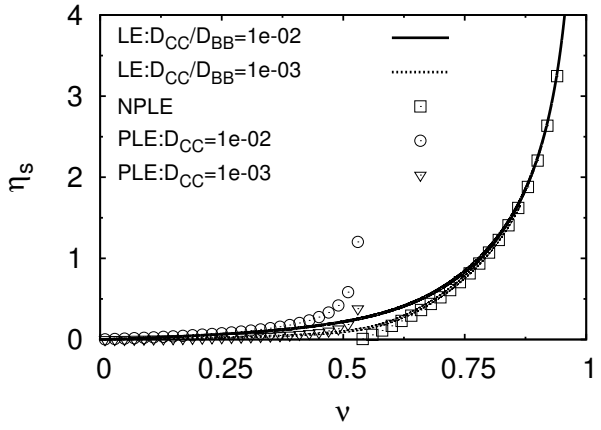

Figure 4.10: The variation of η_s with ν for low diffusivity ratios under local equilibrium as well as under PLE and NPLE approximations obtained by solving the same set of equations as done for Fig. 4.9. The NPLE curve is obtained for a diffusivity of the faster species $D_{BB} = 1.0$. The PLE curves are drawn for two different diffusivities of the slower moving species: $D_{CC} = 1e-02$ and $D_{CC} = 1e-03$. The far field compositions lie on the tie-lines mentioned in the caption to Fig. 4.7.

The tie-line compositions predicted by local equilibrium can be seen to approach the lines given by the limiting conditions of PLE and NPLE with lowering of the diffusivity ratios in Fig. 4.9.

4.5 Summary

In summary, we use numerical simulation methods (phase field, sharp interface) and analytical calculations for the determination of phase equilibria in multi-component systems. There are two developments worth highlighting. Firstly we present an extension of the classical Zener problem for precipitate growth to a generic multi-component alloy. Here, in contrast to Coates [17, 18, 19] and Bourne et al., [20], which are in particular for ternary systems, in our work the expressions for the composition profiles and the selected tie-compositions, are generalized for any multi-component alloy. This is made possible by basing our formulations on the free energy expressions of phases rather than on the information about the co-existence lines/surfaces as has been used in the work by Bourne et al., [20]. Furthermore, we also describe a methodology to analytically calculate the tie-lines and growth velocities for the limiting conditions, PLE and NPLE [19], to local equilibrium when the disparity in diffusivities between the solutes are of several orders of magnitude. Our calculations are able to capture a clear difference in the regimes defined by matrix supersaturations where either of these limiting conditions are appropriate. The predictions of tie-lines and growth constants obtained by solving the full local equilibrium problem can be seen to be approaching these limits with lowering of the diffusivity ratios for both slow and rapid growth conditions.

Secondly, we validate a phase-field model based on a grand-potential formalism for simulating precipitate growth in a multi-component alloy. This validation sets up the model for more complicated simulations of multi-particle growth and coarsening which are difficult to access analytically. Additionally, the simple scheme of incorporating the thermodynamics for (both phase field and sharp interface methods) is similar to previous work [23] where parabolic free-energy extrapolations are used, while for the present chapter, we restrict ourselves to linearized driving forces. The simplicity of the framework allows for easy extension to multi-component alloys for more than three components and incorporation of information from thermodynamic databases. However, the accuracy of the assumption of linearization, must be checked depending on the deviations of phase equilibria from those around which the linearization is performed.

Although, as has been mentioned before in the introduction, experimental verification of the numerical and theoretical work in this chapter is difficult on account of the small time interval in which the scaling regime may obtain during the overall phase transformation. However, one of the possibilities of direct experimental verification of the selection of the tie-lines and velocities is by performing controlled diffusion couple experiments such as those performed in ternary systems, e.g., Cu-Zn-Sn [201], Cu-Zn-Ni [202, 61, 203], Fe-Ni-Al [204, 205], Here extraction of the composition profiles in the phases as well as the interface may be used as an

input for validation of theoretical models. One of the challenges of course in such experiments is to have pure diffusion controlled growth as routinely interfacial reactions cause the phase transformations to become interface controlled.

A strong implication of our work is the need for accurate measurements/ determination of diffusivity/mobility matrices without which results from numerical simulations become less useful in the quantitative understanding of growth in multi-component systems. In particular, the multi-valued nature of the interfacial compositions and its strong dependence on the kinetic parameters in this systems has interesting consequences for phenomena like nucleation [206] and coarsening [207, 208]. In addition, theories of morphological stability of an interface (Mullins-Sekerka theory) [92, 6], lamellar and growth of other morphologies (primarily derived for binary alloys) need to be modified in the context of the results in this chapter, which presents scope for exciting work.

Chapter 5

Diffusive instabilities during single solid phase alloy solidification

In this chapter, we build upon our understanding of the diffusion fields ahead of the interface during steady-state growth of a single phase in a multi-component alloy, and perform a linear stability analysis of such a planar growth front during single phase solidification. We corroborate our analytically predicted behavior of the interface against the predictions from phase-field simulations. Furthermore, we probe the effects of solute interdiffusivities and planar front growth velocities on the characteristic length scales of the instability.

We begin with a theoretical derivation of the rates of amplification of different wavelengths of perturbation of the solid-liquid interface. Following this, we compare the predictions from our linear stability analysis with those obtained from phase-field simulations. This validates our theory, which we then use to predict the behavior of instability as functions of different parameters, like those of the solute interdiffusivities.

5.1 Theory

In this section, we derive an analytical linear stability analysis of the diffusive instability of a planar interface under two conditions. In the first, a) the planar interface is driven in a temperature gradient of defined magnitude (G) with a velocity (V) and secondly, b) for solidification in a uniform undercooled melt. While in a) the velocity of the interface is imposed, in b) the system chooses a growth coefficient that linearly relates the square of the displacement of the interface with time, depending upon the alloy composition and diffusivity matrices. We present a description of all the symbols used in our analytical description in Table. 5.1.

K	the no. of components
c_i	concentration of i-th component in liquid
$c^l_{i,eq}$	concentration of i-th component in liquid at a planar interface in local equilibrium
$c_{i,\Phi}$	concentration of i-th component in liquid at a perturbed interface in local equilibrium
k_i	partition coefficient
$G_{c,i}$	concentration gradient of the i-th component in the liquid at the interface
G	imposed thermal gradient
m^l_i	liquidus slopes
x	coordinate along the interface
z	coordinate normal to the interface along the direction of growth
z_f	the position of the planar solidification front
η	$z/\sqrt{t}$
η_s	$z_f/\sqrt{t}$
t	time
T_m	melting temperature across the planar interface
T_b	reference temperature for the imposed temperature gradient
σ	interfacial energy
Γ	Gibbs-Thomson coefficient
κ	curvature of the interface
μ_i	diffusion potential of the i-th component
$\mu_{i,eq}$	the linearization point of diffusion potential of the i-th component
$\Psi^{l,s}$	the Grand-potential density of the phases
D_{ij}	(i,j)-th component of the diffusivity matrix
ω	wave-number of the perturbation
δ	amplitude of the perturbation
$\dot{\delta}$	rate of change of amplitude of the perturbation
V	velocity of the planar solidification front
$v(x)$	velocity of the perturbed interface

Table 5.1: The symbols used in the analytical derivation.

5.1.1 Directional solidification

Steady state

We begin with steady-state (planar front) solidification of a K component alloy. The $K-1$ independent components have no diffusional interaction (i.e., the diffusivity matrix is diagonal; the general case is treated later) in the liquid, while there is no diffusion in the solid. The governing equation in a frame attached to the interface growing at a velocity V writes as,

$$D_{ii}\frac{\partial^2 c_i}{\partial z^2} + V\frac{\partial c_i}{\partial z} = 0, \tag{5.1}$$

where c_i denotes the concentration and D_{ii} the diffusivity of the i'th component in the liquid, with $i = 1, 2, 3, \ldots, K-1$. z is the direction normal to the solid-liquid interface (located at $z = 0$). Consideration of uncoupled diffusion of solutes enables us to present the following discussion in terms of a generic component i, which stands for all the components in a system.

Eq. 5.1 has a solution whereby the solid grows with a composition that is the same as the liquid composition. This can be easily obtained by integrating the Eq. 5.1 twice and respectively applying the boundary conditions at the interface,

$$Vc^l_{i,eq}(1-k_i) = -D_{ii}\frac{\partial c_i}{\partial z}\bigg|_{z=0} = -D_{ii}G_{c,i}, \tag{5.2}$$

which is the Stefan boundary condition at a solid-liquid interface moving with velocity V, with $G_{c,i}$ as the compositional gradient in c_i at the planar interface and k_i as the equilibrium partition coefficient corresponding to the selected tie-line; the other boundary condition being that of the equilibrium compositions at the interface,

$$c_i = c^l_{i,eq}, \text{ at } z = 0. \tag{5.3}$$

The resultant form of the equation (after the second integration) admits a solution only when the far-field liquid composition is the same as the solid composition. Thereby, the composition of the liquid $c^l_{i,eq}$ as well as the temperature of the interface can be determined uniquely, given the starting alloy composition (far-field liquid composition). This completes the solution to Eq. 5.1 as given by,

$$c_i = c^l_{i,eq} + \frac{G_{c,i}D_{ii}}{V}\left[1 - \exp\left(\frac{-Vz}{D_{ii}}\right)\right]. \tag{5.4}$$

Linear stability analysis

The steady-state solidification described above is now modified by introducing a sinusoidal perturbation given by,

$$z = \Phi = \delta(t) \sin \omega x, \tag{5.5}$$

with x being one of the directions parallel to the unperturbed interface (normal to z). Despite δ being a function of time (t), a stability criterion derivable from the steady state solution will not differ appreciably from that obtained by solving the time dependent problem [28, 92] (quasi-stationary approximation [209]), which leads to the following governing differential equation describing a system with interfacial perturbations,

$$D_{ii}\frac{\partial^2 \widetilde{c_i}}{\partial z^2} + D_{ii}\frac{\partial^2 \widetilde{c_i}}{\partial x^2} + V\frac{\partial \widetilde{c_i}}{\partial z} = 0, \tag{5.6}$$

where the modified composition field of any generic component i, under interfacial perturbation is denoted by $\widetilde{c_i}$. The form of the solution to Eq. 5.6 is obtained by adding a term to the steady-state solution given by Eq. 5.4, which represents a sinusoidal variation in the composition fields in response to the interfacial perturbation of a similar character. It must be taken into account that such an effect diminishes in magnitude with distance from the interface, leading to the following expression,

$$\begin{aligned} \widetilde{c_i} &= c_i + E_i \sin \omega x \ \exp\left(-k_\omega^{(i)} z\right) \\ &= c_{i,eq}^{l} + \frac{G_{c,i} D_{ii}}{V}\left[1 - \exp\left(\frac{-Vz}{D_{ii}}\right)\right] \\ &+ E_i \sin \omega x \ \exp\left(-k_\omega^{(i)} z\right), \end{aligned} \tag{5.7}$$

where $k_\omega^{(i)}$ and E_i are constants. The constant $k_\omega^{(i)}$ is determined by the requirement that the composition profile given by Eq. 5.7 satisfies the governing Eq. 5.6, resulting in a quadratic equation in $k_\omega^{(i)}$, which yields,

$$k_\omega^{(i)} = \frac{V}{2D_{ii}} + \sqrt{\left(\frac{V}{2D_{ii}}\right)^2 + \omega^2}. \tag{5.8}$$

The compositions in the liquid at the perturbed interface are no longer given by the equilibrium tie-lines considered during steady-state growth because of the Gibbs-Thomson correction. The composition deviations conform to the interfacial curvature, which is approximated by the

second derivative of z with respect to x from Eq. 5.5 and can be seen to be of the same form as the perturbation itself. Thus, the composition in the liquid at the perturbed interface is given by,

$$c_{i,\Phi} = c^l_{i,eq} + b_i \delta \sin \omega x, \tag{5.9}$$

where b_i is a constant. Evaluating the solution to the perturbed problem given by Eq. 5.7 at the perturbed interface (see Eq. 5.5), we retrieve,

$$c_{i,\Phi} \approx c^l_{i,eq} + (G_{c,i}\delta + E_i) \sin \omega x, \tag{5.10}$$

where we have retained terms proportional to the first order in the perturbation, Φ. Separately comparing the Fourier coefficients and the leading order constant from Eq. 5.9 and Eq. 5.10, we derive,

$$E_i = \delta(b_i - G_{c,i}). \tag{5.11}$$

Eq. 5.11 is only a reformulation of E_i in terms of b_i, which are still unknown. The b_i's (b_1, b_2, $\cdots$, b_{k-1}) are related to each other through the fact that each of the composition fields ($\widetilde{c_i}$) satisfies the Stefan condition at the perturbed interface, moving at a velocity ($v(x)$). This implies that the same amplification factor ($\dot{\delta}/\delta$) must be obtained by considering the diffusion field of any one of the components. The expression for the Stefan condition at the perturbed interface is given by,

$$\begin{aligned} v(x) &= \left(V + \dot{\delta} \sin \omega x\right) c_{i,\Phi} \left(1 - k_i\right) \\ &= -D_{ii} \frac{\partial \widetilde{c_i}}{\partial z}\bigg|_{z=\delta \sin \omega x}, \end{aligned} \tag{5.12}$$

where $\dot{\delta}$ is $d\delta/dt$. The above equation can be re-expressed as,

$$\left(V + \dot{\delta} \sin \omega x\right) = \frac{-D_{ii}}{c_{i,\Phi}\left(1 - k_i\right)} \frac{\partial \widetilde{c_i}}{\partial z}\bigg|_{z=\delta \sin \omega x}. \tag{5.13}$$

From Eq. 5.9,

$$\frac{1}{c_{i,\Phi}} = \frac{1}{c^l_{i,eq}\left(1 + \frac{b_i}{c^l_{i,eq}} \delta \sin \omega x\right)}$$

$$\approx \frac{1}{c^l_{i,eq}}\left(1-\frac{b_i}{c^l_{i,eq}}\delta\sin\omega x\right), \tag{5.14}$$

where, we have limited ourselves to terms linear in δ. Employing Eq. 5.11 in the expression obtained by differentiating Eq. 5.7 with respect to z, we derive,

$$\begin{aligned}\left.\frac{\partial\widetilde{c_i}}{\partial z}\right|_{z=\delta\sin\omega x} &= G_{c,i}\left(1-\frac{V\delta\sin\omega x}{D_{ii}}\right)\\ &\quad - k_\omega^{(i)}E_i\sin\omega x(1-k_\omega^{(i)}\delta\sin\omega x)\\ &\approx G_{c,i}-\left(\frac{G_{c,i}V}{D_{ii}}+k_\omega^{(i)}(b_i-G_{c,i})\right)\delta\sin\omega x,\end{aligned} \tag{5.15}$$

by limiting ourselves to terms linear in δ. Equating the Fourier coefficients from both sides of Eq. 5.13, we get,

$$\frac{\dot\delta}{\delta}=V\widetilde{\omega_i}\left[-\frac{b_i}{G_{c,i}}+\frac{1}{\widetilde{\omega_i}}\left(k_\omega^{(i)}-\frac{V}{D_{ii}}\right)\right], \tag{5.16}$$

where,

$$\widetilde{\omega_i}=k_\omega^{(i)}-\frac{V}{D_{ii}}\left(1-k_i\right). \tag{5.17}$$

Invoking the fact that $\dot\delta/\delta$ is a quantity unique to the system as a whole regardless of the choice of the component (i.e., i) in Eq. 5.16, leads to $K-2$ relations inter-relating the b_i's (b_1, b_2, $\cdots$ b_{k-1}). To express all b_i's ($i\neq 1$) in terms of b_1, we equate the algebraic expressions for $\dot\delta/\delta$ corresponding to each component, which writes as,

$$\begin{aligned}V\widetilde{\omega_i}\left[-\frac{b_i}{G_{c,i}}+\frac{1}{\widetilde{\omega_i}}\left(k_\omega^{(i)}-\frac{V}{D_{ii}}\right)\right] =\\ V\widetilde{\omega_1}\left[-\frac{b_1}{G_{c,1}}+\frac{1}{\widetilde{\omega_1}}\left(k_\omega^{(1)}-\frac{V}{D_{11}}\right)\right],\end{aligned} \tag{5.18}$$

that leads to,

$$b_i=\frac{G_{c,i}}{\widetilde{\omega_i}}\left[\frac{b_1}{G_{c,1}}\widetilde{\omega_1}+\left(k_\omega^{(i)}-\frac{V}{D_{ii}}\right)-\left(k_\omega^{(1)}-\frac{V}{D_{11}}\right)\right]. \tag{5.19}$$

Now, using Eq. 5.19, the question of determining b_i corresponding to all the $K-1$ components is reduced to the problem of determining b_1 only. This is achieved by writing down the modified

equilibrium temperature as a result of the perturbation, which reads,

$$\begin{aligned} &T_m + \sum_i m_i^l b_i \delta \sin \omega x - \left(T_b + G\left((z+Z) - Vt\right)\right) \\ &= \Gamma\kappa = \Gamma\delta\omega^2 \sin \omega x, \end{aligned} \tag{5.20}$$

where Γ is the Gibbs-Thomson coefficient of the solid-liquid interface, κ is the local curvature, m_i^l's are the respective liquidus slopes, T_m is the melting temperature of the liquid in equilibrium with the solid at the unperturbed interface at Z in the laboratory frame of reference and T_b is an arbitrary reference temperature for the linear temperature gradient. Substituting, $z = \delta \sin \omega x$, expanding $c_{i,\Phi}$, as in Eq. 5.9 and comparing terms proportional to $\sin \omega x$ we derive the condition for the b_i's as,

$$G + \Gamma\omega^2 = \sum_i m_i^l b_i, \tag{5.21}$$

while $T_m = T_b + G\left(Z - Vt\right)$, is the other leading order term.

5.1.2 Isothermal solidification

In this section, we extend the linear stability analysis for the case of isothermal solidification. For this situation, there is no steady-state solution akin to what we used in the previous situation for the case of composition profiles in the liquid ahead of the solidification front.

The planar interface problem

The solution to the planar problem follows the classical Zener [2], Frank [52] analysis of binary alloys, where the interface position z_f w.r.t its starting position at z_0 varies as $\sqrt{t}$, such that $\left(z_f - z_0\right)^2 = \eta_s^2 t$, η_s being the characteristic growth constant. Without going to the complete solution to the problem (which is present elsewhere [5]), we will present the major results here.

The composition profiles in the liquid write as,

$$\frac{c_i\left(\eta\right) - c_i\left(\infty\right)}{c_{i,eq}^l - c_i\left(\infty\right)} = \left\{ \frac{\operatorname{erfc}\left(\dfrac{\eta}{2\sqrt{D_{ii}}}\right)}{\operatorname{erfc}\left(\dfrac{\eta_s}{2\sqrt{D_{ii}}}\right)} \right\}, \tag{5.22}$$

where η_s is the growth coefficient uniquely defined given the alloy composition and the diffusivity matrix, while for any other position in the liquid, the co-ordinate z can be transformed as

$\eta = (z - z_0)/\sqrt{t}$.

The value of η_s is determined by solving the following set of non-linear equations (one each for every component),

$$c_i(\infty) = c^l_{i,eq} - \frac{\sqrt{\pi}}{2} \frac{\eta_s \Delta c_i \operatorname{erfc}\left(\frac{\eta_s}{2\sqrt{D_{ii}}}\right)}{\sqrt{D_{ii}} \exp\left(\frac{-\eta_s^2}{4D_{ii}}\right)}, \tag{5.23}$$

where $\Delta c_i = c^l_{i,eq} - c^s_{i,eq}$, and $c_i(\infty)$ is the far-field composition in the liquid. The number of equations pertaining to the different components are sufficient to determine not only the growth coefficient, but also the equilibrium compositions, $c^{l,s}_{i,eq}$. This requires that we also invoke the condition of local thermodynamic equilibrium that allows us to determine the relation between the equilibrium solid and liquid compositions at the interface.

It must be noted that in contrast to the classical Zener [2], Frank [52] problem for binary alloys which delivers only the solution of the growth coefficient from the preceding relation, for a multi-component system, both the equilibrium compositions as well as the growth coefficient can be determined from the boundary conditions. This implicitly also states that the equilibrium compositions that are selected are a function of not only the inherent thermodynamics but also of the diffusivity matrix.

Linear stability analysis

In order to perform the linear stability analysis, we perform an approximation of the planar problem. Here we choose to perturb the planar state at a given time t, such that the relative change in velocity when the perturbation is analyzed, is small compared to the rate of evolution of that perturbation, and thereby in the time-scale where the linear perturbation analysis is being performed, we assume that the velocity is constant. As a corollary of this assumption, we in addition approximate the composition profiles of the planar problem by the expressions in Eqs. 5.4, where now the equilibrium solutions $c^l_{i,eq}$ are determined using the equations in the previous subsection. As a comparison, we present the composition profiles that represent the exact solution and that determined from the approximation for the state when the velocity of the interface is V, in Fig. 5.1. We see that near to the interface, the diffusion length is well represented by the approximate composition profiles determined by Eqs. 5.4, which is the principal region determining the behavior of a perturbed solid-liquid interface in the linear

regime. The same can be seen by expanding the error function in Eq. 5.22 until the linear term in η, whereby the leading order composition at the interface writes as $c_i = c^l_{i,eq} - \dfrac{V\Delta c_i}{D_{ii}}(z - z_f)$, or $c_i = c^l_{i,eq} + G_{c,i}z$, when z_f is zero in the moving co-ordinate system, which is the same as that obtained from Eqs. 5.4, for small z.

With these assumptions thereby, the perturbation analysis follows in the same manner as described in the section on directional solidification. However, there is now a difference in the Gibbs-Thomson condition deriving the closure condition in Eq. 5.20, which for the present case is determined using the properties of the free-energy expressions of the liquid phase. The Gibbs-Thomson condition is derived by equating the thermodynamic driving force at the interface to the capillary force. The thermodynamic driving force at leading order is written in terms of the departure of the diffusion potentials μ_i from their equilibrium value $\mu_{i,eq}$, i.e., the driving force $\Delta\Psi = \dfrac{1}{V_m}\sum_i (\mu_i - \mu_{i,eq})\left(c^s_{i,eq} - c^l_{i,eq}\right)$. The composition deviations δc_j in the liquid resulting in the appropriate changes in the diffusion potential can additionally be related using the second derivatives of the free energy as, $\mu_i - \mu_{i,eq} = \sum_j \dfrac{\partial \mu_i}{\partial c_j}\delta c_j$. Thus, the Gibbs-Thomson condition, $\Delta\Psi = \sigma\kappa$, ($\sigma$ is the surface tension of the solid-liquid interface, and κ its curvature) in terms of the departure of the equilibrium compositions of the liquid at the interface writes as,

$$\begin{aligned}
&\frac{1}{V_m}\sum_{i=1}^{K-1}\sum_{j=1}^{K-1}\frac{\partial \mu_i}{\partial c_j}(c_{j,\Phi} - c^l_{j,eq})(c^s_{i,eq} - c^l_{i,eq}) = \\
&\frac{1}{V_m}\sum_{i=1}^{K-1}\sum_{j=1}^{K-1}\frac{\partial \mu_i}{\partial c_j}(b_j\delta\sin\omega x)(c^s_{i,eq} - c^l_{i,eq}) = \sigma\kappa \\
&\qquad\qquad = \sigma\delta\omega^2\sin\omega x, \qquad (5.24)
\end{aligned}$$

where we have used Eq. 5.9 to obtain the second equality, with V_m being the molar volume which is assumed to be constant for all the components. The preceding equation is solved along with Eq.5.19 to determine all the b_i's representing the amplitude of perturbation of the interfacial composition of each component. Thereafter, the rate of growth of the perturbation are derived using Eq. 5.16.

5.1.3 Generalization to off-diagonal diffusivity matrices

In this final section on the theoretical linear stability analysis under directional solidification and isothermal conditions, we generalize our results for the case of a general diffusivity matrix with off-diagonal entries. For this, we make the assumption that the diffusivity matrices are

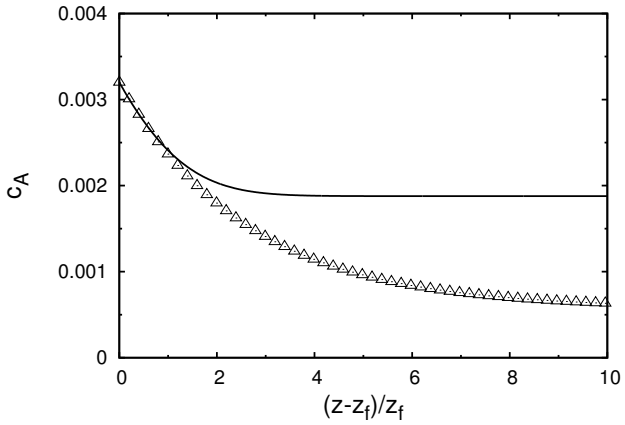

(a)

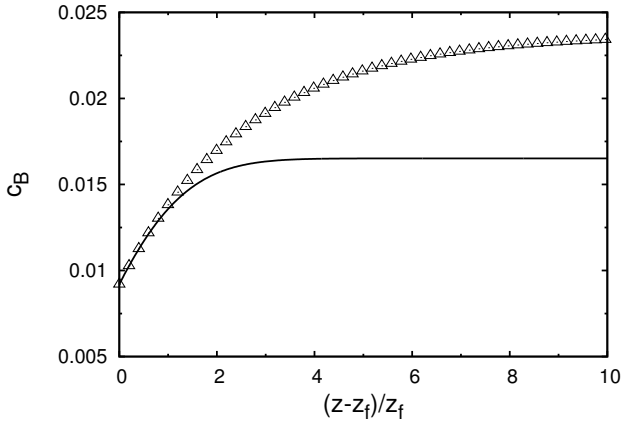

(b)

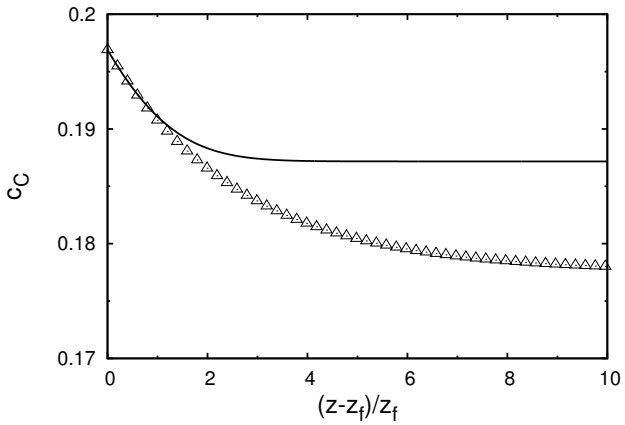

(c)

Figure 5.1: Plots showing comparisons of the composition profiles ahead of the growing interface as predicted by the error function solution in Eq. 5.22 (shown by lines) and the exponential solution in Eq. 5.4 (shown by points) for (a)c_A, (b)c_B and (c)c_C.

diagonalizable. With this, let there exist a diagonalizing matrix P such that a diagonal matrix $\tilde{D} = P^{-1}DP$ can be formulated, where P has its column vectors as the eigenvectors of the original diffusivity matrix D. Following this, the governing equations in Eq. 5.1 can be written down,

$$[P]\,[\tilde{D}][P^{-1}]\left\{\frac{\partial^2 c_i}{\partial z^2}\right\} = -V\left\{\frac{\partial c_i}{\partial z}\right\}. \tag{5.25}$$

For this present discussion, we assume that the diffusivity matrices are not dependent on the composition, and thereby the diagonalizing matrix P is invariant with composition. Therefore, formulating a composition $\{C_i\} = \left[P_{ij}^{-1}\right]\{c_j\}$, and multiplying the preceding equation with P^{-1} on both sides, we derive a diagonalized set of equations, in C_i, as,

$$[\tilde{D}]\left\{\frac{\partial^2 C_i}{\partial z^2}\right\} = -V\left\{\frac{\partial C_i}{\partial z}\right\}. \tag{5.26}$$

Additionally, the partition coefficients K_i are transformed as $K_i = C^s_{i,eq}/C^l_{i,eq}$. Thereafter, the Stefan conditions in Eq. 5.2 can also be transformed accordingly. Following this, the entire stability analysis can be performed in the transformed co-ordinates C_i and K_i, until the point where the closure conditions defined by Eqs. 5.20 and 5.24 are derived. Since, the equilibrium conditions are derived using the original composition space, the transformed compositions need to be accordingly modified with the transformation matrix before the Gibbs-Thomson conditions are written down. The modified closure conditions for the directional solidification derives as,

$$G + \Gamma\omega^2 = [m_i][P]\,\{b_i\}\,, \tag{5.27}$$

while the same for the case of isothermal solidification, writes as,

$$\frac{1}{V_m}\sum_{i=1}^{K-1}\sum_{j=1}^{K-1}\sum_{l=1}^{K-1}\frac{\partial \mu_i}{\partial c_j}(P_{jl}b_l\delta\sin\omega x)(c^s_{i,eq} - c^l_{i,eq}) = \sigma\kappa = \sigma\delta\omega^2\sin\omega x. \tag{5.28}$$

With these modifications, the growth rates of the perturbations derived in Eqs. 5.16 hold true for any generic diffusivity matrix.

This completes our analytical derivations. In the following section, we report a comparison between our theoretical predictions and the ones obtained from phase-field simulations.

We invoke a Grand-Potential model for performing all our phase-field calculations, which is described in detail in Chapter 3. We also invoke thermodynamic relationships, like those of phase compositions as functions of diffusion potentials and that of the driving forces for phase transformation, which are functions of the departures of diffusion potentials to the linear order. These thermodynamic relationships are explained in detail in Chapter 3 in the section titled "Thermodynamics" under the heading "Linearized driving forces".

5.2 Results

In this section, our aim is to compare our analytical results with measurements from phase-field simulations. For this, we set out in the same manner as before, where we first perform simulations in a directional solidification setting, followed by the case of isothermal growth.

5.2.1 Thermodynamic properties

To begin, we choose to *mimic* the thermodynamic properties of a technically relevant Hf-Re-Al-Ni quaternary alloy (super-alloy) for which a thermodynamic database (Thermotech Ni-based Superalloys Database (TTNI8)) is available. However, our thermodynamic construction will only ensure that the composition and the liquidus slopes are reproduced, while the attributes of the free-energies (second-derivatives of the free-energy) of the solid and liquid phases, is assumed to follow a ideal solution model. While discussing our key observations, we will adhere to the generic representation of solutes by A, B and C, with D denoting the solvent in order to remain consistent with our theoretical expressions and discussion of the phase field modelling technique. Thus, for all practical purposes in the discussion that follows, A, B, C and D stand for Hf, Re, Al and Ni respectively.

The equilibrium compositions and the liquidus slopes (in K/mol-frac) derived from the database at 1689K are presented in the Table. 5.2. The $\partial c/\partial \mu$ matrices are derived by assuming that the contribution to the second derivatives of the free-energy expressions arise from the ideal solution contribution term: $\dfrac{RT^*}{V_m}\sum_i c_i \ln c_i$.

Assuming, D to be the solvent we compute $\partial \mu/\partial c = \partial^2 f/\partial c^2$ as,

$$\frac{\partial \mu}{\partial c} = \frac{RT^*}{V_m}\begin{bmatrix} \frac{1}{c_A}+\frac{1}{c_D} & \frac{1}{c_D} & \frac{1}{c_D} \\ \frac{1}{c_D} & \frac{1}{c_B}+\frac{1}{c_D} & \frac{1}{c_D} \\ \frac{1}{c_D} & \frac{1}{c_D} & \frac{1}{c_C}+\frac{1}{c_D} \end{bmatrix}, \tag{5.29}$$

c_A^s	0.000556
c_B^s	0.023831
c_C^s	0.177447
c_A^l	0.0032
c_B^l	0.0092
c_C^l	0.1969
$m_A^{l,s}$	−1948.11
$m_B^{l,s}$	2358.33
$m_B^{l,s}$	−649.59

Table 5.2: Table depicting all the material parameters

where $c_D = 1.0 - c_A - c_B - c_C$. On substituting the equilibrium values of the components for a particular phase in Eq. 5.29, and inverting the resultant matrix, we get,

$$\frac{\partial c^s}{\partial \mu} = \frac{V_m}{RT^*} \begin{bmatrix} 0.000555 & -0.000013 & -0.000099 \\ -0.000013 & 0.023264 & -0.004229 \\ -0.000099 & -0.004229 & 0.145959 \end{bmatrix}, \tag{5.30}$$

$$\frac{\partial c^l}{\partial \mu} = \frac{V_m}{RT^*} \begin{bmatrix} 0.00319 & -0.000029 & -0.00063 \\ -0.000029 & 0.009115 & -0.001811 \\ -0.00063 & -0.001811 & 0.15813 \end{bmatrix}. \tag{5.31}$$

5.2.2 Non-dimensionalization

In this study, all calculations are performed in a non-dimensionalized form. The non-dimensional numbers can be converted back to their dimensional forms for any system, using the following definitions of length (l^*), time (t^*) and energy scales (f^*), determined by the dimensional values of the parameters for that particular system,

$$f^* = \frac{RT^*}{V_m}, \tag{5.32}$$

$$l^* = \frac{\sigma^*}{f^*}, \tag{5.33}$$

$$t^* = \frac{l^{*2}}{[D_{ij}]^*}. \tag{5.34}$$

For this alloy we have used the following values for $V_m = 10.0\ 10^{-6}\ m^3/mol$ and the scale of diffusivity is ($[D_{ij}]^*$) as $1.0\ 10^{-9}\ m^2/s$. Additionally, we have chosen the second-derivatives

$\Delta x, \Delta y$	2.0
Δt	0.08
σ	0.2
ϵ	8.0
G	0.0000005
V	0.02

Table 5.3: Table depicting all the simulation parameters

of the free-energies w.r.t composition to be invariant with temperature, and the values are calculated using $T^* = 1689K$, and the surface tension $\sigma^* = 1.0J/m^2$.

5.2.3 Comparison between theory and phase-field simulations

Directional solidification

We begin our discussion with a comparison of the dispersion plot ($\dot{\delta}/\delta$ versus ω) obtained from phase-field simulation against the one predicted by our analytical theory in Fig. 5.2. The non-dimensional values of the parameters controlling the interfacial energy and width in our phase-field simulations are mentioned in Table. 5.3 alongside the other relevant simulation parameters.

For setting up the phase-field simulations for comparison to the analytical calculations, it is essential to initialize the system very close to the assumptions that are inherent in the analysis. As discussed before, for this condition of solidification, a steady state exists when the solid composition grows with the same composition as that of the far-field liquid. Therefore, in order to initialize the steady-state profile of the composition variation in the liquid ahead of the solid-liquid interface, we first compute the liquid compositions $c^l_{i,eq}$ and the temperature T_{int} that is in equilibrium with the composition of the solid. Thereafter, the steady-state composition profiles are computed using Eq. 5.4 for a given velocity V at which the solid-liquid interface is driven. Thereafter, the planar interface is perturbed using a cosine function with a wavelength that is twice the dimension of the simulation box and amplitude that is equal to half the interface width of the equilibrium phase-field profile. The temperature gradient in the simulation is initialized such that the temperature at the interface is T_{int}, at the start of the simulation. No-flux boundary conditions are assumed for all boundaries, and thereby, we effectively simulate only half the wavelength that is considered for investigation. For all the simulations with a temperature gradient we use a thermal gradient (G) and pulling velocity V mentioned in Table. 5.3 (all in non-dimensional units). The Gibbs-Thomson coefficient comes

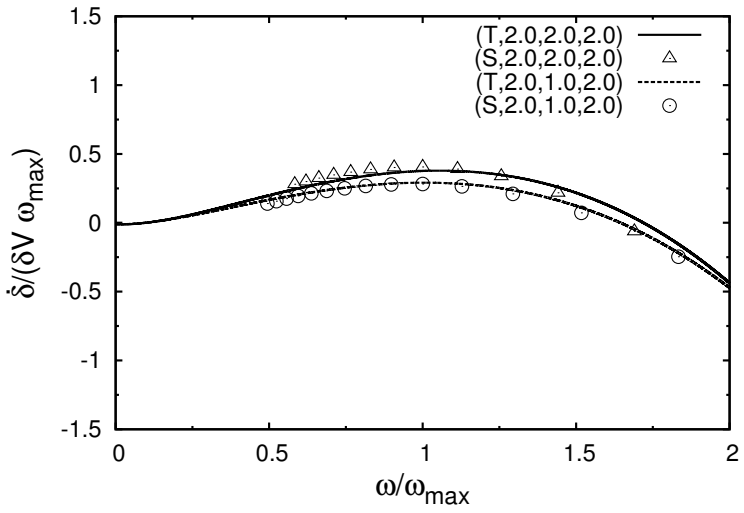

Figure 5.2: $\dot{\delta}/\delta$ versus ω from phase-field and theoretical calculations. The growth rates of the perturbation are scaled with $V\omega_{max}$, while the ω is scaled with ω_{max}, where $\omega_{max} = \dfrac{2\pi}{\lambda_{max}}$, λ_{max} being the maximally growing wavelength (in the phase-field simulation). In the legends the titles T : stands for 'Theoretical', while S : stands for 'Simulation'. The three numbers following T and S in the legends represent the values of D_{AA}, D_{BB} and D_{CC}, respectively.

out to $\Gamma = 0.1614$.

Fig.5.2 represents the simulations performed for two diagonal diffusivity matrices, the first with a diffusivity matrix having all identical entries $D_{AA} = D_{BB} = D_{CC} = 2.0$, and the second for $D_{AA} = 2.0, D_{BB} = 1.0, D_{CC} = 2.0$.

The graph depicts an excellent agreement between the analysis and simulations [1]. Also, we see a small difference in the behavior of the instability with a different choice of the diffusivity matrix. A more elaborate discussion of the influence of the different parameters will follow later.

Isothermal solidification

Following the comparison in the directional solidification setting, we present here the case of solidification under isothermal conditions. As we have seen, the planar composition profiles in the directional and isothermal settings are different. For setting up the phase-field simulations for comparison to the analytical calculations, it is essential to initialize the system very close

[1]It must be mentioned at this point that simulations performed for studying the dispersion behavior are restricted to modes $\omega >= 0.0022$ and $\omega >= 0.0093$ for isothermal and directional solidification, respectively. This is necessitated by an observed tendency of the system to select wavelengths smaller than what the system is initialized with (observed only for small values of ω), as we simulate longer in time.

$\Delta x, \Delta y$	4.0
Δt	0.25
σ	0.1
ϵ	16.0

Table 5.4: Table depicting all the material parameters

to the assumptions that are inherent in the analysis. Therefore, we start from the phase-field simulation of a planar growth front in a supersaturated liquid and let the diffusion potential and phase-field profiles develop well into the scaling regime (where $(z_f - z_0)^2$ scales linearly with time, z_f being the interface position and z_0 the initial position, with a defined constant of proportionality η_s).

We then choose a state in this regime (time t) where the rate of change of velocity $= -\frac{\eta_s}{4t^{3/2}}$ (where $V = \frac{\eta_s}{2\sqrt{t}}$) is much smaller compared to V (for our simulations $\left|\frac{1}{V}\frac{dV}{dt}\right|$ is around $1.0\,10^{-8}$). This ensures that the assumption in the analytical calculations of the change of the velocity being very small during the consideration of linear stability analysis is valid for the phase-field simulations.

The equilibria, along with the planar front velocity (V) recorded from the plane front solidification simulation, are utilized to compute the composition gradients of different components at the interface ($G_{c,i}$), all of which appear in the theoretical calculation of the dispersion curve. This ensures a uniformity in the parameters used across phase field simulations and analytical calculations.

Thereafter, the 1D composition and phase-field profiles in the liquid are perturbed with prescribed wavelengths defined by the width of the simulation domain similar to the directional solidification set up.

As a first case, we first compare the phase-field simulations (for parameters mentioned in Table. 5.4), performed for the diagonal diffusivity matrix with equal diffusivities for all the components, $D_{AA} = D_{BB} = D_{CC} = 1.0$ (see Fig. 5.3). Again, we derive an excellent match between the phase-field simulations and analytical calculations.

An additional complexity that is present for the case of isothermal simulations in contrast to directional solidification conditions, is that the compositions of the solid and the liquid at the interface are functions of not only the alloy compositions, but also of the diffusivity matrices as we have briefly described in the analytical section (further details can also be viewed elsewhere [5]). Thereby, the influence of diffusivities is not merely to change the diffusion lengths pertaining to each component as in the case of directional solidification, but also to modify the

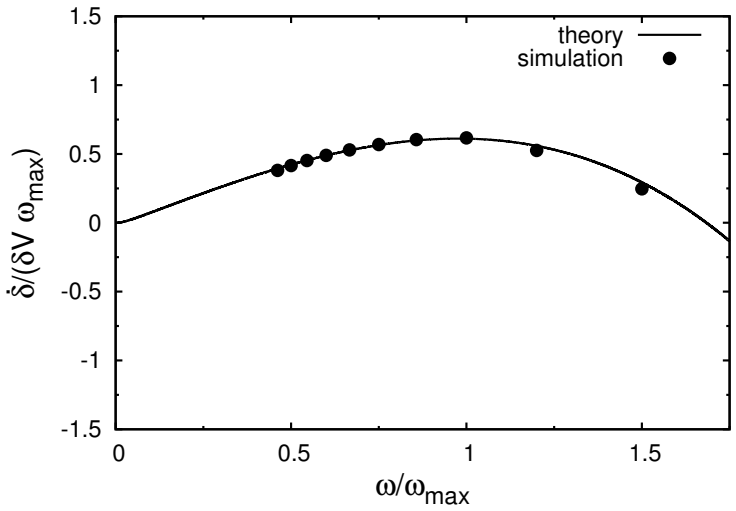

Figure 5.3: $\dot{\delta}/\delta$ versus ω from phase-field and theoretical calculations. The diffusivity matrix is diagonal with $D_{AA} = D_{BB} = D_{CC} = 1.0$. The bulk liquid composition chosen for this study is: $c_A = 0.0018$, $c_B = 0.0165$, $c_C = 0.1872$.

equilibrium compositions themselves. Thus, in the following three figures, we compare our phase-field simulations for different choices of the diffusivity matrix for the same given alloy composition.

In Fig. 5.4, we present three systems with different combinations of D_{BB} and D_{CC} while D_{AA} is held constant. In Fig. 5.5, we study the dispersion relations by maintaining $D_{BB} = 1.0$

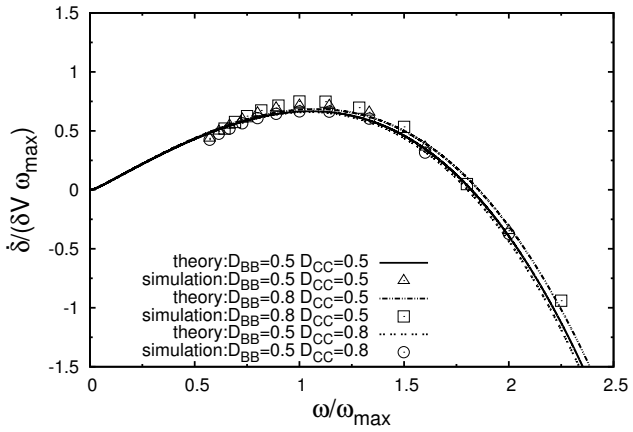

Figure 5.4: $\dot{\delta}/\delta$ versus ω from phase-field and theoretical calculations. The diffusivity matrix is diagonal with $D_{AA} = 1.0$ with the other diagonal components being mentioned in the figure legend. The bulk liquid composition chosen here is the same as in Fig. 5.3.

for three systems with different combinations of D_{AA} and D_{CC} (lower than D_{BB}).

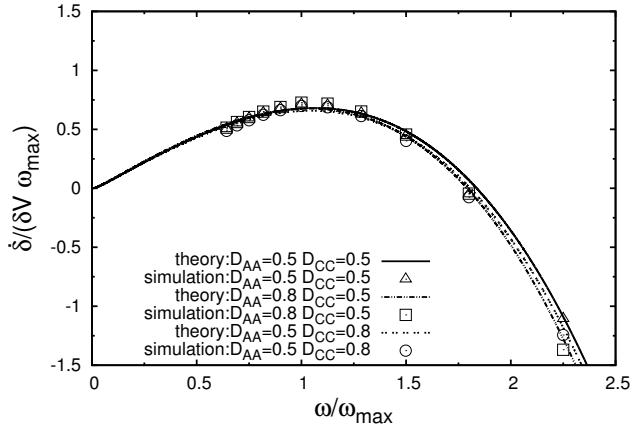

Figure 5.5: $\dot{\delta}/\delta$ versus ω from phase-field and theoretical calculations. The diffusivity matrix is diagonal with $D_{BB} = 1.0$ with the other diagonal components being mentioned in the figure legend. The bulk liquid composition chosen here is the same as in Fig. 5.3.

Subsequently, we investigate the situation where we fix $D_{CC} = 1.0$ and vary D_{AA} and D_{BB} (as shown in Fig. 5.6). While for the variations exhibited in Fig. 5.4 and Fig. 5.5, the differences w.r.t the change in the diffusivities do not bring about a marked difference in the curves, for the case of Fig. 5.6, a higher value of D_{BB} results in a change in the nature of the dispersion curve. This is related to the chosen thermodynamics of this alloy, where several factors such as selection of the tie-lines, amplitudes of the perturbation in the interfacial compositions b_i, as well as the effective Gibbs-Thomson coefficients are non-trivially related to the diffusivity matrix and thereby the properties of the dispersion curve.

5.2.4 Generic diffusivity matrix: off-diagonal terms in the diffusivity matrix

Till now, we have derived excellent comparison between the phase-field simulations and the analytical calculations for different choices of diagonal diffusivity matrices under both isothermal and directional solidification conditions.

As a final subsection on the comparison with our analytical calculations with phase-field simulations, we consider an arbitrary diffusivity matrix with off-diagonal entries. For this, we choose the isothermal setting where Fig.5.7 displays the dispersion curves for different possibilities of the diffusivity matrix. Here again, we achieve a reasonably good match between the simulations and analytical calculations. A slightly higher error is present for the case where the diffusivity matrix entries D_{AC} and D_{CA} differ from 1.0, this is because of the choice of a larger

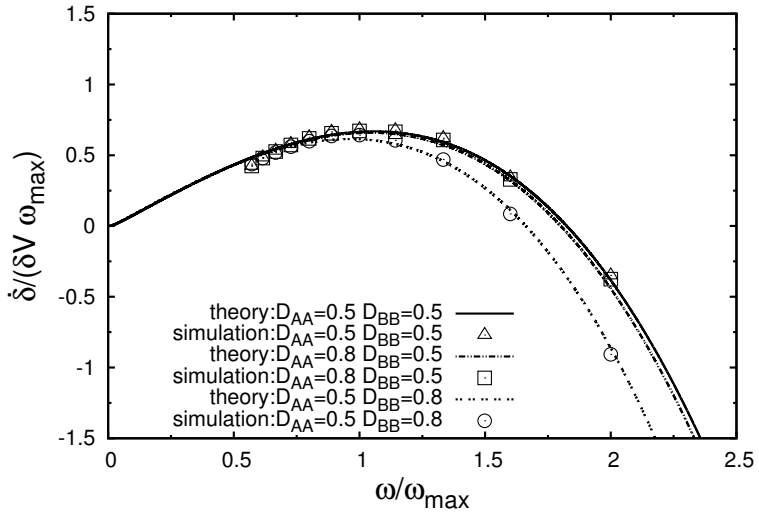

Figure 5.6: $\dot{\delta}/\delta$ versus ω from phase-field and theoretical calculations. The diffusivity matrix is diagonal with $D_{CC} = 1.0$ with the other diagonal components being mentioned in the figure legend. The bulk liquid composition chosen here is the same as in Fig. 5.3.

velocity (and thereby a larger change in velocity during the time for which the perturbations are recorded) used for the perturbation analysis.

In the preceding sections, we have derived an analytical theory to describe the linear perturbation response of a planar interface and compared them with phase-field simulations. In the following, we present a brief discussion on the nature of change of the amplitudes of the perturbations and spatial frequencies (henceforth will be referred to as "frequencies" in short) ω_{max} (frequency at the maximally growing wavelength) and ω_{crit} (frequency at the smallest wavelength beyond which the first instability is seen) upon change in the properties of the diffusivity matrices and velocity.

5.3 Discussion

In this section, we highlight certain properties of the dispersion behavior through the study of the variation of the properties of the instability behavior characterized by the maximum growth rates $\dfrac{\dot{\delta}}{\delta}$, and the critical and maximally growing frequencies ω_{crit} and ω_{max}, using our analytically derived expressions. For this, we will vary properties that bring about changes in the principal length scales in the problem. For the present discussion, we will hence vary the diffusivity matrices (considered to be diagonal), and the velocities of solidification, for either isothermal or directional solidification conditions and the thermal gradients in the case

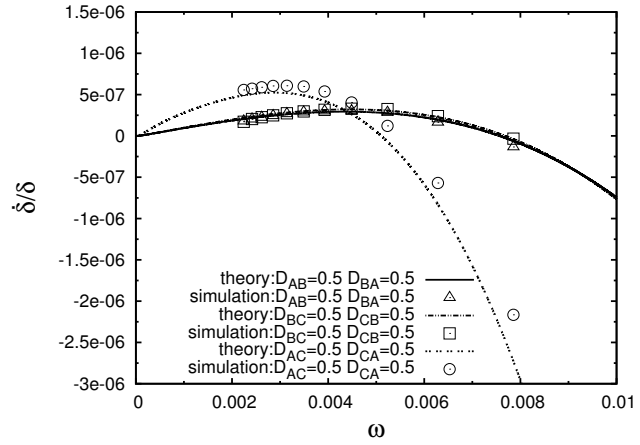

(a)

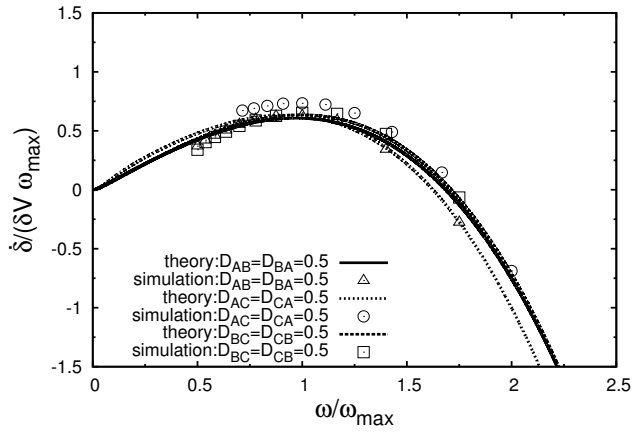

(b)

Figure 5.7: Plots depicting (a) unscaled, and (b) scaled variations of $\dot{\delta}/\delta$ for different choices of the diffusivity matrix. The figure legends report the non-zero off-diagonal components with the diagonal components set to unity.

of directional solidification.

5.3.1 Influence of diffusivity

As a first case, we will vary the diffusivity matrices by changing either of the values D_{AA}, D_{BB}, D_{CC} while the others are left constant. While, it is quite trivial to undertake this investigation for the case of directional solidification, for the case of isothermal solidification, a change in diffusivity must be accompanied with a change in the alloy composition such that the growth coefficient η_s, as well as the equilibrium compositions at the interface remain invariant. These alloy compositions can be worked out using the expressions describing the planar growth problem for isothermal solidification in the analytical section 5.1.2. We have checked our results for both sets of conditions (isothermal and directional) and find that the basic characteristics of the instability in terms of the change in the maximally growing frequencies and growth rates are quite the same for both conditions.

An interesting difference in behavior is observed for the case of low and high velocities. Fig. 5.8 shows the variation of the $\omega_{max}, \omega_{crit}$ as well as $(\dot{\delta}/\delta)_{max}$ for different choices of the diffusivity matrix at higher velocities of $V = 0.02$, while a corresponding variation at lower velocities can be seen in Fig.5.9, where $V = 0.0001$.

At lower velocities, the variation of the $\left(\frac{\dot{\delta}}{\delta}\right)_{max}$, and the variations of the critical frequencies show a gradual decrease with increase in diffusivity (see Figs. 5.9(b) and 5.9(a)). This follows from the increase in the diffusion length causing a decrease in the magnitude of the perturbation in the composition gradients and thereby weakening the instability and shifting the critical wavelengths to higher values. At higher velocities, however, the critical length scales are much smaller, which occurs because of smaller diffusion lengths. Here the influence of capillarity is more pronounced than in the case of lower velocities. For very low values of diffusivity, the critical length scales become comparable to the capillary length. In this regime, the critical length scales therefore become a strong function of the capillarity along with that of the diffusivity matrices which also results in a maximum in the values of ω_{crit} and ω_{max}, with the variation of diffusivities (see Fig.5.8(a)). Physically, capillarity stabilizes the planar interface, and thereby an increase in the value of the diffusivity which has a tendency to increase the critical length scales, in the higher velocity regime, brings about a decrease in the stabilization influence of surface tension. Therefore, we see an increase in the value of the growth rates $\frac{\dot{\delta}}{\delta}$ for a similar variation of the diffusivities at higher velocities (see Fig. 5.8(b) and 5.9(b)). Additionally, to the left of maximum in ω_{crit} and ω_{max} curves (see Fig.5.8(a)) capillarity dominates (in stabi-

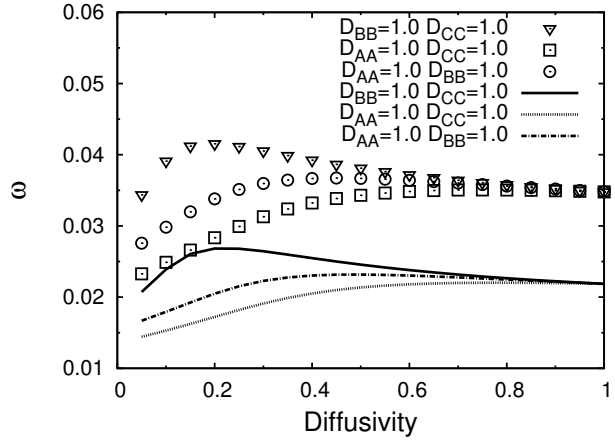

(a)

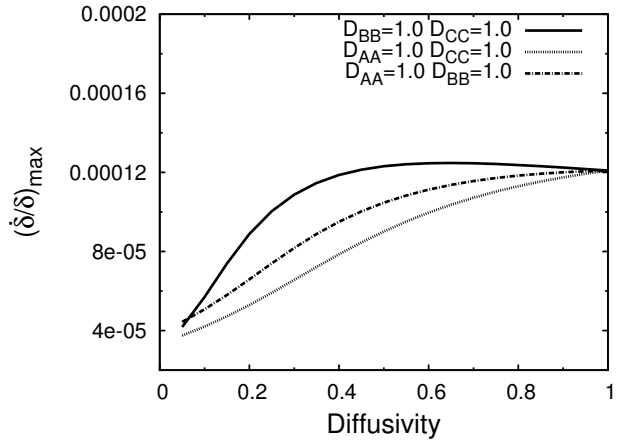

(b)

Figure 5.8: Plots showing variations of, (a)ω_{max} (shown by lines) and ω_{crit} (shown by points), (b) $(\dot{\delta}/\delta)_{max}$, with change in diffusivity of any one of the components A, B and C (the diffusivity matrix is diagonal). The analysis is performed at a planar front velocity of $V = 0.02$. The figure legends reveal the components whose diffusivities are held constant along with the values set for them, while the diffusivity of the component not mentioned in the legend is varied to generate the curve.

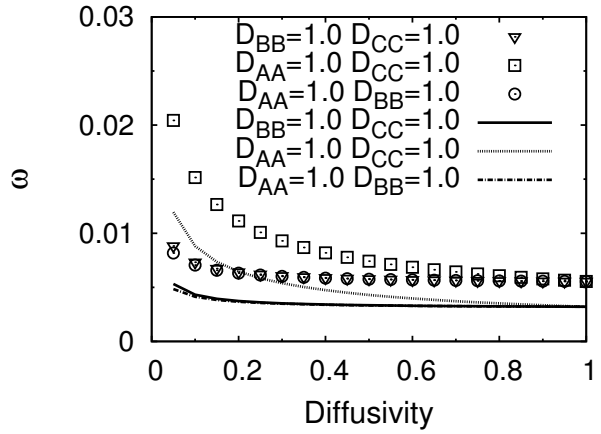

(a)

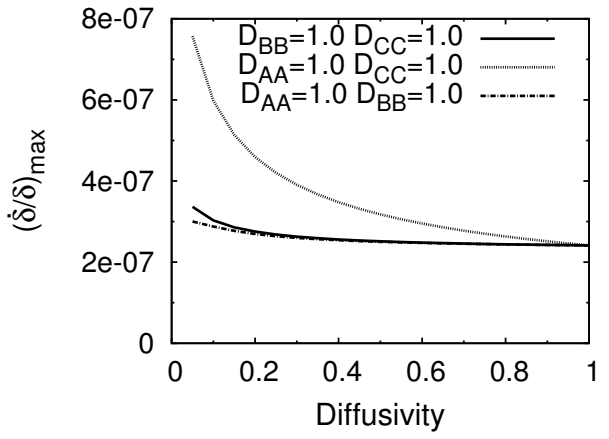

(b)

Figure 5.9: Plots showing variations of, (a)ω_{max} (shown by lines) and ω_{crit} (shown by points), (b) $(\dot{\delta}/\delta)_{max}$, with change in diffusivity of any one of the components A, B and C (the diffusivity matrix is diagonal). The analysis is performed at a planar front velocity of $V = 0.0001$. The figure legends reveal the components whose diffusivities are held constant along with the values set for them, while the diffusivity of the component not mentioned in the legend is varied to generate the curve.

lization of planar interface) and shifts the critical wavelengths to larger values with decreasing diffusivity and a consequent decrease in $\left(\frac{\dot{\delta}}{\delta}\right)_{max}$. Also noteworthy, is the differing response w.r.t the change of the different values of the diffusivities of the different components. This is particular to the alloy under consideration, but it is clear that in general, characterization of the instabilities with respect to the diffusivity matrix may be important in the context of alloy design in multi-component systems.

5.3.2 Influence of velocity

For understanding the instability behavior as a consequence of changes in the velocity, again we can utilize either the isothermal or directional solidification conditions. While the directional solidification case is straightforward, in that only one parameter i.e., the velocity needs to be changed, for the case of isothermal solidification, following our work [5] and the discussion in the analytical section, one can work out a range of alloy compositions, where one can derive the same given equilibrium compositions for different η_s. Although, this consideration does not enter the analytical calculations, it is important to note this difference in the boundary conditions, that will be necessary to conduct a similar study using phase-field simulations.

In Fig. 5.10, we report a behavior at higher velocities, while Fig. 5.11 displays the same at lower velocities. Again, the differences between the two characteristics at lower and higher velocities can be seen as a result of an interplay between capillarity and diffusion. The variation of velocity works in the inverse manner with respect to the change in the diffusivities in the preceding section. Here, for the lower velocity regime, an increase in the velocity, decreases the diffusion length strengthening the instability and thereby the rates $\left(\frac{\dot{\delta}}{\delta}\right)_{max}$ in Fig.5.11(c). Also, as a consequence of decrease in the diffusion length scales, the critical and maximum frequency values shift to higher values (see Fig.5.11(a) and Fig.5.11(b)).

In the higher velocity regime, the length scales become comparable to the capillarity length, and as a consequence, beyond a particular value of velocity the value of the growth rate $\left(\frac{\dot{\delta}}{\delta}\right)_{max}$ begins to drop as in Fig.5.10(c). Given the dominance of capillarity in this regime, the critical and maximally growing wavelengths shift to the right as is described by the decreasing frequencies beyond the maximum in Figs.5.10(a) and 5.10(b).

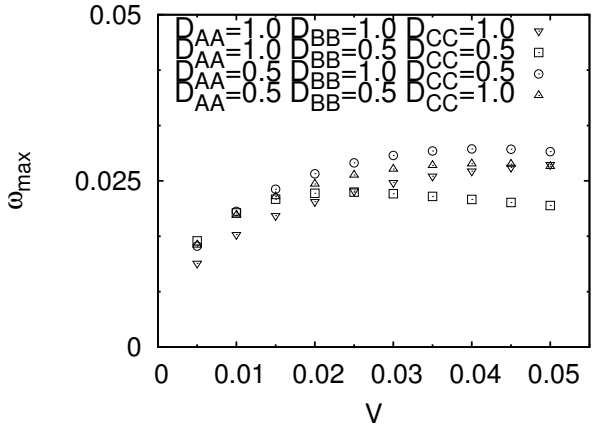

(a)

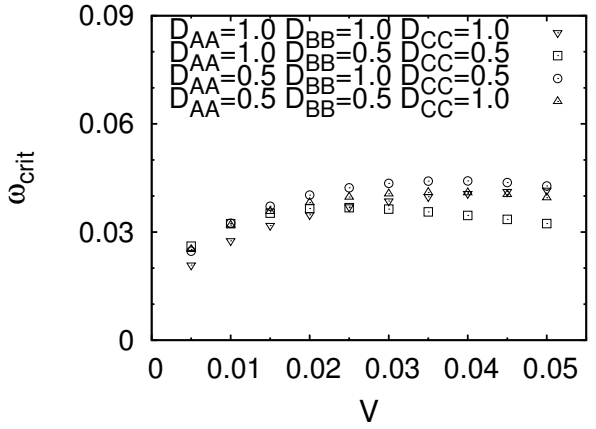

(b)

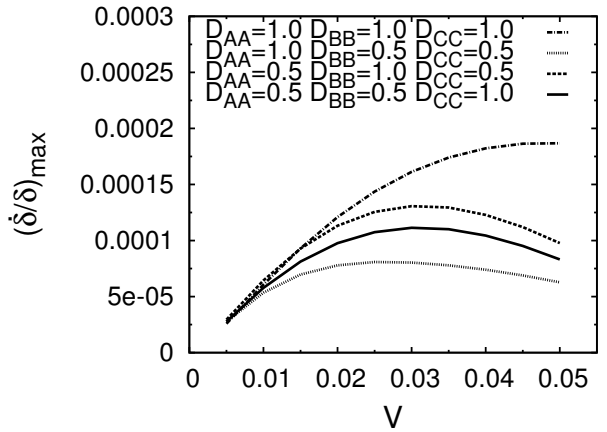

(c)

Figure 5.10: Plots showing variations of (a)ω_{max}, (b) ω_{crit}, (c) $(\dot{\delta}/\delta)_{max}$, with V (from 0.005 to 0.05) for different diagonal diffusivity matrices.

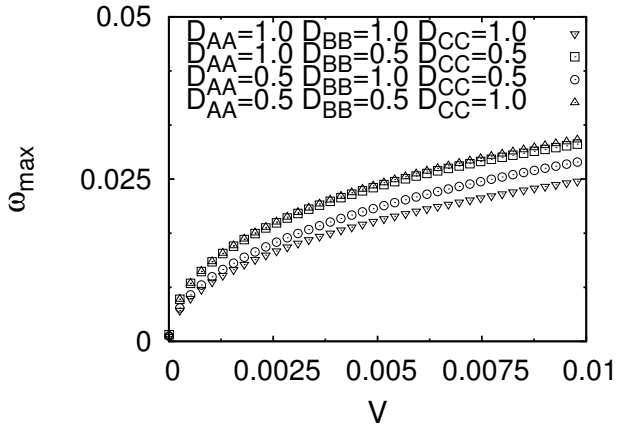

(a)

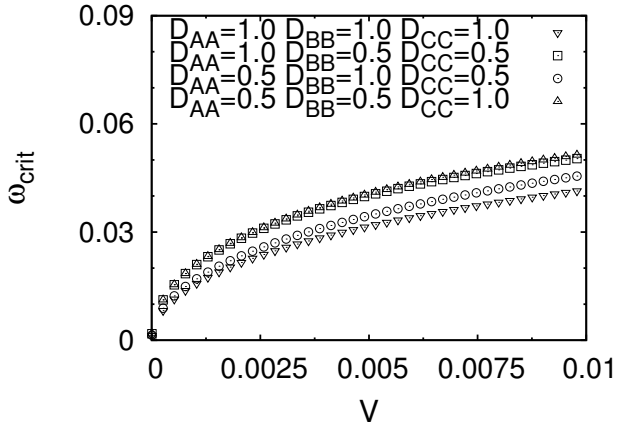

(b)

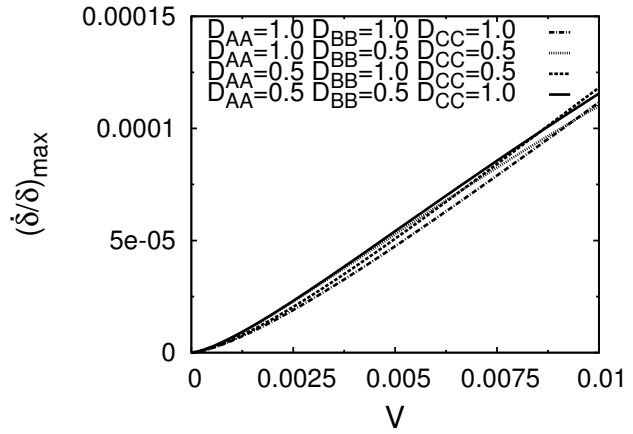

(c)

Figure 5.11: Plots showing variations of (a)ω_{max}, (b) ω_{crit}, (c) $(\dot{\delta}/\delta)_{max}$, with V (from $6\ 10^{-6}$ to 0.01) for different diagonal diffusivity matrices.

5.3.3 Influence of the thermal gradient

In addition to capillarity, a positive thermal gradient brings about a stabilization of the interface. This particular aspect is relevant only for the case of directional solidification, where now an additional length scale described by the variation of the thermal gradient and its relation to the diffusion and capillary length decides the behavior of the instability. For directional solidification, given an alloy system, for a certain velocity, all wavelength perturbations are stable for thermal gradients higher than a critical value, which is different to the case of isothermal solidification. Thereby, we have spanned the range of velocities and recorded the value of the shallowest thermal gradient which results in all wavelength perturbations being stable. This can be seen in Fig.5.12. The lines demarcate the region of absolute stability to perturbations, where above the curve we have absolute stability while below it we have regions of instability depending upon the wavelength of perturbation. Again, for very low velocities, one can see the graph in Fig.5.12 to be linear, which is the classical supercooling limit in the Mullins-Sekerka instability. For higher velocities, the length scales reduce and stabilization due to capillarity brings in the non-linearity in the curve.

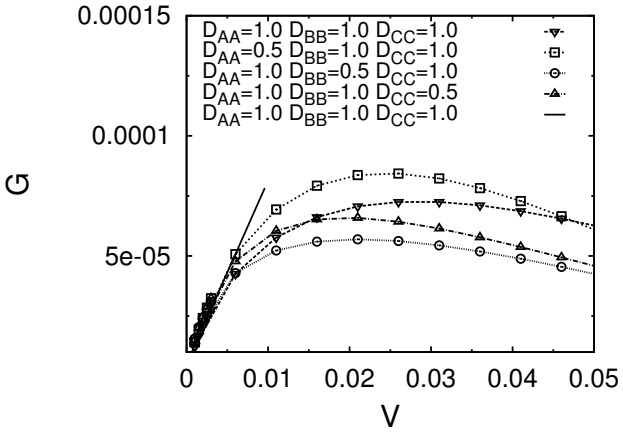

Figure 5.12: Plot showing variations of G, with change in sample pulling velocity (V) at limits of absolute stability. The continuous straight line is obtained by a fit to the data points corresponding to a diagonal diffusivity matrix $D = I$, at low V.

5.4 Summary

In this investigation, we perform a linear stability analysis for solidification in a multi-component alloy under directional and isothermal conditions, for a generic diffusivity matrix. The analytical results are validated against phase-field simulations which show excellent comparison for

varied sets of diffusivity matrices. Thereafter, we have used the analytically derived expressions for deriving the nature of variation of the parameters describing the instability such as ω_{max}, ω_{crit} and $\left(\frac{\dot{\delta}}{\delta}\right)_{max}$ w.r.t the change in the diffusion length (effected through the change in the diffusivity matrices and the velocity). We have also numerically worked out conditions for the absolute stability of a planar interface, for directional solidification conditions.

While, we utilize a uniform set of equations to analyze the linear stability under different solidification conditions, a theoretical difference between the case of directional and isothermal solidification conditions is noteworthy. For the case of directional solidification, considering the steady-state solution to the planar problem, the equilibrium compositions at the interface are invariant w.r.t the choice of the diffusivity matrices, and thereby the variation of the concentration gradients ahead of the interface which influence the behavior of the instability, is readily derived once the velocity of the interface is known. However, for an isothermal solidification setting, the planar problem does not have a steady-state solution, characterized by the system having a constant velocity, but by a growth coefficient, which describes the parabolic growth of the interface. The growth coefficient as well as the equilibrium compositions depend on the choice of the diffusivity matrix as well as the alloy composition. These characteristics of the transformation influence the growth behavior of morphological perturbations and thereby influence the selection of microstructural length scales. Therefore, in order to have equivalent set of solidification conditions (directional and isothermal) for velocity and diffusion lengths, which will behave similarly w.r.t a linear stability analysis, care needs to be taken to initialize the problem with the appropriate alloy compositions. This particular aspect has not been a part of previous investigations regarding a linear instability analysis of multi-component systems.

Chapter 6

Isothermal dendrites in multi-component alloys

The growth of the perturbations at the solid-liquid interface, discussed in the previous chapter, leads to the most commonly observed solidification structures of cells and dendrites. In this chapter, we develop a theoretical understanding of the phenomenon of free dendrite growth from a uniformly undercooled multi-component melt. We extend Ivantsov's [30] solution of solute diffusion to multi-component alloys and invoke the different estimates of the dendrite tip-radius by extending criteria like "Marginal Stability" and "Microsolvability" to multi-component alloys. As we have done in the previous chapters on steady-state growth and diffusive instabilities of the solid-liquid interface, in this chapter too, we perform phase-field simulations to validate our analytical predictions. In addition, our phase-field simulations also provide estimates for the dendrite tip-radius as part of the "Microscopic Solvability" (or "Microsolvability") criterion, integrated with our analytical calculation of the diffusion fields in the melt. We begin with our analytical derivation in the next section, follow it up with a description of our results and discuss the main conclusions of our work.

6.1 Theory

In this section, we present the theory of isothermal dendrite growth in a multi-component alloy with K components, out of which $K-1$ are independent. We restrict ourselves to a 2D system which is representative of solidification of a thin sample. Isothermal growth corresponds to a situation where a super-critical nucleus grows into a uniformly undercooled (ΔT) liquid melt. Here, the solid-liquid interface is always unstable, as any perturbation on the interface would

find undercooled melt ahead, causing it to grow.

Our theory is developed with the objective of determining the velocity (V), the tip-radius (R_{tip}), and phase concentrations at the solid-liquid interface under conditions of local equilibrium. The diffusion in the solid being negligibly small compared to that in the liquid, is neglected in our theoretical analysis. Furthermore, the solute diffusivities are considered to be constant and hence independent of solute concentrations. In our derivation, we also invoke the assumption that the interfacial temperatures stay at the same value as that set in the far-field. This obviates solving for the problem of thermal diffusion which corresponds to situations with very high Lewis number. We begin with the determination of the solute diffusion fields in the liquid, which can be seen as an extension of the work by Ivantsov [30] and Horvay, Cahn [31] to multi-component alloys. Following this, we invoke the condition of local equilibrium across the curved interface of a dendrite, in conjunction with an expression estimating R_{tip}, to determine the unknowns.

We begin with an analysis which corresponds to a situation where the solutes diffuse independently of each other and hence the diffusivity matrix D is diagonal. We will show later that the case of coupled diffusion of solutes can be treated in a similar manner by performing the entire analysis in the composition space determined by the eigen-vectors of the diffusivity matrix. The symbols which are used in our analytical derivation are mentioned in the Table. 6.1.

6.1.1 Diffusion problem

In contrast to the diffusion problem of a planar solidification front, where from the Zener type solution we derive a scaling law which prescribes that the displacement of the interface to vary with the square root of time, in the case of dendrite growth there exists a solution where the displacement is proportional to time. This is because a unique dendrite tip with a defined radius is chosen at a given undercooling. The solutal boundary layer ahead of the interface decays across a length which is proportional to the dendrite tip radius. Thus, in the dendrite problem, both the dendrite tip radius as well as the velocity together describe the kinetics of the dendrite morphology.

During steady-state growth of the dendrite at a constant velocity V, the diffusion fields in the liquid, ahead of the solid-liquid interface, can be described in a scaled (by the dendrite tip-radius R_{tip}) and moving frame, fixed at the interface, as,

$$-V\frac{\partial c_i^l}{\partial z} = D_{ii}\left(\frac{\partial^2 c_i^l}{\partial x^2} + \frac{\partial^2 c_i^l}{\partial z^2}\right), \tag{6.1}$$

K	the no. of components
c_i	concentration of i-th component in liquid
c_i^{∞}	concentration of i-th component in liquid in far-field
c_i^{l*}	concentration of i-th component in liquid at the interface in local equilibrium
$c_i^{\alpha*}$	concentration of i-th component in solid at the interface in local equilibrium
k_i	partition coefficient
$G_{c,i}$	concentration gradient of the i-th component in the liquid at the interface
σ	interfacial energy
κ	curvature of the interface
μ_i	diffusion potential of the i-th component
$\Psi^{l,\alpha}$	the Grand-potential density of the phases
D_{ij}	(i,j)-th component of the diffusivity matrix
ω	wave-number of the perturbation
δ	amplitude of the perturbation
$\dot{\delta}$	rate of change of amplitude of the perturbation
V	velocity of the solidification front
R_{tip}	tip-radius of the dendrite
z	the coordinate along the growth direction of the dendrite
x	the coordinate normal to z
t	the time

Table 6.1: The symbols used in the analytical derivation.

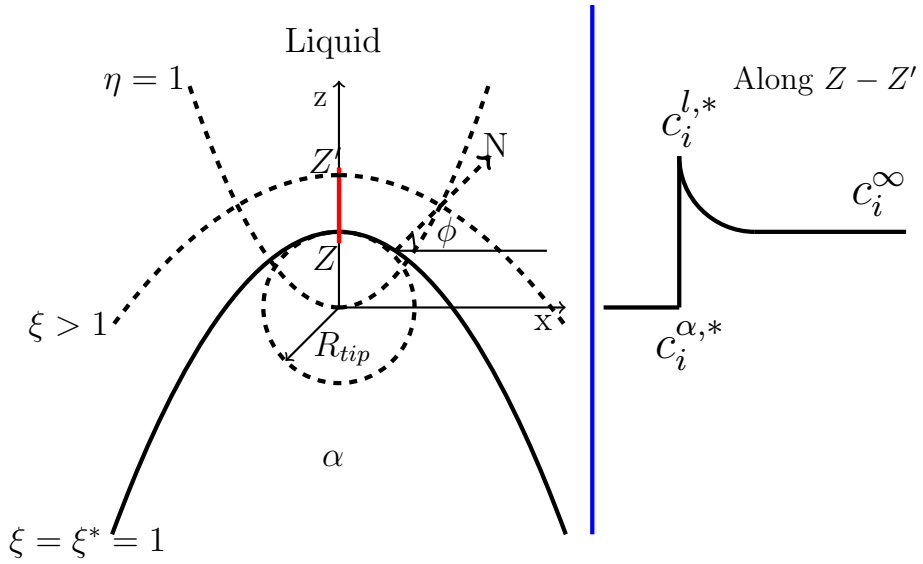

Figure 6.1: Schematic displaying a dendrite growing in liquid on the left. The one on the right shows the composition profile along the line $Z - Z'$.

where, c_i^l, denotes the concentration of the i-th component in the liquid. The dendrite advances in the z direction, x being a direction orthogonal to z as described in the schematic in Fig. 6.1.

The dendrite shape is approximated by a parabola, given by Fig. 6.1,

$$x^2 = 4f(f - z), \tag{6.2}$$

where, f is the scaled (by R_{tip}) focal distance of the parabola which evaluates to $f = 1/2$. The Stefan boundary condition at this parabolic interface writes as,

$$V \sin\phi \Delta c_i^* = -D_{ii} \frac{\partial c_i^l}{\partial N}\bigg|_{interface}, \tag{6.3}$$

where, $\Delta c_i^* = c_i^{l*} - c_i^{\alpha*}$, and, c_i^{l*} and $c_i^{\alpha*}$, denoting the solute concentrations in the liquid and the solid respectively, which are in local equilibrium across the interface. N denotes the local normal, pointing towards the liquid, varying in sense across the parabolic interface. ϕ is the angle between N and x (see Fig. 6.1).

The far-field alloy composition at $z \to \infty$, serves as a second boundary condition, and is

given by,

$$c_i = c_i^{\infty}. \tag{6.4}$$

The composition variable, c_i^l, is scaled to introduce a parameter representing normalized supersaturation in the corresponding component, given by,

$$\Omega_i = \frac{c_i^l - c_i^{\infty}}{c_i^{l*} - c_i^{\alpha *}}. \tag{6.5}$$

Replacing c_i^l, by the corresponding scaled supersaturation, Ω_i, in Eq. 6.1, we obtain,

$$-2Pe_i \frac{\partial \Omega_i}{\partial z} = \frac{\partial^2 \Omega_i}{\partial x^2} + \frac{\partial^2 \Omega_i}{\partial z^2}, \tag{6.6}$$

where, $Pe_i = VR/2D_{ii}$, is the solutal Peclet number corresponding to the i-th solute. Similarly, the Stefan condition in Eq. 6.3 can also be re-written as,

$$-2Pe_i \sin\phi = \left.\frac{\partial \Omega_i}{\partial n}\right|_{interface}, \tag{6.7}$$

where n denotes the scaled normal to the solid-liquid interface given by $n = N/R_{tip}$. The corresponding far-field condition is now written as,

$$\Omega_i = 0. \tag{6.8}$$

Thus, at this point, the diffusion problem comprises of the governing equation given by Eq. 6.6, alongside the boundary conditions given by Eq. 6.7 and 6.8.

By a separation of variables of Eq. 6.6, we can see that the solution to Eq. 6.6 is of the form,

$$\Omega_i = \Theta_i(x, z) \exp\left(-Pe_i z\right). \tag{6.9}$$

By substituting Eq. 6.9 into Eq. 6.6 the governing equation can be re-expressed as,

$$\frac{\partial^2 \Theta_i}{\partial x^2} + \frac{\partial^2 \Theta_i}{\partial z^2} - Pe_i^2 \Theta_i = 0, \tag{6.10}$$

with the corresponding boundary conditions being,

$$-2Pe_i \sin\phi = \left.\frac{\partial\left(\Theta_i \exp(-Pe_i z)\right)}{\partial n}\right|_{interface}, \tag{6.11}$$

and,

$$\Theta_i = 0, \tag{6.12}$$

as $\exp(-Pe_i z) \to 0$ when $z \to \infty$.

The variability of the orientation of the surface normal n across the solid-liquid interface, motivates the re-expression of Eqs. 6.10, 6.11 and 6.12 in a parabolic$(\xi - \eta)$ coordinate system given by,

$$\begin{aligned} \xi^2 &= \sqrt{x^2 + z^2} + z, \\ \eta^2 &= \sqrt{x^2 + z^2} - z, \end{aligned} \tag{6.13}$$

with the inverse relationship being,

$$\begin{aligned} x &= \xi\eta, \\ z &= \frac{1}{2}\left(\xi^2 - \eta^2\right). \end{aligned} \tag{6.14}$$

In this coordinate system a parabola is represented by a constant value of ξ with the η coordinate running orthogonal to it as described in the schematic in Fig. 6.1. Expressing, Eq. 6.2 in this new coordinate system, we obtain,

$$\xi^* = \sqrt{2f} = 1. \tag{6.15}$$

Thus, now the solidification front can be identified with a constant value in the coordinate axis, ξ, which in an orthogonal coordinate system results in the interface normal at every point of the interface being collinear with the local orientation of the other coordinate axis (η). This drastically simplifies the consideration of the Stefan boundary condition, which now becomes,

$$2Pe_i \frac{\xi^*}{\sqrt{\xi^{*2} + \eta^2}} = -\frac{1}{\sqrt{\xi^{*2} + \eta^2}} \frac{\partial}{\partial\xi}\left[\Theta_i \exp\left[-Pe_i\left(\xi^2 - \eta^2\right)/2\right]\right]\Bigg|_{\xi^*=1}. \tag{6.16}$$

In the parabolic coordinate system, Eq. 6.10, becomes,

$$\frac{\partial^2\Theta_i}{\partial\xi^2} + \frac{\partial^2\Theta_i}{\partial\eta^2} - \left(\xi^2+\eta^2\right) Pe^2\Theta_i = 0. \tag{6.17}$$

The far-field remains the same as in Eq. 6.8 at $\xi = \infty$.

Solution to the Eq. 6.17, with the boundary conditions given by Eq. 6.16, and Eq. 6.8 can be expressed as,

$$\Theta_i = \sqrt{\pi Pe_i}\exp(Pe_i)\exp\left(Pe_i(\xi^2-\eta^2)/2\right)\operatorname{erfc}\left(\sqrt{Pe_i}\xi\right). \tag{6.18}$$

with, the final solution written as,

$$\begin{aligned}\Omega_i &= \Theta_i\exp(-Pe_i\left(\xi^2-\eta^2\right)/2) \\ &= \sqrt{\pi Pe_i}\exp(Pe_i)\operatorname{erfc}\left(\sqrt{Pe_i}\xi\right).\end{aligned} \tag{6.19}$$

Eq. 6.19 can be evaluated at the interface given by $\xi = \xi^* = 1$, to write,

$$\Omega_i^* = \frac{c_i^{l*} - c_i^{\infty}}{c_i^{l*} - c_i^{\alpha*}} = \sqrt{\pi Pe_i}\exp(Pe_i)\operatorname{erfc}\left(\sqrt{Pe_i}\right). \tag{6.20}$$

Eq. 6.20 represents a set of $(K-1)$ equations containing $2(K-1)+2$ unknowns in $c_i^{l*,\alpha*}$, V and R_{tip}. Each of the $2(K-1)$ phase concentrations $c_i^{l*,\alpha*}$, which have to be determined, can be expressed as functions of the $K-1$ diffusion potentials μ_i, and the imposed undercooling, ΔT. This functional dependence of compositions on diffusion potentials (μ_i) and undercoolings (ΔT) is described in detail in Chapter 3 in the section "Thermodynamics" under the subsection "Parabolic driving forces". This re-formulation of the problem in terms of the intensive variables of μ_i and ΔT, leaves $K+1$ unknowns ($K-1$ μ_i's, V and R_{tip}) which have to be determined in order to completely solve the diffusion problem.

6.1.2 Local equilibrium

The condition of local equilibrium at the interface is given by,

$$\Delta\Psi = \Psi^l - \Psi^\alpha = \sigma\kappa, \tag{6.21}$$

where, Ψ^l and Ψ^α denotes the grand-potential of the liquid and the solid phases, respectively. σ is the interfacial energy, and κ denotes the curvature of the interface, which is approximated as

$\kappa \approx 1/R_{tip}$ in 2D. As, $\Psi^{l,\alpha} = f^{l,\alpha} - \sum_i \frac{1}{V_m}\mu_i c_i^{l,\alpha}$, and $c_i^{l,\alpha} = c_i^{l,\alpha}(\mu_1, \mu_2, \cdots, \mu_{K-1}, \Delta T)$, Eq. 6.21 is an equation connecting the $K-1$ diffusion potentials, μ_i, ΔT and R_{tip}.

6.1.3 Estimates for R_{tip}

To completely solve for the $K+1$ unknowns in μ_i's, V and R_{tip}, requires the specification of one more equation. An estimate of the characteristic length scale in the problem, R_{tip}, has been historically chosen to provide this required specification. There are several possibilities to estimate R_{tip}. We will present each of these possibilities in a form which is generic to any multi-component alloy, in the following subsections.

Marginal stability criterion

According to Langer-Müller-Krumbhaar [32], an estimate for the dendrite tip-radius R_{tip} can be the smallest critical wavelength of perturbation during growth by a planar front, which neither grows nor shrinks. This is the classical Marginal Stability criterion and has been found to be in reasonable agreement with experiments. In order to extend this to any generic multi-component alloys, we refer to the previous Chapter 5, where we perform a linear stability analysis of a perturbed planar front in a multi-component alloy, to derive an expression of the rate of amplification of each of the wavelengths constituting the perturbation of the interface. This expression can be stated as,

$$\frac{\dot{\delta}}{\delta} = \left[\left(-\frac{b_i}{G_{c,i}}\right) + \frac{1}{\widetilde{\omega}_i}\left(k_\omega^{(i)} - \frac{V}{D_{ii}}\right)\right]. \tag{6.22}$$

The unknown constants b_i's, are determined by invoking the Gibbs-Thomson condition across the perturbed interface, which writes as,

$$\sum_i m_i b_i = \Gamma\omega^2. \tag{6.23}$$

In Eqs. 6.22 and 6.23, $\omega = 2\pi/\lambda$ is the wavenumber corresponding to the wavelength (λ); $G_{c,i} = -V\Delta c_i^*/D_{ii}$ denotes the gradient in concentration of the i-th component in the liquid, ahead of the planar interface; Γ denotes the Gibbs-Thomson coefficient; m_i represents the liquidus slopes corresponding to the i-th component. $k_\omega^{(i)} = (V/2D_{ii}) + \sqrt{(V/2D_{ii})^2 + \omega^2}$ and $\widetilde{\omega}_i = k_\omega^{(i)} - (V(1-k_i)/D_{ii})$, with $k_i = c_i^{\alpha *}/c_i^{l*}$. The growth behavior of an interfacial perturbation of any wavelength being the same regardless of the choice of the component i, whose diffusion field is utilized in Eq. 6.22, leads to $K-2$ equations relating the b_i's. These relations in

conjunction with Eq. 6.23, provides a set of $K-1$ equations to determine b_i's ($K-1$ in number), which leads to a knowledge of the amplification rates of each of the wavelengths and hence the stability of the interface to random perturbations.

A measure of the critical wavelength ($\lambda_{crit} = 2\pi/\omega_{crit}$, can be obtained by setting $\dot{\delta}/\delta = 0$ in Eq. 6.22. This leads to an expression of b_i, given by,

$$b_i = G_{c,i}\frac{k_\omega^{(i)} - \dfrac{V}{D_{ii}}}{\widetilde{\omega}_i}, \tag{6.24}$$

which can be substituted into Eq. 6.23, to obtain an equation which can be for solved for ω to obtain the critical wavenumber ω_{crit}. Now, invoking the "Marginal Stability" criterion, which approximates $R_{tip} \approx \lambda_{crit} = 2\pi/\omega_{crit}$, Eq. 6.23, completes the set of equations needed to consistently solve for all the unknowns.

The process of formally coupling Eq. 6.23 with Eq. 6.20 and Eq. 6.21, in Eq. 6.23 can be expressed as follows. We express $c_i^{l*,\alpha*}$ as functions of μ_i and ΔT and use the same V as in the diffusion problem ahead of a dendrite, in Eqs. 6.23 and 6.24. Furthermore, we substitute ω_{crit} by $2\pi/R_{tip}$ in Eq. 6.24 and 6.23, with the R_{tip} being the one which satisfies the condition of local equilibrium given by Eq. 6.21, and appears in the diffusion problem as well through the solutal Peclet numbers Pe_i in Eq. 6.20. Hence, Eqs. 6.20, 6.21 and 6.23 form a set of $K+1$ equations which allows a determination of $K+1$ unknowns in μ_i's, V and R_{tip}.

A point to note here is that the original Marginal Stability criterion is stated under the approximation of λ_{crit} being very small compared to the solutal diffusion lengths of $2D_{ii}/V$. Under this approximation, Eq. 6.24 becomes,

$$b_i = G_{c,i}, \tag{6.25}$$

which when substituted into Eq. 6.23, leads to an explicit expression for R_{tip} of the form,

$$R_{tip} = 2\pi\sqrt{\frac{\Gamma}{\sum_i m_i\left(\dfrac{-V\Delta c_i^*}{D_{ii}}\right)}}. \tag{6.26}$$

This approximation is valid at low ΔT, where the predictions obtained incorporating Eq. 6.26 are indistinguishable from those obtained using the complete expressions of Eq. 6.24 and Eq. 6.23. In the discussion accompanying our key results, we continue to refer to the usage of Eq. 6.26 as the "Marginal stability criterion", while the incorporation of Eqs. 6.24 and 6.23 is

referred to as the "Complete Marginal stability criterion".

As the "Marginal Stability" criterion is only a conjecture motivated by experimental observations, there has been attempts to tailor this criterion for particular systems in question. Motivated by experiments in succinonitrile-acetone systems, Lipton et al. [4] introduced an additional factor of $\sqrt{2}$ in Eq. 6.26, to accurately predict the dynamics analytically. In this chapter, we perform phase-field simulations of isothermal dendrite growth which can substitute for experiments in deciding the appropriate pre-factor. In order to do so, we re-express Eq. 6.26 as,

$$R_{tip} = \beta^* \sqrt{\frac{\Gamma}{\sum_i m_i \left(\frac{-V\Delta c_i^*}{D_{ii}}\right)}}, \tag{6.27}$$

where, β^* is a constant which can be determined by measuring the slope of the straight line fitted to the simulation data of R_{tip} versus $\sqrt{\Gamma \Big/ \sum_i m_i \left(\frac{-V\Delta c_i^*}{D_{ii}}\right)}$, for the same set of parameters, but for different undercoolings. We will refer to this method as the "Fitted Marginal Stability criterion".

Microsolvability criterion

Langer and Müller-Krumbhaar show in [34] that the side-branching instabilities of a dendrite persist despite the consideration of surface tension. This coupled with the inability of the "Marginal Stability" criterion to predict the growth of dendrites along well-defined crystallographic directions, leaves the possibility of the existence of other criteria which can address these issues.

An analytical solution to the problem of dendrite growth in the presence anisotropic interfacial energies being extremely difficult, Kessler and Levine [35], solve this problem numerically. By conducting numerical experiments they show that stable dendrites shapes are obtained for unique combinations of V and R_{tip}, which follow an empirical rule given by,

$$VR_{tip}^2 = Q, \tag{6.28}$$

where, Q is a constant dependent on the magnitude of the anisotropy ζ. It is subsequently shown to be in great agreement with predictions from phase-field in [118, 119, 120, 121].

We assume the agreement between boundary integral and phase-field calculations observed

for binary alloys, to hold for multi-component alloys as well, and determine the coefficient Q from phase-field simulations. We use the value of this constant in our analytical calculations to close the system of equations as explained during discussion of the "Marginal Stability" criterion.

Having discussed the solution to the dendrite growth problem in multi-component alloys for independent diffusion of solutes, we move on to a discussion of the same for a situation displaying coupled diffusion of solutes.

6.1.4 Coupled diffusion of solutes

In the presence of the coupled diffusion of solutes, Eq. 6.1 can be re-written in the matrix-vector notation as,

$$-V\left\{\frac{\partial c_i^l}{\partial z}\right\} = [D_{ij}]\left\{\left(\frac{\partial^2 c_j^l}{\partial x^2} + \frac{\partial^2 c_j^l}{\partial z^2}\right)\right\}, \tag{6.29}$$

while the corresponding Stefan condition at the interface is written as,

$$V\sin\phi\left\{\Delta c_i^*\right\} = -\left[D_{ij}\right]\left\{\frac{\partial c_j^l}{\partial N}\right\}_{interface}, \tag{6.30}$$

In the above expressions, $[\cdot]$ represents a matrix of dimensions $(K-1)\times(K-1)$, while $\{\cdot\}$ represents a column vector of dimension $(K-1)\times 1$. The diffusivity matrix $[D]$ being constant, independent of solute concentrations, we assume the existence of a constant, invertible matrix $[P]$, such that $[D]$ can be diagonalized as,

$$[\tilde{D}] = [P]^{-1}[D][P], \tag{6.31}$$

where, $[\tilde{D}]$ is a diagonal matrix. Substituting for $[D]$ in Eq. 6.29 in terms of $[\tilde{D}]$, we obtain,

$$-V\frac{\partial \widetilde{c_i^l}}{\partial z} = \widetilde{D_{ii}}\left(\frac{\partial^2 \widetilde{c_j^l}}{\partial x^2} + \frac{\partial^2 \widetilde{c_j^l}}{\partial z^2}\right). \tag{6.32}$$

where, $\{\widetilde{c_i^l}\} = [P^{-1}]\{c_i^l\}$. Performing the same substitution in Eq. 6.30, we obtain,

$$V\sin\phi\widetilde{\Delta c_i^*} = -\widetilde{D_{ii}}\left.\frac{\partial c_i^l}{\partial N}\right|_{interface}. \tag{6.33}$$

With the far-field boundary condition also restated by multiplying both sides by P^{-1}, we can see that the system of equations to be solved for remains exactly the same as in Eq. 6.1, 6.3 and 6.4, but with $\widetilde{c_i^l}$ in place of c_i^l, and $[\widetilde{D}]$ in place of $[D]$. Following the same procedure, hereafter, as done for the case of independent diffusion of solutes, we obtain, an equivalent of Eq. 6.20, for coupled diffusion of solutes, as given by,

$$\widetilde{\Omega_i^*} = \frac{\widetilde{c_i^{l*}} - \widetilde{c_i^{\infty}}}{\widetilde{c_i^{l*}} - \widetilde{c_i^{\alpha*}}} = \sqrt{\pi \widetilde{Pe_i}} \exp(\widetilde{Pe_i}) \operatorname{erfc}\left(\sqrt{\widetilde{Pe_i}}\right), \tag{6.34}$$

where, $\widetilde{Pe_i} = V R_{tip}/2\widetilde{D_{ii}}$. Using the dependence of $c_i^{l*,\alpha*}$ on μ_i and ΔT, we can obtain a similar functional dependence for $\widetilde{c_i^{l*,\alpha*}}$ as well. Thus, Eq. 6.34 can be completely expressed in terms of the $K+1$ unknowns in μ_i, V and R_{tip}. The local equilibrium condition expressed in Eq. 6.21 is stated completely in terms of μ_i and ΔT and so can be invoked as it is, in the solution procedure for the coupled diffusion of solutes.

The consideration of coupled solute diffusivity modifies the "Marginal Stability" criterion as well. The corresponding version of Eq. 6.24 can be obtained by replacing $[D]$ by $[\widetilde{D}]$ and by replacing c_i^l by $\widetilde{c_i^l}$. By relating b_i's to the perturbed composition fields $\widetilde{c_i^l}$, directly, instead of the original composition fields of c_i^l, Eq. 6.23 re-writes as,

$$\{m\}^T [P] \{b\} = \Gamma \omega^2. \tag{6.35}$$

The linear stability analysis of a planar growth front in multi-component alloys which forms the basis of the "Marginal Stability" criterion, is described in considerable detail in [6], which includes the complete analysis for the coupled diffusion of solutes as well. The "Microsolvability" criterion on the other hand, has a form which requires no modification and can be invoked as described in Eq. 6.28 for the situation corresponding to coupled diffusion of solutes.

This concludes our analytical theory to determine the tip growth velocity V, the tip radius R_{tip}, and the phase concentrations at the interface, during isothermal dendrite growth in multi-component alloys. In the next section, we present the key predictions from our theory and benchmark them against observations from phase-field simulations. We employ a quantitative phase-field model based on the grand-potential [198, 199] formulation, the details of which are described in Chapter 3.

6.2 Results

In this section, we first present a comparative study of the predictions from our analytical theory using several different estimates of R_{tip} including that obtained from phase-field simulations as well. Comparison against experimental results are possible in a limited scope, as almost all the the experiments on dendritic solidification in multi-component alloys only report the variation of tip velocity (V) against undercooling (ΔT). In this study, we are going to compare our analytical predictions against phase-field simulations only, with the understanding that both phase-field models and analytical theories embody the same physics and a non-conformity to experimental results if found in future, will be due to physics that is yet to be understood.

In Fig. 6.2 we present the solute fields observed during phase-field simulations of free dendrite growth. We extract the dendrite tip velocities (V), tip-radius (R_{tip}) and the phase concentrations ($c_i^{\alpha,l}$) from these simulations to be compared against our theoretical predictions. Furthermore, the relationships between the dendrite tip velocity and the tip radius as given by the "Microsolvability" criterion, and the "Fitted Marginal Stability criterion" are determined from the phase-field simulations.

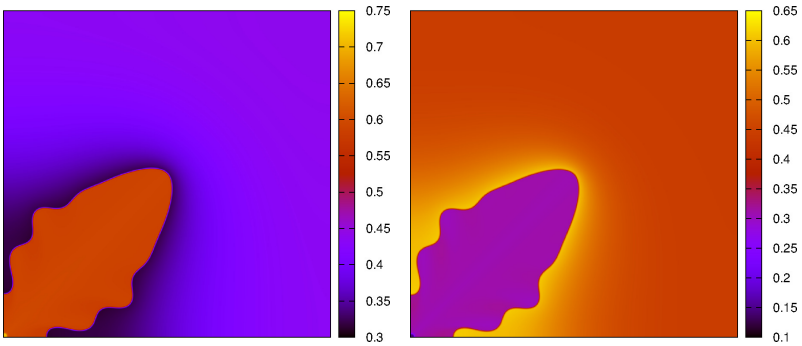

(a) (b)

Figure 6.2: Typical solute fields of (a) c_A, and (b) c_B during isothermal dendritic solidification observed during phase-field simulations. The dendrites are made to grow along the diagonal of the simulation domain (by a suitable rotation of the frame of the crystalline anisotropy) to access larger domain sizes along the growth direction.

In order to determine the tip-radius (R_{tip}) from phase-field simulations we extract the dendritic profile near the tip and fit a parabola to the set of points (see Fig. 6.3). Once the equation describing the profile has been determined we can easily compute the curvature at the tip, whose inverse gives us R_{tip}. The tip-velocity of the dendrite is computed by dividing the distance moved by the tip by the time elapsed between two successive readings and they are reported once they become invariant with time, corresponding to a steady-state.

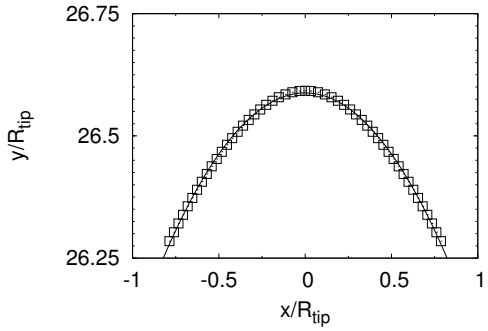

Figure 6.3: The fitting of a parabola to the tip of the dendrite obtained from phase-field simulations. The line represents the fitted function and the points are from a phase-field simulation. The dendritic profiles from phase-field simulations as represented in Fig. 6.2 are rotated such that the axis of the dendrite is vertical which allows a fit by a parabolic function.

c_A^{α}	0.70691
c_B^{α}	0.14645
c_A^{liquid}	0.44
c_B^{liquid}	0.44
m_A	0.45
m_B	-0.25
σ	1.0

Table 6.2: Table depicting all the material parameters

The thermodynamic parameters employed in our model are described in the Table. 6.2, where $c_{A,B}^{\alpha}$ and $c_{A,B}^{liquid}$ are the solid and liquid compositions respectively. The solidus and liquidus are taken to be parallel to each other and are denoted by $m_{A,B}^{s}$ and $m_{A,B}^{l}$ respectively. σ denotes interfacial energy.

A short note on the phase-field simulation parameters is relevant here. The discretization spacing $(\Delta x, \Delta y)$ is determined by ensuring adequate resolution of the of the R_{tip} predicted by the analytical calculations for a particular undercooling (ΔT). The size of the time-step (Δt) is chosen to be the largest value which leads to accurate results. The width of the diffuse interface is determined by ϵ, which is chosen to be 4 times Δx. A simulation box size of 1000×1000 is enough to capture a considerable portion of the steady-state growth regime before the diffusion fields begin to get truncated by the boundaries.

In all of the figures which follow, we have scaled the quantities of interest by employing the following physical scales:

1. Temperature (T^*): Freezing range $\Delta T_0 = \sum_i m_i(c_i^s - c_i^l)$, $T^* = \Delta T_0$,
2. Length (l^*): Capillary length scale $\left(d_0 = \dfrac{\Gamma}{\Delta T_0}\right)$, $l^* = d_0$,
3. Time (t^*): $t^* = \dfrac{d_0^2}{D}$.

Using these definitions the scaling constant for velocity is given by, $V^* = D/d_0$. With the parameters that we have employed these scaling factors come out to be as: $T^* = \Delta T_0 = 0.1935$, $l^* = d_0 = 6.3267$, $t^* = 20.0135$ and $V^* = 0.3161$, where $\Gamma = 1.2240$.

We begin by presenting the variation of V, and R_{tip} against undercooling (ΔT) in an alloy with equal solute diffusivities of $D_{AA} = D_{BB} = 2.0$ and where the magnitude of the anisotropy is $\zeta = 0.01$ in Fig. 6.4. The variation of tip velocity (V) with ΔT is reported in Fig. 6.4(a), while the variation of R_{tip} with ΔT is presented in Fig. 6.4(b).

The variation of phase concentrations is reported in Fig. 6.5 with those belonging to the solid phase are presented in Figs. 6.5(a) and 6.5(c), while the corresponding variations for the liquid phase are reported in Figs. 6.5(e) and 6.5(g).

In Fig. 6.4(a), we find an excellent match between the velocities V predicted by the "Microsolvability" criterion and that predicted by the phase field simulations. It can be seen here that the higher driving forces associated with an increase in ΔT leads to higher tip-velocities (V) of the dendrite. Amongst the predictions from the stability criteria presented in Fig. 6.4(a) the line corresponding to the "Fitted Marginal Stability" is the closest to the simulation predictions. The line corresponding to "Complete Marginal Stability" criterion is almost parallel to the "Fitted Marginal Stability criterion" line with the former predicting smaller tip velocities than the latter, for all ΔT. The "Marginal Stability" line deviates slightly from the "Complete Marginal Stability" line only at higher ΔT. The points obtained from simulations and the "Microsolvability" theory follow a trend which can be seen to have a slightly larger negative curvature than the "Marginal Stability" lines.

Moving on to Fig. 6.4(b), which presents a variation of the dendrite tip-radius R_{tip} with undercooling ΔT, we can confirm again that the simulation results are the closest to the predictions from the "Microsolvability" criterion and the "Fitted Marginal Stability" line, which is again parallel to the "Complete Marginal Stability" line. Here, R_{tip} can be seen to become smaller with an increase in ΔT. The relative positions of the three Marginal Stability lines are reversed compared to what is observed in Fig. 6.4(a). The values of R_{tip} predicted by the "Complete Marginal Stability" and the "Marginal Stability" are slightly higher than the predictions from "Fitted Marginal Stability". The line from the "Marginal Stability" again

deviates from the line of "Complete Marginal Stability" at higher ΔT, similar to what observed for Fig. 6.4(a). The curvature of the series of points obtained from simulations and the Microsolvability theory is now positive and larger than the corresponding lines obtained from the Marginal Stability criteria. Considering Figs. 6.4(a) and 6.4(b) in unison, we can say that the criteria of "Complete Marginal Stability" and "Marginal Stability", underestimate R_{tip} and overestimate V, compared to criteria of "Fitted Marginal Stability" and "Microsolvability".

The variation of the interfacial phase concentrations with undercooling (ΔT) represented in Figs. 6.5(a), 6.5(c), 6.5(e) and 6.5(g) show a very good match with all the analytical predictions, with the line from the "Fitted Marginal Stability" deviating from the others at higher undercoolings. The trends observed in the variation of phase concentrations with ΔT are largely a function of the phase-diagram properties, especially so, in the case of equal solute diffusivities. Each of the Figs. 6.5(a), 6.5(c), 6.5(e) and 6.5(g) are paired with a second plot right next to them. These plots depict variations of the phase concentrations during steady-state growth by a planar front for growth conditions which are identical to conditions employed for dendritic growth. In the context of selection of phase compositions a comparison between similar studies performed for the case of planar growth which is presented in Chapter 4, is useful. For this, instead of plotting the phase compositions as has been performed in Chapter 4 we convert the chosen supersaturations along the tie-line represented by (i.e., $c_A^{\alpha} = 0.70691, c_B^{\alpha} = 0.14645, c_A^{liquid} = c_B^{liquid} = 0.44$), into equivalent undercoolings using the information of the liquidus slopes that is mentioned in this chapter. The tie-line compositions during growth by a planar interface, for alloys with equal solute diffusivities, stay on the original tie-line which can be confirmed from the constancy of values with ΔT. A close examination of these plots reveal that the phase concentrations during dendritic growth approach those observed for planar growth as the undercooling become smaller. This can be understood from the observation that the R_{tip} becomes larger with the lowering of ΔT, which translates to diminished correction of interfacial compositions due to curvature ($\kappa = 1/R_{tip}$), resulting in an approach to phase concentrations observed in planar growth. The procedure for analytically determining the phase concentrations has been described in detail in [5].

We perform a similar study on a system with equal solute diffusivities but with a higher magnitude of the anisotropy parameter $\zeta = 0.02$, reported in Figs. 6.6 and 6.7. The variations of V, R_{tip}, and the phase concentrations appear to follow trends which are similar to what is seen in Figs. 6.4 and 6.5, except for some differences. As discussed earlier, the criteria of "Complete Marginal Stability" and "Marginal Stability" cannot describe the effect of anisotropic interfaces on the dendrite growth dynamics. Thus, predictions from these criteria continue to be exactly the same as reported in Fig. 6.4 and are farther away from the corresponding simu-

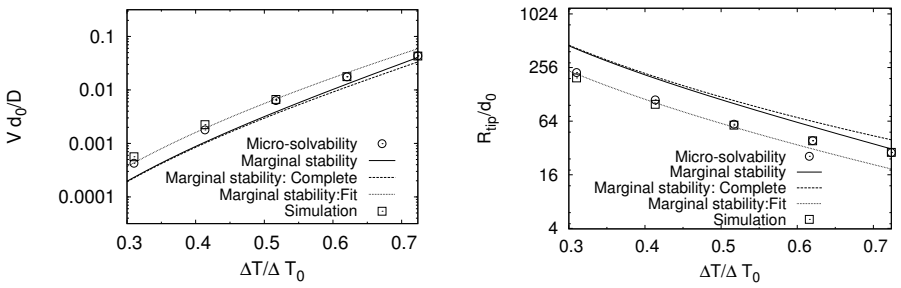

(a) (b)

Figure 6.4: Plots showing the variation of, (a)tip velocity (V), (b) tip radius (R_{tip}) with undercooling (ΔT). The diffusivity matrix is diagonal with $D_{AA} = D_{BB} = 2.0$, and the anisotropy strength is $\zeta = 0.01$.

lation predictions, compared to the situation corresponding to $\zeta = 0.01$. Furthermore, a higher strength of the surface energy anisotropy leads to a smaller R_{tip} (as seen in Fig. 6.6(b)) but a higher growth velocity V (as seen in Fig. 6.6(a)), for a given ΔT, compared to the situation for $\zeta = 0.01$ (in Figs. 6.4(b) and 6.4(a)).

The composition variations presented in Figs. 6.7(a), 6.7(c), 6.7(e) and 6.7(g) also display a similar trend where the variations calculated using "Complete Marginal Stability" and "Marginal Stability" deviate from the predictions from "Fitted Marginal Stability", "Microsolvability" and phase-field simulations to a larger extent compared to Figs. 6.5(a), 6.5(c), 6.5(e) and 6.5(g).

Moving on to the study a system with unequal solute diffusivities of $D_{AA} = 2.0, D_{BB} = 1.0$, with $\zeta = 0.01$, as reported in Figs. 6.8, we observe a selection of a similar tip-velocity (V) (in Fig. 6.8(a)) and tip-radius (R_{tip}) (in Fig. 6.8(b)) compared to the ones selected for $D_{AA} = 2.0, D_{BB} = 2.0$ in Figs. 6.4(a) and 6.4(b). Similar observations hold true for the situation of $D_{AA} = 1.0, D_{BB} = 2.0$ as well, as seen in Fig. 6.12. The change induced by lowering of one of the solute diffusivities is a complicated function of the phase diagram properties. It is possible that the phase diagram properties invoked in our study displays a relative insensitivity to a change in solute diffusivities. Furthermore, with V and R_{tip} being strongly interdependent (they appear together in the solution to the diffusion equation as Peclet numbers), our analytical expressions offer no intuitive way to predict the trends in the variation of either one of these quantities as a function of solute diffusivities. The variations of the individual quantities, V, R_{tip} and the phase concentrations with ΔT, however, display trends which are similar to what seen in Fig. 6.4.

The trends of the variation of phase concentrations with undercooling ΔT continue to display

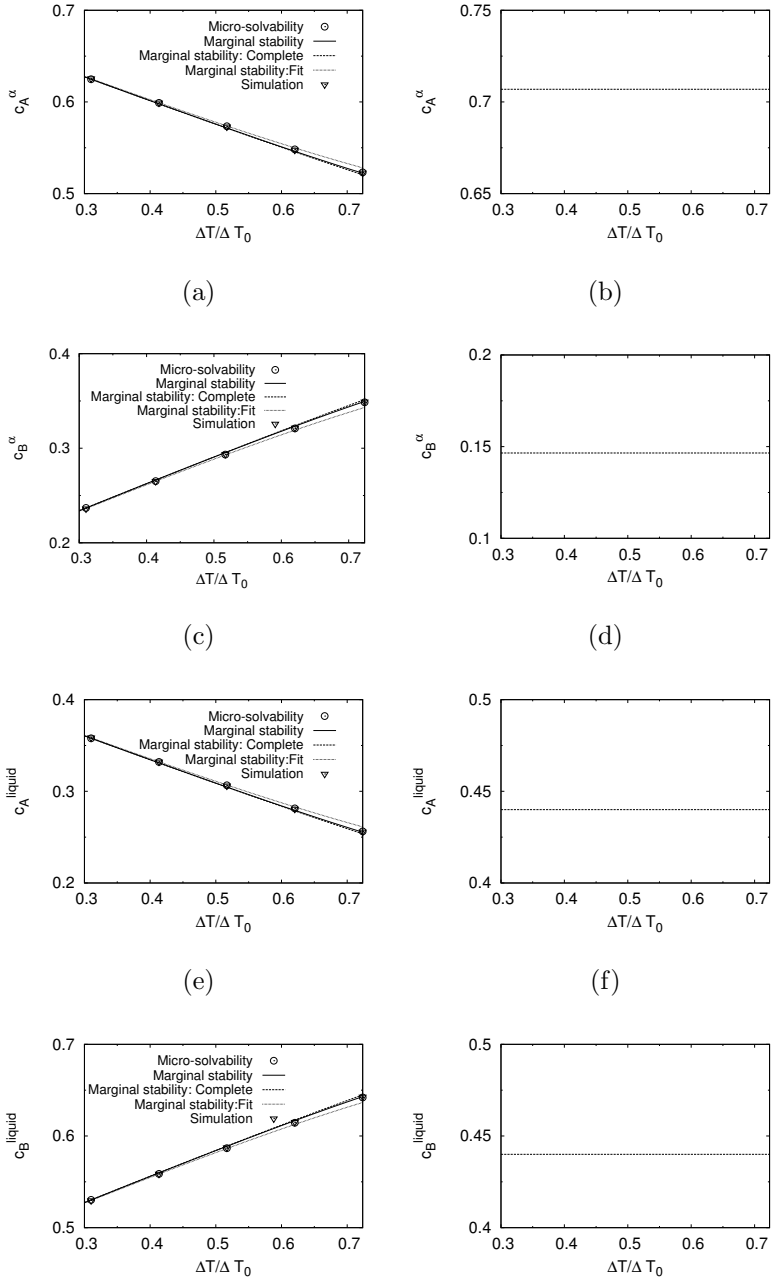

Figure 6.5: Plots showing the variation of the phase compositions, (a)c_A^α, (c) c_B^α, (e) c_A^{liquid}, (g) c_B^{liquid} with undercooling (ΔT). They are compared against the phase concentrations selected at a planar interface during steady-state growth, which are displayed in (b)c_A^α, (d)c_B^α, (f)c_A^{liquid}, and (g)c_B^{liquid}. The diffusivity matrix is diagonal with $D_{AA} = D_{BB} = 2.0$, and the anisotropy strength is $\zeta = 0.01$.

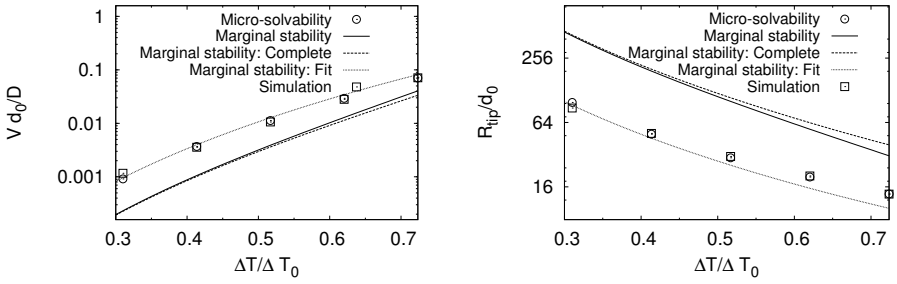

(a) (b)

Figure 6.6: Plots showing the variation of, (a)tip velocity (V), (b) tip radius (R_{tip}) with undercooling (ΔT). The diffusivity matrix is diagonal with $D_{AA} = D_{BB} = 2.0$, and the anisotropy strength is $\zeta = 0.02$.

features similar to situation for equal solute diffusivity(see Figs. 6.13(a) , 6.13(c), 6.13(e), 6.13(g), 6.9(a), 6.9(c), 6.9(e), 6.9(g)). An interesting difference from the situation with equal solute diffusivities is that the variation of the phase concentrations selected at the planar interface as a function ΔT is no longer constant.

The corresponding studies employing a higher strength of anisotropy, $\zeta = 0.02$, in systems with unequal solute diffusivities are reported in Figs. 6.10 and 6.14. Again, we observe lower values of R_{tip} (see Figs. 6.10(b) and 6.14(b)) and higher values of V (see Figs. 6.10(a) and 6.14(a)) compared to the corresponding observations in 6.8(b), 6.8(a), 6.12(b),and 6.12(a).

In order to understand the very minor changes observed in the variation of V and R_{tip} with changes in solute diffusivities, we report the variation of the parameter $Q = VR_{tip}^2$, with ΔT, for all combinations of solute diffusivities considered earlier, in Fig. 6.16. The data from phase-field simulations in Fig. 6.16(a) reveal a minor change in Q with solute diffusivity. An increase in Q with ΔT in Fig. 6.16(a) can be explained by the increase in V dominating over the reduction in R_{tip}, caused by an increase of ΔT. A more pronounced change is observed with a change in ζ (in Fig. 6.16(a)), as confirmed by our earlier observations as well. The variations of Q calculated from the criteria of "Marginal Stability" and "Complete Marginal Stability" are presented in Fig. 6.16(b). The phase diagram chosen for our study has properties, which leads to a constant Δc_i^*, regardless of the variations in μ_i and ΔT, resulting in the constancy of Q observed for the criterion of "Marginal Stability" in Fig. 6.16(b). The variation obtained from the criterion of "Complete Marginal Stability" in Fig. 6.16(b) shows a trend similar to the one obtained from phase-field simulations in Fig. 6.16(a). From Figs. 6.16(a) and 6.16(b) it is clear that the criteria of "Marginal Stability" and "Complete Marginal Stability" overestimate

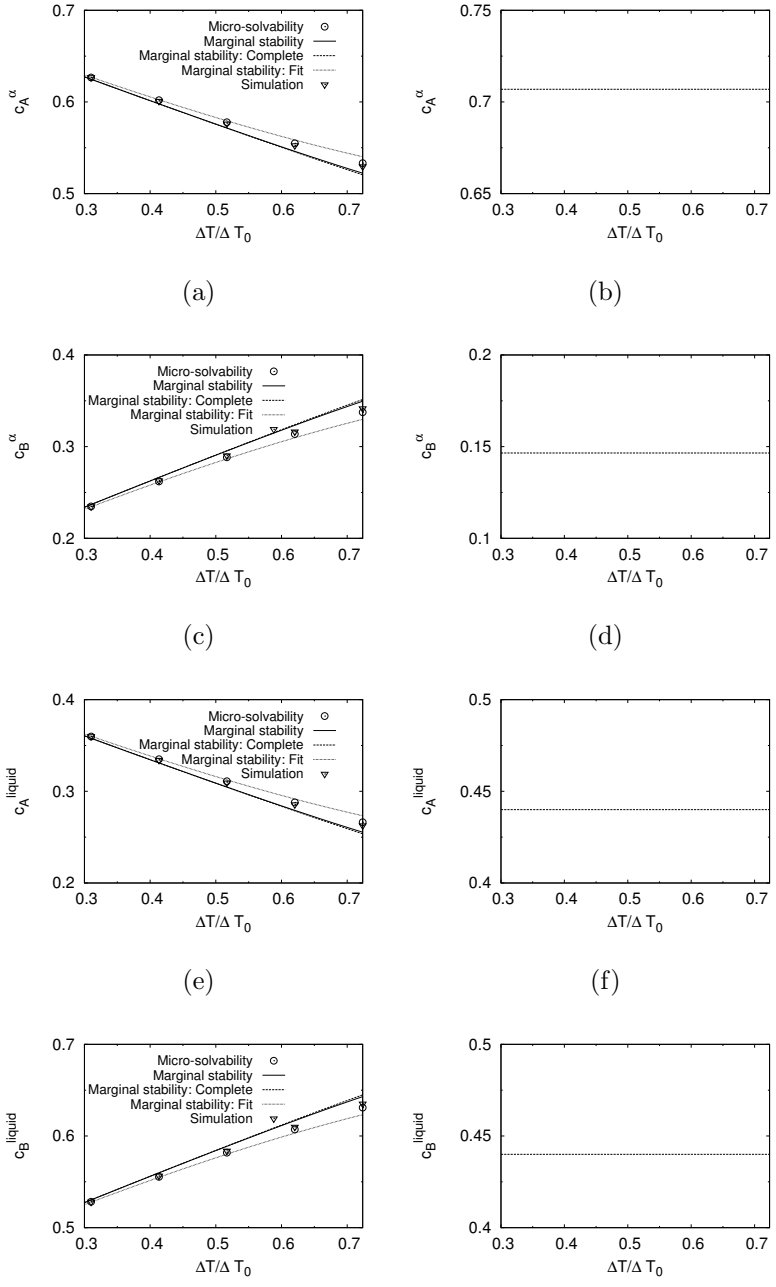

Figure 6.7: Plots showing the variation of the phase compositions, (a)c_A^α, (c) c_B^α, (e) c_A^{liquid}, (g) c_B^{liquid} with undercooling (ΔT). They are compared against the phase concentrations selected at a planar interface during steady-state growth, which are displayed in (b)c_A^α, (d)c_B^α, (f)c_A^{liquid}, and (g)c_B^{liquid}. The diffusivity matrix is diagonal with $D_{AA} = D_{BB} = 2.0$, and the anisotropy strength is $\zeta = 0.02$.

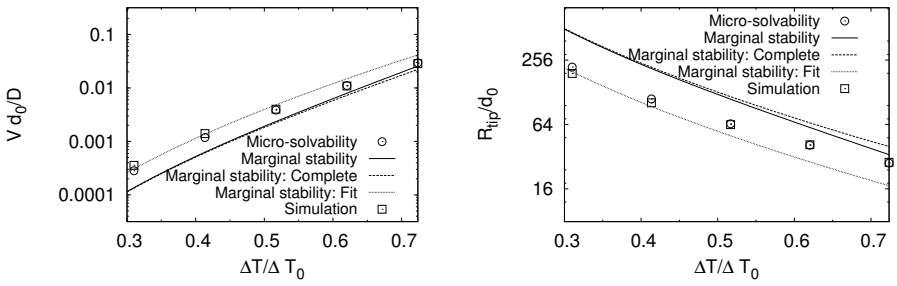

(a) (b)

Figure 6.8: Plots showing the variation of, (a)tip velocity (V), (b) tip radius (R_{tip}) with undercooling (ΔT). The diffusivity matrix is diagonal with $D_{AA} = 2.0, D_{BB} = 1.0$, and the anisotropy strength is $\zeta = 0.01$.

Q, compared to that from the phase-field simulations. Also, our analytical theory allows us to probe the effect of a larger difference in the solute diffusivities as presented in Fig. 6.17, where we plot the variation of dendrite tip-velocity V and tip-radius R_{tip} as a function of undercooling (ΔT) using the "Complete Marginal Stability" criterion. Here, increasing D_{BB} to values which are an order of magnitude larger than D_{AA} produces a much stronger effect on the selection of V and R_{tip} compared to the case where $D_{AA} = 10$ and $D_{BB} = 1$.

The effect of solute diffusivity can also be discerned from Fig. 6.18, where we display the composition fields in the liquid along the dendrite axis. It can be seen that a smaller diffusivity of any one of the solute species leads to a sharper gradient in concentration of the same. It must be added that V and R_{tip} being strong functions of the undercooling (ΔT) and the interfacial energy (σ), they display only a weak variation with a change in solute interdiffusivities.

6.3 Summary

In this chapter, we develop an analytical theory describing the problem of isothermal dendrite growth in multi-component alloys in 2D. Our theory predicts the dendrite tip-velocity (V), dendrite tip-radius (R_{tip}) and the interfacial phase concentrations for any given undercooling ΔT and the interdiffusivity matrix $[D]$ in the liquid. Thus, we generalize the work of Ivantsov [30], and Horvay and Cahn [31], to any generic multi-component alloy, for both independent and coupled diffusion of solutes and consider several different estimates for the dendrite tip-radius (R_{tip}) including the classical "Marginal Stability" [32] and "Microsolvability" [35] criteria. From our previous work in Chapter 5 where we present a linear stability analysis of a planar growth front in a multi-component alloy, we derive the complete expression for the "Marginal Stabil-

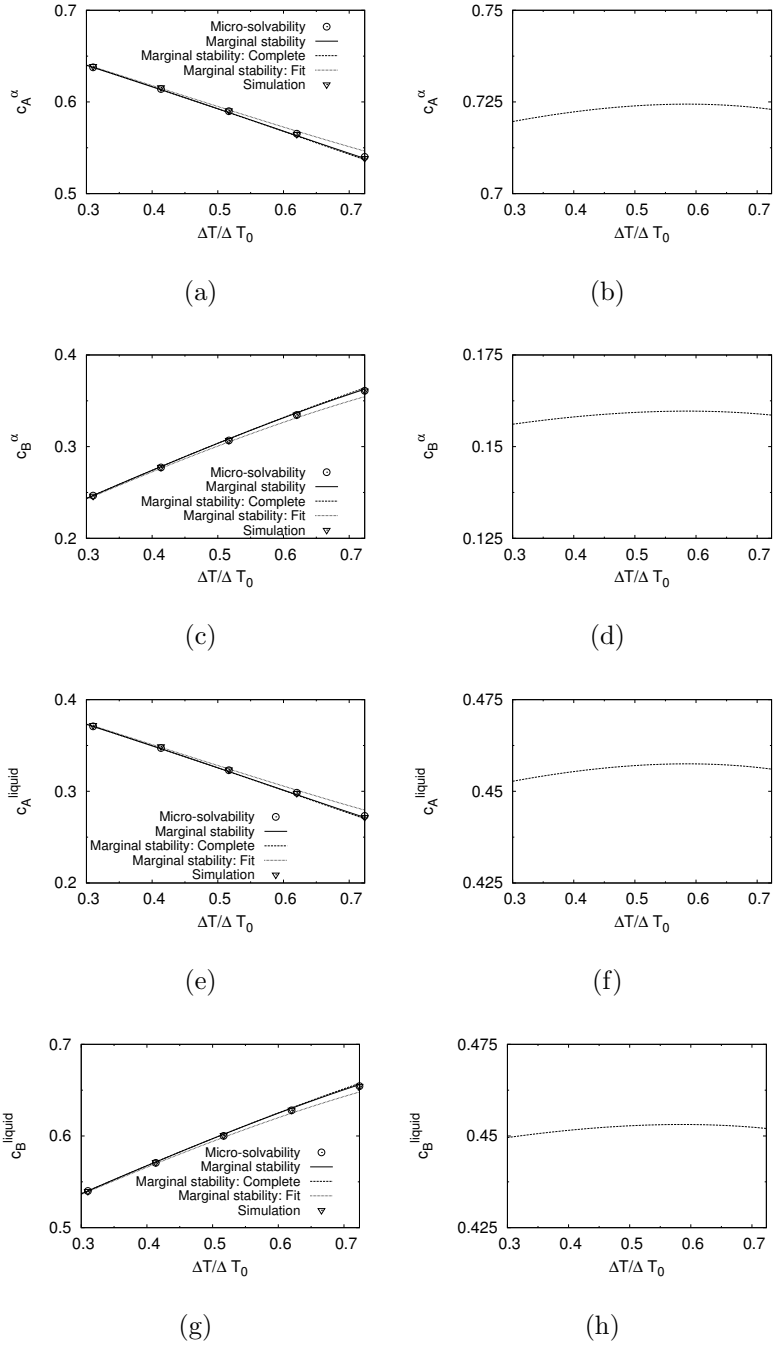

Figure 6.9: Plots showing the variation of the phase compositions, (a)c_A^α, (c) c_B^α, (e) c_A^{liquid}, (g) c_B^{liquid} with undercooling (ΔT). They are compared against the phase concentrations selected at a planar interface during steady-state growth, which are displayed in (b)c_A^α, (d)c_B^α, (f)c_A^{liquid}, and (g)c_B^{liquid}. The diffusivity matrix is diagonal with $D_{AA} = 2.0, D_{BB} = 1.0$, and the anisotropy strength is $\zeta = 0.01$.

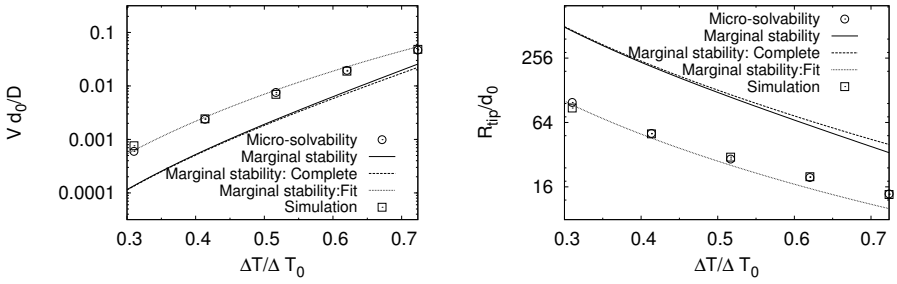

(a) (b)

Figure 6.10: Plots showing the variation of, (a)tip velocity (V), (b) tip radius (R_{tip}) with undercooling (ΔT). The diffusivity matrix is diagonal with $D_{AA} = 2.0, D_{BB} = 1.0$, and the anisotropy strength is $\zeta = 0.02$.

ity" criterion and compare it with the predictions from other conventional estimates of R_{tip}. In this chapter, we present a comparative study of the predictions from all these criteria including the ones from phase-field simulations, for different choices of the diffusivity matrix and the strength of the anisotropy in the solid-liquid interfacial energy (ζ). We show that our analytical calculations, for all estimates of R_{tip}, predict trends which are in very good agreement to those obtained from phase-field simulations with the criteria of "Microsolvability" and "Fitted Marginal Stability" being the closest to simulation predictions.

An understanding of the dependence of tip-radius (R_{tip}) on the solute diffusivities in a multi-component alloy can be naturally extended to the selection of primary arm spacing during directional solidification in such alloys. Also, a study similar to the one reported by Tourret and Karma [210] for binary alloys, can be conducted for multi-component alloys, where the process of microstructure selection during competitive growth of several dendrites with varying misorientations can be attempted to be understood in the context of the differences in diffusion distances associated with the different solutes. This provides an exciting scope for future work and we conclude this chapter by presenting a simple directional solidification simulation in Fig. 6.19 where the dendrites have a well-defined misorientation to the direction of the imposed temperature gradient (which is vertically upwards) which reveals an interesting process of the genesis of the primary arms. Here, the secondary arms grow and impinge on the vertical wall forming a nuclei at the bottom left hand corner of the simulation domain which henceforth grows along the direction of the primary arms.

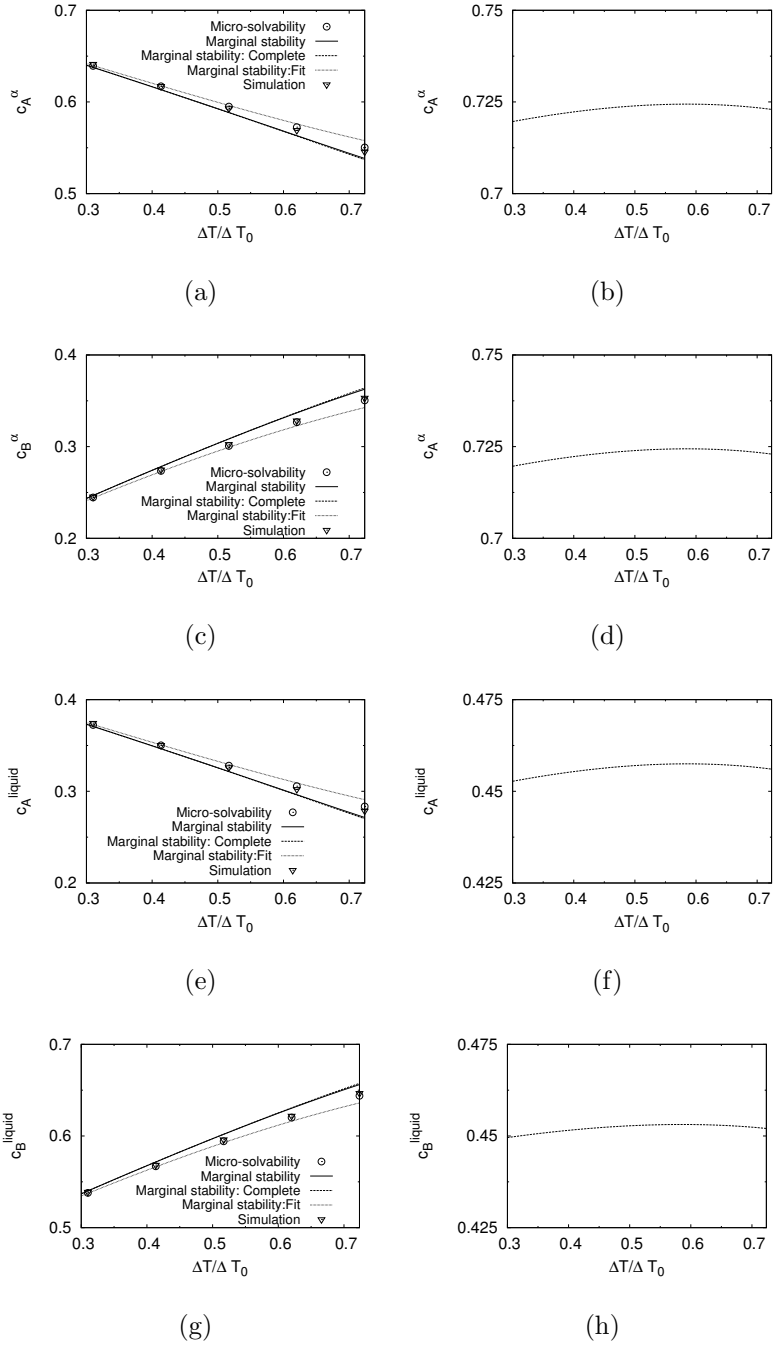

Figure 6.11: Plots showing the variation of the phase compositions, (a)c_A^α, (c) c_B^α, (e) c_A^{liquid}, (g) c_B^{liquid} with undercooling (ΔT). They are compared against the phase concentrations selected at a planar interface during steady-state growth, which are displayed in (b)c_A^α, (d)c_B^α, (f)c_A^{liquid}, and (g)c_B^{liquid}. The diffusivity matrix is diagonal with $D_{AA} = 2.0, D_{BB} = 1.0$, and the anisotropy strength is $\zeta = 0.02$.

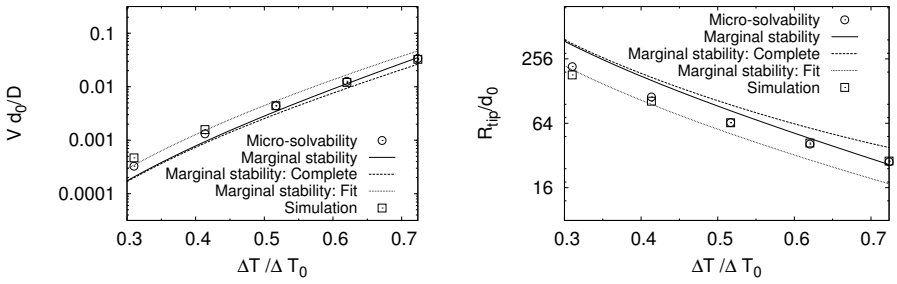

(a) (b)

Figure 6.12: Plots showing the variation of, (a)tip velocity (V), (b) tip radius (R_{tip}) with undercooling (ΔT). The diffusivity matrix is diagonal with $D_{AA} = 1.0, D_{BB} = 2.0$, and the anisotropy strength is $\zeta = 0.01$.

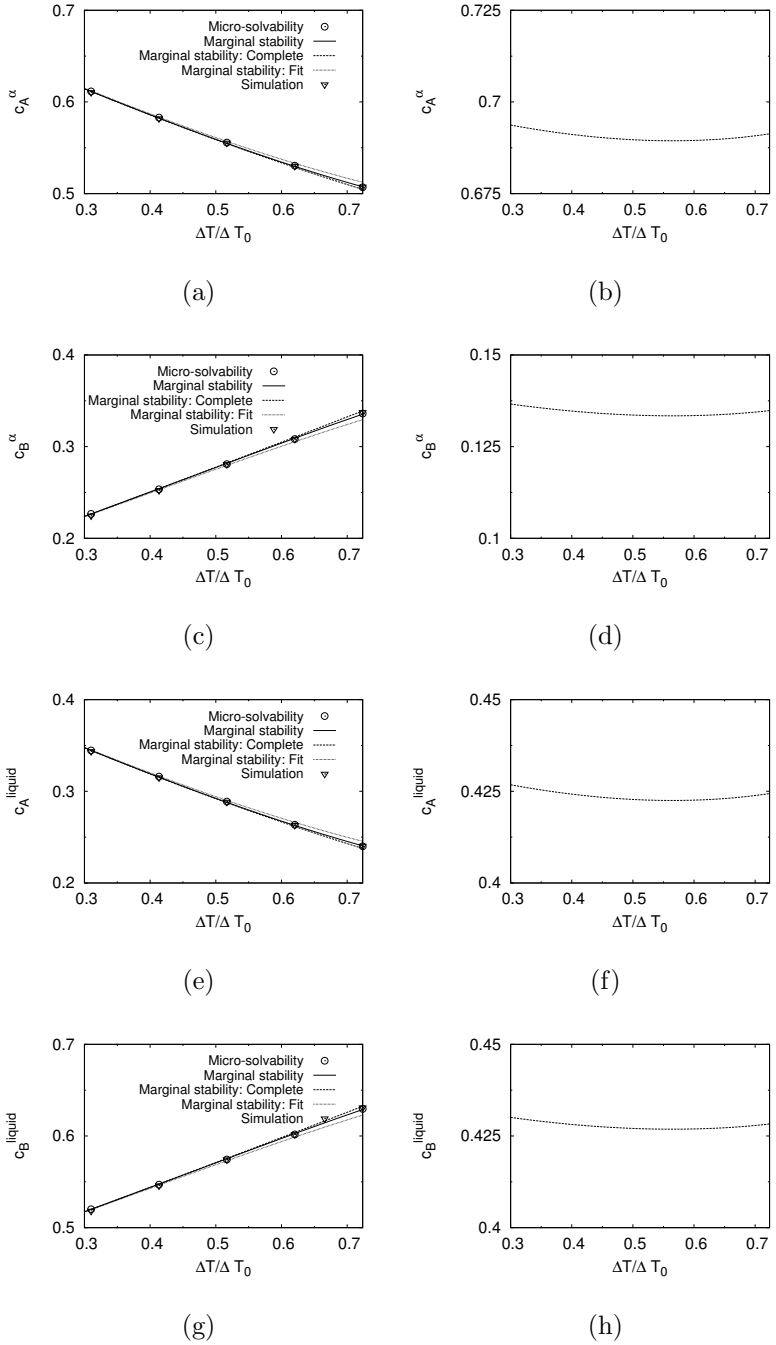

Figure 6.13: Plots showing the variation of the phase compositions, (a)c_A^α, (c) c_B^α, (e) c_A^{liquid}, (g) c_B^{liquid} with undercooling (ΔT). They are compared against the phase concentrations selected at a planar interface during steady-state growth, which are displayed in (b)c_A^α, (d)c_B^α, (f)c_A^{liquid}, and (g)c_B^{liquid}. The diffusivity matrix is diagonal with $D_{AA} = 1.0, D_{BB} = 2.0$, and the anisotropy strength is $\zeta = 0.01$.

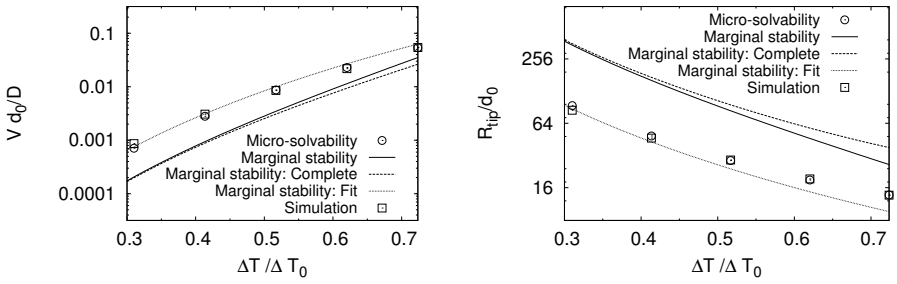

(a) (b)

Figure 6.14: Plots showing the variation of, (a)tip velocity (V), (b) tip radius (R_{tip}) with undercooling (ΔT). The diffusivity matrix is diagonal with $D_{AA} = 1.0, D_{BB} = 2.0$, and the anisotropy strength is $\zeta = 0.02$.

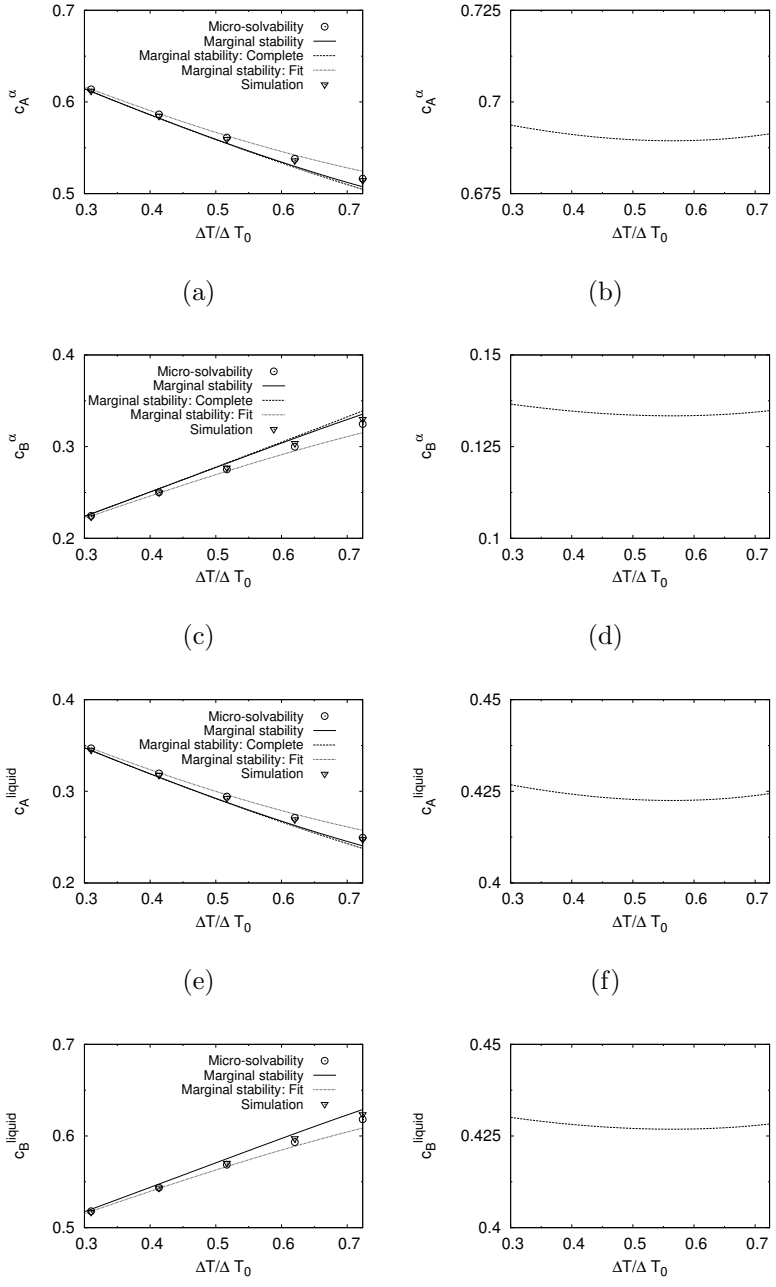

Figure 6.15: Plots showing the variation of the phase compositions, (a)c_A^α, (c) c_B^α, (e) c_A^{liquid}, (g) c_B^{liquid} with undercooling (ΔT). They are compared against the phase concentrations selected at a planar interface during steady-state growth, which are displayed in (b)c_A^α, (d)c_B^α, (f)c_A^{liquid}, and (g)c_B^{liquid}. The diffusivity matrix is diagonal with $D_{AA} = 1.0, D_{BB} = 2.0$, and the anisotropy strength is $\zeta = 0.02$.

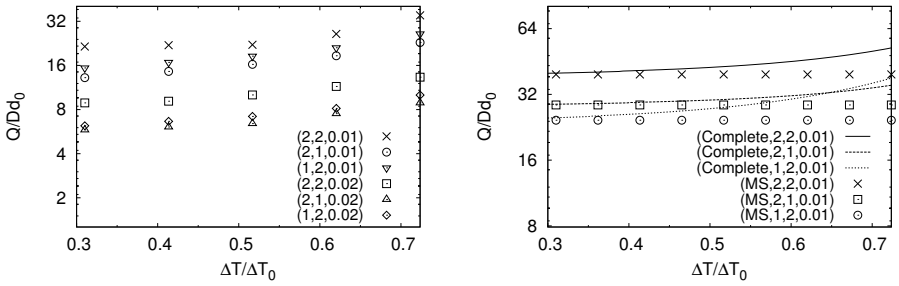

(a) (b)

Figure 6.16: Plots showing the variation of $Q = VR_{tip}^2$ as a function of ΔT, from (a) phase-field simulations, and (b) "Marginal Stability" and "Complete Marginal Stability". The three numbers appearing in the figure legends in (a) denote D_{AA}, D_{BB} and ζ respectively. The first element in the figure legend denotes the criterion for estimating R_{tip}; "MS" denotes "Marginal Stability", and "Complete" stands for "Complete Marginal Stability".

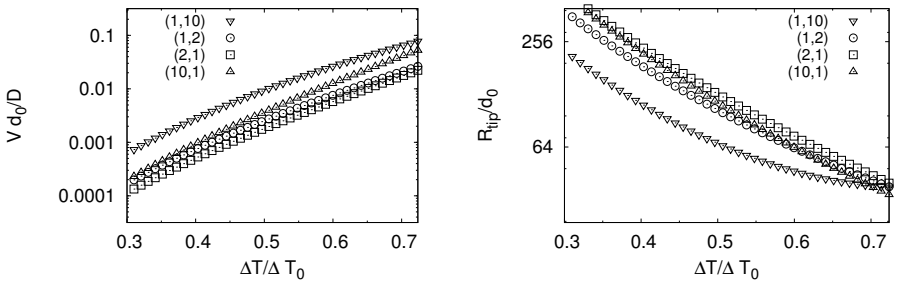

(a) (b)

Figure 6.17: Plots showing the variation of (a) V, and (b) R_{tip}, with undercooling ΔT for different solute diffusivities. The first number in the figure legend denotes D_{AA} and the second denotes D_{BB}.

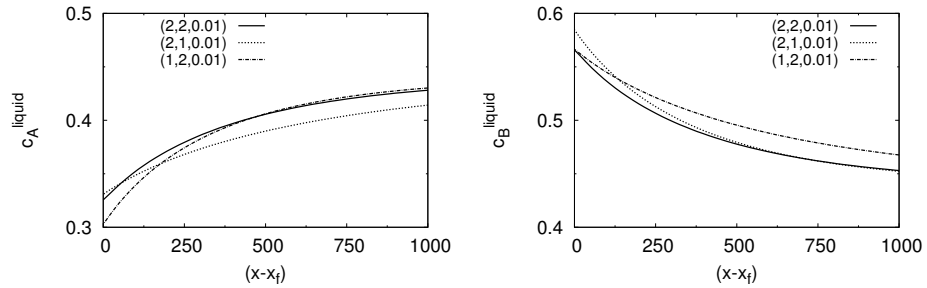

(a) (b)

Figure 6.18: Plots showing the variation of (a) c_A^{liquid}, and (b) c_B^{liquid}, with distance from the interface (denoted by x_f) for an undercooling of $\Delta T = 0.1$. The three numbers appearing in the figure legends in (a) denote D_{AA}, D_{BB} and ζ respectively.

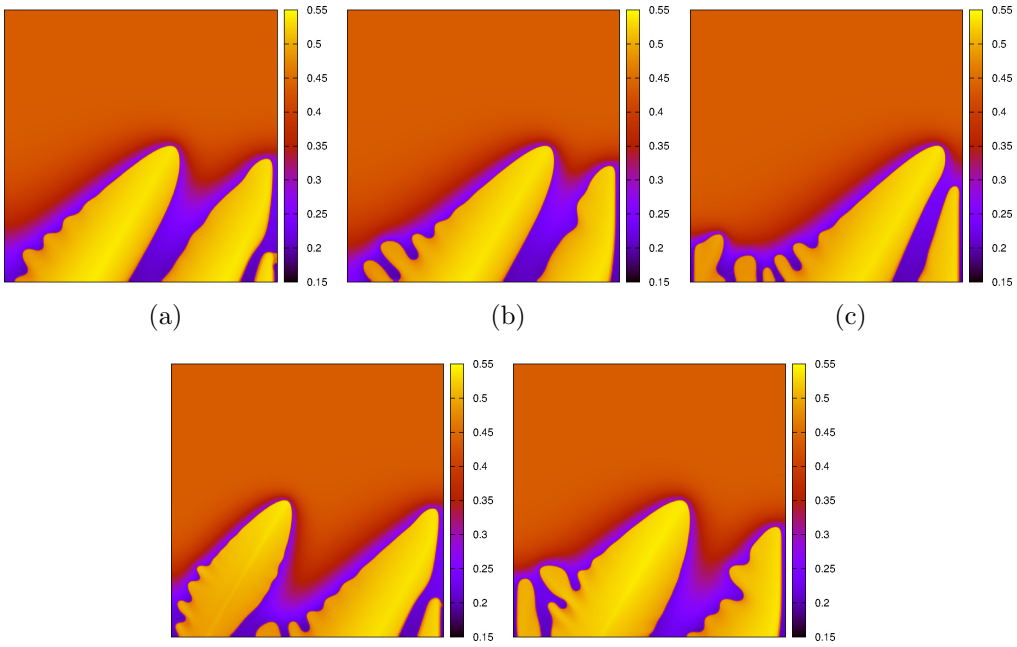

(a) (b) (c)

(d) (e)

Figure 6.19: Dendrite formation during directional solidification at times (non-dimensional) of (a)6×10^6, (b) 6.4×10^6, (c) 7.0×10^6, (d) 7.4×10^6, and (e)8×10^6, shown by plotting the c_A field. The magnitude of the anisotropy is $\zeta = 0.01$ and the frame of the crystalline anisotropy is rotated by 30°(clockwise) to the laboratory frame. The solute diffusivities are: $D_{AA} = D_{BB} = 2.0$. The sample pulling velocity (V) and the thermal gradient (G) are set to: $V = 0.005$ and $G = 9.675 \times 10^{-6}$.

Chapter 7

Theoretical and numerical investigation of multi-phase growth in a multi-component system

Jackson-Hunt [8] proposed an analytical technique to determine the undercooling at the interface separating the parent liquid phase from the product solid phases during eutectic solidification. The calculation is specific to invariant transformations (number of degrees of freedom being zero) and invokes several assumptions. The principal amongst them being the assumption of compositions and volume fractions of the solid phases given by the phase diagram.

In this chapter, we generalize the Jackson-Hunt calculation to be equally valid for invariant as well as non-invariant transformations. Furthermore, instead of assuming compositions and solid phase fractions to be given by the phase-diagram, our theory calculates them as part of the solution process, using the knowledge of the functional dependence of the free energies on composition and temperature. In the following sections, we successively revisit the classical JH calculation as proposed by Jackson and Hunt [8], following which we present our theory and compare its predictions against those obtained from phase-field simulations. We conclude with a short discussion on the accuracy of our theoretical predictions.

7.1 Analytical theory

7.1.1 The Jackson-Hunt calculation

In order to motivate our present work let us re-visit the main results of the classical Jackson-Hunt analysis as detailed in [8], for deriving the undercooling vs spacing relationships for

two-phase growth in a binary alloy. The situation is modeled by considering a repeating representative unit of two phases α and β growing in a directional solidification set-up where the imposed temperature gradient (G) at the interface traverses with a velocity V, that sets the rate of solidification. The undercooling at each interface can be written as,

$$\Delta T^{\nu} = -m_B^{\nu}(\widetilde{c_B^{\nu}} - c_B^E) + \Gamma_{\nu}\widetilde{\kappa_{\nu}}, \tag{7.1}$$

where, $\widetilde{c_B^{\nu}}$ represents the average composition in the liquid in local equilibrium with the ν-th phase ($\nu = \alpha, \beta$) and c_B^E represents the eutectic composition. m_B^{ν} is the liquidus slope. Γ_{ν} and κ_{ν} denote the Gibbs-Thomson coefficient and the interfacial curvature, respectively.

The classical Jackson-Hunt solution starts by writing the composition profiles as a Fourier series (see Eq.7.2). The solution to Fourier amplitudes (all except the boundary layer composition, or the zeroth order Fourier mode I_0) is derived as described in sec. 7.1.2 such that the governing equations as well as the Stefan conditions are satisfied. A corresponding generic analysis for invariant eutectic growth in multi-component systems is laid out in [39].

A short description about the zeroth order mode which also partly sets the motivation of the rest of the chapter is in order. The zeroth order Fourier mode I_0 as described by Eq.7.11 for a binary alloy with solute $I = B$ reads, $B_0 = \left[c_B^{\alpha l}\eta_{\alpha} + c_B^{\beta l}(1-\eta_{\alpha})\right] - \left[c_B^{\alpha}\eta_{\alpha} + c_B^{\beta}(1-\eta_{\alpha})\right]$, where $c_B^{\alpha/\beta,l}$ represents the liquid compositions in equilibrium with the α/β interfaces, η_{α} is the volume fraction of the α phase. If one uses the volume fractions and compositions at the eutectic temperature (as for the other Fourier modes) for determining the boundary layer composition B_0 (far-field composition is at the eutectic) it would result in zero and the corresponding undercoolings at the interface using Eq.7.1 would not be equal. This calculation, would also be physically incorrect, as the phase compositions deviate from their values at the eutectic temperature. Jackson and Hunt in their analysis, treat this difficulty by keeping the B_0 as an unknown which is fixed by the condition that the undercoolings at both solid-liquid interfaces are equal, while the volume fractions η_{α} at the eutectic temperature are utilized for computing both the constitutional and curvature undercoolings. In general, one can solve this problem of invariant growth for a multi-component system as in [39], where it has been shown to agree well with experiments as well as phase-field simulations.

For the mono-variant reaction however, for instance in a two-phase growth in a ternary alloy, there would be two boundary layer compositions, whereas the equality of a common undercooling imparts only a single equation, thereby the system of equations become under-determined. The system of equations can only be made deterministic by invoking the functional dependence of the boundary layer compositions on the phase compositions and the solid-fractions. This mo-

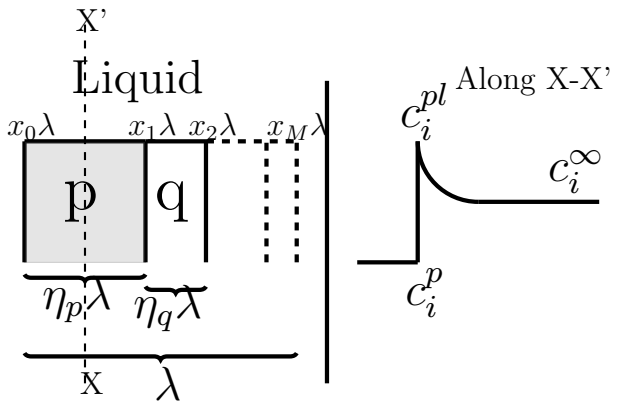

Figure 7.1: Schematic showing the different variables characterizing the steady-state eutectic growth.

tivates our present derivation, which in spirit unifies the theories of in-variant and multi-variant eutectic growth.

7.1.2 Theory

The following discussion is generic to a directionally solidifying multi-component alloy of K components (with $K-1$ of them being independent), displaying a eutectic reaction with N solid phases, possessing $F = K - N$ degrees of freedom. In the following discussion, the indices i and j are reserved for solutes, while ν and p denote the solid phases appearing due to eutectic solidification. In this subsection, we describe the process of determining the composition fields in the liquid (c_i) ahead of the eutectic front as functions of the lamellar width (λ), the solid phase fractions (η_p, for the p-th solid phase), and the solute diffusivities in the liquid (D_{ii}). We present an expression of the undercooling at every solid (p)-liquid interface by summing the constitutional undercooling determined by the liquid compositions in local equilibrium with the solid phase p (c_i^{pl}), and the curvature undercooling determined by the solid phase fraction (η_p), alongside the lamellar width (λ). The different composition variables and the solid phase fractions are also pictorially defined in the schematic in Fig. 7.1. We conclude this subsection by stating our approach for solving the set of equations stemming from the assumed equality of undercoolings ahead of the different solid-liquid interfaces in a periodic unit of lamellae. The key symbols employed in the mathematical description is presented in Table. 7.1.

Though, we present the theory assuming independent diffusion of solutes in the liquid (no diffusion in the solid), it can be considered to be representative of a system with non-zero off-diagonal terms in the diffusivity matrix, when such an analysis is carried out in the basis

7. THEORETICAL AND NUMERICAL INVESTIGATION OF MULTI-PHASE GROWTH IN A MULTI-COMPONENT SYSTEM

K	the no. of components
N	the no. of phases
λ	the lamellar width
η_p	the solid-phase fracton of the p-th phase
c_i	concentration of i-th component in liquid
c_i^∞	concentration of i-th component in liquid at far-field
$\overline{c_i^{pl}}$	average concentration of i-th component in liquid at the interface in local equilibrium with the p-th solid
$\overline{c_i^p}$	average concentration of i-th component in the p-th solid at the interface in local equilibrium with the liquid
m_i^p	the liquidus slope corresponding to the $p-l$ equilibrium
$\overline{\kappa_p}$	average curvature of the solid(p)-liquid interface
$\overline{\Delta T^p}$	average undercooling ahead of the solid(p)-liquid interface
$\overline{\mu_i^p}$	average diffusion potential of the i-th component in the liquid in local equilibrium with solid p
D_{ij}	(i,j)-th component of the diffusivity matrix
Γ_p	the Gibbs-Thomson coefficient of the $p-l$ equilibrium
$c_i^{p,*}$	the concentration of the i-th component in the p-th solid at the eutectic
$c_i^{pl,*}$	the concentration of the i-th component in the liquid at the eutectic
V	the pulling velocity
$\mu_i^{p,*}$	the linearization point of the diffusion potential of i-th component for the $p-l$ equilibrium
T^*	the eutectic temperature

Table 7.1: The symbols used in the analytical derivation.

system of the eigenvectors of the diffusivity matrix.

Assuming a flat interface, the composition variation in the liquid is of the form [39],

$$c_i = c_i^{\infty} + \sum_{n=-\infty}^{n=\infty} I_n e^{\hat{i}k_n x - q_n^i z}, \tag{7.2}$$

where, $\hat{i} = \sqrt{-1}$, and $k_n = 2\pi n/\lambda$, are wavenumbers characterizing the variation of solute concentrations in the liquid across a solid-liquid interface aligned along x with the eutectic solids growing in z. Conformity of Eq. 7.2 to the stationary form of the diffusion equation given below,

$$V\frac{\partial c_i}{\partial z} + D_{ii}\nabla^2 c_i = 0, \tag{7.3}$$

leads to,

$$q_n^i = \left(\frac{V}{2D_{ii}}\right) + \sqrt{k_n^2 + \left(\frac{V}{2D_{ii}}\right)^2}, \tag{7.4}$$

where D_{ii} denotes the diffusivity of the ith component and V represents the sample pulling velocity. Following the discussion in [39], a single wavelength of the eutectic consists of M units ($M >= N$) of the eutectic solids with each one of the M units corresponding to one of the N phases. The periodic variation starts at $x_0 = 0$ and terminates at $x_M = 1$ with the width of the ν-th unit being given by $(x_\nu - x_{\nu-1})\,\lambda$; the entire wavelength being $(x_M - x_0)\,\lambda$. Thus, the volume fraction of a particular phase p, denoted by η_p, can be calculated from a single wavelength of the eutectic lamellae as,

$$\eta_p = \sum_{\nu=0}^{M-1} (x_{\nu+1} - x_\nu)\,\delta_{\nu p}, \tag{7.5}$$

where,

$$\delta_{\nu p} = \begin{cases} 1, & \text{if } \nu = p, \\ 0, & \text{if } \nu \neq p. \end{cases} \tag{7.6}$$

The mass balance across a particular location at the solid-liquid interface for the ν-th unit

can be written as,

$$V\Delta c_i^{\nu} = -D_{ii}\frac{\partial c_i}{\partial z}\bigg|_{z=0,x_\nu^*}, \tag{7.7}$$

with $\Delta c_i^{\nu} = c_i^{\nu l} - c_i^{\nu}$, where $c_i^{\nu l}$ and c_i^{ν} denote the liquid and the solid compositions in local equilibrium at a location x_ν^* on the $\nu - l$ interface, respectively.

An expression for the Fourier constants I_n, is obtained by invoking the orthogonality of the Fourier basis functions while integrating Eq. 7.7 over an entire period (λ) of the eutectic, leading to,

$$q_n^i I_n \lambda = \frac{2}{l_i}\sum_{\nu=0}^{M-1}\int_{x_\nu\lambda}^{x_{\nu+1}\lambda}\exp(-ik_n x)\Delta c_i^{\nu} dx, \tag{7.8}$$

where, $l_i = 2D_{ii}/V$, is the diffusion length associated with the i-th component. For the mode corresponding to $n = 0$, Eq. 7.8 yields for the i-th component,

$$I_0 = \frac{1}{\lambda}\sum_{\nu=0}^{M-1}\int_{x_\nu\lambda}^{x_{\nu+1}\lambda}\Delta c_i^{\nu} dx. \tag{7.9}$$

It is beneficial to define average compositions in front of a particular phase p as,

$$\overline{\Delta c_i^{p}} = \frac{\sum_{\nu=0}^{M-1}\delta_{\nu p}\int_{x_\nu\lambda}^{x_{\nu+1}\lambda}\Delta c_i^{\nu} dx}{\sum_{\nu=0}^{M-1}(x_{\nu+1} - x_\nu)\lambda\delta_{\nu p}}, \tag{7.10}$$

which allows us to re-express Eq. 7.9 as,

$$I_0 = \sum_{p=1}^{N}\eta_p\overline{\Delta c_i^{p}}. \tag{7.11}$$

Similarly, the average interfacial composition in the solid ($\overline{c_i^{p}}$) and the liquid $\overline{c_i^{pl}}$ ahead of it is defined as,

$$\overline{c_i^{p,pl}} = \frac{\sum_{\nu=0}^{M-1}\delta_{\nu p}\int_{x_\nu\lambda}^{x_{\nu+1}\lambda} c_i^{\nu,\nu l} dx}{\sum_{\nu=0}^{M-1}(x_{\nu+1} - x_\nu)\lambda\delta_{\nu p}}. \tag{7.12}$$

The theory in [39] following that of Jackson and Hunt [8] provides an expression for $\overline{c_i^{pl}}$, which

has the form,

$$\begin{aligned}\overline{c_i^{pl}} &= c_i^{\infty} + I_0 \\ &+ \frac{\lambda}{\eta_p l_i} f_i\Big(P_1(\eta_1,\cdots,\eta_N),\cdots,P_r(\eta_1,\cdots,\eta_N), \\ &\overline{\Delta c_i^1},\cdots,\overline{\Delta c_i^N}\Big),\end{aligned} \tag{7.13}$$

where, each of one of the k infinite series' $P_k(\eta_p)$, $k = 1,\cdots,r$, $p = 1,\cdots,N$, are composed of terms which are trigonometric functions of η_p. The value of r and the form of $P_k(\eta_p)$ are determined by the number and repetitions of solid phases in a single periodic unit of wavelength λ. It must be mentioned at this point that the term I_0 represents the principal term determining the liquid compositions $\overline{c_i^{pl}}$ at the flat interface, with the secondary influence being due to that of the higher order modes averaged over the lamellar widths denoted by the final term in the RHS of Eq. 7.13. An example of such a term for a ternary monovariant eutectic [39],

$$f_i = 2P(\eta_\alpha)\left(\overline{\Delta c_i^{\alpha}} - \overline{\Delta c_i^{\beta}}\right), \tag{7.14}$$

$$P(\eta_\beta) = P(\eta_\alpha) = \sum_{n=1}^{\infty} \frac{1}{(\pi n)^3}\sin^2(\pi n \eta_\alpha). \tag{7.15}$$

The average undercooling ($\overline{\Delta T^p}$) ahead of a particular solid (p)-liquid (l) interface is given by,

$$\overline{\Delta T^p} = T^* - T^p = \sum_{i=0}^{K-1} m_i^p\left(c_i^{l,*} - \overline{c_i^{pl}}\right) + \Gamma_p\overline{\kappa_p}, \tag{7.16}$$

where, m_i^p are the liquidus slopes, Γ_p denotes the Gibbs-Thomson coefficient with the average curvature of the solid(p)-liquid interface ($\overline{\kappa_p}$) given by,

$$\overline{\kappa_p} = \frac{2\sin\overline{\theta_{pm}}}{\eta_p\lambda}, \tag{7.17}$$

where, $\overline{\theta_{pm}}$ is the angle made by the tangent to the solid(p)-liquid(l) interface and the horizontal towards the side of the p-th phase when located adjacent to the m-th phase, and averaged over all such contiguous arrangements of the solid phases m and p in the entire period.

The fact that the imposed thermal gradient has a length scale much larger than the lamellar width, implies the growth of all the eutectic solids at equal undercoolings, which can be

expressed as,

$$\overline{\Delta T^1} = \overline{\Delta T^2} = \cdots = \overline{\Delta T^N} = \overline{\Delta T}. \tag{7.18}$$

Also, the sum of volume fractions of the phases in a single period of the lamellae must be equal to unity,

$$\sum_{p=1}^{N} \eta_p = 1. \tag{7.19}$$

Here, one needs to solve the Eqs. 7.11, 7.13, 7.16, 7.18 and 7.19 simultaneously, in order to retrieve the phase compositions, the solid fractions and the undercooling of the eutectic growth front. For this, we need to describe the functional dependence between the solid compositions $\overline{c_i^p}$ and the liquid compositions $\overline{c_i^{pl}}$. We do this by calling upon the relations of the phase compositions $\overline{c_i^{p,pl}}\left(\overline{\mu_i^p}, T\right)$, where $\overline{\mu_i^p}$ corresponds to the diffusion potential of $p-l$ equilibrium, averaged over all occurrences of the solid phase p in a periodic unit of the eutectic. This then reduces the above system, Eqs. 7.11, 7.13, 7.16, 7.18 and 7.19 in terms of $\overline{\mu_i^p}$, T, and η_p.

A point to note here is that, Senninger and Voorhees [43], replace the Eqs.7.11 with a mass conservation constraint. Mass conservation is implicit in our set of equations. This can be seen by considering only those N equations out of the $N(K-1)$ in Eqs.7.13 which represent the composition fields of a particular component i in the liquid in equilibrium with different solids (p). Summing over all such equations after multiplying both sides of each of them with the respective volume fractions η_p, gives $I_0 = \sum_p \overline{c_i^{pl}}\eta_p - c_i^\infty$. This along with Eqs.7.11 implies that $\sum_p \overline{c_i^p}\eta_p = c_i^\infty$, which is the mass conservation equation used by Senninger and Voorhees [43].

However, given that the thermodynamical relations $\overline{c_i^{p,pl}}\left(\overline{\mu_i^p}, T\right)$ are routinely non-linear, the resultant set of equations become difficult to resolve. Given that most departures from equilibrium in case of eutectic reactions are small, we therefore linearize our set of equations about the chosen eutectic temperature T^*, the average diffusion potentials $\mu_j^{p,*}$ and the solid phase fractions η_p^*, corresponding to T^*. It must be noted that the equilibrium solid and liquid phase compositions corresponding to T^*, $\mu_j^{p,*}$ and η_p^*, are $c_i^{p,*}$ and $c_i^{pl,*}$ (same as $c_i^{l,*}$), respectively. This results in a set of linear equations which can be solved for, consistently.

7.1.3 Linearized theory

In this subsection, we express the departures in diffusion potentials, $\overline{\Delta\mu_j^p} = \overline{\mu_j^p} - \mu_j^{p,*}$, as functions of the departures of solid phase fractions from values given by the phase diagram,

$\Delta\eta_p = \eta_p - \eta_p^*$, and the undercoolings ΔT. These relationships are in turn utilized to express the condition of equality of undercoolings ahead of the different solid-liquid interfaces in terms of the unknowns $\Delta\eta_p$ and ΔT. After this operation, we obtain a consistent system of linear equations from which we determine the unknowns $\Delta\eta_p$ and ΔT.

We express the average compositions in the solid ($\overline{c_i^p}$) and the liquid ($\overline{c_i^{pl}}$) as functions of diffusion potentials ($\overline{\mu_j^p}$) as,

$$\overline{c_i^p} = c_i^{p,*} + \sum_{j=1}^{K-1} \left[\frac{\partial c_i^p}{\partial \mu_j}\right]_{\mu_j^{p,*}} \overline{\Delta\mu_j^p} - \left.\frac{\partial c_i^p}{\partial T}\right|_{T^*} \overline{\Delta T^p}, \tag{7.20}$$

and,

$$\overline{c_i^{pl}} = c_i^{pl,*} + \sum_{j=1}^{K-1} \left[\frac{\partial c_i^l}{\partial \mu_j}\right]_{\mu_j^{p,*}} \overline{\Delta\mu_j^p} - \left.\frac{\partial c_i^l}{\partial T}\right|_{T^*} \overline{\Delta T^p}, \tag{7.21}$$

where, $\overline{\Delta\mu_j^p} = \overline{\mu_j^p} - \mu_j^{p,*}$, denote the change in average diffusion potentials from their values at the chosen eutectic point $\mu_j^{p,*}$, under an additional constraint of constant $[\partial c_i/\partial\mu_j]$ matrices. The vector $\partial c_i^p/\partial T$ determine the change in composition with temperature at constant diffusion potentials. The process of determining the constant matrix $[\partial c_i/\partial\mu_j]$ and the vector $\partial c_i^p/\partial T$ is mentioned in Chapter 3 under the section "Thermodynamics" in the subsection "Parabolic driving forces". The symbol $c_i^{pl,*}$ is used in favor to $c_i^{l,*}$ in Eq. 7.21 as it generalizes Eq. 7.21 as a representation of the solid(p)-liquid equilibrium which can be linearized at any temperature of choice.

Employing Einstein's indicial notation which conveys summation over repeated indices (except for p in our analysis, which denotes a particular phase), the above equations can be written as,

$$\overline{c_i^p} = c_i^{p,*} + \chi_{ij}^p \overline{\Delta\mu_j^p} - \zeta_i^p \overline{\Delta T^p}, \tag{7.22}$$

and,

$$\overline{c_i^{pl}} = c_i^{pl,*} + \chi_{ij}^l \overline{\Delta\mu_j^p} - \zeta_i^l \overline{\Delta T^p}, \tag{7.23}$$

where,

$$\chi_{ij}^{p} = \left.\frac{\partial c_i^p}{\partial \mu_j}\right|_{\mu_j^{p,*}}, \tag{7.24}$$

$$\chi_{ij}^{l} = \left.\frac{\partial c_i^l}{\partial \mu_j}\right|_{\mu_j^{p,*}}, \tag{7.25}$$

$$\zeta_{i}^{p} = \left.\frac{\partial c_i^p}{\partial T}\right|_{T^*}, \tag{7.26}$$

$$\zeta_{i}^{l} = \left.\frac{\partial c_i^l}{\partial T}\right|_{T^*}. \tag{7.27}$$

Thus, the difference in the average compositions of the solid and the liquid as obtained from Eqs. 7.20, 7.21, 7.22 and 7.23,

$$\begin{aligned}
\overline{\Delta c_i^p} &= \overline{c_i^{pl}} - \overline{c_i^p}, \\
&= \left(c_i^{pl,*} - c_i^{p,*}\right) + \sum_{j=1}^{K-1} \left(\frac{\partial c_i^l}{\partial \mu_j} - \frac{\partial c_i^p}{\partial \mu_j}\right)_{\mu_j^{p,*}} \overline{\Delta \mu_j^p} \\
&\quad - \left(\frac{\partial c_i^l}{\partial T} - \frac{\partial c_i^p}{\partial T}\right)_{T^*} \overline{\Delta T^p} \\
&= \Delta c_i^{p,*} + \Delta \chi_{ij}^p \overline{\Delta \mu_j^p} - \Delta \zeta_i^p \overline{\Delta T^p},
\end{aligned} \tag{7.28}$$

where, to obtain the last equality expressed in indicial notation, we have used,

$$\begin{aligned}
\Delta c_i^{p,*} &= c_i^{pl,*} - c_i^{p,*}, \\
\Delta \chi_{ij}^p &= \chi_{ij}^l - \chi_{ij}^p, \\
\Delta \zeta_i^p &= \zeta_i^l - \zeta_i^p.
\end{aligned} \tag{7.29}$$

Using, Eqs. 7.22, 7.23 and 7.28, the $2N(K-1)$ composition variables have been expressed as functions of $N(K-1)$ intensive variables in the form of change in diffusion potentials $\overline{\Delta \mu_j^p}$, which can be further related to $\Delta\eta_p (= \eta_p - \eta_p^*)$ and $\overline{\Delta T^p}$ by invoking equality of Eqs. 7.13 and 7.21 which provide additional $N(K-1)$ equations, stated in the indicial notation (with no sum over p and i) as,

$$\overline{c_i^{pl}} = c_i^{pl,*} + \chi_{ij}^l \overline{\Delta \mu_j^p} - \zeta_i^l \overline{\Delta T^p}$$

$$
\begin{aligned}
&= c_i^{\infty} + I_0 \\
&+ \frac{\lambda}{\eta_p l_i} f_i\Big(P_1(\eta_1, \cdots, \eta_N), \cdots, P_r(\eta_1, \cdots, \eta_N), \\
&\overline{\Delta c_i^1}, \cdots, \overline{\Delta c_i^N}\Big)
\end{aligned} \tag{7.30}
$$

The RHS of Eq. 7.30 (or Eq. 7.13), is in general non-linear in $\overline{\Delta\mu_j^p}$, $\Delta\eta_p$ and $\overline{\Delta T^p}$. Thus, to express $\overline{\Delta\mu_j^p}$ as an explicit function of $\Delta\eta_p$ and $\overline{\Delta T^p}$, we linearly expand each term in the RHS of Eq. 7.30 starting with I_0, given by,

$$
\begin{aligned}
I_0 = I_0^* &+ \sum_{m=1}^{N} \frac{\partial I_0}{\partial \overline{\Delta c_i^m}} \sum_{j=1}^{K-1} \frac{\partial \overline{\Delta c_i^m}}{\partial \mu_j}\bigg|_{\mu_j^{m,*}} \overline{\Delta\mu_j^m} \\
&- \sum_{m=1}^{N} \frac{\partial I_0}{\partial \overline{\Delta c_i^m}} \frac{\partial \overline{\Delta c_i^m}}{\partial T}\bigg|_{T^*} \overline{\Delta T^m} \\
&+ \sum_{m=1}^{N} \frac{\partial I_0}{\partial \eta_m}\bigg|_{\eta_m^*} \Delta\eta_m,
\end{aligned} \tag{7.31}
$$

where, $\mu_i^{p,*}$, T^* and η_p^* are the quantities corresponding to the equilibrium in the phase diagram. The different terms in the RHS of Eq. 7.31 can be computed from Eqs. 7.11, 7.28 and 7.29 as,

$$
\frac{\partial I_0}{\partial \overline{\Delta c_i^p}} = \eta_p^*, \tag{7.32}
$$

$$
\frac{\partial \overline{\Delta c_i^p}}{\partial \mu_j}\bigg|_{\mu_j^{p,*}} = \left(\frac{\partial c_i^l}{\partial \mu_j} - \frac{\partial c_i^p}{\partial \mu_j}\right)_{\mu_j^{p,*}} = \Delta\chi_{ij}^p, \tag{7.33}
$$

$$
\frac{\partial \overline{\Delta c_i^p}}{\partial T}\bigg|_{T^*} = \left(\frac{\partial c_i^l}{\partial T} - \frac{\partial c_i^p}{\partial T}\right)_{T^*} = \Delta\zeta_i^p, \tag{7.34}
$$

$$
\frac{\partial I_0}{\partial \eta_p}\bigg|_{\eta_p^*} = \Delta c_i^{p,*}. \tag{7.35}
$$

At this point we introduce the following quantities (no sum over p),

$$
\begin{aligned}
\overline{\Delta\chi_{ij}^p} &= \eta_p^* \Delta\chi_{ij}^p, \\
\overline{\Delta\zeta_i^p} &= \eta_p^* \Delta\zeta_i^p,
\end{aligned} \tag{7.36}
$$

to express Eq. 7.31 in indicial notation as,

$$I_0 = I_0^* + \overline{\Delta\chi_{ij}^m \Delta\mu_j^m} - \overline{\Delta\zeta_i^m \Delta T^m} + \Delta c_i^{m,*} \Delta\eta_m, \tag{7.37}$$

with m and j being the indices representing phases and components respectively, which are summed over. The second term in the RHS of Eq. 7.30, being only a second-order correction to the interfacial liquid composition is assumed to be a function of $1/\eta_p$ only, with all the other quantities evaluated at the conditions prevailing at the eutectic. This simplifying assumption is necessary to maintain tractability of the equations. Thus, writing,

$$\begin{aligned} f_i = f_i^* \Big(& P_1(\eta_1^*, \cdots, \eta_N^*), \cdots, P_r(\eta_1^*, \cdots, \eta_N^*), \\ & \overline{\Delta c_i^{1,*}}, \cdots, \overline{\Delta c_i^{N,*}} \Big), \end{aligned} \tag{7.38}$$

we re-write the linearized version of Eq. 7.30 indicially, as,

$$\begin{aligned} & \overline{c_i^{pl}} = c_i^{pl,*} + \chi_{ij}^l \overline{\Delta\mu_j^p} - \zeta_i^l \overline{\Delta T^p} = \\ & c_i^\infty + \Big[I_0^* + \overline{\Delta\chi_{ij}^m \Delta\mu_j^m} - \overline{\Delta\zeta_i^m \Delta T^m} \\ & + \Delta c_i^{m,*} \Delta\eta_m \Big] + \left[\left(\frac{\lambda}{\eta_p^*} - \frac{\lambda}{\eta_p^{*2}} \Delta\eta_p \right) \tilde{f}_i \right], \end{aligned} \tag{7.39}$$

where,

$$\tilde{f}_i = \frac{f_i^*}{l_i}, \tag{7.40}$$

and, p is the index which represents a particular solid phase and is not summed over in Eq. 7.39 as well as in the following equations. The quantities enclosed in square brackets in the RHS of Eq. 7.39 represent expressions obtained by linearizing the individual terms in the RHS of Eq. 7.30. Eq. 7.39 can be re-written to express the diffusion potentials as a function of the interfacial undercoolings and solid phase volume fractions as,

$$\begin{aligned} & \left[\chi_{ij}^l - \overline{\Delta\chi_{ij}^p} \right] \overline{\Delta\mu_j^p} - \overline{\Delta\chi_{ij}^{m'} \Delta\mu_j^{m'}} = \\ & \left(c_i^\infty + I_0^* + \frac{\lambda}{\eta_p^*} \tilde{f}_i - c_i^{pl,*} \right) \\ & - \overline{\Delta\zeta_i^{m'} \Delta T^{m'}} - \left(\overline{\Delta\zeta_i^p} - \zeta_i^l \right) \overline{\Delta T^p} \end{aligned}$$

$$+ \Delta c_i^{m',*} \Delta\eta_{m'} + \left(\Delta c_i^{p,*} - \frac{\lambda}{\eta_p^{*2}} \tilde{f}_i \right) \Delta\eta_p, \tag{7.41}$$

where, a summation over the index m' runs from $1, \cdots, N$ leaving out p. So, Eq. 7.41 represents a system of $N(K-1)$ equations which relates the $N(K-1)$ $\overline{\Delta\mu_i^p}$'s to $\Delta\eta_p$'s and $\overline{\Delta T^p}$'s. To describe this dependence, we utilize the linearity of Eq. 7.41 to write an explicit relation of the form,

$$\overline{\Delta\mu_i^p} = \overline{R_i^p} + R_i^{p,T^m} \overline{\Delta T^m} + R_i^{p,\eta_m} \Delta\eta_m, \tag{7.42}$$

where, $\overline{R_i^p}$, R_i^{p,T^m}, and R_i^{p,η_m} are coefficients determined by solving Eq. 7.41 with m being the lone index which is summed over in Eq. 7.42. These relationships will enable the elimination of $\overline{\Delta\mu_i^{pl}}$ completely from the expressions of the undercoolings ahead of every solid phase given in Eq. 7.16. Substituting Eq. 7.42 into Eq. 7.37 we write in the indicial notation,

$$\begin{aligned} I_0 &= I_0^* + \overline{\Delta\chi_{ij}^m} \left(\overline{R_j^m} + R_j^{m,T^v} \overline{\Delta T^v} + R_j^{m,\eta_v} \Delta\eta_v \right) \\ &\quad - \overline{\Delta\zeta_i^m \Delta T^m} + \Delta c_i^{m,*} \Delta\eta_m, \\ &= \left(I_0^* + \overline{\Delta\chi_{ij}^m} \overline{R_j^m} \right) + \left(\overline{\Delta\chi_{ij}^m} R_j^{m,T^v} \overline{\Delta T^v} - \overline{\Delta\zeta_i^m \Delta T^m} \right) \\ &\quad + \left(\overline{\Delta\chi_{ij}^m} R_j^{m,\eta_v} \Delta\eta_v + \Delta c_i^{m,*} \Delta\eta_m \right), \end{aligned} \tag{7.43}$$

where v is an index running over the phases $1, \cdots, N$ and is summed over along with the other phase index m. The index j denoting the components is also summed over while i continues to represent a particular component. Terms of similar character are collected within the parentheses in Eq. 7.43.

The resulting set of equations in 7.16 (N in number) are then solved for the $2N$ unknowns in $\overline{\Delta T^p}$ and $\Delta\eta_p$ under the constraints of equality of undercoolings ahead of the solid phases given by Eq. 7.18 ($N-1$ in number) and the sum of the volume fractions of the solid phases adding up to unity in Eq. 7.19. Substituting Eq. 7.13 into Eq. 7.16, we obtain, in Einstein's notation, without summing over p, but summing over i,

$$\begin{aligned} \overline{\Delta T^p} &= m_i^p \left(c_i^{l,*} - \overline{c_i^{pl}} \right) + \Gamma_p \overline{\kappa_p} \\ &= m_i^p \left[c_i^{l,*} - \left(c_i^\infty + I_0 + \frac{\lambda}{\eta_p} \tilde{f}_i \right) \right] \\ &\quad + \Gamma_p \overline{\kappa_p}. \end{aligned} \tag{7.44}$$

Linearizing the RHS of the above equation about equilibrium quantities and employing Eq. 7.43 leads to,

$$\begin{aligned}\overline{\Delta T^p} = &\left[m_i^p\left(c_i^{l,*} - \left(c_i^\infty + I_0^* + \overline{\Delta\chi_{ij}^m R_j^m} + \frac{\lambda}{\eta_p^*}\tilde{f}_i\right)\right)\right.\\ &\left.+\Gamma_p\overline{\kappa_p^*}\right]\\ &-\left[m_i^p\left(\overline{\Delta\chi_{ij}^m}R_j^{m,T^v}\overline{\Delta T^v} - \overline{\Delta\zeta_i^m\Delta T^m}\right)\right]\\ &-\left[m_i^p\left(\overline{\Delta\chi_{ij}^m}R_j^{m,\eta_v}\Delta\eta_v + \Delta c_i^{m,*}\Delta\eta_m\right.\right.\\ &\left.\left.-\frac{\lambda}{\eta_p^{*2}}\tilde{f}_i\Delta\eta_p\right) + \frac{\Gamma_p\overline{\kappa_p^*}}{\eta_p^*}\Delta\eta_p\right],\end{aligned} \tag{7.45}$$

where κ_p^* is obtained by evaluating Eq. 7.17 for η_p^*. The three terms each enclosed in square brackets in the RHS of the above equation contain the constants, and the terms linear in $\overline{\Delta T^m}$ and $\Delta\eta_m$ respectively. We now impose Eq. 7.18 on Eq. 7.45 to re-express it in terms of $\overline{\Delta T}$ and $\overline{\Delta\eta_p}$'s, as follows,

$$\begin{aligned}&\left[1 + m_i^p\left(\overline{\Delta\chi_{ij}^m}\sum_{v=1}^{N}R_j^{m,T^v} - \sum_{m=1}^{N}\overline{\Delta\zeta_i^m}\right)\right]\overline{\Delta T}\\ &+\left[m_i^p\left(\overline{\Delta\chi_{ij}^m}R_j^{m,\eta_p} + \Delta c_i^{p,*} - \frac{\lambda}{\eta_p^{*2}}\tilde{f}_i\right)\right.\\ &\left.+\frac{\Gamma_p\overline{\kappa_p^*}}{\eta_p^*}\right]\Delta\eta_p\\ &+\left[m_i^p\left(\overline{\Delta\chi_{ij}^m}R_j^{m,\eta_{v'}} + \Delta c_i^{v',*}\right)\right]\Delta\eta_{v'} =\\ &\left[m_i^p\left(c_i^{l,*} - \left(c_i^\infty + I_0^* + \overline{\Delta\chi_{ij}^m R_j^m} + \frac{\lambda}{\eta_p^*}\tilde{f}_i\right)\right)\right.\\ &\left.+\Gamma_p\overline{\kappa_p^*}\right],\end{aligned} \tag{7.46}$$

where, v' is another phase index running from 1 to N except p and is summed over along with the other phase index m. The component indices i and j are also summed over in Eq. 7.46. At this stage, we will invoke Eq. 7.19 to eliminate $\Delta\eta_N$ from the above set of equations. Now, Eq. 7.46 represents a system of N linear equations containing the same number of unknowns in

$\overline{\Delta T}$ and $\Delta\eta_1, \cdots, \Delta\eta_{N-1}$. Solving Eq. 7.46 to compute $\overline{\Delta T}$ and $\Delta\eta_1, \cdots, \Delta\eta_{N-1}$, enables the calculation of $\overline{\Delta\mu_j^1}, \cdots, \overline{\Delta\mu_j^N}$ from Eq. 7.42. Thereafter, the phase compositions can be directly obtained from Eqs. 7.20 and 7.21.

To summarize, our analytical method involves the following steps:

- For every solid-liquid equilibrium in a single period of the eutectic, the solid and the liquid compositions averaged over their corresponding lamellar widths are expressed as linear functions of the corresponding changes in diffusion potentials and undercoolings.
- We also determine the average composition in the liquid in equilibrium with the different solid phases from the Jackson-Hunt type analysis involving the superposition of multiple Fourier modes, which is again linearized about the chosen eutectic point to obtain the liquid compositions as functions of changes in diffusion potentials, undercoolings and changes in solid phase volume fractions. This also involves expressing the boundary layer compositions in terms of the departure of diffusion potentials and phase fractions from their corresponding values at the eutectic temperature along with the undercooling at the solid-liquid interface.
- Using the equality of the liquid compositions obtained from the earlier steps we derive expressions of the diffusion potentials as functions of undercoolings and changes in solid phase fractions.
- Substituting for the liquid compositions using the linearized version of the Fourier series representation in terms of undercoolings, diffusion potentials and solid phase fractions into the expressions of the undercoolings at each solid-liquid interface, and enforcing the isothermal nature of the interface we compute the magnitude of the interfacial undercooling and solid phase fractions.
- Phase compositions get automatically determined due to their explicit and implicit (due to diffusion potentials) dependence on undercooling alongside their dependence on solid phase fractions.

A point to note over here is while Eq. 7.42 relates the deviations of the diffusion potentials $\overline{\Delta\mu_i^p}$ with the deviations of the solid fractions and the undercoolings, one can additionally invoke the condition of local thermodynamic equilibrium at the interface (including curvature) and thereby eliminate the undercoolings from the relation in Eq. 7.42. A similar approach has been used by Senninger and Voorhees [43]. We have tried this out as well and the results from both approaches are comparable. This completes our theoretical derivation of generic

multi-component multi-phase eutectic growth. In the following section, we validate our theory against phase-field simulations of invariant and mono-variant eutectic growth. The phase-field model used for benchmarking our analytical results is the Grand-Potential model proposed by [200, 151], with the driving forces assumed to be parabolic functions of diffusion potentials. The concerned formulations are described in details in Chapter 3. We begin with the study of a monovariant eutectic growth problem.

7.2 Results: Two-solid phases in a ternary system

In this section we employ both the analytical and phase-field models described above to study the solidification of two solid phases in a ternary alloy and compare the predictions from these two techniques for different solute interdiffusivities in the liquid. Although, the analytical theory and phase field model are general enough to describe the solidification at off-eutectic compositions, we restrict our study to eutectic compositions only.

The solid phases in the ternary monovariant eutectic are anointed as α and β with the independent components constituting the ternary alloy being A and B. All our studies assume negligible solute diffusivity in the solid compared to the liquid. We will first consider a model alloy whose solid compositions are symmetrically located with respect to that of the liquid and follow it up with a similar study of a monovariant eutectic reaction in the Ni-Al-Zr alloy system.

7.2.1 Calculation of η_α^* and η_β^*

A three phase equilibrium (α, β and liquid) in a ternary system is associated with a single degree of freedom as it can exist over a range of temperatures. During directional solidification, the far-field liquid composition can be found to correspond to a particular temperature (T^*) in the equilibrium phase diagram at which it is in equilibrium with two other solid phases. If such a liquid is assumed to solidify at this temperature, the volume fractions of the resultant α and β phases are what we refer to as η_α^* and η_β^*, respectively. As there are two independent far-field compositions in a ternary system, we invoke two artificial phase fractions η'_α and $\eta'_\beta \neq (1-\eta'_\alpha)$ to solve for,

$$\begin{aligned} c_A^\infty &= c_A^\alpha \eta'_\alpha + c_A^\beta \eta'_\beta, \\ c_B^\infty &= c_B^\alpha \eta'_\alpha + c_B^\beta \eta'_\beta, \end{aligned} \tag{7.47}$$

c_A^α	0.74
c_B^α	0.18
c_A^β	0.18
c_B^β	0.74
c_A^{liquid}	0.36
c_B^{liquid}	0.36
m_A^α	0.45
m_B^α	0.0
m_A^β	0.0
m_B^β	0.45
G	0.0005
V	0.01

Table 7.2: Table depicting all the material parameters

consistently. In general, $\eta'_\alpha + \eta'_\beta \neq 1$ and we compute the normalized volume fractions,

$$\eta^*_\alpha = \frac{\eta'_\alpha}{\eta'_\alpha + \eta'_\beta},$$
$$\eta^*_\beta = \frac{\eta'_\beta}{\eta'_\alpha + \eta'_\beta}, \tag{7.48}$$

obeying $\eta^*_\alpha + \eta^*_\beta = 1$ and serving as values of the volume fractions about which linearization is performed.

7.2.2 Model symmetric system

To isolate and understand the effect of differences in solute diffusivities on the eutectic growth dynamics, we select a system where the equilibrium phase compositions of solid phases are symmetric with respect to the liquid composition (see Table. 7.2). Also, as this is a model system, we consider arbitrary non-dimensional model parameters for different properties of the phase diagram like the liquidus slopes, which are chosen to be consistent with this symmetry, (see Table. 7.2) as well as the thermodynamics related to the free-energy densities of the phases. Also, all quantities having dimensions of length can be understood in the context of the diffusion length $2D_{ii}/V = 400$, (corresponding to $D_{AA} = D_{BB} = 2.0$) and the width of the diffuse interface in the phase-field simulations, which is ≈ 15.

The phase compositions are denoted by c_i^p, and the liquidus slopes by m_i^p where $i = A, B$ and $p = \alpha, \beta, liquid$. G denotes the thermal gradient and V the pulling velocity.

7. THEORETICAL AND NUMERICAL INVESTIGATION OF MULTI-PHASE GROWTH IN A MULTI-COMPONENT SYSTEM

We begin with the study of a system with identical α-liquid and β-liquid interfacial energies which serves as a reference when we attempt to understand the dynamics of systems displaying dissimilar interfacial energies of the eutectic solids with liquid.

Equal α-liquid and β-liquid interfacial energies

The equality of α-liquid and β-liquid interfacial energies leads to $\theta_{\alpha\beta} = \theta_{\beta\alpha} = 30°$with the Gibbs-Thomson coefficients computed to be $\Gamma_\alpha = \Gamma_\beta = 0.77$ for the particular thermodynamics employed. We present analytically calculated variations of interfacial undercoolings (ΔT), solid phase volume fractions (η_α) and compositions of the α and the β phases with scaled lamellar widths (λ) in Figs. 7.2 and 7.3 and compare them against predictions obtained from phase field simulations. The diffusion lengths given by $2D/V$ is used to scale the lamellar widths, D corresponds to the maximum among the solute diffusivities. It is important to describe the process of extracting the different quantities of interest from phase-field simulations at this point, which is common to all the plots in this chapter containing simulation data. The undercooling at each point on the interface are determined by their location in the imposed temperature field which are then averaged to yield the average undercooling at the interface ΔT. The phase-fields ϕ_p corresponding to one of the solid phases indicate the local volume fraction of the same at a particular grid point. Hence, a ratio of the sum of the phase field representing a particular solid phase p over the entire domain to the sum of all the phase-fields representing solid phases over the same domain is a measure of the solid phase fraction of p denoted by η_p (in short, $\eta_p = \sum_\Omega \phi_p / \sum_\Omega \sum_{m \in solid} \phi_m$, Ω refers to the simulation domain). The compositions of a solid phase p are determined by averaging over the compositions from every grid point belonging to the solid (given by $\phi_p = 1$).

As can be seen from Fig. 7.2(a), the analytical and phase-field calculations are in very good agreement as far as the predictions in λ_{min} (the lamellar width corresponding to the minimum in ΔT) are concerned. The close agreement between the analytical theory and the phase field simulations are also evident from the variations of η_α versus λ presented in Fig. 7.2(b) and the variation of the average solid phase compositions in Fig. 7.3. The deviations of analytically computed values of ΔT (in Fig. 7.2(a)) from those obtained from phase field simulations can be attributed to the inherent assumptions in the Jackson-Hunt calculations, where a planar interface is used to approximate the diffusion-field ahead of the solid interfaces, which are in reality curved for a system with isotropic surface energies. This mismatch has also been shown before [148], and a concomitant comparison of the phase-field method with calculations based on the boundary-integral method have proved that the predictions of the phase-field

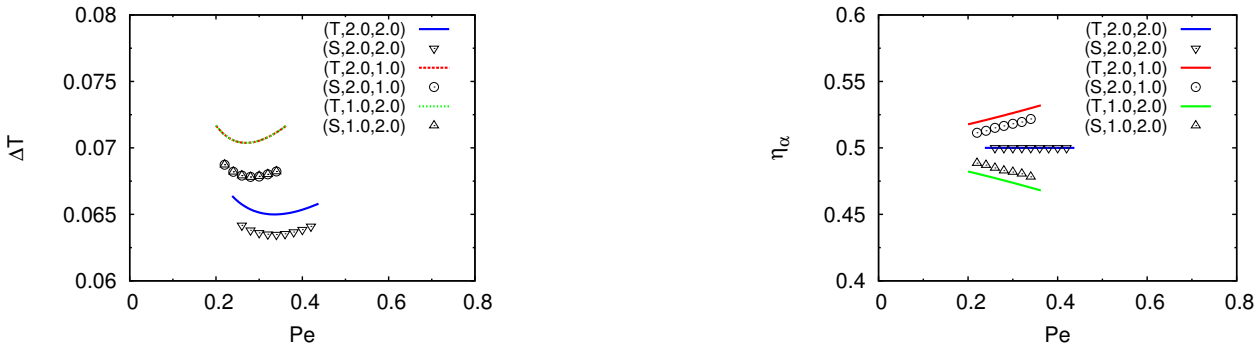

Figure 7.2: Plots showing variations of (a)ΔT, and, (b) η_α, with Peclet number $Pe = \lambda V/2D$, during two phase growth in a model symmetric ternary alloy. The pulling velocity is $V = 0.01$ and D is taken to be the largest solutal interdiffusivity and is set at 2. The first position in the figure legends in (a) and (b) indicates whether the plotted data comes from theory (T) or simulations (S); the second and third positions represent values of D_{AA} and D_{BB} respectively.

method are more accurate in this regard. Fig. 7.3 also reflects that although the trends in the composition variations derived from the analytical calculations are captured well in the phase-field simulations, the differences in magnitude of the errors are dependent on the magnitude of asymmetry in the problem. A discussion on this particular aspect can be appreciated in the later discussion on the limitations of the analytical calculations. Additionally deriving the average interfacial compositions from the phase-field simulations is error prone, due to which we see larger errors in the average compositions than in the corresponding volume fractions.

From Fig. 7.2(a), it can be seen that lowering either of the solute diffusivities leads to a reduction in the length scale of the eutectic (λ_{min}) with a consequent rise in ΔT. This is a result of a lowered effective diffusivity leading to a lower effective diffusion length. As a reflection of the inherent symmetry in the system, the theoretical calculations for ΔT vs λ are exactly identical for $D_{AA} = 2.0, D_{BB} = 1.0$ and $D_{AA} = 1.0, D_{BB} = 2.0$.

For equal solute diffusivities the volume fractions of the eutectic solids are the same, but Fig. 7.2(b) reveals that for $D_{AA} = 2.0, D_{BB} = 1.0$, α phase occupies a larger solid fraction ($\eta_\alpha > 0.5$) of the lamellar width (λ); the same observation being valid for β when $D_{AA} = 1.0, D_{BB} = 2.0$.

Physically, the change in the volume fractions can be seen as a consequence of asymmetric changes in the constitutional undercooling at each solid-liquid interface. Starting from a purely symmetric state with equal volume fractions, a situation of higher D_{AA} in comparison to D_{BB}

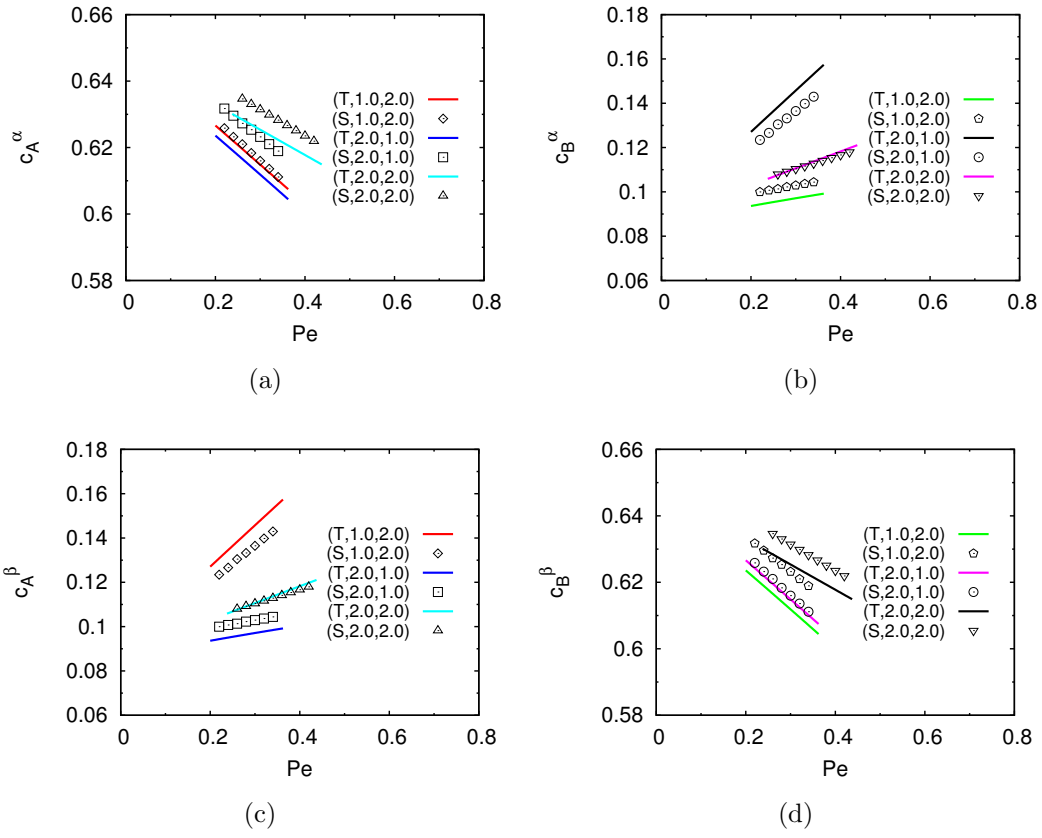

Figure 7.3: Plots showing variations of phase concentrations, (a)c_A^α, (b) c_B^α, (c) c_A^β and (d) c_B^β, with Peclet number $Pe = \lambda V/2D$, during two phase growth in a model symmetric ternary alloy. The values of V and D are the same as described in the caption to Fig. 7.2. The figure legends can be interpreted in the same way as described in the caption of Fig. 7.2.

would result in a lower undercooling ahead of the $\alpha - l$ interface than the $\beta - l$ interface. To recover an isothermal situation between the two interfaces, would require the $\alpha - l$ interface to assume an interfacial curvature that is greater than that acquired by the $\alpha - l$ interface when mechanical equilibrium is maintained at the trijunction. This departure from equilibrium acts as a driving force, where mechanical equilibrium is re-established through an increase in the volume fractions of the phase α. This explains the observed variation of η_α with λ in Fig. 7.2(b). A similar argument can be made with respect to the lowering of the value of D_{AA} with respect to D_{BB} (see Fig. 7.2(b)), where it must be noted that as a consequence of the underlying symmetry in the system that the η_α vs λ curve for $D_{AA} = 1.0, D_{BB} = 2.0$ can be reflected about the $\eta_\alpha = 0.5$ line to obtain the variation for $D_{AA} = 2.0, D_{BB} = 1.0$. In general, any change(change in diffusivity, interfacial energies etc.) which causes an increase in the undercooling of a particular phase-liquid interface would need to be offset through an appropriate decrease in the interfacial curvature which can be affected only through a departure of the angles at the triple-point to lower values than that exists at equilibrium, keeping the same phase fractions. This departure acts as a driving force to establish equilibrium which is achieved by a decrease in the volume fraction of this phase.

Model system with unequal α-liquid and β-liquid interfacial energies

Here we probe the effect of unequal surface energies on the steady-state monovariant eutectic growth dynamics while retaining the symmetry in the phase compositions and the liquidus slopes from the model system just discussed. The thermal gradient G and the sample pulling velocity V are also kept to be the same as in the previous section. The interfacial energies are so chosen such that $\theta_{\alpha\beta} = 30^\circ$and $\theta_{\beta\alpha} = 45^\circ$with the Gibbs-Thomson coefficients being $\Gamma_\alpha = 0.77$ and $\Gamma_\beta = 0.94$. Fig. 7.4 shows the variation in ΔT and η_α, while, Fig. 7.5, depicts the variation in solid phase compositions with λ obtained from both analytical and phase field calculations.

The variation of ΔT with λ reported in Fig. 7.4(a) presents a departure from the symmetry observed in Fig. 7.2(a) as the curves corresponding to $D_{AA} = 2.0, D_{BB} = 1.0$ and $D_{AA} = 1.0, D_{BB} = 2.0$ do not overlap. This is a consequence of the dissimilar energies of the two eutectic solid-liquid interfaces. However, the variation of the phase compositions, minimum undercooling spacings and the variation of the undercoolings are similarly captured by the simulations and the theoretical calculations.

Furthermore, while the trends in the variation of the η_α with λ are effectively captured for all the cases, the magnitude of variation between the simulations and theory is larger than the previous simulations with the symmetric interface properties. The reason for this is the

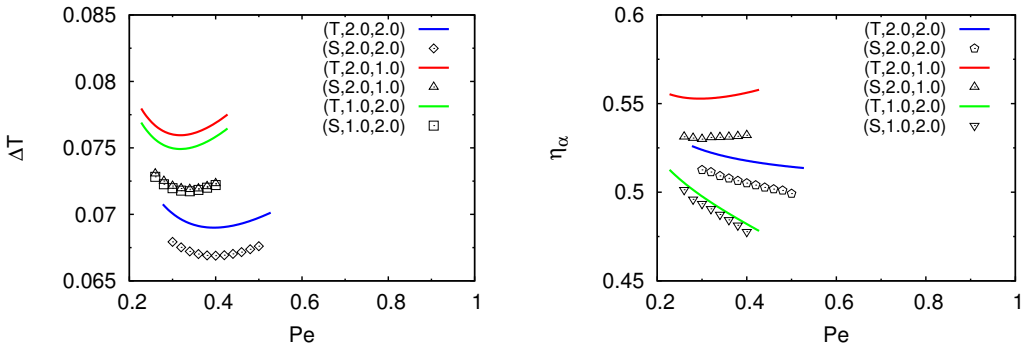

(a) (b)

Figure 7.4: Plots showing variations of (a)ΔT, and, (b) η_α, with Peclet number $Pe = \lambda V/2D$, during two phase eutectic growth in a model symmetric ternary alloy with unequal interfacial energies. The values of V and D are the same as described in the caption to Fig. 7.2. The figure legends can be interpreted in the same way as described in the caption of Fig. 7.2.

asymmetric nature of the interface shapes, where in the phase-field simulation the $\beta-l$ interface is ahead of the $\alpha-l$ interface (see Fig.7.6) and thereby clearly the interfacial undercoolings of the two phases are not the same. Additionally, the departure from a planar interface is higher for the $\beta-l$ interface compared to the $\alpha-l$ interface, which also implies that this brings in added asymmetry with respect to a mismatch with the analytical calculations which are performed for a planar interface. Thereby, now any change in the interface shape which reduces the curvature of the $\beta-l$ interface decreases the disparity between the analytical calculations and phase-field simulations and additionally with increasing curvature differences between the $\alpha-l$ and $\beta-l$ interfaces, the discrepancies between the theoretical predictions and simulation results also increases. Thus, this brings to light a limitation of the analytical calculations, which work best when interfacial shapes of the solid-liquid interfaces are similar.

7.2.3 Ni-Al-Zr alloy system

In this section, we study the steady-state dynamics of monovariant eutectic growth in a Ni-Al-Zr alloy at the backdrop of the insights developed in the previous section. Our calculations are performed using non-dimensionalized numbers. The non-dimensionalization of the dimensional numbers are carried out by scaling them using the characteristic length scale (l^*), time scale (t^*) and energy scale (f^*), computed as,

$$f^* = \frac{RT^*}{V_m}, \tag{7.49}$$

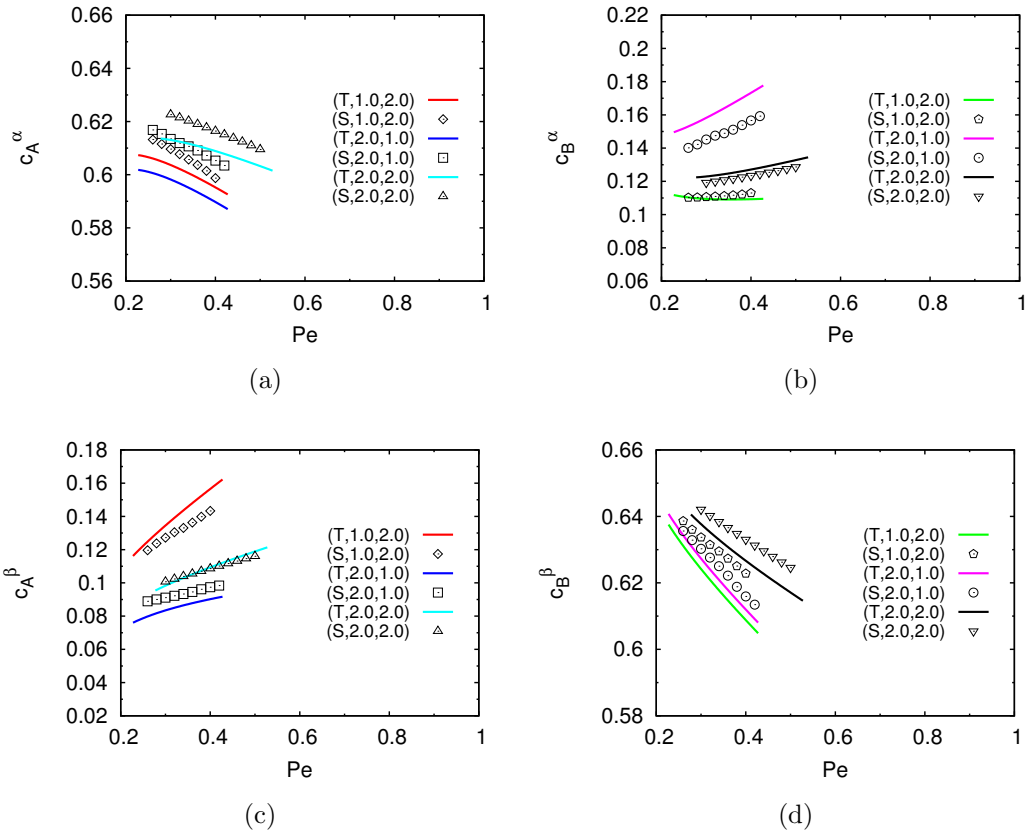

Figure 7.5: Plots showing variations of phase concentrations, (a)c_A^α, (b) c_B^α, (c) c_A^β and (d) c_B^β, with Peclet number $Pe = \lambda V/2D$, during two phase eutectic growth in a model symmetric ternary alloy with unequal interfacial energies. The values of V and D are the same as described in the caption to Fig. 7.2. The figure legends can be interpreted in the same way as described in the caption of Fig. 7.2

.

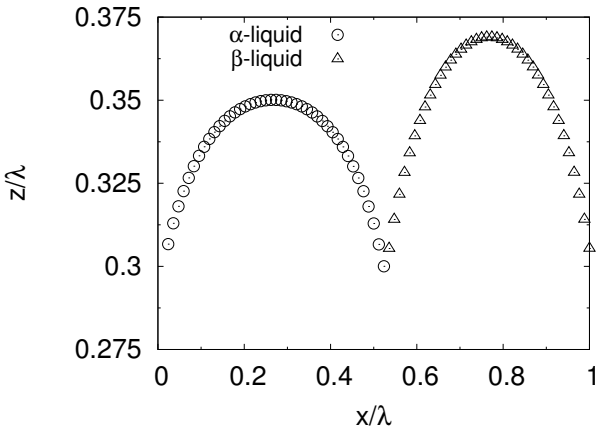

Figure 7.6: Plot showing the locations of the $\alpha - l$ and the $\beta - l$ interfaces in the system with unequal $\alpha - l$ and $\beta - l$ interfacial energies with $D_{AA} = D_{BB} = 2.0$.

$$l^* = \frac{\sigma^*}{f^*}, \tag{7.50}$$

$$t^* = \frac{l^{*2}}{[D_{ij}]^*}. \tag{7.51}$$

The scale of the diffusivity for the alloys used in our study is $[D_{ij}]^* = 1.0\ 10^{-9}\ m^2/s$, and, the molar volumes are given by, $V_m = 10.0\ 10^{-6}\ m^3/mol$. The temperature scale is set by the liquidus slope, $\partial T/\partial c_{Al} = -3000K$ corresponding to the Ni_7Zr_2 phase. The second-derivatives of free energies w.r.t composition are treated as constants. The surface tension is taken to be $\sigma^* = 1.0 J/m^2$. The equilibrium phase compositions at the temperature of interest are: $c_A^\alpha = 0.67, c_B^\alpha = 0.32, c_A^\beta = 0.74, c_B^\beta = 0.0034, c_A^l = 0.69, c_B^l = 0.19$ with the liquidus slopes being $m_A^\alpha = 0.37, m_B^\alpha = 1.08, m_A^\beta = -0.07, m_B^\beta = -1.0$. The Gibbs-Thomson coefficients are $\Gamma_\alpha = 1.13, \Gamma_\beta = 0.81$ with the contact angles $\theta_{\alpha\beta} = \theta_{\beta\alpha} = 30°$. The non-dimensional thermal gradient (G) and the sample pulling velocity (V) both have the same value as reported in the sections on model alloys which when converted back to the dimensional setting, yields $V = 0.025 m/s$ and $G = 3.75\,10^9 K/m$. We present the variations in ΔT and η_α in Fig. 7.7 while the corresponding variations in solid phase compositions are presented in Fig. 7.8.

From all the diffusivity combinations studied it can be said that the equilibrium phase compositions and the liquidus slopes are such that a higher volume fraction of α is the preferred morphology. Furthermore, it can be seen from Figs. 7.7(a) and 7.7(b), that the dynamics is much more sensitive to a change in D_{BB} compared to a change in D_{AA}. The undercoolings are found to be much higher for $D_{AA} = 2.0, D_{BB} = 1.0$ than for the other two situations studied, with an accompanied shift in length scales (λ_{min}) towards smaller values. Also, η_α displays a

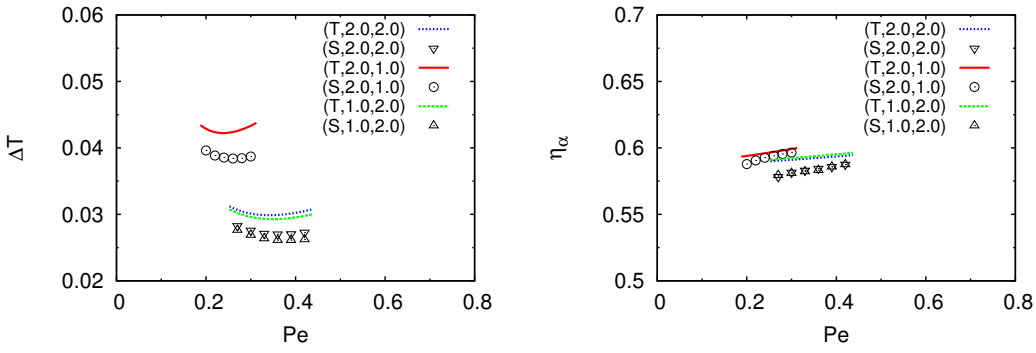

(a) (b)

Figure 7.7: Plots showing variations of (a)ΔT, and, (b) η_α, with Peclet number $Pe = \lambda V/2D$, during two-phase growth in a Ni-Al-Zr alloy. The values of V and D are the same as described in the caption to Fig. 7.2. The figure legends can be interpreted in the same way as described in the caption of Fig. 7.2.

steady rise with λ which is much steeper for $D_{AA} = 2.0, D_{BB} = 1.0$ compared to the other two diffusivity configurations studied. The variations of the solid phase compositions are depicted in Fig. 7.8.

7.3 Results: Three phases in a model ternary system

Following up from the previous studies on two-phase mono variant growth, in this section we investigate three-phase invariant growth. Contrary to two-phase growth where there is a single possibility for the lamellar arrangement of the phases, for the case of three-phase growth there exist infinitely many configurations (e.g., $\alpha\beta\gamma, \alpha\beta\alpha\gamma \ldots$). In the following discussion, we consider two such possibilities for study, using both analytical calculations and phase-field simulations. Here, we conduct simulations for the different choices of the diffusivity matrices and compare the predictions of the phase compositions and the volume fractions between the phase-field simulations and the theoretical predictions. The equilibrium phase compositions at the temperature of the invariant eutectic alongwith the liquidus slopes are presented in Table. 7.3. The Gibbs-Thomson coefficients are $\Gamma_\alpha = \Gamma_\beta = \Gamma_\gamma = 1.558$ with the contact angles $\theta_{\alpha\beta} = \theta_{\beta\alpha} = \theta_{\beta\gamma} = \theta_{\gamma\beta} = \theta_{\alpha\gamma} = \theta_{\gamma\alpha} = 30°$. The directional solidification conditions are kept the same as in the study of monovariant eutectic growth in ternary alloys. Again, this being a model system, the non-dimensional parameters reported, can be understood in reference to the diffusion length and the phase-field interface width which remain the same as in the model monovariant eutectic system.

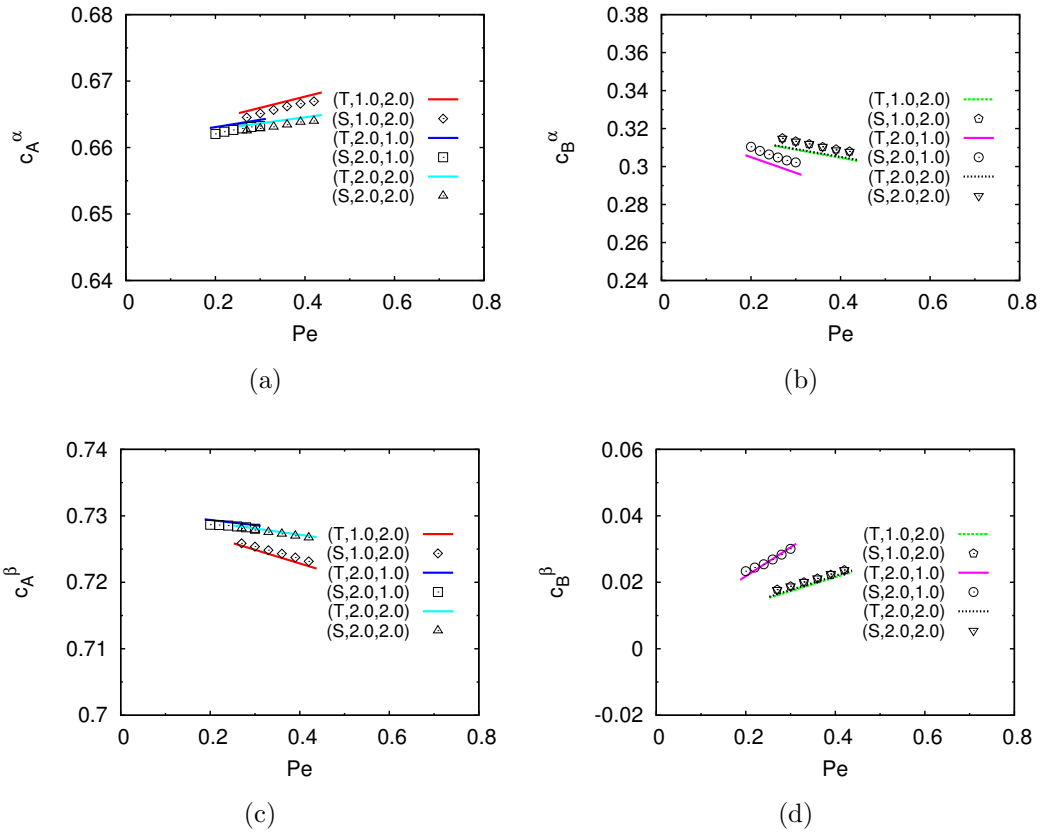

Figure 7.8: Plots showing variations of phase concentrations, (a)c_A^α, (b) c_B^α, (c) c_A^β and (d) c_B^β with Peclet number $Pe = \lambda V/2D$, during two-phase growth in a Ni-Al-Zr alloy. The values of V and D are the same as described in the caption to Fig. 7.2. The figure legends can be interpreted in the same way as described in the caption of Fig. 7.2.

c_A^α	0.706
c_B^α	0.146
c_A^β	0.146
c_B^β	0.706
c_A^γ	0.146
c_B^γ	0.146
c_A^l	0.333
c_B^l	0.333
m_A^α	0.91
m_B^α	0.0
m_A^β	0.0
m_B^β	0.91
m_A^γ	-0.91
m_B^γ	-0.91

Table 7.3: Table depicting all the material parameters

We first consider the simplest arrangement $\alpha\beta\gamma$, where for the case of equal diagonal diffusivities, we get excellent agreement between our theory and phase-field simulation results (see Fig. 7.9), which is reflected not only in the variations of the undercooling with spacing, but also in the compositions of the phases (see Fig. 7.10). The equality of solute diffusivities along with the symmetry of the phase diagram result in the same constitutional undercooling ahead of the $\alpha - liquid$ and the $\beta - liquid$ interfaces, which, in combination with the equal $\alpha - liquid$ and the $\beta - liquid$ interfacial energies, ensure that there is no driving force for a change in the solid phase volume fractions which remain at $(\eta_\alpha, \eta_\beta, \eta_\gamma)$:(1/3,1/3,1/3) for all λ.

However, for the case of unequal diffusivities, an inference from the phase-field simulations can be seen in Fig. 7.11 where we notice a tilt in the lamellar arrangement with respect to the growth direction.

We note that this tilt is not an "instability" that occurs beyond a spacing as has been reported during two and three-phase growth [211, 212], rather is a growth mode that is selected, which has also been found in previous three-phase growth simulations although due to different conditions [157]. The origin of the tilt may be associated with a loss of equality of phase fractions as seen in Fig.7.11(c) which is in contrast to the completely symmetric situation with equal diffusivities. In an earlier paper [39], we discuss that in the completely symmetric phase diagram with equality of all interfacial energies and diffusivities, quasi-symmetry planes may be thought to exist passing through the center of each phase lamella where a reflection operation followed by a phase inversion restores the original configuration. This symmetry is lost with

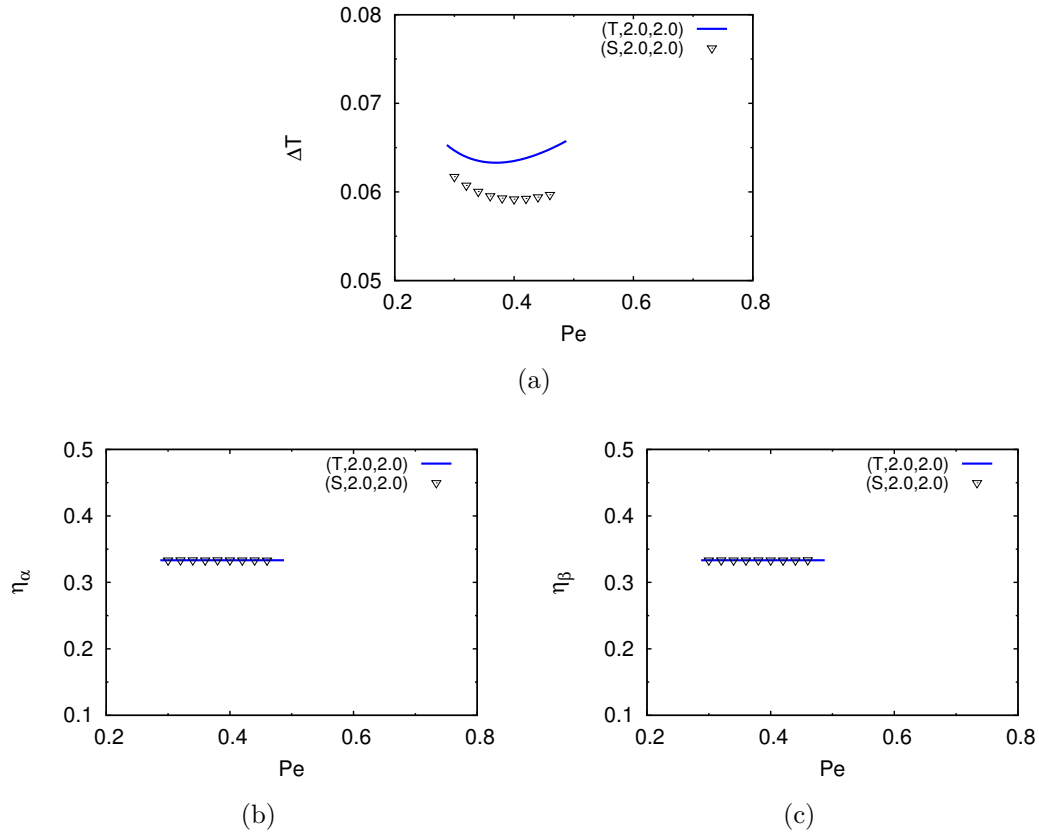

Figure 7.9: Plots showing variations of (a)ΔT, (b) η_α, and (c) η_β, with Peclet number $Pe = \lambda V/2D$, during three phase eutectic growth in a model symmetric ternary alloy. A single wavelength of the eutectic solids has the configuration: $\alpha\beta\gamma$. The values of V and D are the same as described in the caption to Fig. 7.2. The figure legends can be interpreted in the same way as described in the caption of Fig. 7.2.

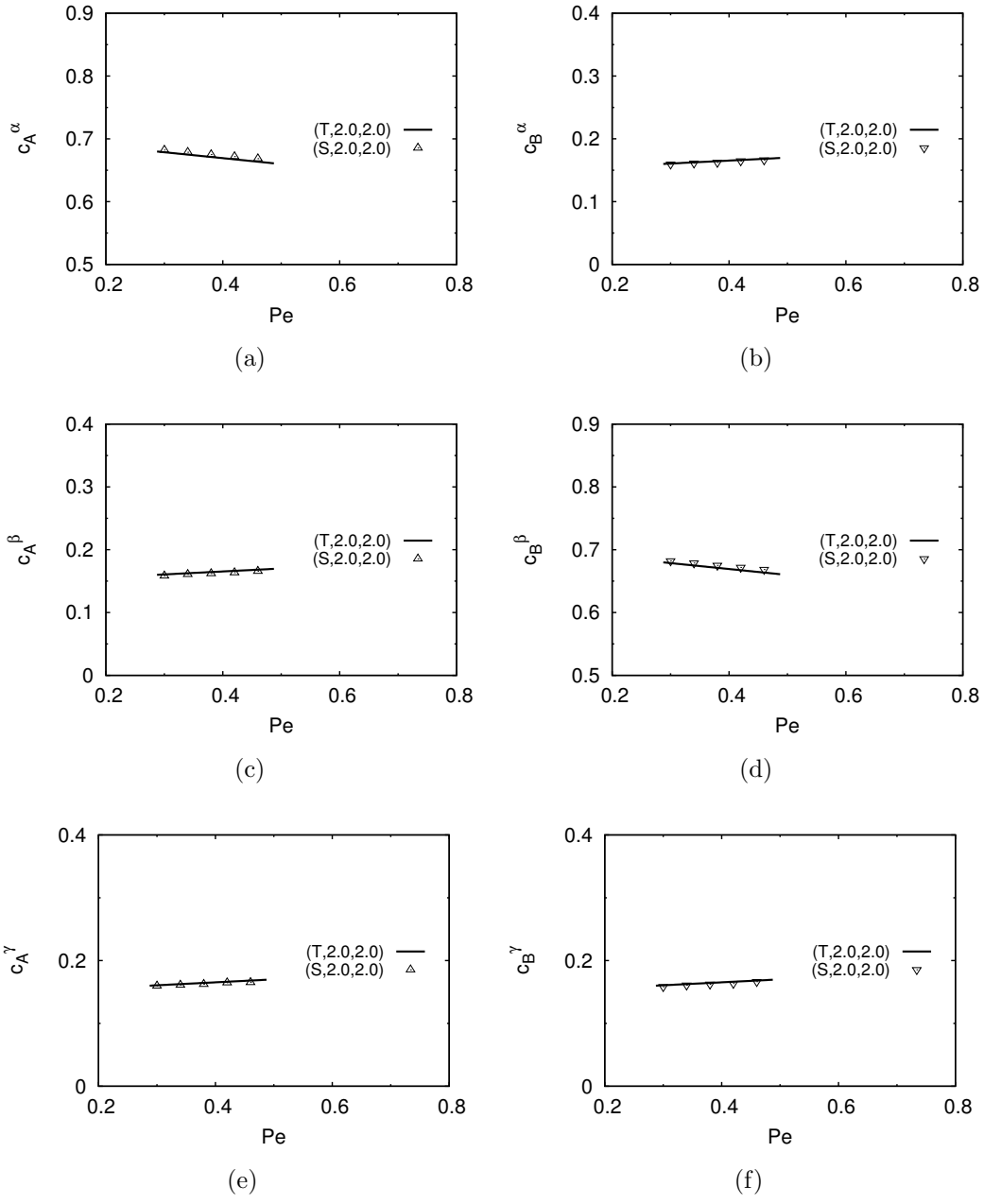

Figure 7.10: Plots showing variations of phase concentrations, (a)c_A^α, (b) c_B^α, (c) c_A^β, (d) c_B^β, (e) c_A^γ, and (f) c_B^γ with Peclet number $Pe = \lambda V/2D$, during three phase eutectic growth in a model symmetric ternary alloy. A single wavelength of the eutectic solids has the configuration: $\alpha\beta\gamma$. The values of V and D are the same as described in the caption to Fig. 7.2. The figure legends can be interpreted in the same way as described in the caption of Fig. 7.2.

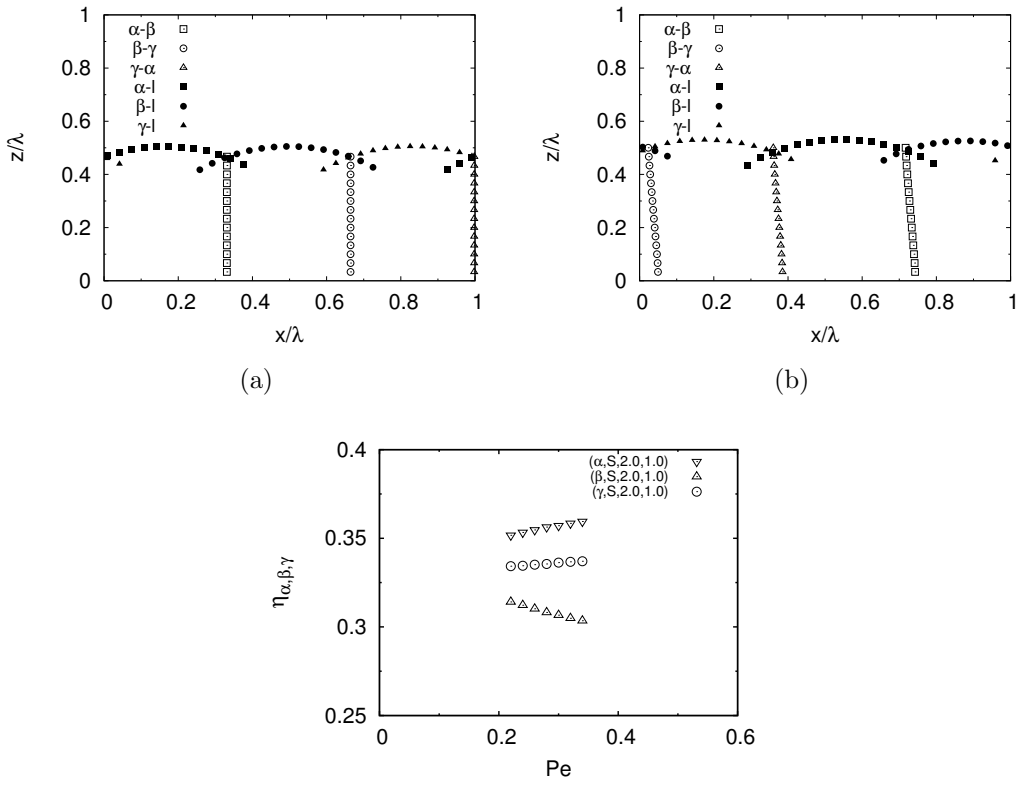

Figure 7.11: Plots showing orientations of all the interfaces for, (a)$D_{AA} = D_{BB} = 2.0$, and (b)$D_{AA} = 2.0, D_{BB} = 1.0$, during three phase eutectic growth in a model symmetric ternary alloy. A single wavelength of the eutectic solids has the configuration $\alpha\beta\gamma$. The differential phase fractions of α, β and γ phases as a function of Peclet number $Pe = \lambda V/2D$, during steady state growth, when $D_{AA} = 2.0, D_{BB} = 1.0$, is depicted in Fig. 7.11(c). The values of V and D are the same as described in the caption to Fig. 7.2

.

the change in the volume fractions, where all three volume fractions become different with the change in the diffusivities (see Fig. 7.11(c)). Clearly, this is a prediction that is impossible to derive from the theoretical calculations that we present in this chapter, and is certainly a limitation of the applicability of such calculations. More elaborately, in order for the theoretical predictions to be effective, one must have the information about the steady-state growth mode that is either derived experimentally, or through simulations.

The next arrangement $\alpha\beta\alpha\gamma$ however, possesses, two mirror axes, passing through the β and the γ phases. Going by the symmetry arguments placed in a previous paper [39], a steady-state growth mode where the lamellae are aligned with the growth direction, is therefore expected. We repeat the simulation and analytical calculations for this configuration for different diffusivities, and the results are reported in Figs. 7.12 and 7.13. It is important to note that for this configuration a short wavelength instability exists which results in the transformation of the $\alpha\beta\alpha\gamma$ to $\alpha\beta\gamma$ occurring below a critical wavelength (see discussion in [39]). Thereby, we limit our analysis to only the stable lamellar states. For these spacings, we again derive an excellent agreement for the undercooling vs spacing variations, volume fractions and the phase compositions, between phase-field simulations and theoretical predictions. Due to the variation in the stability regimes we have limited our calculations for the case of only unequal diffusivities $D_{AA} = 1.0, D_{BB} = 2.0$, as the stability region for the contrary case of $D_{AA} = 2.0, D_{BB} = 1.0$ is very small.

7.4 Limitations of the assumptions in the analytical calculations

In this section, we discuss the potential errors and limitations of the analytical calculations based upon the comparison with results obtained from the phase-field simulations. One of the major assumptions in the analytical calculations is that of equal undercooling at the solid-liquid interfaces, that is required for the closure of the equations. The plots in Figs.7.14(a) and 7.14(b) highlight the differences between the undercoolings along the solid-liquid interfaces and those derived from the analytical calculations. It can readily be seen, that while for the symmetric situation in Fig.7.14(a), the equality of average undercoolings at the two solid interfaces seems quite adequate, the same however cannot be said for the asymmetric situation of unequal diffusivities as seen in the Figs.7.14(b), where the difference between the average undercoolings from the phase-field simulations between the solid phases also varies with the spacings.

Additionally, in Fig.7.14(a), the difference between the magnitude of the undercooling pre-

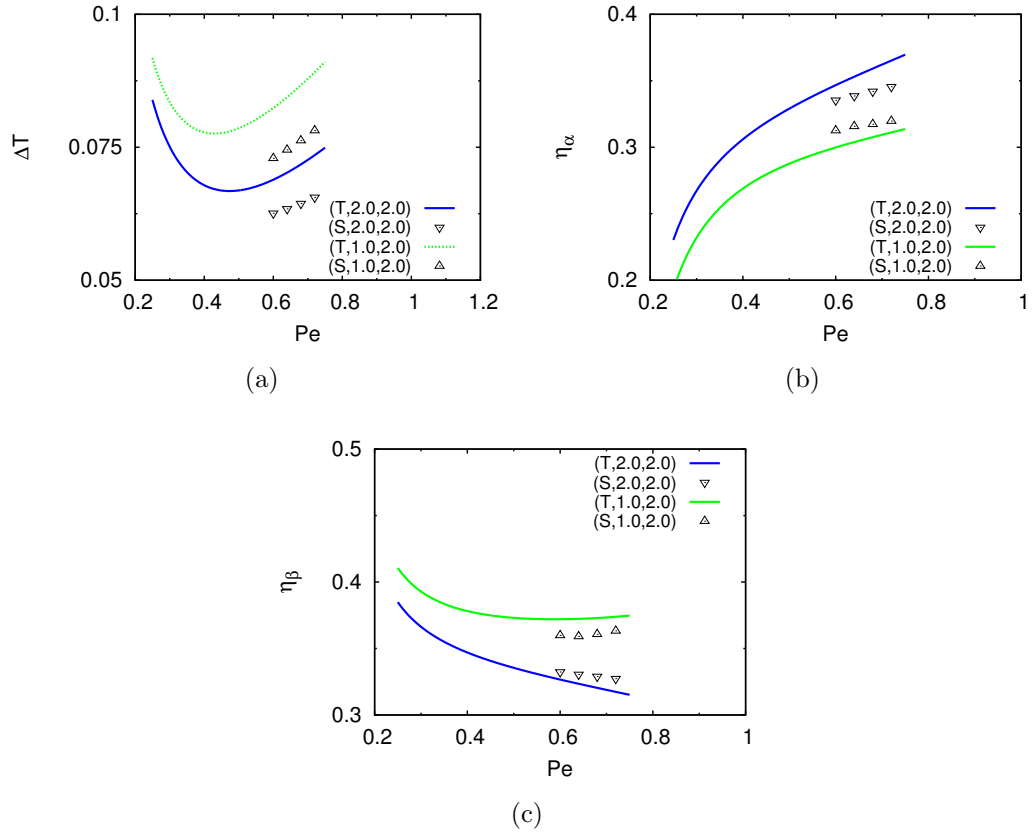

Figure 7.12: Plots showing variations of (a)ΔT, (b) η_α, and (c) η_β, with Peclet number $Pe = \lambda V/2D$, during three phase eutectic growth in a model symmetric ternary alloy. A single wavelength of the eutectic solids has the configuration $\alpha\beta\alpha\gamma$. The values of V and D are the same as described in the caption to Fig. 7.2. The figure legends can be interpreted in the same way as described in the caption of Fig. 7.2.

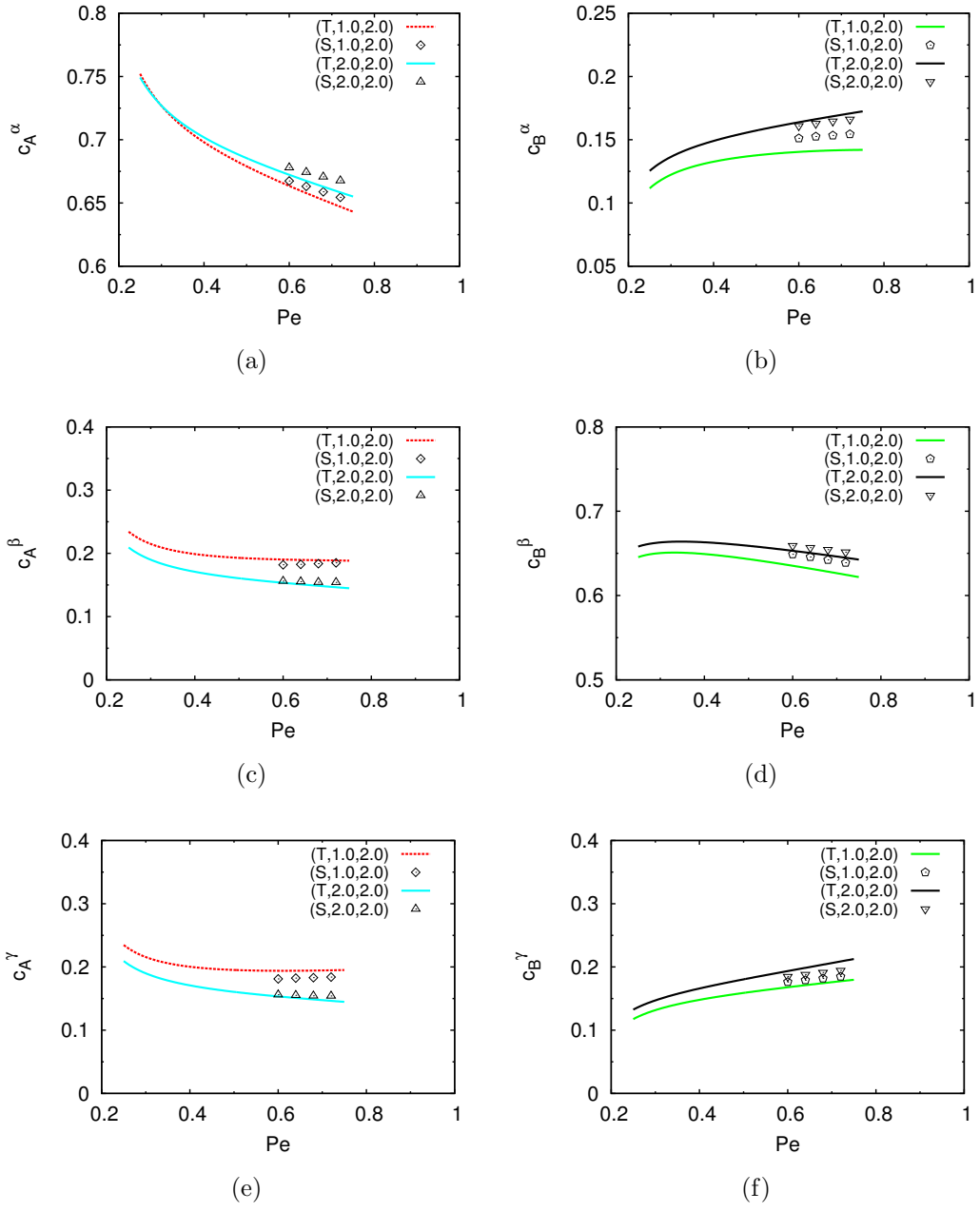

Figure 7.13: Plots showing variations of phase concentrations, (a)c_A^α, (b) c_B^α, (c) c_A^β, (d) c_B^β, (e) c_A^γ, and (f) c_B^γ with Peclet number $Pe = \lambda V/2D$, during three phase eutectic growth in a model symmetric ternary alloy. A single wavelength of the eutectic solids has the configuration: $\alpha\beta\alpha\gamma$. The values of V and D are the same as described in the caption to Fig. 7.2. The figure legends can be interpreted in the same way as described in the caption of Fig. 7.2.

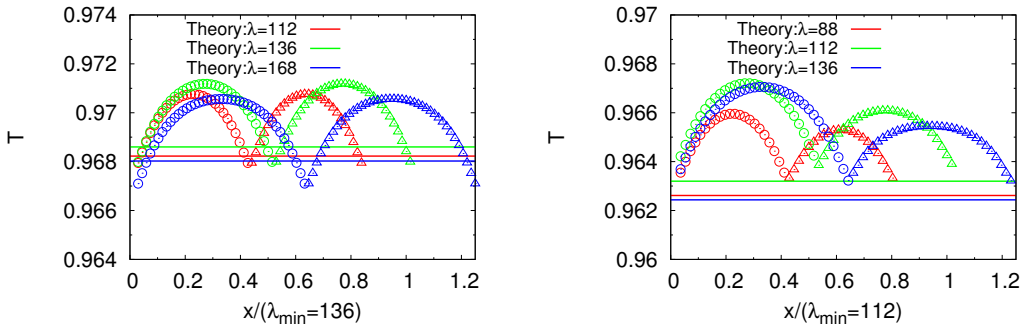

(a) (b)

Figure 7.14: Plots showing temperature variation across the solid-liquid interface, during two-phase growth in a model symmetric alloy, with diffusivities, (a)$D_{AA} = 2.0, D_{BB} = 2.0$, and, (b) $D_{AA} = 2.0, D_{BB} = 1.0$. The three different colors correspond to three different lamellar widths, as described in the figure legend. The open-circles correspond to points on the $\alpha - liquid$ interface while the open-triangles correspond to points on the $\beta - liquid$ interface.

dicted by the phase-field simulation and the analytical calculation can be attributed to the assumption of a planar interface (for the diffusion field) in the theoretical calculations. This error therefore, should become smaller with increase in the spacing, which is also reflected in Fig.7.14(a). For the asymmetric case in Fig.7.14(b), there is an additional effect of change in volume fractions with the change in spacing. As seen from the results in the phase-field simulations the interface shapes of the two solid phases are similar for smaller λ and thereby the error due to the assumption of equal undercoolings of the phases should be the least. With increase in λ, due to the change in the volume fractions, while one of the solid phases moves closer to a planar interface, the converse occurs for the smaller solid phase. Thus, the two assumptions of equal undercoolings of the solid-liquid interfaces and planarity become increasingly non-realistic with increase in the spacing, which is evident from the comparison between the average undercoolings obtained from the analytical calculations and those derived from phase-field simulations. The arguments placed herein, are also valid in explaining the deviations in other asymmetric simulation situations involving different interfacial energies which have been studied in the previous sections. Following this discussion, for ternary three phase eutectics, lamellar units involving multiple appearance of the same phases, e.g., $\alpha\beta\alpha\gamma$, where the α phase fractions are half of the thicknesses of the β and γ phases, and $\alpha\beta\alpha\beta\gamma$, where even the individual α phases may not be of the same width, the assumption of equal undercoolings at the different solid-liquid interfaces is not very appropriate for equal as well as unequal solute diffusivities.

An alternate way to predict the dynamics where we do not invoke the equality of undercoolings at the solid-liquid interfaces, would be to generalize the approach in [166, 165] to multi-phase, multi-component systems. The undercoolings may be expressed as $\Delta T^p = \Delta T^0 - G I^p(x)$, where ΔT^0 is the undercooling at the triple-points, G is the temperature gradient, and $I^p(x)$ is the shape of the interface, x being the direction normal to the growth direction. In this procedure, the equality of undercoolings at the different solid-liquid interfaces is replaced with corresponding relations of the average interface positions which of course require the solution of the interface shapes. This does add to the already complicated analytical calculation procedure outlined in the chapter, but there is certainly scope for some future work in this direction.

The second assumption that we have imposed in our phase-field as well as analytical calculations is the assumption of equal partial molar volume of the components in each of the phases. With respect to experiments, this is certainly restrictive for situations where there is a difference between the molar volumes of the components. Magnin and Trivedi [166] treat one of the influences of having different densities with respect to the change in volume fractions of the phases in binary eutectics. Physically, however different densities would also result in microscopic fluid flow accompanying solidification. While both of these effects can certainly be accounted for in the Stefan problem through a coupling to the hydrodynamic flow equations driven by density differences, this would make the analytical calculations far more complicated. So, while the analytical calculations, give an idea of the minimum undercooling spacing which is close to the operating length scale in experiments, its relevance must be ascertained with respect to the assumptions of equal molar volumes. The quantification of the magnitude of the error requires the solution to the complete numerical problem involving fluid flow, which is certainly a scope for future work in this area.

7.5 Summary

In this study, we derive an analytical theory to determine the interfacial undercoolings, volume fractions and compositions of the solid phases in directionally solidifying lamellar eutectics for a generic multi-component, multi-phase alloy. While our work bears similarities to the recently published work of Senninger and Voorhees [43] which is particular for two-phase growth, our work gives a generic prescription for treating any given multi-phase,
multi-component alloy and in this respect can be seen as an extension of the previous work in [39]. A principal point in our theoretical calculations is that we treat the multi-variant and invariant eutectic reactions alike, by expressing the boundary layer compositions as functions of the respective state variables, which for our derivation are the diffusion potentials, the phase

fractions and the undercooling. This allows us to solve the system of equations self-consistently for the undercoolings, phase fractions and the phase compositions along with the boundary layer compositions irrespective of the number of degrees of freedom in the system. Our derivation, thus unifies the method of theoretical calculations of the Jackson-Hunt type for any given multi-variant/invariant eutectic growth.

We also perform phase-field simulations to corroborate our theoretical predictions and they are found to be in reasonably good match with each other where we investigate the case of monovariant two-phase and three-phase invariant growth. Both the phase-field and the analytical theory exhibit the same trends in the variation of interfacial undercooling, solid phase volume fractions and compositions with change in lamellar width. It is important to highlight that the numerical differences in the predictions obtained from the two techniques are attributed to the assumption of a flat interface in the analytical calculations. Particularly, asymmetry in the interfacial shapes brought about either by strongly different phase fractions or interfacial energies result in asymmetric discrepancies between the theoretical predictions and the phase-field predictions. Thus we expect the match between the two methods w.r.t the predictions of the phase fractions and phase compositions to be the best for situations where the interfacial shapes of the phases are similar. Furthermore, we note in passing that while the theoretical expressions are generic in the spirit in which they have been derived, the existence of a steady-state lamellar growth mode needs to be ascertained through either phase-field simulations or experiments, before applying the results.

Secondly, our study clearly highlights the importance of understanding the dependence of phase fractions on the diffusivity matrices. Changes in volume fractions can be associated with microstructural changes during two-phase growth(lamellar to rod), and many further possibilities during three-phase growth as seen in [152, 213]. Therefore, dependence of the volume fractions on the diffusivity matrices needs to be accounted for in order to derive a better understanding of pattern formation during bulk eutectic growth in multi-phase systems.

Chapter 8

Eutectic colony formation in systems with interfacial energy anisotropy

Eutectic colonies are observed in systems where there is at least a common solute which is rejected (or absorbed) by the all the solid-phases during coupled growth. This leads to the creation of an impurity boundary layer akin to the one observed during single phase solidification which is susceptible to interfacial perturbations leading to the formation of eutectic colonies (two-phase cells/dendrites). Most systems which display eutectic colony formation in experiments have anisotropic interfacial energies. We have presented an evidence of such a system in a Ni-Al-Zr alloy, in our introduction to this thesis in Chapter 1 and repeat the information here as well in Fig. 8.1. Eutectic colonies are observed in this system (see lower figure in Fig. 8.1(c)) with the two eutectic solids displaying a well-defined orientation relationship (see Figs. 8.1(a) and 8.1(b)). In this chapter, we investigate the eutectic colony dynamics, finger morphologies and the constituent lamellar structures in systems with anisotropic interfacial energies. We perform phase-field simulations in 2D and 3D to consider the effects of both solid-solid and solid-liquid interfacial energies on pattern formation in such systems. The phase-field model employed in this study is different from the ones employed in the previous chapters. This is because we intend to augment the ability to simulate the effects of anisotropic interfacial energies to the phase-field models traditionally employed to study colony formation in isotropic systems [16], and in systems with kinetic anisotropy [50, 51]. Thus, the possibility of simulating such structures with the Grand-Potential model remains open, which when addressed can lead to interesting comparisons between the numerical efficiencies of the two approaches.

We begin with a description of the model for 2D systems, which represents eutectic solidification in samples which are thin in one of the directions normal to the growth direction. This is

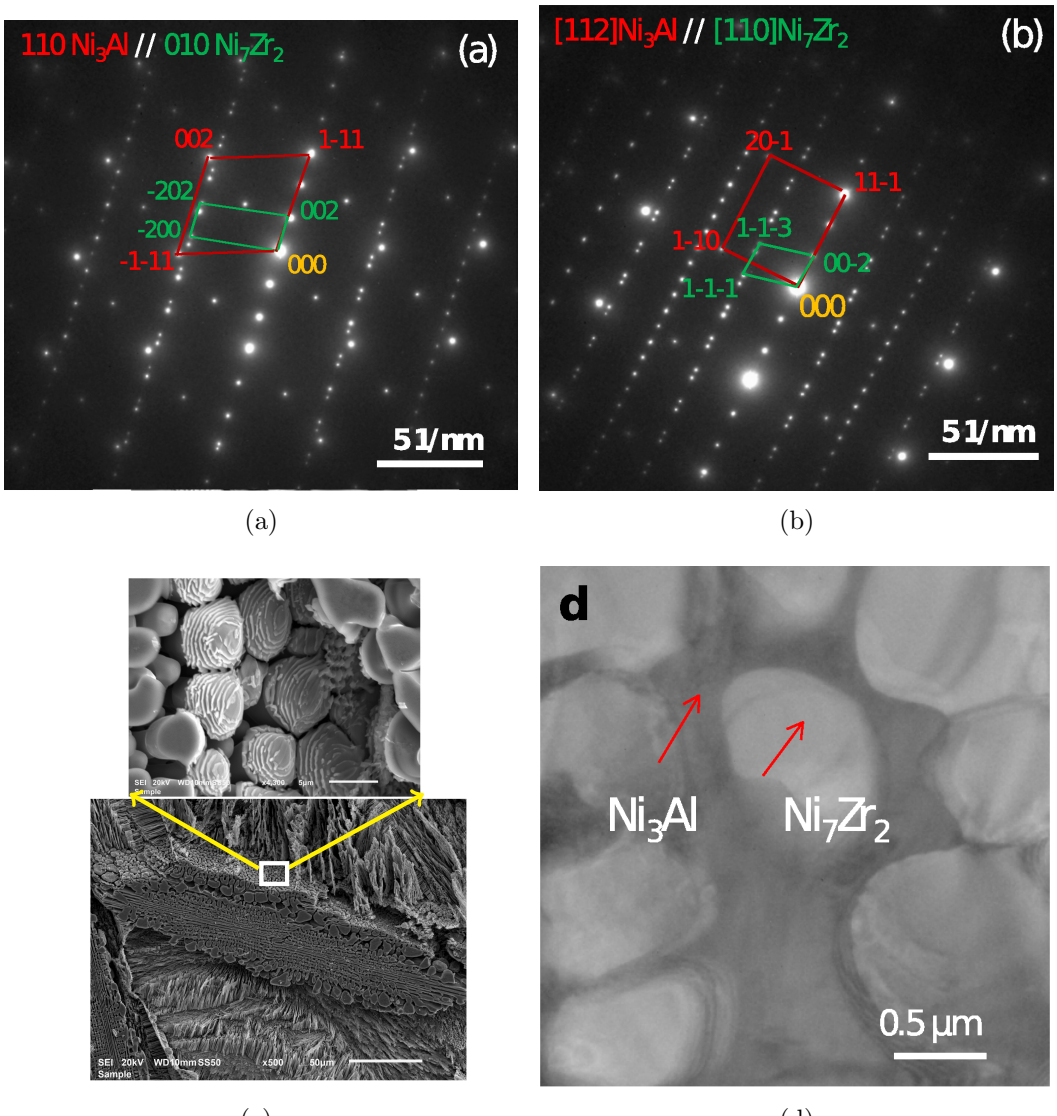

(a) (b)

(c) (d)

Figure 8.1: The anisotropy in solid–solid interfacial energy is indicated by the existence of a well defined orientation relationship between the two phases in (a) and (b). The orientation of the lamellae along the axis of the colony finger along with some spiral like features is displayed in (c). The two eutectic phases are identified from their contrast in (d).

extended to bulk solidification where we perform 3D simulations to understand the formation of eutectic colonies.

8.1 2D: Isotropic system

We begin our discussion with the isotropic system where we briefly review the mathematical model developed by Plapp and Karma [16]. The colony formation dynamics and the resulting lamellar and cellular morphologies are also discussed here.

8.1.1 Phase-field model

The two independent components chosen to describe the ternary system are u and $\tilde{c}$: u participates in the eutectic reaction by being redistributed between the two eutectic solids and $\tilde{c}$ is partitioned equally between either of the eutectic solids and the liquid phase (K being the equilibrium partition coefficient) to set up the Mullins-Sekerka (MS) instability [1] during directional growth. The solid and liquid free energy densities are given by:

$$\begin{aligned} f_{sol} &= \frac{1}{8}(u^2-1)^2 + (\tilde{c}\ln\tilde{c} - \tilde{c}) - (\ln K)\tilde{c} - \frac{\Delta T}{T_E}, \\ f_{liq} &= \frac{1}{2}u^2 + (\tilde{c}\ln\tilde{c} - \tilde{c}), \end{aligned} \tag{8.1}$$

where $\Delta T/T_E = (T - T_E)/T_E$ is the scaled and non-dimensionalized undercooling in the system with T_E and T denoting the non-dimensional eutectic temperature and the temperature field in the system, respectively. The equilibrium values of u and $\tilde{c}$ in the solid and the liquid phases (i.e., u_s, u_l, $\tilde{c_s}$ and $\tilde{c_l}$) are computed by solving for a set of equations mentioned as,

$$\begin{aligned} \frac{\partial f_{sol}}{\partial u}\Big|_{u_s} &= \frac{\partial f_{liq}}{\partial u}\Big|_{u_l}, \\ \frac{\partial f_{sol}}{\partial \tilde{c}}\Big|_{\tilde{c_s}} &= \frac{\partial f_{liq}}{\partial \tilde{c}}\Big|_{\tilde{c_l}}, \\ f_{sol} - \frac{\partial f_{sol}}{\partial u}\Big|_{u_s} u_s - \frac{\partial f_{sol}}{\partial \tilde{c}}\Big|_{\tilde{c_s}} \tilde{c_s} &= f_{liq} - \frac{\partial f_{liq}}{\partial u}\Big|_{u_l} u_l - \frac{\partial f_{liq}}{\partial \tilde{c}}\Big|_{\tilde{c_l}} \tilde{c_l}. \end{aligned} \tag{8.2}$$

Eqs. 8.2 represent the equality of chemical potentials of u and $\tilde{c}$ with an equality of grand potentials of the two phases as the third criterion of equilibrium.

For the u field, solving for the equilibrium phase compositions yield $u_s = \pm 1$ and $u_l = 0$. This allows identification of the eutectic solids with the solid phase corresponding to $u_s = 1$

named α and the one corresponding to $u_s = -1$ called β.

The temperature profile (T) in the Bridgman furnace is given by:

$$T = T_0 + G(z - Vt), \tag{8.3}$$

where G is the imposed thermal gradient along the vertically upward direction, V is the pulling velocity, t is the time and z is the distance measured in a frame attached to the solidification front at $t = 0$. The constant T_0 is calculated by setting the undercooling at the solid-liquid interface at $t = 0$ to a pre-determined value.

The free energy functional representing a solidifying system containing diffuse interfaces is given by [174, 214],

$$F = \int_V \Bigg[(h(\phi) f_{sol} + (1 - h(\phi)) f_{liq}) + \frac{W_u^2}{2} (\nabla u)^2 + \frac{W_\phi^2}{2} (\nabla \phi)^2 \Bigg] dV, \tag{8.4}$$

where V is the volume undergoing eutectic solidification. W_u and W_ϕ are the parameters determining the energy penalty associated with the presence of gradients in u and ϕ respectively. A liquid-to-solid phase transformation is modeled by solving the Allen-Cahn equation [175] which represents a minimization of F w.r.t the spatial variation of ϕ, where $\phi = 0$ denotes liquid and $\phi = 1$ represents the solid with values between 0 and 1 existing at the diffuse solid-liquid interface. The governing equation for ϕ evolution can be written as,

$$\tau \frac{\partial \phi}{\partial t} = W_\phi^2 \nabla^2 \phi - g'(\phi) + h'(\phi)(f_{liq} - f_{sol}), \tag{8.5}$$

where $'$ indicate derivatives with respect to ϕ. τ is the relaxation time for ϕ evolution. The potential barrier between the solid and the liquid phases is given by: $g(\phi) = \phi^2(1 - \phi)^2$, and the last term in the RHS of Eq. 8.5 represents the driving force for solidification obtained from the relative difference in the bulk free energy densities of the solid and the liquid phases with the total bulk energy density of the system at any point in space being given by:

$$f = h(\phi) f_{sol} + (1 - h(\phi)) f_{liq}, \tag{8.6}$$

where $h(\phi) = \phi^2(3-2\phi)$ is a polynomial interpolant ($h(\phi) = 1$ for solid and $h(\phi) = 0$ for liquid). The evolution of u and $\tilde{c}$ with time are obtained by solving the Cahn-Hilliard equation [176] as

given by:

$$\frac{\partial u}{\partial t} = \nabla \cdot \left[M \nabla \left(\frac{\partial f}{\partial u} - W_u^2 \nabla^2 u \right) \right], \tag{8.7}$$

and,

$$\frac{\partial \widetilde{c}}{\partial t} = \nabla \cdot \left[\widetilde{M} \nabla \left(\frac{\partial f}{\partial \widetilde{c}} \right) \right]. \tag{8.8}$$

M and $\widetilde{M}$ are the mobilities corresponding to evolution of u and $\widetilde{c}$ respectively, which are given by,

$$\begin{aligned} M &= D\left(1-\phi^n\right), \\ \widetilde{M} &= \widetilde{D}\left(1-\phi^n\right)\widetilde{c}, \end{aligned} \tag{8.9}$$

where D and $\widetilde{D}$ represent constants set to unity. Eq. 8.9 ensures that there is no diffusion of solutes inside the solid compared to that in the liquid. As the exchange of u between α and β happens only at the advancing solidification front, higher values of the constant n will be required to allow for complete solute re-distribution in simulations of directional solidification at higher pulling velocities (V).

The Eqs. 8.5, 8.7 and 8.8 are discretized by the finite difference technique, employing a 9-point stencil on a square grid for the space dimensions in 2D, to correctly represent the interfacial energy anisotropies when they are introduced. The time discretization is done explicitly, with the RHS of the equations in question evaluated at the current time-step in order to compute the evolution at the next time-step. The time-step (dt) and the grid spacing sizes (dx) are maintained constant throughout the course of the simulations. The non-dimensionalized simulation parameters are mentioned in the caption to Fig. 8.2. The computer programs are written in C. Parallelized implementations of our program on CPU clusters (using MPI) and on the GPU (using CudaC) led to all the simulation microstructures presented later.

All of the ϕ, u and $\widetilde{c}$ fields undergo changes across a solid-liquid interface: ϕ changes from 1 to 0, u changes from ± 1 to 0 and $\widetilde{c}$ from $\widetilde{c_s}$ to $\widetilde{c_l}$. So, a solid-liquid interface can be isolated from the ϕ field by identifying locations where it has values lying between 1 and 0. But across a solid-solid (α-β) interface only the u field can be seen to be varying, (i.e., it changes from 1 to -1 as we go from α to β) while ϕ and $\tilde{c}$ remain constant; this provides the only means of identifying the solid-solid interfaces.

G	0.001
V	0.015
τ	1.0
D	1.0
$\tilde{D}$	1.0
n	4
$\Delta x, \Delta y$	1.0
Δt	0.0025
W_ϕ	3.2
W_u	1.7
$\tilde{c_s}$	0.025
$\tilde{c_l}$	0.125

Table 8.1: Table depicting all the material parameters

8.1.2 Results

The 2D simulation of such a system (see Fig. 8.2) illustrates the fundamental eutectic cell formation dynamics. The introduction of some random noise at the solid-liquid interface at $t = 0$, sets up the MS-type instability through the $\tilde{c}$ component (see Fig. 8.2(c)). The simulation parameters are mentioned in the Table. 8.1 which are non-dimensionalized by employing the following length (l^*), time (t^*) and energy (f^*) scales,

$$f^* = \frac{RT^*}{V_m}, \tag{8.10}$$

$$l^* = \frac{\sigma^*}{f^*}, \tag{8.11}$$

$$t^* = \frac{l^{*2}}{[D_{ij}]^*}. \tag{8.12}$$

For our alloy of study, we have considered, $V_m = 10.0\,10^{-6}\ m^3/mol$, and the scale of diffusivity ($[D_{ij}]^*$) as $1.0\ 10^{-9}\ m^2/s$. The temperature (T^*) corresponds to the eutectic solidification temperature of the Ni-Al-Zr system, given by $T^* = 1425K$. The surface tension is taken to be $\sigma^* = 1.0J/m^2$.

It is important to mention a few more details regarding the simulations at this stage: The parameter T_0 in Eq. 8.3 is computed by setting the initial undercooling at the solid-liquid interface to 0.1. Periodic boundary conditions are imposed at the vertical boundaries and no-flux at the horizontal ones in a simulation box of dimensions 1440 by 1000 containing 40 lamellae pairs. The snapshots from all our 2D simulations are obtained using Gnuplot.

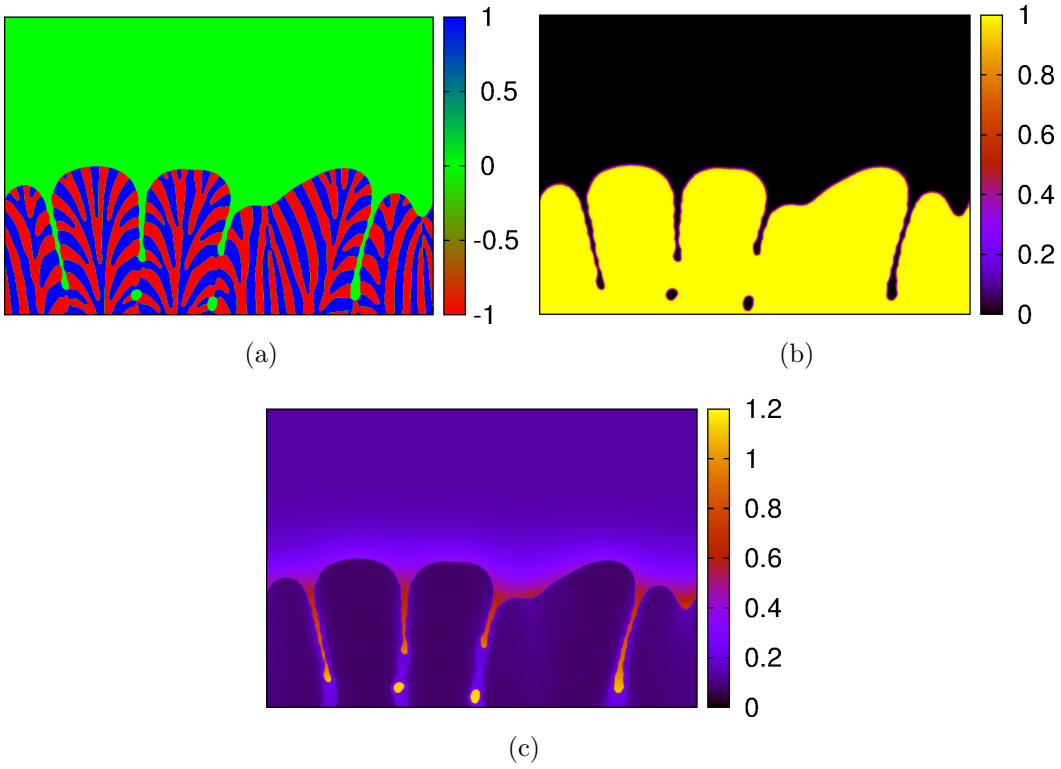

Figure 8.2: Colonies in an isotropic system at a total time of 150000 as seen from the (a)u field, (b)ϕ field, and (c)$\tilde{c}$ field, with no diffusivity in the solid. Colorbars report values of the u, ϕ and $\tilde{c}$ fields in (a), (b) and (c) respectively.

The morphological instability of the solid-liquid interface leads to formation of fingers, which are identified by digit like protuberances of the solid into the liquid (see Fig. 8.2). Here, the system does not select a particular eutectic finger spacing and the morphological evolution of the fingers display a cyclical character, as represented in Fig. 8.3. The fingers that are already formed continue to broaden and ultimately develop solid-liquid interface concavities which continue to deepen and lead to their splitting, forming new fingers. These fingers are randomly oriented with respect to the pulling direction.

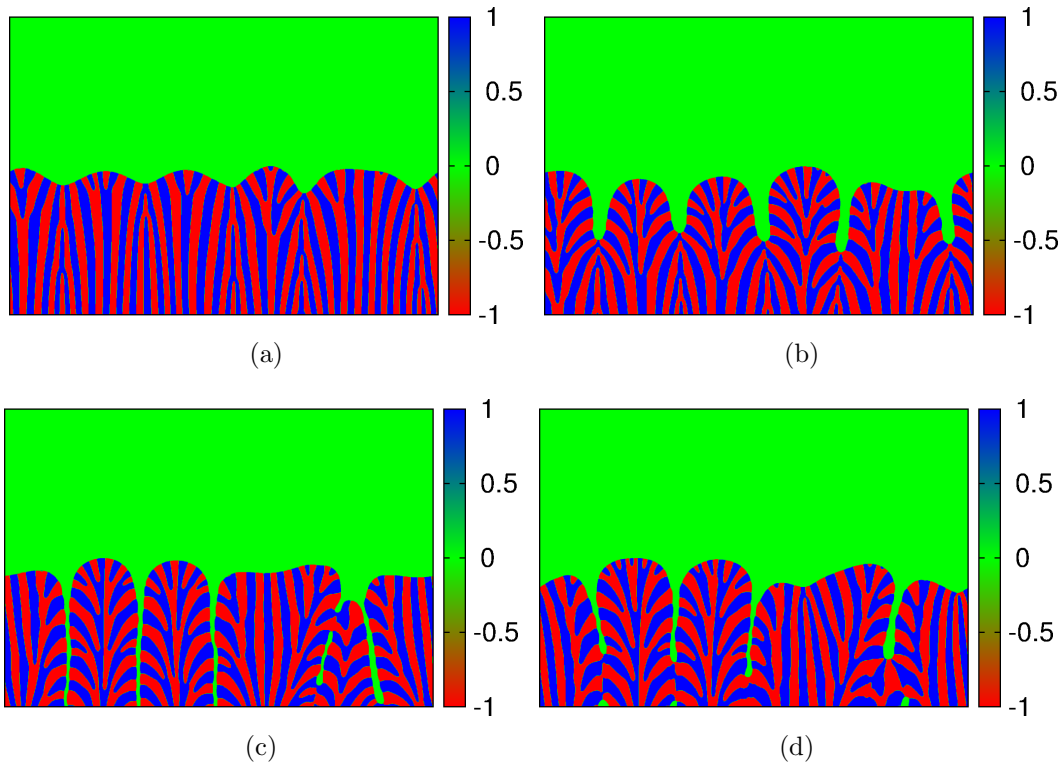

Figure 8.3: The evolution of the two-phase fingers captured at times of (a)75000, (b)90000, (c)125000, and (d)140000, which show the growth of perturbations at the interface to full-fledged cells.

Throughout the course of the simulation, lamellae can be seen to undergo either termination or broadening followed by the formation of new lamellae by spinodal decomposition. Lamellae pairs converge and ultimately terminate at locations where the solid-liquid interface is concave inwards. At locations where the solid-liquid interface is convex outwards (usually at the tip of the fingers), the eutectic phase (either α or β) present there broadens till it develops a concavity at its interface with the liquid, prompting formation of the conjugate eutectic solid phase there. It must be noted at this point, that the mechanism of lamellae broadening followed

by formation of a new phase by spinodal decomposition, prevents finger splitting, which would happen with the concavity deepening without a new phase appearing ahead. These mechanisms can be confirmed from Figs. 8.3(c) and 8.3(d), where the second and third fingers from the left display conjugate phases forming at the wider lamellae constituting the convex growth front. On the other hand, the fourth finger from the left displays a concavity which continues to deepen leading to lamellae termination and would eventually lead to its splitting at later times.

The new lamellae which come out as a result of spinodal decomposition possess a lamellar width (λ) which is different to the one selected by the criterion of minimum undercooling at the solid-liquid interface due to Jackson and Hunt [8]. Phase separation (the liquid composition $u = 0$ decomposing to give $u = \pm 1$ corresponding to the two eutectic solids) happens only at the solidification front (ϕ having values between 0 and 1) where the spinodal length scale can be determined by following the analysis in [176], considering only the double welled part of the potential (f_{sol}) in Eq. 8.7 as,

$$\begin{aligned}\frac{\partial u}{\partial t} &= \nabla \cdot \left[M \nabla \left(\frac{\partial f_{sol}}{\partial u} - W_u^2 \nabla^2 u \right) \right] \\ &= \nabla \cdot \left[M \left(\frac{\partial^2 f_{sol}}{\partial u^2} \nabla u - W_u^2 \nabla \left(\nabla^2 u \right) \right) \right] \\ &= M \left[\frac{\partial^2 f_{sol}}{\partial u^2} \nabla^2 u - W_u^2 \left(\nabla^4 u \right) \right]. \end{aligned} \tag{8.13}$$

where we have assumed M to be a constant (but less than D) at the interface and retained only linear terms in order to obtain the last equality. An expression describing the amplification of a sinusoidal variation in $u (= u_0 + A(t) \cos \omega x)$, with time, whose evolution is governed by Eq. 8.13, is given by:

$$\begin{aligned} A(t) &= A_0 \exp \left[R(\omega) t \right] \\ &= A_0 \exp \left[-M\omega^2 \left(\frac{\partial^2 f_{sol}}{\partial u^2} + W_u^2 \omega^2 \right) t \right], \end{aligned} \tag{8.14}$$

where A and A_0 are the amplitudes at times t and $t = 0$ respectively and ω is the wavenumber of the sinusoidal variation in u. The amplification factor,
$R(\omega) = -M\omega^2 \left(\partial^2 f_{sol} / \partial u^2 + W_u^2 \omega^2 \right)$, has a maximum for a wavenumber of,

$$\omega_{max} = \sqrt{ -\frac{\dfrac{\partial^2 f_{sol}}{\partial u^2}}{2 W_u^2} }, \tag{8.15}$$

which leads us to an expression for $\lambda_{max}^{spin}(=2\pi/\omega_{max})$, the dominant length scale of spinodal decomposition. Using, the simulation parameters mentioned in the caption to Fig. 8.2, and evaluating $\partial^2 f/\partial u^2$ at $u = 0$ we retrieve $\lambda_{max}^{spin} = 21.3$. It must be noted at this point that the dominating wavelength of spinodal decomposition (λ_{max}^{spin}) is decided only by an interplay of bulk and gradient energies as can be seen from Eq. 8.15 and is independent of the sample pulling velocity (V).

The other important length scale in the problem is the lamellar width (λ_{JH}) corresponding to the minimum undercooling at the eutectic front, which can be obtained by evaluating the expressions in [16]. For the parameters of our study, the Gibbs-Thomson coefficient evaluates to $\Gamma = 1.38$, and the contact angles are $\theta = 23.87°$, leading to $\lambda_{JH} = 40.6$ for $V = 0.01$. Invoking the theory of marginal stability of eutectics [215], all the eutectic length scales that are smaller than λ_{JH}, disappear with time under a long wavelength perturbation of the interface, leading to an average lamellar width in the system which is larger than λ_{JH}. This conclusively establishes that the microstructural length scales in our simulations are not determined by spinodal decomposition unless at pulling velocities of $V > 0.04$ (from the scaling of λ_{JH} with $V^{-0.5}$ given by [8]). At such high velocities, λ_{JH} becomes smaller than λ_{max}^{spin} (which remains invariant with change in V) and the lamellar width set by spinodal decomposition becomes the dominating microstructural length scale in the absence of perturbations of the solid-liquid interface.

Thus in 2D, nucleation in this manner offers only a mechanism to obtain the conjugate phase at a solid-liquid concavity. This is however unrealistic given that the undercoolings are not sufficiently high for such nucleation to occur. In reality it is a 3D mechanism, where a single phase rod rotates to appear from planes in front or behind to occupy the concavity. Therefore, here we will treat this formation of the second phase as only a mechanism allowing one to maintain the scale of the simulation.

Furthermore, in Fig. 8.2(a), there is no specific orientation relationship between the lamellae and the direction of solidification (vertically upwards) that is selected by the system. The lamellae appear oriented roughly orthogonal to the solidification envelope (Cahn's hypothesis) close to the solid-liquid interface (set by the force balance at the triple points) and take up more random orientations inside the fingers.

By reviewing the isotropic system, we have gained an understanding of the phase-field model which we are going to build upon in order to study the implications of incorporating anisotropic solid-liquid and solid-solid interfacial energies on colony formation. The colony dynamics and morphology observed in the 2D simulations of isotropic systems also provide a reference against which we can attempt to understand the effect of anisotropic interfaces on the lamellar and

cellular morphologies, beginning in the next section.

8.2 2D: Effect of anisotropic interfacial energies on the colony dynamics

In this section, we describe phase-field models of systems possessing anisotropic interfacial energies and attempt to understand eutectic colony dynamics from 2D simulations. We begin our discussion by considering a system with anisotropic solid-liquid interfaces and follow it up with a discussion on systems with anisotropic solid-solid interfaces.

8.2.1 Anisotropic solid-liquid interface

In this section we study the cellular features and lamellar orientations in the presence of anisotropic solid-liquid interfaces. We draw upon our observations for an isotropic system as a context to understand the simulation results for this situation. We begin with a description of the phase-field model.

Phase-field model

A convenient way to identify the solid-liquid interface is with gradients in ϕ. So, in order to understand the effect of a solid-liquid interfacial energy anisotropy on the microstructural features obtained during directional solidification, we introduce the anisotropy through the gradient energy term in the evolution equation of the ϕ field as given by the modified Allen-Cahn equation which writes:

$$\tau\frac{\partial\phi}{\partial t} = \left(\nabla\cdot\frac{\partial}{\partial\nabla\phi}\right)a - g'(\phi) + h'(\phi)(f_{liq} - f_{sol}), \tag{8.16}$$

where,

$$a = \frac{1}{2}W_\phi^2 a_c^2(\theta)(\nabla\phi)^2. \tag{8.17}$$

The anisotropy function (a_c) given by:

$$a_c = 1 + \zeta cos(4(\theta - \theta_R)) = 1 - \zeta\left(3 - 4\left(\frac{\phi^{*4}_x + \phi^{*4}_y}{(\phi^{*2}_x + \phi^{*2}_y)^2}\right)\right), \tag{8.18}$$

introduces the four-fold anisotropy into the solid-liquid interfacial energy and is the same as what suggested in [121]. The *'s in the above equation indicate that the derivatives (with respect to either x or y as denoted by the subscripts) are computed in the reference frame of the crystal. The crystal reference frame can be rotated by an angle θ_R to the laboratory frame and this allows us to explore different relative orientations of the equilibrium solid-liquid interfaces with respect to the sample pulling direction (which is vertically downwards). ζ sets the strength of the anisotropy. Fig. 8.4(a) displays a_c as a function of θ (γ plot), also highlighting the effect of a rotation of a crystal frame to the laboratory frame.

The other equations employed to model a system with anisotropic solid-liquid interfaces remain the same as reported in the isotropic situation.

Results

The selection of particular orientations of the solid-liquid interface under different rotations of crystal frame can also be understood by referring to Fig. 8.4(b).

The dynamics of colony formation in such a system is explored for a situation where the crystal frame is rotated clockwise by $\theta_R = 10°$to the laboratory frame (see Fig. 8.4(a)) for two different strengths of the ϕ anisotropy, i.e., $\zeta = 0.015$, and 0.03, but for a single sample pulling velocity ($V = 0.015$) (see Fig. 8.5).

A lot of features in these simulations are in contrast to the isotropic case. First of all, the finger envelopes tend to favor certain orientations dictated by an interplay between the anisotropy and the direction of the imposed temperature gradient (vertically upward). To illustrate this further, we can imagine that the nucleus in Fig. 8.4(b) being subjected to a temperature gradient prompting it to grow in the vertically upward direction. Now, the two corners (indicated by arrows) in the top half of the crystal are the ones which could grow such that the nucleus continues to be bounded by interfaces which are favored by anisotropy. But the one on the right (identified by the red arrow in Fig. 8.4(b)) is usually favored because of it being closer to the pulling direction. This can be clearly confirmed in Fig. 8.5(b) where the fingers have an orientation given by a slight clockwise rotation from the vertical (represented by the arrow in Fig. 8.5(b)). In situations where the solid-liquid interface is not as anisotropic (lower ζ, as in Fig. 8.5(a)), the selection of growth direction is not as strict as in the case with higher ζ (see Fig. 8.5(b)). This manifests as the growth of fingers along directions which are not the closest to that suggested by anisotropy under a temperature gradient. Another consequence of this is the broader appearance of fingers for $\zeta = 0.015$ (Fig. 8.5(a)) than for $\zeta = 0.03$ (Fig. 8.5(b)).

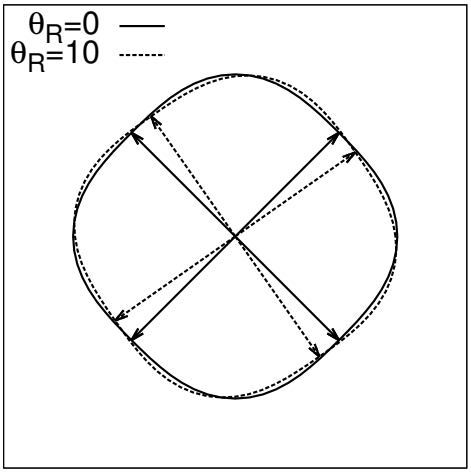

(a)

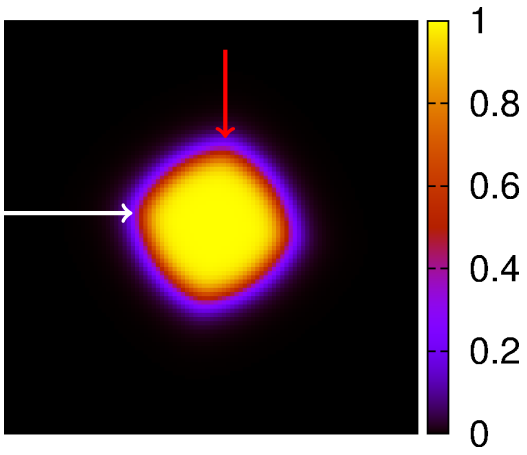

(b)

Figure 8.4: γ plot obtained by evaluating a_c from Eq. 8.18 is shown in (a). The arrows indicate the orientations of the plane normals with the least energy. Figure legends report θ_R in degrees. (b) A phase field simulation of an α nuclei growing in the liquid, with $\theta_R = 10°$, clockwise, with $\zeta = 0.05$. The arrows denote the corners which can advance under directional solidification conditions. The corner identified by the red arrow dominates over the one indicated by the white one due to its closer alignment to the vertically imposed temperature gradient. Colorbar reports values from the ϕ field.

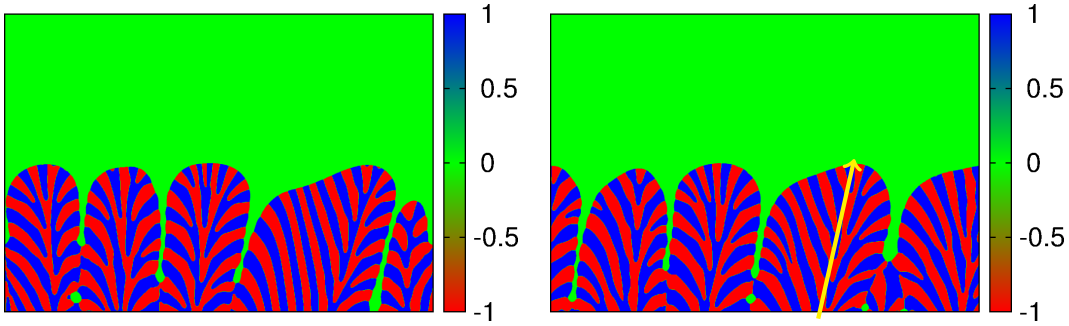

(a) (b)

Figure 8.5: Microstructures (u field) of a system with no solid diffusivity and solid-liquid interfacial energy anisotropy, at a total time of $t = 150000$, for (a)$\zeta = 0.015$, and (b)$\zeta = 0.03$, with $V = 0.015$, $n = 4$ and $\theta_R = 10°$, clockwise. Colorbars report values of the u field. The other simulation parameters are the same as mentioned in the caption to Fig. 8.2. The arrow roughly indicates the orientation of the finger envelope.

Also, the tilted orientation of the fingers from the vertical as observed in Fig. 8.5(b), during growth implies a non-zero component of their growth velocity in the horizontal direction. This leads to an observed motion of the fingers across the width of the simulation box (traveling waves of fingers) during eutectic colony growth.

Emergence of a stable finger spacing can be observed in Fig. 8.5(b), which is not observed in the isotropic case. In the system with lower anisotropy shown in Fig. 8.5(a), the fingers do broaden and bifurcate, but not as frequently as in Fig. 8.2, which suggests that with an increase in the magnitude of anisotropy the stability of the solid-liquid interface is enhanced.

Similar to the isotropic situation, the lamellae appear to be oriented orthogonally to the solidification envelope at the solid-liquid interface which gets modified inside the fingers due to interactions between lamellae approaching the finger axis from either side of the finger tip.

An incomplete partitioning of the solutes (also known as solute trapping) hindering the formation of the eutectic at the solid-liquid interface, is observed for higher values of V and ζ when using solute mobilities of the form, $M = D\,(1-\phi^n)$ and $\widetilde{M} = \widetilde{D}\,(1-\phi^n)\,\tilde{c}$, even with higher values of n. Thus, for studying the effects of higher V and ζ on the colony dynamics, we introduce another approximation in the form of equal and constant mobility of solutes in both solid and liquid phases. Mathematically, this manifests as setting $M = \widetilde{M} = 1$ in the model formulation. We report two simulations in Fig. 8.6 with $\zeta = 0.03$ (Fig. 8.6(a)) and $\zeta = 0.05$ (Fig. 8.6(b)) at a sample pulling velocity of $V = 0.04$. The enhanced solid diffusivity should lead to a λ_{JH} larger than the value computed for the system with no solid diffusivity which should prevent length scales due to spinodal decomposition becoming dominant even at higher

pulling velocities of $V = 0.04$.

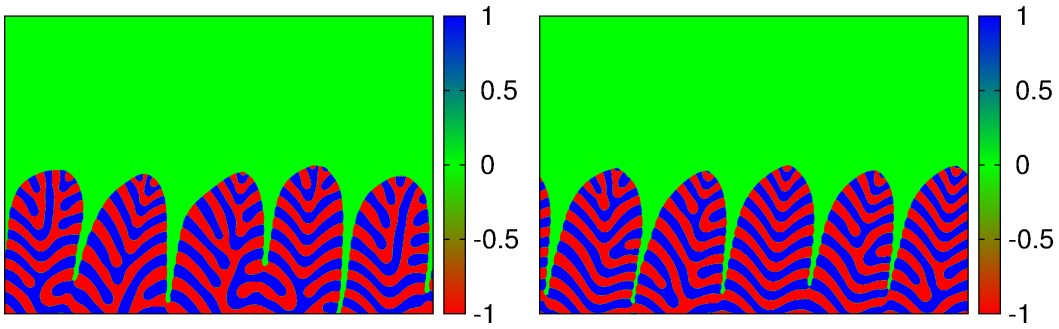

(a) (b)

Figure 8.6: Microstructures (u field) of a system having equal diffusivity in the solid and the liquid phases with solid-liquid interfacial energy anisotropy, for (a)$\zeta = 0.03$, $t = 150000$, and (b)$\zeta = 0.05$, $t = 100000$ with $V = 0.04$ and $\theta_R = 10°$, clockwise. Colorbars report values of the u field. The other simulation parameters are the same as mentioned in the caption to Fig. 8.2.

The fingers in Fig. 8.6 appear to possess a smaller tip-radius than what is observed for the cells in Fig. 8.5, which is expected at higher velocities due to the inverse scaling of tip-radius (ρ), with pulling velocity (V) given by the constancy of $\rho^2 V$. Furthermore, an increase in ζ can also be seen to promote a stronger selection of the dendrite tip radius as observed from Figs. 8.6(a) and 8.6(b). Also, the tilt of the fingers becomes more pronounced with increase in ζ, as can be confirmed from Figs. 8.6(a) and 8.6(b).

An interesting difference in the lamellar appearance can be observed at the central axis of the fingers. In Fig. 8.5, the individual phases from the solid-liquid interface on either side of the tip of a finger do not unite at the central axis of the finger, as they do in Fig. 8.6. The tree-like arrangement of phases seen in Fig. 8.5 is not replicated in Fig. 8.6, where the phases from either side of the finger, join with each other in the middle of the fingers. This difference is a consequence of the lack of solute diffusivity in the solid in Fig. 8.5, where the local orthogonality of the lamellae to the solidification envelope remains frozen even inside the fingers, with the emanation of phases from the central stem being a record of the lamellar bifurcation that has happened earlier.

Having considered the effect of anisotropic solid-liquid interfaces on the colony dynamics, we move on to studying systems with anisotropic solid-solid interfacial energies.

8.2.2 Anisotropic solid-solid interface

In this section we are going to study the effect of an anisotropic interface between the two eutectic solids on the lamellar morphologies constituting the eutectic colonies and also on the orientation and stability of the fingers. We begin with a description of the phase-field model.

Phase-field model

In order to explore the eutectic colony formation dynamics in situations where the solid-solid (i.e., α-β) interfaces have a specific orientation with respect to the pulling direction, the anisotropy must be introduced through the u field. But considering the fact u changes in value across all the three possible interfaces (α-β, α-liquid and β-liquid), we introduce the anisotropy through the the bulk free energy density in solid, to minimize its influence on the solid-liquid interface which results in the modified free-energy density expression of the solid given by,

$$f_{sol} = \frac{1}{8}(u^2-1)^2 a_c^2(\theta) + (\tilde{c}\ln\tilde{c} - \tilde{c}) - (\ln K)\tilde{c} - \frac{\Delta T}{T_E}, \tag{8.19}$$

where a_c is the same as in Eq. 8.18 with ϕ's being replaced by u's. From Eq. 8.19, we can see that the free energy density contribution from the u field has a maximum at $u = 0$ and minima at $u = \pm 1$. Now by observing that the total energy density of the system is an interpolation between the solid and liquid energy densities through an interpolant(h) which is a non-linear but monotonic function of ϕ (see Eq. 8.6), it can be verified that at a solid-liquid interface (u varying between 0 and ± 1; ϕ varying between 0 and 1) the influence of anisotropy is mellowed down by u being non-zero and h being non-unity. To confirm this observation, we can refer to Fig. 8.7, given below. The equilibrium orientations of the α-β interfaces under solid-solid anisotropy can be discerned from Fig. 8 in [213] and are exactly similar to the features observed for solid-liquid interfacial energies in Fig. 8.4(b).

Results

For a given rotation of the crystal frame relative to the laboratory frame, the orientation of the α-β interface is going to be determined by the force balance at the triple points. This can be predicted for the situation of steady-state growth using symmetry arguments that are motivated from experiments [48, 49] which claim that the resultant surface tension must still be oriented along the growth direction. This condition can then be used to derive an analytical expression for the α-β interfacial orientation with the vertical [47] which we are going to henceforth refer to as the tilt angle (θ_t) (explained in Fig. 8.8(a)). The tilt of the solid-solid interface for a given

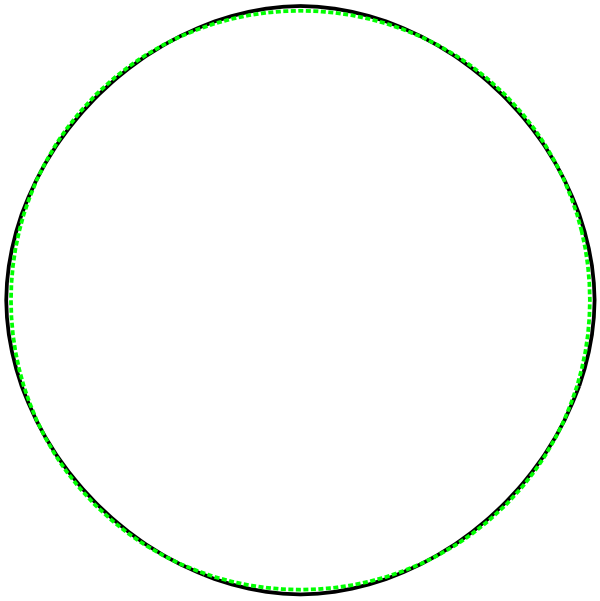

Figure 8.7: Iso-contours at $\phi = 0.5$ for $\zeta = 0.05$(black) and $\zeta = 0$(green) with $\theta_R = 0$

rotation of the crystal frame can be seen in Fig. 8.8(a). For the four-fold anisotropy function we have implemented, we compared the tilt angles from steady-state growth simulations of a single lamella pair against theoretical predictions in Fig. 8.8(b).

The colony formation dynamics with anisotropic solid-solid interfacial energy is explored in Fig. 8.9 with two different magnitudes of anisotropy, i.e., $\zeta = 0.015$ in Fig. 8.9(a) and $\zeta = 0.03$ in Fig. 8.9(b) at a single pulling velocity of $V = 0.015$.

Here, the microstructural feature that is strikingly different from the previous cases of isotropy and solid-liquid anisotropy is the presence of straight, parallel, lamellae pairs running through the center of the fingers and are very similar to what is observed in Fig. 8.1. This qualitative agreement between our simulations and experiments substantiates our conjecture that the structures observed in Fig. 8.1 are a result of anisotropic interfaces and more specifically anisotropy of the interface between the two eutectic solids.

Though there is a theoretical prediction available for the orientation of the α-β interfaces during steady-state growth, for an unsteady situation of cellular or dendritic growth we can only attempt to qualitatively understand the lamellar orientations in the absence of an analytical expression. Focusing closely on Figs. 8.9(a) and 8.9(b), the simulation proceeds from the destabilization of a tilted state of the lamellae during steady-state growth (as seen in Fig. 8.8(a)), giving rise to cells which globally have lamellae oriented along the direction of the temperature gradient. The solidification envelope corresponding to each cell however develops small tilts

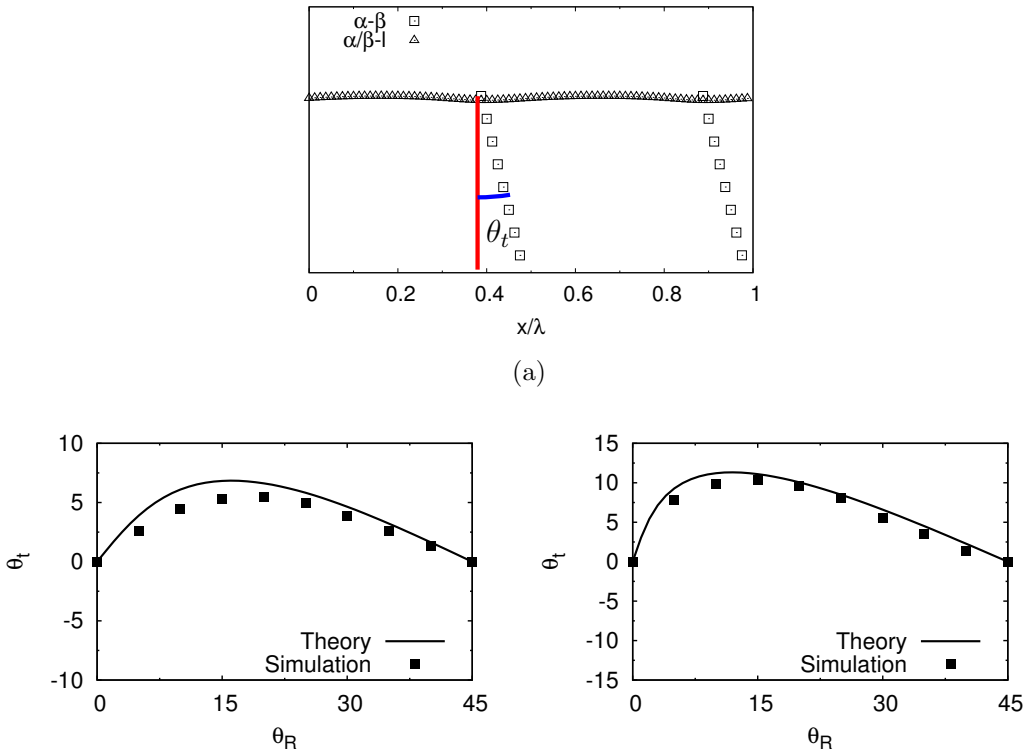

(a)

(b)

(c)

Figure 8.8: Tilt of the solid-solid interface for $\theta_R = 10°$, clockwise, and the corresponding tilt angle θ_t is shown in (a). Tilt angles (θ_t) are plotted versus angle between the crystal frame and the laboratory frame (θ_R), for (b) $M = \widetilde{M} = 0$, for the eutectic solids; $\zeta = 0.03$, and (c) $M = \widetilde{M} = 1$ for the eutectic solids; $\zeta = 0.05$.

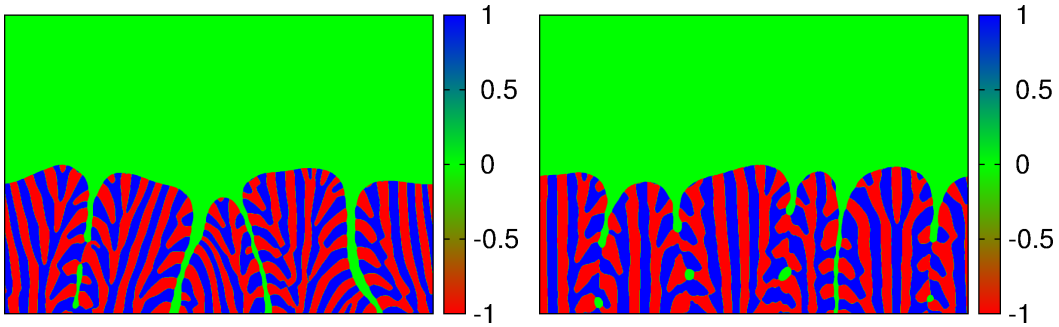

(a)

(b)

Figure 8.9: Microstructures (u field) of a system with no solid diffusivity and solid-solid interfacial energy anisotropy, for (a)$\zeta = 0.015$, $n = 16$, $t = 125000$, and (b)$\zeta = 0.03$, $n = 32$, $t = 150000$, with $V = 0.015$. Colorbars report values of the u field. The other simulation parameters are the same as mentioned in the caption to Fig. 8.2.

with respect to the growth direction, which can be thought of as the tilted steady state at lower velocities being rotated such that the solid-solid interfaces become aligned with temperature gradient, while the solid-liquid interface develops a tilt.

The magnitude of anisotropy also appears to play a role in lamellar orientations, as for a smaller $\zeta(= 0.015)$, as seen in Fig. 8.9(a), the straight lamellae pairs are not strictly aligned with the vertical, whereas with $\zeta = 0.03$, the lamellae display a strong alignment with the imposed temperature gradient, as can be seen from Fig. 8.9(b).

An outcome of the presence of lamellae oriented as closely as possible to the direction of imposed temperature gradient is the broadening of fingers, as can be clearly observed in Fig. 8.9(b). The shapes of the individual fingers can be understood as a result of a combined influence of the propensity of the lamellae to remain aligned with the direction of the imposed temperature gradient and that of the thermodynamically predicted relative orientations of the solid-solid and the solid-liquid interfaces under solid-solid interfacial energy anisotropy presented in Fig. 8.8. Thus, the vertically oriented lamellae emanate from sides of the fingers which appear roughly flat, but display a small deviation from horizontal.

Furthermore, with regards to the stability of the finger width, an increase in ζ leads to stabler features, which is the same as seen for the case of anisotropic solid-liquid interfacial energy.

As mentioned in conjunction to the discussion on colony dynamics with solid-liquid anisotropy, we relax the criterion of negligible solute diffusivities in the solid in order to negate the solute-trapping that impedes probing of colony formation in systems pulled at higher velocities or displaying higher anisotropy in the interfacial energy. A variation of tilt angles (θ_t) as a function of θ_R for equal diffusivity of solutes in the solid and the liquid is also reported in Fig. 8.8(c) as a confirmation that this approximation preserves the ability of the model to capture the essential physics. This enables us to simulate the effects of a pulling velocity of $V = 0.04$ on systems with $\zeta = 0.03$ (see Fig. 8.10(a)) and $\zeta = 0.05$ (see Fig. 8.10(b)).

Most of the features seen in Fig. 8.9 is replicated in Fig. 8.10 except for a few exceptions. One of them being the absence of the deep cells observed in Fig. 8.9. This is a result of the enhanced diffusivity in the solid which allows adjoining fingers to fuse wherever they are in close proximity. Another important feature of these simulations is the lateral orientation (towards the left in Fig. 8.10) of the two-phase finger-tips in their bid to choose a smaller tip radius (ρ) consistent with a larger pulling velocity V while allowing the maximum number of lamellae to remain vertical at the same time maintaining the necessary orientation relationship between the solid-solid and solid-liquid interfaces. Furthermore, the lamellae in Fig. 8.10 also appears

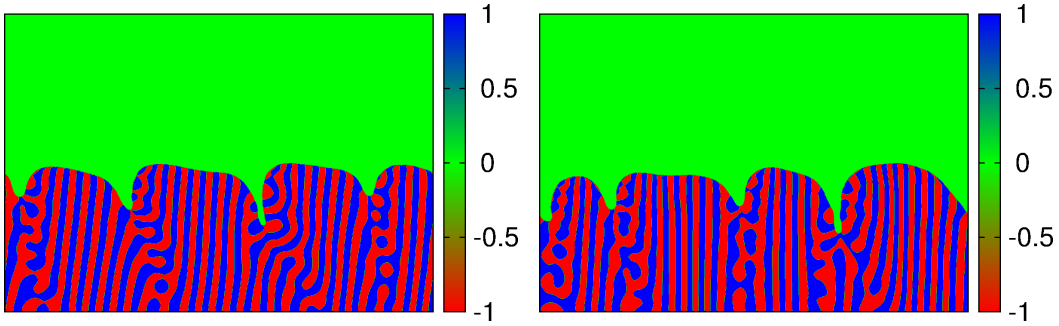

(a) (b)

Figure 8.10: Microstructures (u field) of a system with equal solute diffusivity in the solid and the liquid phases, with solid-solid interfacial energy anisotropy, for (a)$\zeta = 0.03$; $t = 150000$ and (b)$\zeta = 0.05$; $t = 150000$, with $V = 0.04$. Colorbars report values of the u field. The other simulation parameters are the same as mentioned in the caption to Fig. 8.2.

finer consistent with the higher pulling velocities employed for these simulations [1].

Having studied the lamellar orientations and the two-phase cell morphologies for systems with anisotropic solid-solid and solid-liquid interfacial energies in 2D, we now move on to 3D simulations where we probe the effect of a third dimension on the colony dynamics in systems with anisotropic interfacial energies. We begin with a discussion of an isotropic system.

8.3 3D: Isotropic

The 2D simulations provide important insights into the physics of the colony formation problem in terms of both lamellar and finger morphologies. But these observations from 2D simulations suffer from a limitation of being representative only of directional solidification in thin samples. In order to gain a complete understanding of the problem in situations where both dimensions of the solidified cross-section are comparable, we resort to 3D studies beginning with the isotropic system. The governing equations 8.5, 8.7 and 8.8 are expressed in a tensorial form which are numerically solved in a 3D cartesian system, employing a 27-point stencil for discretizing the space dimensions in order to accurately capture the effect of anisotropies in the interfacial energies when they are introduced. The other parameters relevant to the solution of equations remain the same as in 2D.

The high computational cost of 3D simulations, constrain us to perform them for a set of

[1] λ scales as ρ with change in velocity, with the scaling constant depending on the simulation conditions. Thus, changes in lamellar widths can be understood in the context of the concurrent changes tip radius with velocity (V), which is also indicative of the magnitude of the scaling constant connecting λ and ρ for the current simulation.

parameters which lead to a quicker destabilization of the solidification front. Hence, we employ a high pulling velocity of $V = 0.1$ to computationally access the colony dynamics in 3D. This approach necessitates equal diffusivity of solutes in the solid to that in the liquid, due to the high solute trapping observed in this model at higher pulling speeds.

It must be mentioned at this point that though for $V = 0.1$ the spinodal decomposition length scale λ_{max}^{spin} becomes larger than λ_{JH}, the scale of the simulation in 3D is always maintained at λ_{JH} due to the presence of 3D topological mechanisms for lamellar interactions.

We report a 3D simulation in Fig. 8.11 carried out in a $288 \times 288 \times 300$ box containing 8 lamellae pairs along each dimension with the remaining parameters being identical to the 2D isotropic simulation shown in Fig. 8.6. The simulations are done in a directional solidification setting with the direction of the imposed temperature gradient being vertically upwards. The boundary conditions are set to be no-flux on faces of the box normal to the pulling direction and periodic on faces parallel to it. We have utilized the "isosurface" feature in MATLAB (MATLAB 8.2, The MathWorks Inc., Natick, MA, 2013) to visualize our 3D simulations, where the α-liquid and β-liquid interfaces are extracted at particular values of the phase-field ϕ to capture the colony microstructure.

In Fig. 8.11(c), a single lamella pair appears to construct each finger by growing continuously in a helical fashion. This structure has already been observed experimentally by Akamatsu and Faivre [10] and has been anointed by them as a "spiraling eutectic".

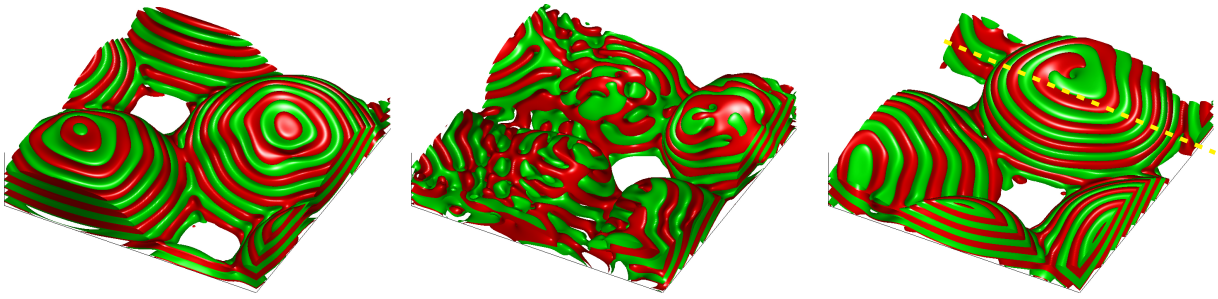

(a) (b) (c)

Figure 8.11: Eutectic colonies at a total time of (a)21000, (b)45000, and (c)55000 in an isotropic system with $V = 0.1$. The yellow dashed line in (c) represents the orientation of the vertical sections reported in Fig. 8.12. The red phase represents α and the green phase represents β.

The morphology of the spiral can be better understood by considering 2D sections of the microstructure in Fig. 8.11(c) by planes parallel and perpendicular to the growth direction as reported in Figs. 8.12 and 8.13, respectively. The apparent discontinuity in the solid phases across the central axis of the finger seen in Fig. 8.12(a) coupled with the particular arrangement

of phases in Fig. 8.13 allow an understanding of the spiral as a helical arrangement of a single pair of lamella plates. Figs. 8.11(c), 8.12 and 8.13 considered in unison points to the possibility of the shape of the spiraling eutectic fingers being approximated by a paraboloid.

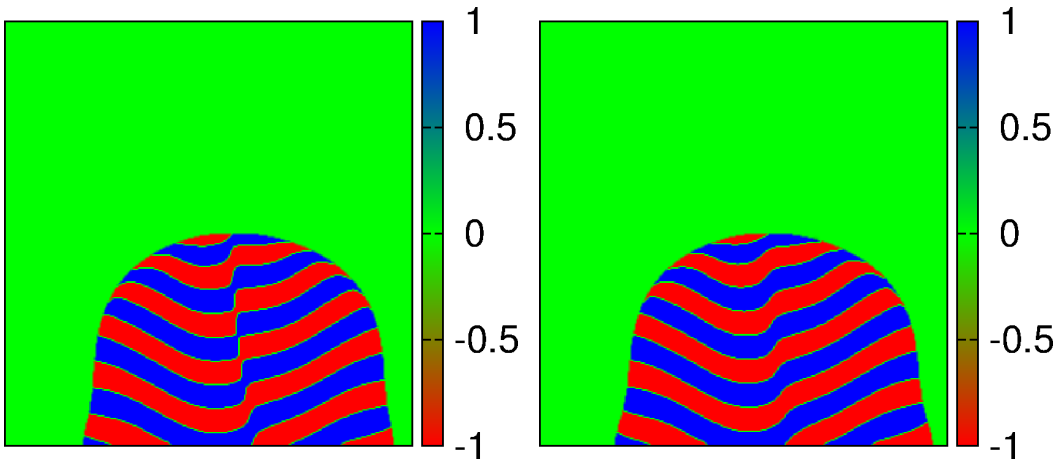

(a) (b)

Figure 8.12: 2D sections (u field) of Fig. 8.11(c) by a plane parallel to the pulling direction whose orientation is indicated by the yellow dotted line in Fig. 8.11(c), showing solid phase arrangements at (a)the spiral axis, and (b)a little away from the spiral axis. Colorbars report values from the u field.

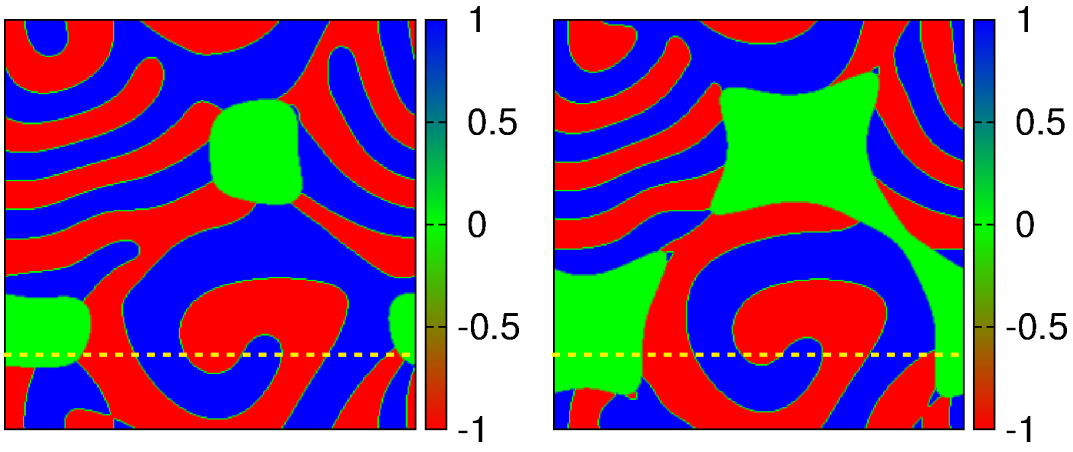

(a) (b)

Figure 8.13: 2D sections (u field) of Fig. 8.11(c) by a plane normal to the pulling direction. The sectioning height is lower in (a) than in (b). Colorbars report values from the u field. The yellow line is the projection of the same from Fig. 8.11(c).

The 3D simulation of the isotropic system confirms the major observations from the 2D

simulation in terms of the randomness of the finger orientations, the lack of specificity of the lamellar orientations and the absence of a particular finger spacing selected by the same. The solid-liquid interface is found to be unstable with spirals forming and disintegrating throughout the course of the simulation as can be seen by considering the Figs. 8.11(a), 8.11(b) and 8.11(c).

The discussion of an isotropic system in 3D, provides a reference against which we will seek to understand the eutectic colony features under interfacial anisotropy presented in the following sections.

8.4 3D: Effect of anisotropic interfacial energies on the colony dynamics

Like in 2D, we will consider the effect of both solid-liquid and solid-solid anisotropy on the colony formation dynamics in 3D. We begin with the former.

8.4.1 Anisotropic solid-liquid interface

To explore the effect of anisotropy on the solid-liquid interface on the colony formation dynamics in a 3D system, we introduce the anisotropy through the $\phi-$ field with the expression for a_c being:

$$a_c = 1 - \zeta \left(3 - 4 \left(\frac{\phi^{*4}_x + \phi^{*4}_y + \phi^{*4}_z}{(\phi^{*2}_x + \phi^{*2}_y + \phi^{*2}_z)^2} \right) \right), \tag{8.20}$$

which is a simple extension of the 2D case. In reality, the crystal frame can have any arbitrary orientation to the pulling direction. But any such orientation can be decomposed into a combination of a rotation about the pulling direction and the ones normal to it. In view of that, we can attempt to understand the microstructure formation for two basic configurations: the one where the axis of rotation of the crystal frame is the same as the pulling direction and the other where it is perpendicular. We will begin the discussion with the former.

Crystal frame rotated about the pulling direction

The microstructure shown in Fig. 8.14(b) is similar to Fig. 8.11(c) in terms of lamellar and finger morphologies with the influence of anisotropy showing up clearly only in the transverse section of the finger (see Fig. 8.16) which becomes polygonal. The longitudinal section in Fig. 8.15 reveals a lamellar arrangement which is also akin to its isotropic counterpart in Fig. 8.12.

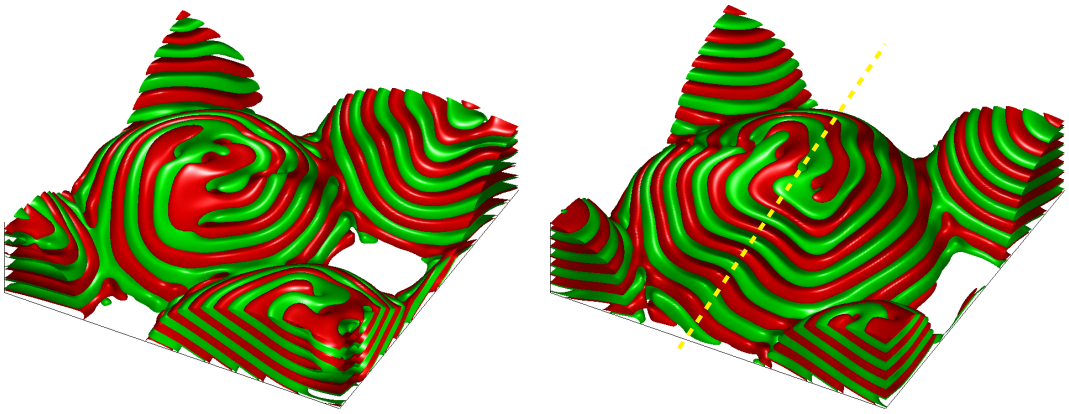

(a) (b)

Figure 8.14: Eutectic colonies at a total time of (a)28000, and (b)55000 in a system with solid-liquid interfacial energy anisotropy with $V = 0.1$, $\zeta = 0.015$, and $\theta_R = 10°$, clockwise, about the pulling direction. The yellow dashed line in (b) represents the orientation of the vertical sections reported in Fig. 8.15.

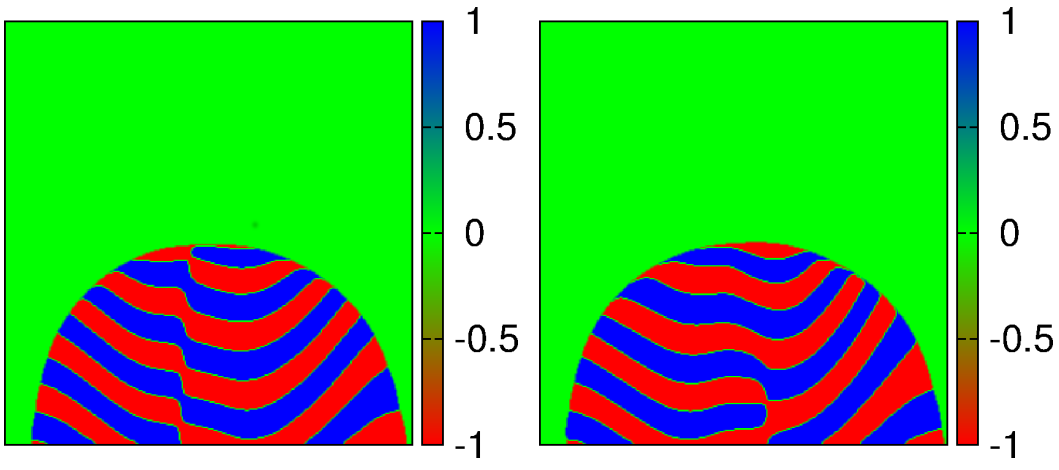

(a) (b)

Figure 8.15: 2D sections (u field) by a plane parallel to the pulling direction in Fig. 8.14(b), whose orientation is denoted by the yellow dotted line in Fig. 8.14(b). The section passes through and a little away from the axis of the finger in (a) and (b), respectively. Colorbars report values from the u field.

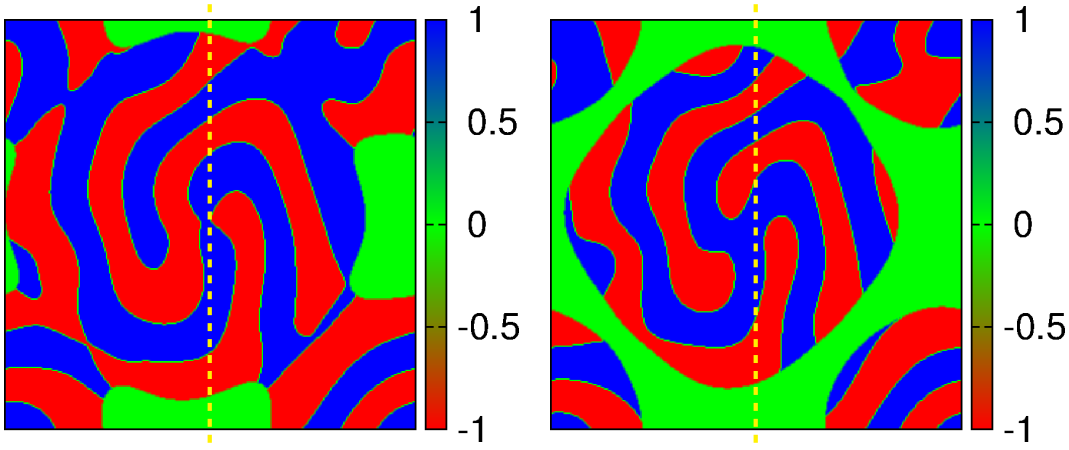

(a) (b)

Figure 8.16: 2D sections (u field) by a plane normal to the pulling direction in Fig. 8.14(b). The sectioning height is lower in (a) than in (b). Colorbars report values from the u field. The yellow line is the projection of the same from Fig. 8.14(b).

Crystal frame rotated about an axis normal to the pulling direction

Moving onto the situation where the reference frame of the crystal is rotated about an axis perpendicular to the direction of the imposed temperature gradient (see Fig. 8.17), we find fingers taking up well-defined orientations with respect to the pulling direction. The eutectic spirals in this case can be seen to be traversing the simulation box in a direction perpendicular to the pulling direction. This is due to the non-zero angle to the pulling direction taken up by the fingers while growth. Thus, the growth velocity has a lateral component which creates a traveling wave of eutectic fingers across the simulation box during growth.

Again, we consider sections of Fig. 8.17 which are parallel (Fig. 8.18) and normal (Fig. 8.19) to the pulling direction. The lack of a section which clearly demonstrates the axis as we have seen in Fig. 8.12(a), suggests that the finger axis is not completely contained in a single plane of such an orientation. The orientation of spirals is determined by a force balance along the tri-junction lines during its formation via the amplification of an instability, which being an unsteady phenomenon, can lead to orientations which deviate from the equilibrium orientation of interfacial planes. We can also add that, the observation of a finger axis in Fig. 8.12(a) is accidental and it could very well have been like the situation depicted here.

The sections in Fig. 8.19 are the ones which are taken to be perpendicular to the pulling direction and parallel to the axis of rotation. Here the individual phases are either elongated or curved with the concavity towards the solid-liquid interface which is quite different to what we observe for the isotropic case in Fig. 8.13 and can be understood as a consequence of the

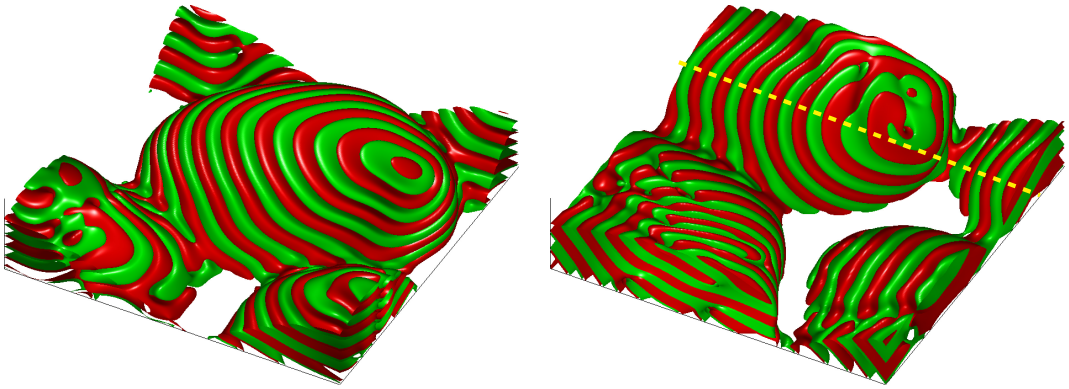

(a) (b)

Figure 8.17: Eutectic colonies at a total time of (a)22000, and (b)50000 in a system with solid-liquid interfacial energy anisotropy with $V = 0.1$, $\zeta = 0.015$ and $\theta_R = 10°$, clockwise, about an axis normal to the pulling direction. The yellow dashed line in (b) represents the orientation of the vertical sections reported in Fig. 8.18.

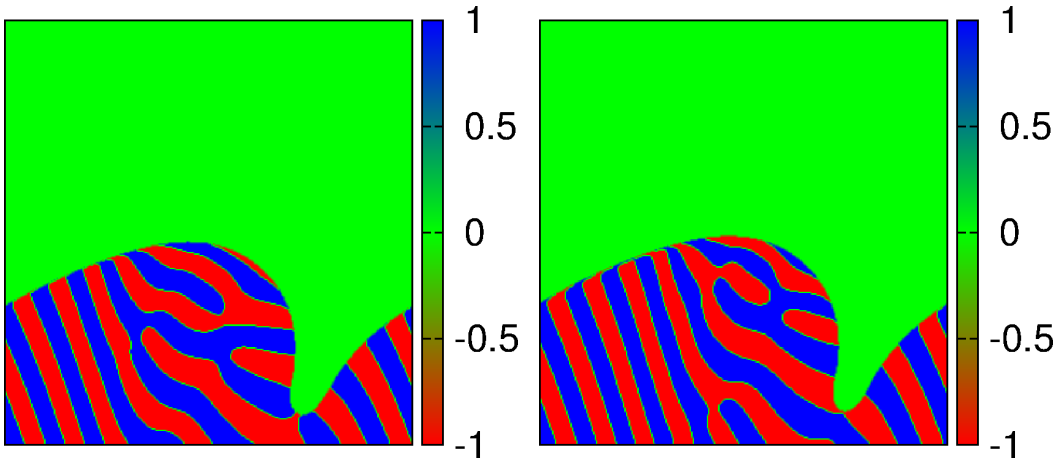

(a) (b)

Figure 8.18: 2D sections (u field) by a plane parallel to the pulling direction and normal to the axis of rotation of Fig. 8.17(b), whose orientation is denoted by the yellow dotted line in Fig. 8.17(b). Both figures (a) and (b) highlight that the axis of the finger is not straight. Colorbars report values from the u field.

tilt of the spirals.

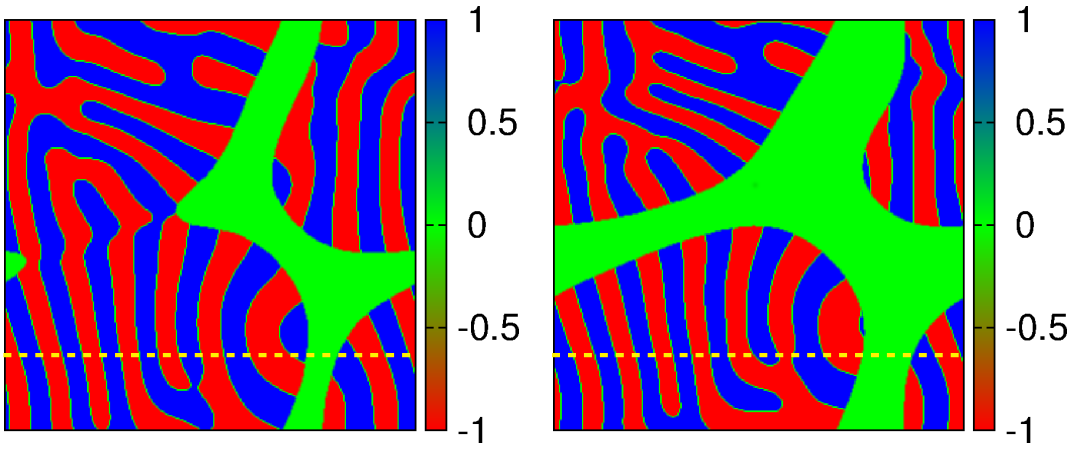

(a) (b)

Figure 8.19: 2D sections (u field) by a plane normal to the pulling direction and parallel to the axis of rotation of Fig. 8.17(b). The sectioning height is lower in (a) than in (b). Colorbars report values from the u field. The yellow line is the projection of the same from Fig. 8.17(b).

As we saw in 2D, the simulations done with an anisotropic solid-liquid interface leads to a stable finger width and orientation (see Figs. 8.14(a), 8.14(b), 8.17(a) and 8.17(b)) being selected. Thus, as opposed to the isotropic case, the spirals once formed never disintegrate, but only split when they coarsen beyond the system selected finger width.

Having understood the effect of anisotropic solid-liquid interface on the colony features in 3D, we do the same for solid-solid interfacial anisotropy in the following section.

8.4.2 Anisotropic solid-solid interface

The α-β interface can also have preferred orientations with respect to the direction of the imposed temperature gradient, resulting in novel patterns in the eutectic colonies. The introduction of anisotropy is done in the same way as in 2D (see Eq. 8.19); the anisotropy function a_c being given by Eq. 8.20 with u's taking the place of ϕ's.

In contrast to the stable spirals obtained for solid-liquid anisotropic interfacial energies, we do not get any spiraling for the crystal frame rotated about the pulling direction (Fig. 8.20(a)) and only intermittent spiraling for the situation where the crystal frame is rotated about a normal to the pulling direction (Fig. 8.20(b)) with the eutectic solids taking up certain well-defined orientations.

As can be seen from Fig. 8.20, that the consideration of a four-fold anisotropy in the solid-solid interfacial energy leads to individual eutectic solids to arrange themselves as alternate

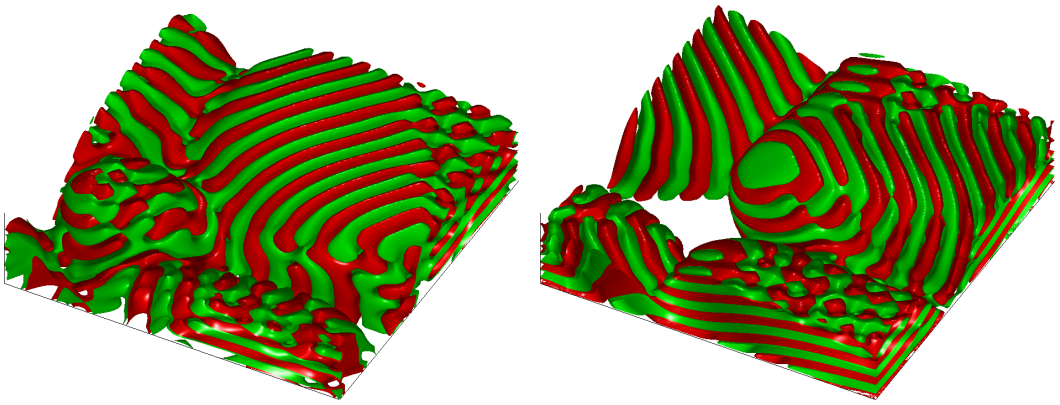

(a) (b)

Figure 8.20: Eutectic colonies in a system with α-β interfacial energy anisotropy with $V = 0.1$, $\zeta = 0.015$ and $\theta_R = 10°$, clockwise, about, (a)the pulling direction, and (b)normal to the pulling direction.

plates which take up orientations dictated by the anisotropy. The lack of a stabilizing influence of the imposed anisotropy required for forming spirals indicates that the equilibrium interfacial orientations do not allow the formation stable spirals.

8.5 Summary

We studied eutectic colony formation in both 2D and in 3D, in systems with preferred orientation of the solid-liquid as well as the solid-solid (α-β) interfaces. The 2D simulations with anisotropic solid-liquid interfacial energy display a stable finger spacing which has a definite orientation to the pulling direction decided by the imposed temperature gradient from the possibilities offered by equilibrium orientations of the solid-liquid interface under anisotropy. The stability of finger spacing is a function of the magnitude of anisotropy (ζ), with the system selecting a well defined finger width and tip radius only at higher ζ. Higher values of ζ also lead to a selection of a more pronounced orientation of the fingers with respect to the pulling direction. These observations stand in stark contrast to the isotropic simulation in 2D where neither a stable finger spacing nor a well-defined orientation is taken up by the fingers. At the solidification envelope, the lamellae are oriented normal to the solid-liquid interface (also observed in the isotropic case), with no specific orientation at the center of the fingers. The effect of a higher pulling velocity (V) on the simulations is to modify the length scales manifesting as smaller lamellar width and tip radius.

When studying 2D systems with anisotropic solid-solid (α-β) interfaces, we find a significant

portion of the lamellae to assume vertical or near-vertical orientations in conjunction with a slight tilt of the solid-liquid interface from the horizontal. As a consequence of this, the fingers appear much broader than what is seen for the isotropic and solid-liquid anisotropy case. With increase in ζ, the lamellae appear to favor the vertical orientation strongly, as more and more of them take up such orientations. Higher pulling velocities V, resulted in finer length scales in accordance to our observation in the solid-liquid anisotropy case.

Though eutectic spirals are observed in 3D isotropic simulations, they are not stable. The existing spirals disintegrate while new ones come into existence with this process repeating throughout the course of the simulation.

The 3D simulations performed with anisotropic solid-liquid interfaces, with the crystal frame rotated about the pulling direction, revealed spirals similar to the isotropic case with the solidification envelope appearing angular. While another study done with the crystal frame rotated about an axis normal to the pulling direction led to tilted spirals. A stable finger width is selected in both the simulations.

The introduction of anisotropy in the solid-solid (α-β) interfaces lead to unstable fingers in the simulations. The rotation of the crystal frame about the pulling direction does not create spirals, rather we find elongated lamellae along particular directions normal to the vertical, which modifies to form unstable spirals when the crystal frame is rotated about an axis normal to the pulling direction.

Our 2D simulations with solid-solid anisotropy have offered a possible explanation for the existence of lamellae oriented along the finger axis in Fig. 8.1. Through our 3D simulations, we are able to delineate the features of eutectic spirals [10] for anisotropic solid-liquid and solid-solid interfaces. Anisotropic solid-liquid interfaces lead to the formation of stable spirals while the choice of solid-solid anisotropy leads to unstable structures occasionally resembling spirals.

8.6 Discussion

We have attempted to understand pattern formation in eutectics in the presence of a ternary impurity under conditions of solid-liquid and solid-solid anisotropy. Here, through 2D simulations, we have tried to understand the effect of pulling velocity (V) and magnitude of the anisotropy (ζ) on the eutectic colony microstructures for a single given rotation of the crystal frame with respect to the laboratory frame (θ_R). The patterns possible for other θ_R's under different values of V remain unexplored. The 3D simulations are carried out at a single value of both θ_R and V. The existence of novel microstructures at other combinations of these two parameters cannot be ruled out and stands as a promising area for further study. Furthermore,

the absence of a stable spiral in 3D when considering solid-solid anisotropy, prompts a closer look at spiral formation and conditions which allow or impede spiraling. Experimental studies of colony formation in anisotropic systems are critical to this end which will serve as a guide for choosing appropriate anisotropy functions in models.

Though we have been able to present and understand a lot of features of eutectic colonies for anisotropic solid-liquid and solid-solid interfaces in this study, the high solute trapping encountered for higher values of ζ and V in this model point towards the possibility of employing classic solidification models [148, 200] for studying this problem to obviate this difficulty.

Chapter 9

Summary & Conclusions

In this thesis, we have studied several problems involving microstructure formation in multi-component alloys which have been investigated in detail in the preceding chapters. The phenomena considered range from growth of a single product phase to microstructure formation by coupled growth of multiple phases. In this chapter we review the key inferences from our study of each of the phenomena considered in the preceding chapters. The progress made in each of the topics in this thesis naturally points towards several phenomena which are closely aligned with the subjects considered but are yet to be theoretically understood for multi-component alloys. Hence, in the following paragraphs we mention all of these possible extensions of our theoretical framework which would encompass a larger proportion of phenomena leading to microstructure formation in multi-component alloys.

9.1 Single phase growth in multi-component alloys in the scaling regime

We extend Zener's theory [2] of growth in the scaling regime for binary alloys to multi-component alloys in Chapter 4. Our theory can predict not only the scaling constant, but also the tie-line compositions which are kinetically determined for multi-component alloys, unlike binary systems. We validate our theoretical predictions against phase-field simulations for both independent and coupled diffusion of solutes. We also generalize two limiting cases of diffusion controlled growth to multi-component alloys, which are relevant for large disparities in the solute diffusivities and clearly identify regimes in supersaturation over which they are applicable.

We have also shown that the predictions from a quantitative phase-field model (the Grand-

Potential model) are in great agreement with our analytical predictions. The mutual validation of the analytical theory and the phase-field model accomplished by this exercise justifies resorting to phase-field simulations when studying phase transformations in alloys producing complex microstructures which are analytically inaccessible. Growth and coarsening of multi-particle systems in multi-component alloys is one such problem which can be addressed by phase-field simulations.

9.2 Diffusive instabilities during single solid phase alloy solidification

In Chapter 5, we present a linear stability analysis of the solidification front during single phase solidification in multi-component alloys. Our analytical theory, corroborated by phase-field models, allows us to predict trends in the instability behavior as functions of solute diffusivities and velocities of steady-state growth fronts. Our theoretical analysis in Chapter 5 is concerned with the stability of a planar front during directional as well as isothermal solidification conditions. The corresponding analysis investigating the stability of a spherical nuclei in an undercooled melt is yet to be performed, which would complete the understanding of stability of interfaces having different geometries to random perturbations in multi-component alloys.

9.3 Isothermal dendrites in multi-component alloys

Free dendrite growth in uniformly undercooled multi-component alloys is analyzed next in Chapter 6. We solve for the solute diffusion problem in the liquid which is then combined with estimates of dendrite tip radius (in terms of the other parameters) to solve for the growth velocities and phase compositions. Our analytical predictions are found to be in reasonably good agreement with the ones from phase-field simulations.

Our theory can also be extended to steady-state growth of dendrites during directional solidification. The understanding of the selection of the tip-radius during growth of free dendrites leads to the question of how primary arm spacing of the dendrites are influenced by the solute interdiffusivities. This is a problem which is of direct importance to the selection of microstructural length scales in dendritic microstructures and will be addressed by us in future.

9.4 Theoretical and numerical investigation of multi-phase growth in a multi-component system

We present a unified Jackson-Hunt type calculation applicable to both invariant and non-invariant systems, in multi-component alloys in Chapter 7. Jackson and Hunt [8], in their original analysis for invariant growth, assume the compositions and volume fractions of the solid phases to be given by the equilibrium phase diagram. In our analysis, we relax these assumptions and determine these parameters as part of the solution itself. Our analysis is also able to capture the effects of solute diffusivities on the operating point of the eutectic, as confirmed by phase-field simulations.

Though the presented theory can describe situations involving growth of any number of solid phases in a multi-component alloy and allows us to determine departures of solid-phase fractions and phase compositions from those predicted by the phase diagram due to dissimilar diffusivities, it is still limited by some key assumptions. Our calculations of composition fields in the liquid are obtained assuming a planar interface, where from our phase-field simulations we know that they are far from being so. The assumption of equal undercoolings ahead of each of the solid-liquid interfaces is also not accurate, as the average location of each of the curved solid-liquid interface differ from each other whenever the solute diffusivities are not equal. So a more accurate theory where we compute the interface shapes along the lines of Magnin and Trivedi [166] for multi-component alloys can be proposed relaxing all these approximations.

9.5 Eutectic colony formation in systems with interfacial energy anisotropy

In Chapter 8 we explore the eutectic colony morphologies in the presence of anisotropic interfacial energies. Anisotropy leads to stable structures with well-defined finger orientations. The lamellae constituting individual fingers take up specific orientations when the interface separating the two eutectic solids are anisotropic.

Our simulations of colonies in 3D reveal structures where the two eutectic solid phases are arranged in a helical fashion about the finger axis. These structures have also been observed experimentally but the preference for such a morphological arrangement of phases is still unclear. A theoretical justification for such structures presents an exciting scope for future work.

9.6 Outlook

The central theme of this thesis is the development of an analytical framework for determining the length scales and phase-compositions during steady-state as well as unstable modes of phase-transformations in multi-component alloys. For transformations from one phase to another, a specific example of which considered in this thesis is the problem of single phase solidification, we have been able to provide analytical theories starting from the problem of stable growth by a planar front, to a linear stability analysis of such a front in the presence of infinitesimal perturbations, and finally an analysis of the steady-state growth of dendrites which are the products of instability. A similar route is taken for multi-phase systems where a generalized analytical theory is derived to describe steady-state eutectic solidification. Due to the complexity of such systems, a linear stability analysis of the perturbed solidification front and a theory for steady-state growth of multi-phase dendrites could not be presented, but instead they are addressed through phase-field simulations. All of our analytical theories have been validated against predictions from phase-field models and this exercise has led to a deeper understanding of the advantages and limitations of either approaches. In future, the work presented in this thesis can pave the way to a better understanding and appreciation of complicated experiments in multi-component solidification.

In this thesis, our primary focus has been solidification in multi-component alloys, and it deals exclusively with driving forces of chemical origin. But there are numerous transformations in multi-component systems where driving forces of mechanical, electrical, magnetic and electrochemical nature play a central role. Comprehensive analytical treatments of such systems are rare, although some progress has already been made through phase-field simulations. The derivation of analytical theories to predict the length scales, phase compositions and the rate of transformation for such systems would serve to unify the theoretical understanding of phase transformations in multi-component systems. An example of an interesting question in this regard could be the problem of determining interfacial compositions and growth rates in a solid-state precipitation system with lattice misfit. Another problem which has important technological implications, is the formation of dendrites during charging of Li-ion batteries. The dendrites in this case are primarily a result of electrochemical and capillary interactions in contrast to that of solute diffusion and capillary forces in case of dendrites observed during alloy solidification. A linear stability analysis along the lines of the one proposed in this thesis for solidification can be presented for the case where destabilization of the interface is due to electrochemical forces.

Developing phase-field models and their numerical implementation to study transformations

due to such myriad driving forces pose a challenge of their own. As these problems are defined by an interplay of different length scales originating from solute diffusion, surface tension and the length scales of the associated driving force of non-chemical nature, the model should be able to effectively resolve all of them. Another important factor to consider for making the models quantitatively accurate are the formulation of counterparts of anti-trapping current for problems encompassing different physics in addition to solute diffusion and capillary forces.

Multi-component alloys are key systems of interest today. Understanding the plethora of transformations in such systems are one of the foremost concerns of the materials science community. We hope that the ideas presented in this thesis contribute to the progress of the science of multi-component alloys in future.

Bibliography

[1] W. W. Mullins and R. F. Sekerka. Stability of a planar interface during solidification of a dilute binary alloy. *Journal of Applied Physics*, 35(2):444–451, 1964. iii, 2, 3, 8, 12, 19, 20, 172

[2] C. Zener. Theory of growth of spherical precipitates from solid solution. *Journal of Applied Physics*, 20(10):950–953, 1949. iv, v, 3, 5, 16, 24, 82, 83, 200

[3] J. Lipton, M. E. Glicksman, and W. Kurz. Dendritic growth into undercooled alloy metals. *Materials Science and Engineering*, 65(1):57–63, 1984. iv, 23

[4] J. Lipton, M. E. Glicksman, and W. Kurz. Equiaxed dendrite growth in alloys at small supercooling. *Metallurgical and Materials Transactions A*, 18(2):341–345, 1987. iv, 23, 113

[5] A. Lahiri, T. A. Abinandanan, and A. Choudhury. Theoretical and numerical study of growth in multi-component alloys. *Metallurgical and Materials Transactions A*, 2017. doi:10.1007/s11661-017-4215-6. v, 82, 91, 99, 119

[6] A. Lahiri and A. Choudhury. Theoretical and numerical investigation of diffusive instabilities in multi-component alloys. *Journal of Crystal Growth*, 459:1–12, 2017. vi, 75, 115

[7] A. Lahiri and A. Choudhury. Revisiting Jackson-Hunt calculations: Unified theoretical analysis for generic multi-phase growth in a multi-component system. *Acta Materialia*, 2017. ix

[8] K. A. Jackson and J. D. Hunt. Lamellar and rod eutectic growth. *Transactions of the Metallurgical Society of AIME*, 236:1129–1142, 1966. ix, 3, 10, 24, 25, 26, 134, 139, 178, 179, 202

[9] S. Akamatsu and G. Faivre. Traveling waves, two-phase fingers, and eutectic colonies in thin-sample directional solidification of a ternary eutectic alloy. *Physical Review E*, 61(4):3757, 2000. x, 15, 27

[10] S. Akamatsu, M. Perrut, S. Bottin-Rousseau, and G. Faivre. Spiral two-phase dendrites. *Physical Review Letters*, 104(5):056101, 2010. x, 3, 15, 27, 190, 198

[11] A. Lahiri, C. Tiwary, K. Chattopadhyay, and A. Choudhury. Eutectic colony formation in systems with interfacial energy anisotropy: A phase field study. *Computational Materials Science*, 130:109–120, 2017. x

[12] S. C. Huang and M. E. Glicksman. Overview 12: Fundamentals of dendritic solidification—i. steady-state tip growth. *Acta Metallurgica*, 29(5):701–715, 1981. 2, 20, 21, 22, 23

[13] P. K. Galenko, S. Reutzel, D. M. Herlach, S. G. Fries, I. Steinbach, and M. Apel. Dendritic solidification in undercooled Ni–Zr–Al melts: Experiments and modeling. *Acta Materialia*, 57(20):6166–6175, 2009. 2, 21

[14] M. Ginibre, S. Akamatsu, and G. Faivre. Experimental determination of the stability diagram of a lamellar eutectic growth front. *Physical Review E*, 56(1):780, 1997. 3, 23

[15] R. J. Contieri, C. T. Rios, M. Zanotello, and R. Caram. Growth and three-dimensional analysis of a Nb–Al–Ni ternary eutectic. *Materials Characterization*, 59(6):693–699, 2008. 3, 23

[16] M. Plapp and A. Karma. Eutectic colony formation: A phase-field study. *Physical Review E*, 66(6):061608, 2002. 3, 11, 13, 26, 28, 170, 172, 179

[17] D. E. Coates. Diffusion-controlled precipitate growth in ternary systems I. *Metallurgical Transactions*, 3(5):1203–1212, 1972. 5, 6, 17, 74

[18] D. E. Coates. Diffusion controlled precipitate growth in ternary systems: II. *Metallurgical Transactions*, 4(4):1077–1086, 1973. 5, 6, 17, 74

[19] D. E. Coates. Diffusional growth limitation and hardenability. *Metallurgical Transactions*, 4(10):2313–2325, 1973. 5, 7, 18, 59, 60, 61, 74

[20] J. P. Bourne, C. Atkinson, and R. C. Reed. Diffusion-controlled growth in ternary systems. *Metallurgical and Materials Transactions A*, 25(12):2683–2694, 1994. 5, 6, 17, 74

[21] A. Choudhury. *Quantitative phase-field model for phase transformations in multi-component alloys*, volume Band 21. KIT Scientific Publishing, 2012. 6, 8, 38, 40, 41

[22] M. Plapp. Unified derivation of phase-field models for alloy solidification from a grand-potential functional. *Physical Review E*, 84(3):031601, 2011. 6, 8

[23] A. Choudhury, M. Kellner, and B. Nestler. A method for coupling the phase-field model based on a grand potential formalism to databases. *Current Opinion in Solid State and Materials Science*, 19:287–300, 2015. 6, 74

[24] M. Hillert. Solute drag, solute trapping and diffusional dissipation of gibbs energy. *Acta Materialia*, 47(18):4481–4505, 1999. 7, 18

[25] M. Hillert, J. Odqvist, and J. Ågren. Comparison between solute drag and dissipation of gibbs energy by diffusion. *Scripta materialia*, 45(2):221–227, 2001. 7, 18

[26] J. Odqvist, B. Sundman, and J. Ågren. A general method for calculating deviation from local equilibrium at phase interfaces. *Acta Materialia*, 51(4):1035–1043, 2003. 7, 18

[27] K. Fisher and W. Kurz. Fundamentals of solidification. *Trans Tech Publications*, 1986. 7

[28] D. E. Coates, S. V. Subramanian, and G. R. Purdy. Solid-liquid interface stability during solidification of dilute ternary alloys. *Transactions of the Metallurgical Society of AIME*, 242(5):800–809, 1968. 8, 20, 79

[29] O. Hunziker. Theory of plane front and dendritic growth in multicomponent alloys. *Acta materialia*, 49(20):4191–4203, 2001. 8, 9, 10, 20, 22

[30] G. P. Ivantsov. Temperature field around a spherical, cylindrical, and needle-shaped crystal, growing in a pre-cooled melt. *Temperature field around a spherical, cylindrical, and needle-shaped crystal, growing in a pre-cooled melt Transl. into ENGLISH of"" Temperaturnuye Pole Vokrug Sharoobraznogo Tsilindricheskogo i Igloobrazno go Kristalla Rastushchego v Pereokhlazhdennom Rasplave"Doklady, Akademiya Nauk SSR, v. 58, 1947 p 567-569*, 1985. 9, 21, 104, 105, 124

[31] G. Horvay and J. W. Cahn. Dendritic and spheroidal growth. *Acta Metallurgica*, 9(7):695–705, 1961. 9, 21, 105, 124

[32] J. S. Langer and H. Müller-Krumbhaar. Theory of dendritic growth—I. elements of a stability analysis. *Acta Metallurgica*, 26(11):1681–1687, 1978. 9, 22, 111, 124

[33] J. S. Langer and H. Müller-Krumbhaar. Theory of dendritic growth—II. instabilities in the limit of vanishing surface tension. *Acta Metallurgica*, 26(11):1689–1695, 1978. 9, 22

[34] H. Müller-Krumbhaar and J. S. Langer. Theory of dendritic growth—III. effects of surface tension. *Acta Metallurgica*, 26(11):1697–1708, 1978. 9, 22, 113

[35] D. A. Kessler and H. Levine. Velocity selection in dendritic growth. *Physical Review B*, 33(11):7867, 1986. 9, 22, 113, 124

[36] W. Kurz. Eutectic growth before and after Jackson & Hunt 1966. *Solidification science and technology,John Hunt Intern. Symp.,Z. Fan and IC Stone, eds*, pages 1–15, 2011. 10

[37] D. G. Mccartney, J. D. Hunt, and R. M. Jordan. The structures expected in a simple ternary eutectic system: Part 1. theory. *Metallurgical Transactions A*, 11(8):1243–1249, 1980. 11, 26

[38] T. Himemiya and T. Umeda. Three-phase planar eutectic growth models for a ternary eutectic system. *Materials Transactions, JIM*, 40(7):665–674, 1999. 11, 26

[39] A. Choudhury, M. Plapp, and B. Nestler. Theoretical and numerical study of lamellar eutectic three-phase growth in ternary alloys. *Physical Review E*, 83:051608, May 2011. 11, 26, 135, 138, 139, 140, 160, 164, 168

[40] R. Trivedi, P Magnin, and W. Kurz. Theory of eutectic growth under rapid solidification conditions. *Acta Metallurgica*, 35(4):971–980, 1987. 11, 25, 26

[41] L. F. Donaghey and W. A. Tiller. On the diffusion of solute during the eutectoid and eutectic transformations, part I. *Materials Science and Engineering*, 3(4):231 – 239, 1968. 11, 25

[42] A. V. Catalina, P. W. Voorhees, R. K. Huff, and A. L. Genau. A model for eutectic growth in multicomponent alloys. *IOP Conference Series: Materials Science and Engineering*, 84(1):012085, 2015. 12, 27

[43] O. Senninger and P. W. Voorhees. Eutectic growth in two-phase multicomponent alloys. *Acta Materialia*, 116:308 – 320, 2016. 12, 27, 141, 148, 168

[44] M. Plapp and A. Karma. Eutectic colony formation: A stability analysis. *Physical Review E*, 60(6):6865, 1999. 13, 28

[45] R. L. Fullman and D. L. Wood. Origin of spiral eutectic structures. *Acta Metallurgica*, 2(2):188191–189193, 1954. 13, 28

[46] H. Y. Liu and H. Jones. Solidification microstructure selection and characteristics in the zinc-based Zn-Mg system. *Acta metallurgica et materialia*, 40(2):229–239, 1992. 13, 28

[47] S. Ghosh, A. Choudhury, M. Plapp, S. Bottin-Rousseau, G. Faivre, and S. Akamatsu. Interphase anisotropy effects on lamellar eutectics: A numerical study. *Physical Review E*, 91(2):022407, 2015. 13, 28, 185

[48] S. Akamatsu, S. Bottin-Rousseau, M. Şerefoğlu, and G. Faivre. A theory of thin lamellar eutectic growth with anisotropic interphase boundaries. *Acta Materialia*, 60(6):3199–3205, 2012. 13, 28, 185

[49] S. Akamatsu, S. Bottin-Rousseau, M. Şerefoğlu, and G. Faivre. Lamellar eutectic growth with anisotropic interphase boundaries: Experimental study using the rotating directional solidification method. *Acta Materialia*, 60(6):3206–3214, 2012. 13, 28, 185

[50] T. Pusztai, L. Rátkai, A. Szállás, and L. Gránásy. Spiraling eutectic dendrites. *Physical Review E*, 87(3):032401, 2013. 13, 28, 170

[51] L. Rátkai, A. Szállás, T. Pusztai, T. Mohri, and L. Gránásy. Ternary eutectic dendrites: Pattern formation and scaling properties. *The Journal of Chemical Physics*, 142(15):154501, 2015. 13, 28, 170

[52] F. C. Frank. Radially symmetric phase growth controlled by diffusion. *Proceedings of the Royal Society of London A: Mathematical, Physical and Engineering Sciences*, 201(1067):586–599, 1950. 16, 82, 83

[53] F. S. Ham. Theory of diffusion-limited precipitation. *Journal of Physics and Chemistry of Solids*, 6(4):335–351, 1958. 16

[54] J. A. Van Beek, A. A. Kodentsov, and F. J. J. Van Loo. Phase relations in the Ag-Fe-Ti system at 1123 K. *Journal of Alloys and Compounds*, 221(1-2):108–113, 1995. 17

[55] J.A. van Beek, A.A. Kodentsov, and F.J.J. van Loo. Phase equilibria in the Cu-Fe-Ti system at 1123 k. *Journal of Alloys and Compounds*, 217(1):97 – 103, 1995. 17

[56] A. A. Kodentsov, G. F. Bastin, and F. J. J. Van Loo. The diffusion couple technique in phase diagram determination. *Journal of Alloys and Compounds*, 320(2):207–217, 2001. 17

[57] A. Paul, T. Laurila, V. Vuorinen, and S. V. Divinski. *Thermodynamics, diffusion and the Kirkendall effect in solids*. Springer, 2014. 17

[58] A. Kodentsov and A. Paul. Chapter 6 - diffusion couple technique: A research tool in materials science. In A. Paul, , and S. Divinski, editors, *Handbook of Solid State Diffusion, Volume 2*, pages 207 – 275. Elsevier, 2017. 17

[59] P. Maugis, W. D. Hopfe, J. E. Morral, and J. S. Kirkaldy. Degeneracy of diffusion paths in ternary, two-phase diffusion couples. *Journal of Applied Physics*, 79(10):7592–7595, 1996. 17

[60] P. Maugis, W. D. Hopfe, J. E. Morral, and J. S. Kirkaldy. Multiple interface velocity solutions for ternary biphase infinite diffusion couples. *Acta materialia*, 45(5):1941–1954, 1997. 17

[61] D. E. Coates and J. S. Kirkaldy. Morphological stability of α-β phase interfaces in the Cu-Zn- Ni system at 775°C. *Metallurgical and Materials Transactions B*, 2(12):3467–3477, 1971. 17, 74

[62] S. R. Coriell, G. B. McFadden, R. F. Sekerka, and W. J. Boettinger. Multiple similarity solutions for solidification and melting. *Journal of Crystal Growth*, 191(3):573–585, 1998. 17

[63] S. R. Coriell, G. B. McFadden, and R. F. Sekerka. Selection mechanisms for multiple similarity solutions for solidification and melting. *Journal of Crystal Growth*, 200(1):276–286, 1999. 17

[64] J. Andersson and J. Ågren. Models for numerical treatment of multicomponent diffusion in simple phases. *Journal of Applied Physics*, 72(4):1350–1355, 1992. 18

[65] A. Borgenstam, L. Höglund, J. Ågren, and A. Engström. Dictra, a tool for simulation of diffusional transformations in alloys. *Journal of Phase Equilibria*, 21(3):269–280, 2000. 18

[66] B. Sundman, B. Jansson, and J. Andersson. The thermo-calc databank system. *Calphad*, 9(2):153–190, 1985. 18

[67] S. L. Chen, S. Daniel, F. Zhang, Y. A. Chang, X. Y. Yan, F. Y. Xie, R. Schmid-Fetzer, and W. A. Oates. The pandat software package and its applications. *Calphad*, 26(2):175–188, 2002. 18

[68] W. Cao, S. L. Chen, F. Zhang, K. Wu, Y. Yang, Y. A. Chang, R. Schmid-Fetzer, and W. A. Oates. Pandat software with panengine, panoptimizer and panprecipitation for multi-component phase diagram calculation and materials property simulation. *Calphad*, 33(2):328–342, 2009. 18

[69] A. Engström, L. Höglund, and J. Ågren. Computer simulation of diffusion in multiphase systems. *Metallurgical and Materials Transactions A*, 25(6):1127–1134, 1994. 18

[70] Q. Chen, J. Jeppsson, and J. Ågren. Analytical treatment of diffusion during precipitate growth in multicomponent systems. *Acta materialia*, 56(8):1890–1896, 2008. 18

[71] A. Schneider and G. Inden. Simulation of the kinetics of precipitation reactions in ferritic steels. *Acta Materialia*, 53(2):519–531, 2005. 18

[72] H. Larsson and R. C. Reed. On the numerical simulation of diffusion-controlled reactions under local equilibrium conditions. *Acta Materialia*, 56(15):3754–3760, 2008. 18

[73] J. B. Gilmour, G. R. Purdy, and J. S. Kirkaldy. Thermodynamics controlling the proeutectoid ferrite transformations in Fe-C-Mn alloys. *Metallurgical Transactions*, 3(6):1455–1464, 1972. 18

[74] R. Mukherjee, T.A. Abinandanan, and M.P. Gururajan. Phase field study of precipitate growth: Effect of misfit strain and interface curvature. *Acta Materialia*, 57(13):3947 – 3954, 2009. 18

[75] R. Mukherjee, T.A. Abinandanan, and M.P. Gururajan. Precipitate growth with composition-dependent diffusivity: Comparison between theory and phase field simulations. *Scripta Materialia*, 62(2):85 – 88, 2010. 18

[76] Q. Chen, N. Ma, K. Wu, and Y. Wang. Quantitative phase field modeling of diffusion-controlled precipitate growth and dissolution in Ti–Al–V. *Scripta Materialia*, 50(4):471–476, 2004. 18

[77] R.S. Qin, E.R. Wallach, and R.C. Thomson. A phase-field model for the solidification of multicomponent and multiphase alloys. *Journal of Crystal Growth*, 279(1–2):163 – 169, 2005. 18

[78] B. Böttger, J. Eiken, and I. Steinbach. Phase field simulation of equiaxed solidification in technical alloys. *Acta materialia*, 54(10):2697–2704, 2006. 18, 21

[79] I. Steinbach, B. Böttger, J. Eiken, N. Warnken, and S. G. Fries. Calphad and phase-field modeling: A successful liaison. *Journal of Phase Equilibria and Diffusion*, 28(1):101–106, 2007. 18

[80] N. Warnken, D. Ma, A. Drevermann, R.C. Reed, S.G. Fries, and I. Steinbach. Phase-field modelling of as-cast microstructure evolution in nickel-based superalloys. *Acta Materialia*, 57(19):5862 – 5875, 2009. 18

[81] B. Böttger, A. Carré, J. Eiken, G. J. Schmitz, and M. Apel. Simulation of microstructure formation in technical aluminum alloys using the multiphase-field method. *Transactions of the Indian Institute of Metals*, 62(4):299–304, 2010. 18

[82] J. Lentz, A. Röttger, and W. Theisen. Solidification and phase formation of alloys in the hypoeutectic region of the Fe–C–B system. *Acta Materialia*, 99:119 – 129, 2015. 18

[83] J. Heulens, B. Blanpain, and N. Moelans. Phase-field analysis of a ternary two-phase diffusion couple with multiple analytical solutions. *Acta Materialia*, 59(10):3946 – 3954, 2011. 18

[84] D. H. Yeon, P. R. Cha, and J. K. Yoon. A phase field study for ferrite–austenite transitions under para-equilibrium. *Scripta Materialia*, 45(6):661–668, 2001. 18

[85] J. W. Rutter and B. Chalmers. A prismatic substructure formed during solidification of metals. *Canadian Journal of Physics*, 31(1):15–39, 1953. 19

[86] W. A. Tiller, K. A. Jackson, J. W. Rutter, and B. Chalmers. The redistribution of solute atoms during the solidification of metals. *Acta metallurgica*, 1(4):428–437, 1953. 19

[87] D. E. Temkin. Growth rate of the needle-crystal formed in a supercooled melt. In *Soviet Physics Doklady*, volume 5, page 609, 1960. 19, 21, 22

[88] B. Echebarria, R. Folch, A. Karma, and M. Plapp. Quantitative phase-field model of alloy solidification. *Physical Review E*, 70(6):061604, 2004. 19, 31

[89] R. Trivedi and W. Kurz. Morphological stability of a planar interface under rapid solidification conditions. *Acta metallurgica*, 34(8):1663–1670, 1986. 20

[90] G. J. Merchant and S. H. Davis. Morphological instability in rapid directional solidification. *Acta metallurgica et materialia*, 38(12):2683–2693, 1990. 20

[91] D. A. Huntley and S. H. Davis. Thermal effects in rapid directional solidification: linear theory. *Acta metallurgica et materialia*, 41(7):2025–2043, 1993. 20

[92] S. R. Coriell, G. B. McFadden, P. W. Voorhees, and R. F. Sekerka. Stability of a planar interface during solidification of a multicomponent system. *Journal of Crystal Growth*, 82(3):295–302, 1987. 20, 75, 79

[93] F. Weinberg and B. Chalmers. Dendritic growth in lead. *Canadian Journal of Physics*, 29(5):382–392, 1951. 20

[94] F. Weinberg and B. Chalmers. Further observations on dendritic growth in metals. *Canadian Journal of Physics*, 30(5):488–502, 1952. 20

[95] M. E. Glicksman, R. J. Schaefer, and J. D. Ayers. Dendritic growth-a test of theory. *Metallurgical Transactions A*, 7(11):1747–1759, 1976. 20

[96] M. E. Glicksman. Free dendritic growth. *Materials Science and Engineering*, 65(1):45–55, 1984. 20, 21, 22, 23

[97] C. S. Lindenmeyer and B. Chalmers. Growth rate of ice dendrites in aqueous solutions. *The Journal of Chemical Physics*, 45(8):2807–2808, 1966. 20

[98] M. E. Glicksman, N. B. Singh, M. Chopra, and G. E. Rindone. Materials processing in the reduced gravity environment of space. In *Proc. Symp. of the Materials Research Society, North-Holland, Amsterdam*, page 461, 1982. 20

[99] R. Trivedi and K. Somboonsuk. Constrained dendritic growth and spacing. *Materials science and engineering*, 65(1):65–74, 1984. 20

[100] M. A. Chopra, M. E. Glicksman, and N. B. Singh. Dendritic solidification in binary alloys. *Metallurgical Transactions A*, 19(12):3087–3096, 1988. 20

[101] L. X. Liu and J. S. Kirkaldy. Thin film forced velocity cells and cellular dendrites—I. experiments. *Acta metallurgica et materialia*, 43(8):2891–2904, 1995. 21

[102] T. Haxhimali, A. Karma, F. Gonzales, and M. Rappaz. Orientation selection in dendritic evolution. *Nature Materials*, 5(8):660–664, 2006. 21

[103] S. A. David, S. S. Babu, and J. M. Vitek. Welding: Solidification and microstructure. *JOM Journal of the Minerals, Metals and Materials Society*, 55(6):14–20, 2003. 21

[104] Jan Schroers, Dirk Holland-Moritz, Dieter M Herlach, and Knut Urban. Growth kinetics of quasicrystalline and polytetrahedral phases of al-pd-mn, al-co, and al-fe from the undercooled melt. *Physical Review B*, 61(21):14500, 2000. 21

[105] R. Kobayashi. Modeling and numerical simulations of dendritic crystal growth. *Physica D: Nonlinear Phenomena*, 63(3-4):410–423, 1993. 21, 30

[106] A. A. Wheeler, B. T. Murray, and R. J. Schaefer. Computation of dendrites using a phase field model. *Physica D: Nonlinear Phenomena*, 66(1-2):243–262, 1993. 21, 30

[107] J. A. Warren and W. J. Boettinger. Prediction of dendritic growth and microsegregation patterns in a binary alloy using the phase-field method. *Acta Metallurgica et Materialia*, 43(2):689–703, 1995. 21, 30

[108] C. W. Lan and C. J. Shih. Phase field simulation of non-isothermal free dendritic growth of a binary alloy in a forced flow. *Journal of Crystal Growth*, 264(1):472–482, 2004. 21

[109] C. W. Lan and C. J. Shih. Efficient phase field simulation of a binary dendritic growth in a forced flow. *Physical Review E*, 69(3):031601, 2004. 21

[110] J. C. Ramirez, C. Beckermann, A. Karma, and H. J. Diepers. Phase-field modeling of binary alloy solidification with coupled heat and solute diffusion. *Physical Review E*, 69(5):051607, 2004. 21

[111] J. C. Ramirez and C. Beckermann. Examination of binary alloy free dendritic growth theories with a phase-field model. *Acta Materialia*, 53(6):1721–1736, 2005. 21

[112] B. Böttger, J. Eiken, and M. Apel. Phase-field simulation of microstructure formation in technical castings–a self-consistent homoenthalpic approach to the micro–macro problem. *Journal of Computational Physics*, 228(18):6784–6795, 2009. 21

[113] M. Wang, T. Jing, and B. Liu. Phase-field simulations of dendrite morphologies and selected evolution of primary α-Mg phases during the solidification of Mg-rich Mg–Al-based alloys. *Scripta Materialia*, 61(8):777–780, 2009. 21

[114] E. Ben-Jacob, N. Goldenfeld, J. S. Langer, and G. Schön. Boundary-layer model of pattern formation in solidification. *Physical Review A*, 29(1):330, 1984. 21

[115] R. Trivedi. Growth of dendritic needles from a supercooled melt. *Acta Metallurgica*, 18(3):287–296, 1970. 22

[116] G. E. Nash and M. E. Glicksman. Capillarity-limited steady-state dendritic growth—I. theoretical development. *Acta Metallurgica*, 22(10):1283–1290, 1974. 22

[117] W. Oldfield. Computer model studies of dendritic growth. *Materials Science and Engineering*, 11(4):211–218, 1973. 22

[118] A. Karma and W. J. Rappel. Phase-field method for computationally efficient modeling of solidification with arbitrary interface kinetics. *Physical Review E*, 53(4):R3017, 1996. 22, 31, 113

[119] A. Karma and W. J. Rappel. Numerical simulation of three-dimensional dendritic growth. *Physical Review Letters*, 77(19):4050, 1996. 22, 113

[120] A. Karma and W. J. Rappel. Phase-field simulation of three-dimensional dendrites: is microscopic solvability theory correct? *Journal of Crystal Growth*, 174(1-4):54–64, 1997. 22, 113

[121] A. Karma and W. J. Rappel. Quantitative phase-field modeling of dendritic growth in two and three dimensions. *Physical review E*, 57(4):4323, 1998. 22, 31, 113, 181

[122] W. Kurz, B. Giovanola, and R. Trivedi. Theory of microstructural development during rapid solidification. *Acta Metallurgica*, 34(5):823–830, 1986. 22

[123] M. Bobadilla, J. Lacaze, and G. Lesoult. Influence des conditions de solidification sur le déroulement de la solidification des aciers inoxydables austénitiques. *Journal of Crystal Growth*, 89(4):531–544, 1988. 22

[124] M. Rappaz, S. A. David, J. M. Vitek, and L. A. Boatner. Analysis of solidification microstructures in Fe-Ni-Cr single-crystal welds. *Metallurgical transactions A*, 21(6):1767–1782, 1990. 22

[125] J. S. Langer. Dendritic solidification of dilute solutions. *Physico-Chemical Hydrodynamics*, 1:44, 1980. 22

[126] A. Karma and J. S. Langer. Impurity effects in dendritic solidification. *Physical Review A*, 30(6):3147, 1984. 23

[127] J. P. Chilton and W. C. Winegard. Solidification of a eutectic made from zone-refined lead and tin. *Journal of the Institute of Metals*, 89(5):162–164, 1961. 23, 27

[128] A. S. Yue. Microstructure of magnesium-aluminum eutectic. *Transactions of the Metallurgical Society of AIME*, 224(5):1010, 1962. 23

[129] G. A. Chadwick. Eutectic alloy solidification. *Progress in materials science*, 12:99–182, 1963. 23

[130] V. Seetharaman and R. Trivedi. Eutectic growth: Selection of interlamellar spacings. *Metallurgical Transactions A*, 19(12):2955–2964, 1988. 23

[131] G. Faivre and J. Mergy. Tilt bifurcation and dynamical selection by tilt domains in thin-film lamellar eutectic growth: Experimental evidence of a tilt bifurcation. *Physical Review A*, 45(10):7320, 1992. 23

[132] S. Akamatsu, G. Faivre, and S. Moulinet. The formation of lamellar-eutectic grains in thin samples. *Metallurgical and Materials Transactions A*, 32(8):2039–2048, 2001. 23

[133] J. D. Hunt and J. P. Chilton. An investigation of lamella-rod transition in binary eutectics. *Journal of the Institute of Metals*, 91(10):338, 1963. 23

[134] M. G. Day and A. Hellawell. The lamellar-fibre transition in the aluminium-zinc eutectic. *J. Aust. Inst. Metals*, 9:21, 1964. 23

[135] F. D. Lemkey, R. W. Hertzberg, and J. A. Ford. Microstructure crystallography and mechanical behavior of unidirectionally solidified Al-Al_3Ni eutectic. *Transactions of the Metallurgical Society of AIME*, 233(2):334, 1965. 23

[136] H. W. Kerr, A. Plumtree, and W. C. Winegard. Structure of tin-lead-cadmium eutectic. *Journal of the Institute of Metals*, 93(2):63, 1964. 23

[137] H. Bao and F. C. L. Durand. Morphologie eutectique dans le système Cd-Pb-Sn. *Journal of Crystal Growth*, 15(4):291–295, 1972. 23

[138] J. D. Holder and B. F. Oliver. The directional solidification of Pb-Sn-Cd alloys. *Metallurgical Transactions*, 5(11):2423–2437, 1974. 23

[139] DJS Cooksey and A Hellawell. The microstructures of ternary eutectic alloys in the systems Cd-Sn-(Pb, In, Tl), Al-Cu-(Mg, Zn, Ag), and Zn-Sn-Pb. *Journal of the Institute of Metals*, 95(6):183–187, 1967. 23

[140] M. D. Rinaldi, R. M. Sharp, and M. C. Flemings. Growth of ternary composites from the melt: Part II. *Metallurgical Transactions*, 3(12):3139–3148, 1972. 23, 27

[141] M. A. Ruggiero and J. W. Rutter. Origin of microstructure in 350 K eutectic of Bi–In–Sn ternary system. *Materials science and technology*, 11(2):136–142, 1995. 23

[142] S. Rex, B. Böttger, V. Witusiewicz, and U. Hecht. Transient eutectic solidification in In–Bi–Sn: two-dimensional experiments and numerical simulation. *Materials Science and Engineering: A*, 413:249–254, 2005. 23

[143] A. L. Genau and L. Ratke. Crystal orientation and morphology in Al-Ag-Cu ternary eutectic. In *IOP Conference Series: Materials Science and Engineering*, volume 27, page 012032. IOP Publishing, 2012. 23

[144] A. Dennstedt and L. Ratke. Microstructures of directionally solidified Al–Ag–Cu ternary eutectics. *Transactions of the Indian Institute of Metals*, 65(6):777–782, 2012. 23

[145] A. Dennstedt, L. Ratke, A. Choudhury, and B. Nestler. New metallographic method for estimation of ordering and lattice parameter in ternary eutectic systems. *Metallography, Microstructure, and Analysis*, 2(3):140–147, 2013. 23

[146] K. A. Jackson and J. D. Hunt. Transparent compounds that freeze like metals. *Acta Metallurgica*, 13(11):1212–1215, 1965. 23

[147] V. T. Witusiewicz, L. Sturz, U. Hecht, and S. Rex. Phase equilibria and eutectic growth in quaternary organic alloys amino-methyl-propanediol–(D) camphor–neopentylglycol–succinonitrile (AMPD–DC–NPG–SCN). *Journal of Crystal Growth*, 297(1):117–132, 2006. 23

[148] R. Folch and M. Plapp. Quantitative phase-field modeling of two-phase growth. *Physical Review E*, 72(1):011602, 2005. 23, 31, 151, 199

[149] A. Parisi and M. Plapp. Stability of lamellar eutectic growth. *Acta Materialia*, 56(6):1348–1357, 2008. 23

[150] A. Parisi and M. Plapp. Defects and multistability in eutectic solidification patterns. *Europhysics Letters*, 90(2):26010, 2010. 23

[151] A. Choudhury. Pattern-formation during self-organization in three-phase eutectic solidification. *Transactions of the Indian Institute of Metals*, 68(6):1137–1143, 2015. 23, 149

[152] A. Choudhury, Y. C. Yabansu, S. R. Kalidindi, and A. Dennstedt. Quantification and classification of microstructures in ternary eutectic alloys using 2-point spatial correlations and principal component analyses. *Acta Materialia*, 110:131–141, 2016. 23, 169

[153] P. Steinmetz, J. Hötzer, M. Kellner, A. Dennstedt, and B. Nestler. Large-scale phase-field simulations of ternary eutectic microstructure evolution. *Computational Materials Science*, 117:205–214, 2016. 23

[154] P. Steinmetz, M. Kellner, J. Hötzer, A. Dennstedt, and B. Nestler. Phase-field study of the pattern formation in Al–Ag–Cu under the influence of the melt concentration. *Computational Materials Science*, 121:6–13, 2016. 23

[155] J. Hötzer, M. Jainta, P. Steinmetz, B. Nestler, A. Dennstedt, A. Genau, M. Bauer, H. Köstler, and U. Rüde. Large scale phase-field simulations of directional ternary eutectic solidification. *Acta Materialia*, 93:194–204, 2015. 23, 28

[156] J. H., P. Steinmetz, M. Jainta, S. Schulz, M. Kellner, B. Nestler, A. Genau, A. Dennstedt, M. Bauer, H. Köstler, and U. Rüde. Phase-field simulations of spiral growth during directional ternary eutectic solidification. *Acta Materialia*, 106:249 – 259, 2016. 23

[157] U. Hecht, L. Gránásy, T. Pusztai, B. Böttger, M. Apel, V. Witusiewicz, L. Ratke, J. De Wilde, L. Froyen, D. Camel, B. Drevet, G. Faivre, S.G. Fries, B. Legendre, and S. Rex. Multiphase solidification in multicomponent alloys. *Materials Science and Engineering: R: Reports*, 46(1):1 – 49, 2004. 23, 160

[158] C. Zener. Kinetics of the decomposition of austenite. *Trans. AIME*, 167(550595.8), 1946. 23, 24

[159] W. H. Brandt. Solution of the diffusion equation applicable to the edgewise growth of pearlite. *Journal of Applied Physics*, 16(3):139–146, 1945. 24

[160] W. A. Tiller. Liquid metals and solidification. *ASM, Cleveland, Ohio*, 276, 1958. 24

[161] W. A. Tiller. Liquid metals and solidification. *Jernkontorets Annaler*, 144:520, 1960. 24

[162] K. A. Jackson, G. A. Chadwick, and Klugert A. Thermal effects in rapid directional solidification: linear theory. *Transactions of the Metallurgical Society of AIME*, 230:1547, 1964. 24

[163] R. W. Series, J. D. Hunt, and K. A. Jackson. The use of an electric analogue to solve the lamellar eutectic diffusion problem. *Journal of Crystal Growth*, 40(2):221–233, 1977. 25

[164] A. Ludwig and S. Leibbrandt. Generalised 'Jackson–Hunt' model for eutectic solidification at low and large Peclet numbers and any binary eutectic phase diagram. *Materials Science and Engineering: A*, 375–377:540 – 546, 2004. 25, 26

[165] P. Magnin, J. T. Mason, and R. Trivedi. Growth of irregular eutectics and the Al-Si system. *Acta metallurgica et materialia*, 39(4):469–480, 1991. 26, 168

[166] P. Magnin and R. Trivedi. Eutectic growth: A modification of the Jackson and Hunt theory. *Acta metallurgica et materialia*, 39(4):453–467, 1991. 26, 168, 202

[167] R. W. Kraft and D. L. Albright. Microstructure of unidirectionally solidified Al-$CuAl_2$ eutectic. *Transactions of the Metallurgical Society of AIME*, 221(1):95–102, 1961. 27

[168] J. D. Hunt and K. A. Jackson. Binary eutectic solidification. *Transactions of the Metallurgical Society of AIME*, 236(6):843, 1966. 27

[169] W. M. Rumball. Cellular growth in eutectic systems. *Metallurgia*, 78(468):141–145, 1968. 27

[170] P. K. Rohatgi and C. M. J. R. Adams. Colony and dendritic structures produced on solidification of eutectic aluminum copper alloy. *Transactions of the Metallurgical Society of AIME*, 245(7):1609–1613, 1969. 27

[171] J. B. Bullock, C. J. Simpson, J. A. Eady, and W. C. Winegard. Cell formation as the result of adding Cd or Sb to the Pb-Sn eutectic. *Journal of the Institute of Metals*, 99:212–214, 1971. 27

[172] S. A. Souza, C. T. Rios, A. A. Coelho, P. L. Ferrandini, S. Gama, and R. Caram. Growth and morphological characterization of Al–Cr–Nb eutectic alloys. *Journal of Alloys and Compounds*, 402(1):156–161, 2005. 27

[173] S. Akamatsu, S. Bottin-Rousseau, G. Faivre, and E. A. Brener. Scaling theory of two-phase dendritic growth in undercooled ternary melts. *Physical Review Letters*, 112(10):105502, 2014. 28

[174] J. W. Cahn and J. E. Hilliard. Free energy of a nonuniform system. I. interfacial free energy. *The Journal of Chemical Physics*, 28(2):258–267, 1958. 29, 32, 173

[175] S. M. Allen and J. W. Cahn. A microscopic theory for antiphase boundary motion and its application to antiphase domain coarsening. *Acta Metallurgica*, 27(6):1085–1095, 1979. 29, 32, 173

[176] J. W. Cahn. On spinodal decomposition. *Acta metallurgica*, 9(9):795–801, 1961. 29, 32, 173, 178

[177] S. Y. Hu and L. Q. Chen. A phase-field model for evolving microstructures with strong elastic inhomogeneity. *Acta materialia*, 49(11):1879–1890, 2001. 29

[178] M. P. Gururajan and T. A. Abinandanan. Phase field study of precipitate rafting under a uniaxial stress. *Acta Materialia*, 55(15):5015–5026, 2007. 29

[179] A. Lahiri, T. A. Abinandanan, M. P. Gururajan, and S. Bhattacharyya. Effect of epitaxial strain on phase separation in thin films. *Philosophical Magazine Letters*, 94(11):702–707, 2014. 29

[180] J. S. Langer. Models of pattern formation in first-order phase transitions. *Directions in Concensed Matter Physics: Memorial Volume in Honor of Shang-Keng Ma. Edited by GRINSTEIN S ET AL. Published by World Scientific Publishing Co. Pte. Ltd., 1986. ISBN# 9789814415309, pp. 165-186*, pages 165–186, 1986. 29, 30

[181] B. I. Halperin, P. C. Hohenberg, and S. Ma. Renormalization-group methods for critical dynamics: I. recursion relations and effects of energy conservation. *Physical Review B*, 10(1):139, 1974. 30

[182] Joseph B. Collins and H. Levine. Diffuse interface model of diffusion-limited crystal growth. *Physical Review B*, 31(9):6119, 1985. 30

[183] O. Penrose and P. C. Fife. Thermodynamically consistent models of phase-field type for the kinetic of phase transitions. *Physica D: Nonlinear Phenomena*, 43(1):44–62, 1990. 30

[184] S. L. Wang, R. F. Sekerka, A. A. Wheeler, B. T. Murray, S. R. Coriell, R. J. Braun, and G. B. McFadden. Thermodynamically-consistent phase-field models for solidification. *Physica D: Nonlinear Phenomena*, 69(1-2):189–200, 1993. 30

[185] I. Steinbach, F. Pezzolla, B. Nestler, M. Seeßelberg, R. Prieler, G. J. Schmitz, and J. L. L. Rezende. A phase field concept for multiphase systems. *Physica D: Nonlinear Phenomena*, 94(3):135–147, 1996. 30

[186] B. Stinner, B. Nestler, and H. Garcke. A diffuse interface model for alloys with multiple components and phases. *SIAM Journal on Applied Mathematics*, 64(3):775–799, 2004. 30

[187] B. Nestler, H. Garcke, and B. Stinner. Multicomponent alloy solidification: phase-field modeling and simulations. *Physical Review E*, 71(4):041609, 2005. 30

[188] G. Caginalp and W. Xie. Phase-field and sharp-interface alloy models. *Physical Review E*, 48(3):1897, 1993. 30

[189] S. Wang and R. F. Sekerka. Computation of the dendritic operating state at large supercoolings by the phase field model. *Physical Review E*, 53(4):3760, 1996. 30

[190] W. Losert, D. A. Stillman, H. Z. Cummins, P. Kopczyński, W.-J. Rappel, and A. Karma. Selection of doublet cellular patterns in directional solidification through spatially periodic perturbations. *Physical Review E*, 58:7492–7506, 1998. 31

[191] A. A. Wheeler, W. J. Boettinger, and G. B. McFadden. Phase-field model for isothermal phase transitions in binary alloys. *Physical Review A*, 45(10):7424, 1992. 31

[192] S. G. Kim, W. T. Kim, and T. Suzuki. Interfacial compositions of solid and liquid in a phase-field model with finite interface thickness for isothermal solidification in binary alloys. *Physical Review E*, 58(3):3316, 1998. 31

[193] S. G. Kim, W. T. Kim, and T. Suzuki. Phase-field model for binary alloys. *Physical Review E*, 60(6):7186, 1999. 31

[194] R. Folch and M. Plapp. Towards a quantitative phase-field model of two-phase solidification. *Physical Review E*, 68(1):010602, 2003. 31

[195] N. A. Ahmad, A. A. Wheeler, W. J. Boettinger, and G. B. McFadden. Solute trapping and solute drag in a phase-field model of rapid solidification. *Physical Review E*, 58(3):3436, 1998. 31

[196] A. Karma. Phase-field formulation for quantitative modeling of alloy solidification. *Physical Review Letters*, 87(11):115701, 2001. 31

[197] B. Nestler and A. Choudhury. Phase-field modeling of multi-component systems. *Current opinion in solid state and Materials Science*, 15(3):93–105, 2011. 32

[198] M. Plapp. Unified derivation of phase-field models for alloy solidification from a grand-potential functional. *Physical Review E*, 84(3):031601, 2011. 32, 33, 115

[199] A. Choudhury and B. Nestler. Grand-potential formulation for multicomponent phase transformations combined with thin-interface asymptotics of the double-obstacle potential. *Physical Review E*, 85(2):021602, 2012. 32, 33, 115

[200] A. Choudhury and B. Nestler. Grand-potential formulation for multicomponent phase transformations combined with thin-interface asymptotics of the double-obstacle potential. *Physical Review E*, 85:021602, 2011. 40, 41, 149, 199

[201] J. S. Kirkaldy and D. G. Fedak. Nonplanar interfaces in two-phase ternary diffusion couples. *AIME TRANS*, 224(3):490–494, 1962. 74

[202] C. W. Taylor, M. A. Dayananda, and R. E. Grace. Multiphase diffusion in ternary Cu-Zn-Ni alloys. *Metallurgical and Materials Transactions B*, 1(1):127–131, 1970. 74

[203] C. W. Kim and M. A. Dayananda. Zero-flux planes and flux reversals in the Cu-Ni-Zn system at 775°C. *Metallurgical Transactions A*, 15(4):649–659, 1984. 74

[204] G. H. Cheng and M. A. Dayananda. Multiphase diffusion in Fe- Ni- Al system at 1000°C: I. diffusion structures and diffusion paths. *Metallurgical and Materials Transactions A*, 10(10):1407–1414, 1979. 74

[205] Y. H. Sohn and M. A. Dayananda. Diffusion studies in the β (B2), β'(bcc), and γ (fcc) Fe-Ni-Al alloys at 1000 °C. *Metallurgical and Materials Transactions A*, 33(11):3375–3392, 2002. 74

[206] T. Philippe, D. Blavette, and P. W. Voorhees. Critical nucleus composition in a multicomponent system. *The Journal of Chemical Physics*, 141(12):124306, 2014. 75

[207] C. J. Kuehmann and P. W. Voorhees. Ostwald ripening in ternary alloys. *Metallurgical and Materials Transactions A*, 27(4):937–943, 1996. 75

[208] T. Philippe and P. W. Voorhees. Ostwald ripening in multicomponent alloys. *Acta Materialia*, 61(11):4237–4244, 2013. 75

[209] J. S. Langer. Instabilities and pattern formation in crystal growth. *Reviews of Modern Physics*, 52(1):1, 1980. 79

[210] D. Tourret and A. Karma. Growth competition of columnar dendritic grains: A phase-field study. *Acta Materialia*, 82:64–83, 2015. 126

[211] A. Karma and A. Sarkissian. Morphological instabilities of lamellar eutectics. *Metallurgical and Materials Transactions A*, 27(3):635–656, 1996. 160

[212] S. Bottin-Rousseau, M. Şerefoğlu, S. Yücetürk, G. Faivre, and S. Akamatsu. Stability of three-phase ternary-eutectic growth patterns in thin sample. *Acta Materialia*, 109:259–266, 2016. 160

[213] A. Lahiri and A. Choudhury. Effect of surface energy anisotropy on the stability of growth fronts in multiphase alloys. *Transactions of the Indian Institute of Metals*, 68(6):1053–1057, 2015. 169, 185

[214] A. Karma. Phase-field model of eutectic growth. *Physical Review E*, 49(3):2245, 1994. 173

[215] J. S. Langer. Eutectic solidification and marginal stability. *Physical Review Letters*, 44(15):1023, 1980. 179